Université de Montréal

Thawing permafrost and land-atmosphere interactions of boreal forest-wetland landscapes in northwestern Canada

par
Manuel Helbig

Département de géographie
Faculté des arts et des sciences

Thèse présentée à la Faculté des études supérieures
en vue de l'obtention du grade de Philosophiæ Doctor (Ph.D.)
en géographie

mars, 2017

Université de Montréal
Faculté des études supérieures

Cette thèse intitulée:

Thawing permafrost and land-atmosphere interactions of boreal forest-wetland landscapes in northwestern Canada

présentée par:

Manuel Helbig

a été évaluée par un jury composé des personnes suivantes:

Daniel Fortier,	président-rapporteur
Oliver Sonnentag,	directeur de recherche
Olivier Blarquez,	membre du jury
Michael Loranty,	examinateur externe
Pierre-Luc Chagnon,	représentant du doyen de la FES

Thèse acceptée le: . . . . . .

RÉSUMÉ

Les forêts boréales stockent de grandes quantités de carbone organique et jouent un rôle important dans le climat planètaire. Le climat est étroitement associé à la surface terrestre à travers les flux de gaz à effet de serre, d'énergie et de vapeur d'eau. Dans la zone de pergélisol sporadique nord-américaine, l'affaissement du sol attribuable au dégel provoque l'expansion de milieux humides sans pergélisol remplaçant des forêts avec pergélisol. Cependant, l'étendue spatiale de ces changements et leurs conséquences sur le climat sont inconnues. Dans cette étude, j'analyse les flux turbulents d'un paysage comprenant des forêts boréales et des milieux humides dans la partie sud de la Taïga des plaines, T.N.-O., Canada. J'associe ces flux avec la modélisation d'empreintes de flux, des données satellite, des données paléoécologiques, et des projections climatiques afin de caractériser l'impact des changements de la couverture terrestre sur les interactions entre la terre et l'atmosphère.

Dans la Taïga des plaines, la perte de forêt boréale attribuable au dégel est d'une importance égale à celle due aux feux de forêt. La perte de forêt modifie les flux turbulents d'énergie à travers des changements dans les propriétés aérodynamiques et écophysiologiques de la surface terrestre. L'accroissement de l'albédo cause de petites réductions dans la somme des flux turbulents de chaleur sensible (H) et de chaleur latente (LE)). La diminution de la rugosité et l'augmentation de l'humidité de la surface augmentent toutefois LE tout en réduisant H, ce qui mènerait à une baisse des températures estivales et à une augmentation de l'humidité de l'air, d'après des simulations réalisées à l'aide d'un modèle de la couche limite planétaire.

Contrairement à l'effet biophysique de refroidissement du climat régional dû à la perte de couvert forestier, l'expansion des milieux humides et l'augmentation des émissions de méthane (CH_4) provoque un réchauffement du climat. L'expansion des milieux humides dans la partie sud de la Taïga des plaines entraîne une augmentation des émissions de 0.034 g CH_4 m^{-2} a^{-1}. Les taux d'absorption de CO_2 caractéristiques de ces paysages sont trop faibles pour neutraliser le réchauffement du climat dû aux émissions de CH_4 d'ici la fin du $21^{ème}$ siècle.

Tout en dégelant rapidement, ces paysages boréaux restent des puits de CO_2, absorbant 74 g CO_2 m^{-2} a^{-1}. L'expansion des milieux humides n'affecte pas les émissions nettes de CO_2, les changements de la productivité primaire brute (PPB) et de la respiration de l'écosystème (RE) étant d'une magnitude similaire. Les répercussions négligeables sur les flux nets de CO_2 sont largement compensées par les répercussions climatiques directes d'un réchauffement de la température de l'air. Un scénario de réchauffement élevé mène à un accroissement de RE dépassant significativement l'accroissement de PPB.

Dans la Taïga des plaines, le dégel du pergélisol a donc des répercussions climatiques qui s'opposent aux plans biophysiques et biogéochimiques. Dans un climat plus chaud, le dégel modifie la façon dont les paysages interagissent avec le climat, ce qui souligne la nécessité d'intégrer les changements dans la couverture terrestre attribuable au dégel dans les modèles du système Terre.

Mots clés: Changement climatique, forêt boréale, tourbière, covariance des turbulences, changement dans la couverture terrestre, pergélisol, dioxyde de carbone, méthane, évapotranspiration, télédétection.

ABSTRACT

Boreal forests store large amounts of organic carbon and are an important component of the regional and global climate systems. Climate and land surface are closely coupled through the land-atmosphere exchange of greenhouse gases, such as CO_2 and CH_4, and of energy and water vapor. In lowlands of the North American sporadic permafrost region, thaw-induced surface subsidence leads to expansion of permafrost-free wetlands at the expense of boreal forests underlain by permafrost. However, the spatial extent of these land cover changes and their implications for land-atmosphere interactions are unknown. In this study, I analyze eddy covariance flux measurements from an organic-rich boreal forest-wetland landscape in the southern Taiga Plains, NT, Canada. I combine these measurements with flux footprint modeling, satellite remote sensing data, paleoecological records, and downscaled climate projections to characterize how thaw-induced land cover change affects land-atmosphere interactions and climate.

In the Taiga Plains ecozone, thaw-induced boreal forest loss currently transforms the composition and structure of the boreal zone in North America and is of equal importance for tree cover dynamics as wildfire disturbance. Forest loss modifies land-atmosphere energy fluxes through changes in aerodynamic and ecophysiological land surface properties. On the one hand, increasing albedo decreases total turbulent energy fluxes (i.e., sensible (H) and latent heat (LE) flux), and on the other hand decreasing surface roughness and increasing wetness enhances LE at the expense of H. The resulting maximum summer air temperatures and humidity would be substantially colder (1-2 $^{\circ}$C) and wetter (2 mmol mol^{-1}) in a hypothetical permafrost-free wetland landscape, as indicated by planetary boundary layer model simulations.

In contrast to the regional biophysical climate cooling impact of thaw-induced land cover change, wetland expansion and related increases in landscape CH_4 emissions induce a net global biogeochemical climate warming impact. At the current rate of wetland expansion in the southern Taiga Plains of 0.26 % yr^{-1}, landscape CH_4 emissions increase by 0.034 g CH_4 m^{-2} yr^{-1}. Typical rates of long-term net CO_2 uptake in these landscapes are too small to neutralize the associated climate warming effect until the end of the 21st

century.

The rapidly thawing boreal forest-wetland landscape still acts as a net CO_2 sink taking up 74 g CO_2 m^{-2} yr^{-1}. Wetland expansion does not affect landscape-level net CO_2 uptake as changes in gross primary productivity (GPP) and ecosystem respiration (ER) are of similar magnitude. The negligible thaw-induced effects on net CO_2 fluxes are contrasted by larger direct climate change impacts of warming air temperatures and reduced incoming shortwave radiation. For a high warming scenario (RCP8.5), increases in modeled ER outpace the increasing GPP significantly. For a moderate warming scenario (RCP4.5), ER and GPP increase are of similar magnitude.

Thaw-induced land cover change in the Taiga Plains causes thus biophysical and biogeochemical climate impacts of opposite sign and at contrasting scales of impacts (regional vs. global). In an increasingly warmer climate, thawing permafrost alters how boreal landscapes interact with climate highlighting the need to incorporate thaw-induced land cover changes into global Earth system models.

Keywords: Climate change, boreal forest, wetlands, eddy covariance, land cover change, permafrost, carbon dioxide, methane, evapotranspiration, remote sensing.

CONTENTS

LIST OF TABLES

LIST OF FIGURES

LIST OF APPENDICES

LIST OF ABBREVIATIONS

A	Radiative efficiency
AoI	Area of interest
C	Carbon
CH_4	Methane
CI	Confidence interval
CLM	Community Land Model
CMIP5	Coupled Model Intercomparison Project
CNDFB	Canadian National Fire Database
CO_2	Carbon dioxide
CORDEX	Coordinated Regional Climate Downscaling Experiment
C_p	Heat capacity of air
d_0	Zero-plane displacement height
DOC	Dissolved organic carbon
EBC	Energy balance closure
ER	Ecosystem respiration
ESM	Earth system model
F_{CH4}	net methane flux
FOR	Forest
FP	Footprint
FR_{fire}	Fraction of pixel affected by recent fires
$FR_{regrowth}$	Fraction of pixel affected by historical fires
g_H	Aerodynamic conductance fpr heat and water vapor
G	Soil heat flux
GPP	Gross primary productivity
g_s	Bulk surface conductance for water vapor
G_{s_bound}	Maximum surface conductance for water vapor
GWP	Global warming potential
H	Turbulent sensible heat flux

H_2O	Water
LAND	Landscape
LARCA	Long-term apparent rates of carbon accumulation
LiDAR	Light-Detection And Ranging
LE	Turbulent latent heat flux
MAAT	Mean annual air temperature
MAP	Mean annual precipitation
MODIS	Moderate Resolution Imaging Spectroradiometer
mPZI	mean permafrost zonation index
MST	Mountain Standard Time
NE	Nebraska
NEE	net ecosystem carbon dioxide exchange
NT	Northwest Territories
PBL	Planetary boundary layer
POT	Potential
PTC	Precent tree cover
PZI	Permafrost zonation index
Q_{10}	Temperature sensitivity parameter
q_a	Specific humidity of air
Q_m	Snowmelt energy
q_s	Saturated specific humidity of air
R_n	Net radiation
RCM	Regional climate model
RCP	Representative Concentration Pathway
r_{CH4} & r_{CO2}	Atmospheric CH_4 & CO_2 concentration perturbation
S	Rate of change of heat storage
SLC	Soil Landscape of Canada database
SSA	Singular spectrum analysis
SW_{in}	Short-wave incoming radiation
T_a	air temperature

T_{as}	Aerodynamic surface temperature
T_{rs}	Radiometric surface temperature
T_s	Soil temperature
u*	friction velocity
U	wind speed
UT	Utah
VPD	Vapor pressure deficit
WET	Wetland
WSA	White-sky albedo
WTD	Water table depth
z_{0m}	Aerodynamic roughness length for momentum
α_i	Initial canopy quantum efficiency
ζ	Stability parameter
θ_m	potential air temperature
λ	Latent heat of vaporization
ρ	Density of air
τ_{CH4} & τ_{CO2}	Atmospheric lifetime of CH_4 & CO_2
Ψ	Stability function

ACKNOWLEDGMENTS

I would like to thank my PhD advisor Oliver Sonnentag for his great support during the last four years. His enthusiasm for science encouraged me to broaden my horizon by exploring new approaches to investigate land-atmosphere interactions. Also, I will always be grateful to him for introducing me to a broader research network.

I had the pleasure to work with and learn from many colleagues during the last four years. I learned a lot on footprint modeling and remote sensing by working with Laura Chasmer and Natascha Kljun, on permafrost hydrology from Bill Quinton, on the fundamentals of eddy covariance measurements from Ivan Bogoev, Gerardo Fratini, and George Burba, and on peatland science from Lars Kutzbach, Nigel Roulet, and Tim Moore. I benefited from insightful and fruitful discussions with Ankur Desai, Julie Talbot, Claire Treat, and many other colleagues. Throughout my PhD, I met many inspiring colleagues and fellow graduate students at various summer schools. It was a tremendous help and motivation for my PhD research to share and discuss my ideas with them. Therefore, I would like to express my sincere gratitude to the organizers, instructors, and participants of these summer schools.

I gratefully acknowledge the financial support through the Fonds de recherche du Québec - Nature et technologies (FRQNT), the German Academic Exchange Service (DAAD), and the J. Armand Bombardier Foundation and the scientific instrument support from Decagon Devices and Campbell Scientific. Operational and infrastructure funding to study land-atmosphere interactions at Scotty Creek was provided through the Canada Research Chairs, the Canada Foundation for Innovation Leaders Opportunity Fund, and the Natural Sciences and Engineering Research Council Discovery Grant programs. I acknowledge logistics support received through the Polar Continental Shelf Program.

I am grateful to everybody working with me at the Scotty Creek Research Station. You made my field trips always enjoyable and without your help in the field, this thesis would not have been possible. In particular, Karo Wischnewski and Gabriel Gosselin helped collecting and processing most of the field data for this thesis. I am also thankful

to the Liidlii Kue First Nation and Jean-Marie River First Nation for supporting our research at Scotty Creek.

I am thankful for the academic and non-academic support of my fellow students and friends in Montréal and elsewhere: Tanja Živković, Avni Malhotra, Luc Pelletier, Nicolas Pelletier, Chris Pappas, Gabriel Gosselin, Martine Verdy, and Silvie Harder. You made my PhD enjoyable and I will keep these years in good memory.

In my thesis, I have used a wide range of freely-available datasets. Sharing scientific data benefits the entire scientific community and enables new, exciting discoveries. Therefore, I wish to express my appreciation to everybody involved in collecting, processing, and distributing these datasets.

For more than three decades, my parents Silvia and Volkmar and my sister Elisa have supported and assisted me making this thesis possible. I am deeply grateful that you have always supported me in my decisions; even if it involved crossing an ocean. Our numerous family travels across Europe sparked my interest to pursue Earth system science research. And of course, Tanja's support, humor, and love helped me finishing my PhD. Thank you for being on my side!

Contributions of authors

Chapter 2 to 5 in this thesis are published in peer-reviewed scientific journals with contributions from various co-authors:

Chapter 2: **Helbig M**, Pappas C and O Sonnentag (2016), Permafrost thaw and wildfire: equally important drivers of boreal tree cover change in the Taiga Plains, Canada, *Geophysical Research Letters, 43,* 1598-1606.

Chapter 3: **Helbig M**, Wischnewski K, Kljun N, Chasmer L E, Quinton W L, Detto M and O Sonnentag (2016), Regional atmospheric cooling and wetting effect of permafrost thaw-induced boreal forest loss, *Global Change Biology, 22,* 4048–4066.

Chapter 4: **Helbig M**, Chasmer L E, Kljun N, Quinton W L, Treat C C and O Sonnentag (2016), The positive net radiative greenhouse gas forcing of increasing methane emissions from a thawing boreal forest-wetland landscape, *Global Change Biology,*

doi:10.1111/gcb.13520.

The initially submitted version of Chapter 5 (November 2016) was in review at *Global Change Biology*. The revised version, as included in the final version of the thesis, was published in *Global Change Biology* in January 2017:

Chapter 5: **Helbig M**, Chasmer L E, Desai A R, Kljun N, Quinton W L, and O Sonnentag (2017), Direct and indirect climate change effects on carbon dioxide fluxes in a thawing boreal forest-wetland landscape, *Global Change Biology,* doi:10.1111/gcb.13638.

For all manuscripts, I designed and performed the research, was the main contributor to the analysis and intepretation of the data, and wrote the papers. All co-authors contributed to the writing by providing critical reviews and comments on the manuscripts. For chapters 2 to 5, Oliver Sonnentag was involved in planning and acquiring funds for the research and contributed to the development of ideas and conceptualization of the studies. Christoforos Pappas contributed to the analysis and interpretation of the data for chapter 2.

For chapters 3 to 5, Laura Chasmer contributed land cover classification data and helped interpreting spatio-temporal dynamics in eddy covariance fluxes. Natascha Kljun performed the flux footprint modeling for chapters 3 to 5 and helped interpreting spatio-temporal dynamics in eddy covariance fluxes. For chapters 3 to 5, William Quinton provided resources in the form of scientific instrumentation and access to the Scotty Creek field station.

For chapter 3, Karoline Wischnewski helped conducting and maintaining eddy covariance flux measurements and contributed to the processing of high-frequency eddy covariance data. Matteo Detto contributed to the development of ideas and to the interpretation of eddy covariance fluxes in chapter 3. For chapter 4, Claire Treat provided paleoecological data on long-term apparent recent carbon accumulation rates and helped in their interpretation. For chapter 5, Ankur Desai contributed to the development of ideas and conceptualization of the study and to the interpretation of downscaled climate projections.

CHAPTER 1

INTRODUCTION

1.1 Boreal forests and permafrost in the climate system

In the boreal zone, climate change is expected to alter landscape composition and structure (e.g., *Koven*, 2013). Warmer air temperatures improve growing conditions at the boreal-tundra ecotone inducing enhanced growth of shrubs and northward tree-line shifts (e.g., *Myers-Smith et al.*, 2011; *Ohse et al.*, 2012). Enhanced fire frequency, size, and severity may increase the cover of deciduous tree species at the expense of coniferous species (e.g., *Beck et al.*, 2011b; *Weber and Flannigan*, 1997), and thawing permafrost results in the expansion of permafrost-free wetlands at the expense of black spruce forests in lowland regions of the sporadic permafrost zone (e.g., *Quinton et al.*, 2011). Such climate-induced land cover changes potentially influence regional and global climates through altered land-atmosphere interactions (*Davies-Barnard et al.*, 2015). The resulting effects on climate can be classified into biogeochemical and biophysical impacts (*Chapin et al.*, 2000). Biogeochemical impacts are caused by changes in the net exchange of well-mixed greenhouse gases between land and atmosphere and directly affect the global climate through their effect on atmospheric long wave radiation (e.g., *Davin et al.*, 2007). In the boreal zone, such climate impacts are mainly related to fluxes of carbon dioxide (CO_2) and methane (CH_4). Biophysical impacts are caused by changes in the net land-atmosphere exchange of energy and water vapor (H_2O) resulting in altered atmospheric longwave radiation (through atmospheric water vapor content) and in shifts in net shortwave radiation (through albedo) or in the partitioning of available energy into latent and sensible heat. Biophysical climate impacts are most pronounced on regional scales (e.g., *Alkama and Cescatti*, 2016), while biogeochemical climate impacts affect global climate through changes in the global atmospheric greenhouse gas budget (*Davin et al.*, 2007) (Fig. 1.1). The net climate impacts from both biogeochemical and biophysical changes will thus determine how thaw-induced land cover change

affects the climate of the boreal zone (*Chapin et al.*, 2000). Local studies have reported an acceleration of thaw-induced wetland expansion in the sporadic permafrost zone of Alaska and northwestern Canada (*Baltzer et al.*, 2014; *Lara et al.*, 2016; *Quinton et al.*, 2011), but it remains unclear how these land cover changes interact with regional and global climates.

In this thesis, I aim to provide a better functional understanding of the impact of permafrost thaw-induced wetland expansion on land-atmosphere interactions in lowland boreal forest-wetland landscapes, more specifically on the land-atmosphere exchange of energy, H_2O, CO_2, and CH_4. Understanding how these interactions change in a warming climate is an important prerequisite to predict climate feedbacks in the boreal zone (e.g., *Euskirchen et al.*, 2016).

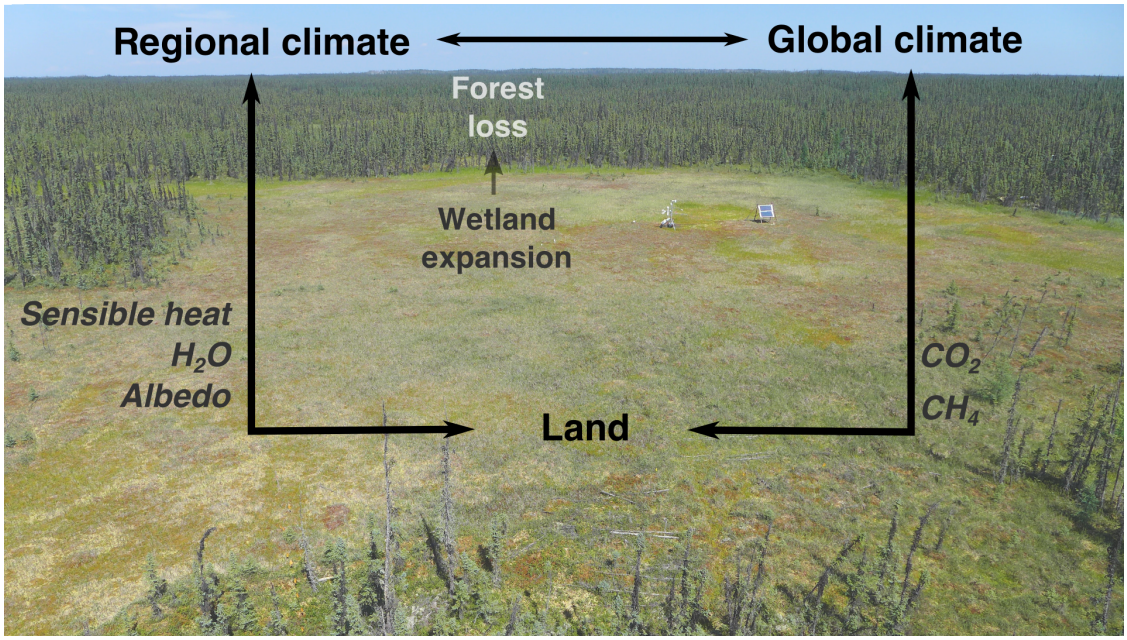

Figure 1.1 – Land-atmosphere interactions and their impact on the regional and the global climate. Photograph shows thawing boreal forest-wetland landscape at Scotty Creek. Adapted from *Chapin et al.* (2000).

I focus on land-atmosphere interactions in the southern Taiga Plains, a lowland region at the southern limit of permafrost in northwestern Canada. There, wetland expansion and forest loss has been observed as a result of accelerated permafrost thaw

(*Baltzer et al.*, 2014; *Quinton et al.*, 2011). Boreal landscapes in the Taiga Plains have accumulated large soil organic carbon (C) stocks as peat (*Robinson and Moore*, 1999). With about 70 Pg organic C, surface soils (0 - 3m) in the Taiga Plains store about 15 % of the surface organic C pool of the North American permafrost zone and 7 % of the surface organic C pool of the northern circumpolar permafrost zone (data from *Hugelius et al.*, 2013, Fig. 1.2). Large parts of the Taiga Plains are characterized by landscapes comprising a mix of peat-accumulating forest and wetland ecosystems (i.e., peatlands) with a maximum peat thickness of 5 m (*Aylsworth et al.*, 1993). In the southern Taiga Plains, thawing permafrost in organic-rich soils leads to rapid surface subsidence (i.e., thermokarst) abruptly increasing moisture in the surface soils (*Baltzer et al.*, 2014; *Olefeldt et al.*, 2016). The altered growing conditions favor the growth of aquatic species (e.g., *Sphagnum* spp. and *Carex*) and lead to a decline of black spruce (*Picea mariana*) and shrub cover, overall changing the vegetation composition of these landscapes (*Camill et al.*, 2001). Both changing hydrological and thermal soil conditions and shifts in vegetation composition and structure may result in a modified net land-atmosphere exchange of energy, H_2O, CO_2, and CH_4.

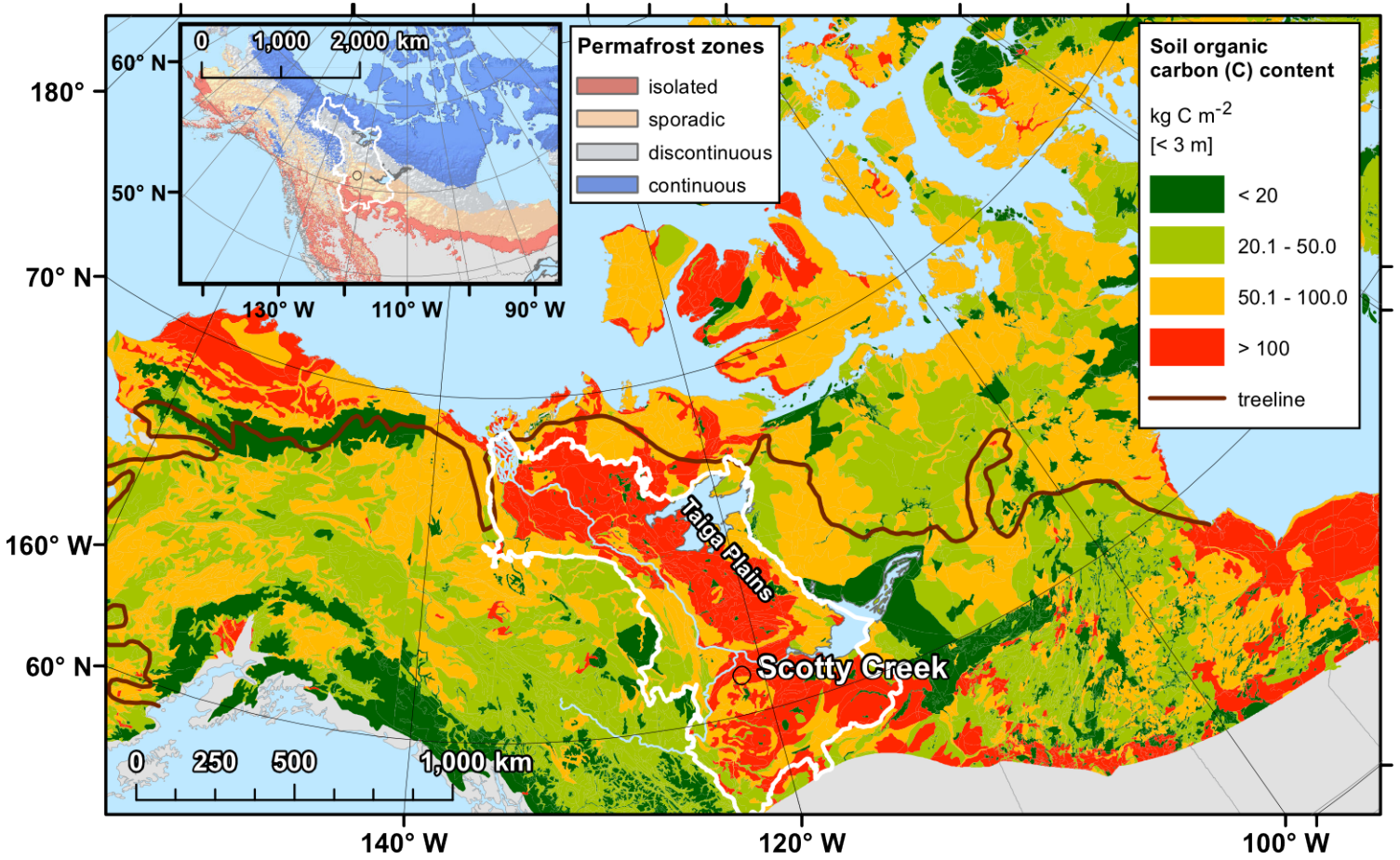

Figure 1.2 – Surface organic carbon stocks (0 - 3 m) in the North American permafrost zone (data from *Hugelius et al.*, 2013). The white solid line delineates the Taiga Plains ecozone and the black circle indicates the location of the Scotty Creek watershed. The inset map shows the distribution of permafrost zones in North America (data from *Gruber*, 2012).

Quantifying impacts of thaw-induced land cover change on regional and global climates requires knowledge on both the rate of land cover change (e.g., percentage of wetland expansion per year) and on the direct effect of land cover change on land-atmosphere interactions (e.g., increase in net CH_4 flux per m^2 of forest-to-wetland conversion). Land-atmosphere interactions are the result of interactions between atmospheric (meteorological) forcing (e.g., air temperature or solar radiation) and an ecosystem (or landscape) response to such a forcing (e.g., light-response curve of gross canopy photosynthesis, surface conductance response to water vapor pressure deficit, *Sellers et al.*, 1997, Fig. 1.3). In a warmer climate, net exchanges of energy, H_2O, CO_2, and CH_4 in the boreal zone will be altered directly by changes in meteorological forcing (e.g., warmer air and soil temperatures; Fig. 1.3b) and indirectly through changes in the ecosystem (or landscape) response to meteorological forcing (e.g., stronger sensitivity of methane production to temperature; Fig. 1.3b). In this thesis, I mainly focus on how thaw-induced wetland expansion alters landscape responses to meteorological forcing.

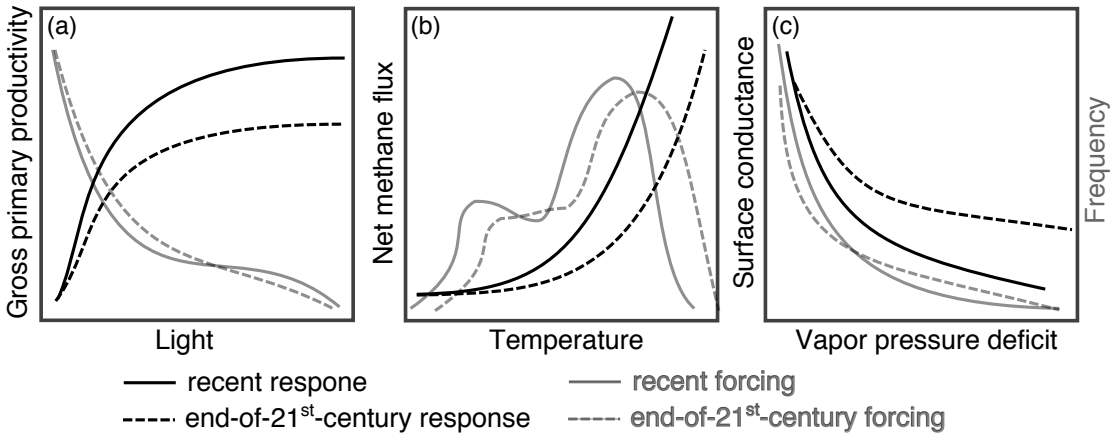

Figure 1.3 – Conceptual models of direct and indirect climate change effects on land-atmosphere interactions. Solid and dashed black lines indicate a change in ecosystem response (i.e., indirect) to a meteorological forcing regarding **(a)** gross primary productivity (light), **(b)** methane production (temperature), and **(c)** surface conductance (vapor pressure deficit). Solid and dashed gray lines indicate a change in the respective meteorological forcing (i.e., direct effect).

1.2 Land-atmosphere interactions and their meteorological and environmental drivers

Net landscape exchanges of sensible heat, H_2O (i.e., latent heat), CO_2, and CH_4 are controlled by different environmental and meteorological conditions. Thaw-induced wetland expansion, and related changes in environmental conditions, could therefore result in impacts on land-atmosphere interactions differing in magnitude or in direction, depending on the specific changes in their respective environmental and meteorological drivers. For example, forest-to-wetland conversion increases albedo and directly reduces the total energy available for sensible, latent, and ground heat flux (*Betts and Ball*, 1997), but thaw-induced eco-physiological changes in soil moisture conditions and vegetation structure and composition control how much of this energy is partitioned into sensible and latent heat (*Stiegler et al.*, 2016). Together, albedo and eco-physiological changes may modify both surface temperatures and air temperature and humidity in the planetary boundary layer, and thus regional climate (*Juang et al.*, 2007b).

The net ecosystem and landscape exchanges of CO_2 and CH_4 are the result of complex interactions of a multitude of processes. Net CO_2 exchange is the balance of two larger component fluxes: gross primary productivity (GPP) and ecosystem respiration (ER) (*Chapin et al.*, 2006). GPP is mainly controlled by the interaction of light, air temperature, and atmospheric water demand as meteorological forcing (e.g., *Hill et al.*, 2011; *Lasslop et al.*, 2010; *Luyssaert et al.*, 2007; *Novick et al.*, 2016; *Tanja et al.*, 2003) and by vegetation and ecosystem characteristics such as leaf area index, nutrient and soil moisture availability determing the response to these forcing variables (e.g., *Kimball et al.*, 1997; *Krishnan et al.*, 2006; *Ueyama et al.*, 2013; *Wieder et al.*, 2015). ER is mainly driven by air and soil temperature and moisture controlling temporal dynamics in the rate of autotrophic (i.e., living biomass) and heterotrophic (i.e., microbial decomposition in soils) respiration (*Dunn et al.*, 2007; *Krishnan et al.*, 2006; *Lafleur et al.*, 2005; *Ueyama et al.*, 2014). How ER responds to these meteorological and environmental forcings depends on biomass and vegetation composition (e.g., young versus old forest stands) and on litter quality, nutrient availability, and the amount of decompos-

able soil organic C (e.g., *Cleveland et al.*, 2013; *Davidson and Janssens*, 2006; *Kimball et al.*, 1997; *Larmola et al.*, 2013; *Yuan et al.*, 2008). In boreal permafrost peatlands, the amount of soil organic C available for microbial decomposition depends on soil thaw depth as microbial activity is strongly suppressed below the freezing point (e.g., *Dioumaeva et al.*, 2002; *McConnell et al.*, 2013; *Schädel et al.*, 2016; *Schuur et al.*, 2015). Thus, increasing thaw and eventual disappearance of permafrost in these soils may enhance heterotrophic respiration and, consequently, also ER (*Schädel et al.*, 2016).

Being a microbial process similar to heterotrophic respiration of CO_2, CH_4 production by methanogens in soils responds to variations in soil temperature, litter quality, and nutrient availability (*Chanton et al.*, 2008; *Dunfield et al.*, 1993; *Prater et al.*, 2007; *Yavitt et al.*, 2006). In contrast to heterotrophic respiration of CO_2, CH_4 production is enhanced under anoxic conditions (e.g., *Lee et al.*, 2012; *Schädel et al.*, 2016) and varies therefore with water table fluctuations (*Bubier et al.*, 2005; *Kettunen et al.*, 1999). However, only a fraction of the produced CH_4 reaches the surface and is transported into the atmosphere. How much CH_4 is oxidized by methanotrophs depends again on several environmental factors such as water table depth (i.e., depth of the oxic soil layers), soil temperature and moisture, and the density of plants with aerenchyma tissue allowing CH_4 to bypass the oxidation layers through the roots (e.g., *Flessa et al.*, 2008; *Joabsson et al.*, 1999; *Sundh et al.*, 1994; *Treat et al.*, 2007).

At the southern limit of the permafrost zone in North America, both meteorological conditions (see climate change projections for a boreal landscape in the sporadic permafrost zone of northwestern Canada in Fig. 1.4) and landscape structure and composition (e.g., landscape hydrology, leaf area index; *Baltzer et al.*, 2014) are rapidly changing in a warming climate. An improved understanding of the impact of these changes on the close coupling between land surface and atmosphere is therefore needed to improve future climate projections. Many of the above-mentioned individual controls on land-atmosphere interactions are well understood. However, the magnitude, or in some cases even the direction of the impacts of thaw-induced wetland expansion on land-atmosphere interactions remains poorly constrained due to the multitude of complex interactions between meteorological and environmental controls and the respective

ecosystem responses. Better constraining these climate change impacts requires efforts to quantify thaw-induced land cover change rates and their effect on land surface characteristiscs. At the southern edge of the permafrost zone, where thawing boreal landscapes are rapidly being transformed, direct measurements of net landscape exchanges of sensible heat, H_2O, CO_2, and CH_4 provide an important opportunity to monitor, investigate, and quantify impacts of thaw-induced land cover change on land-atmosphere interactions.

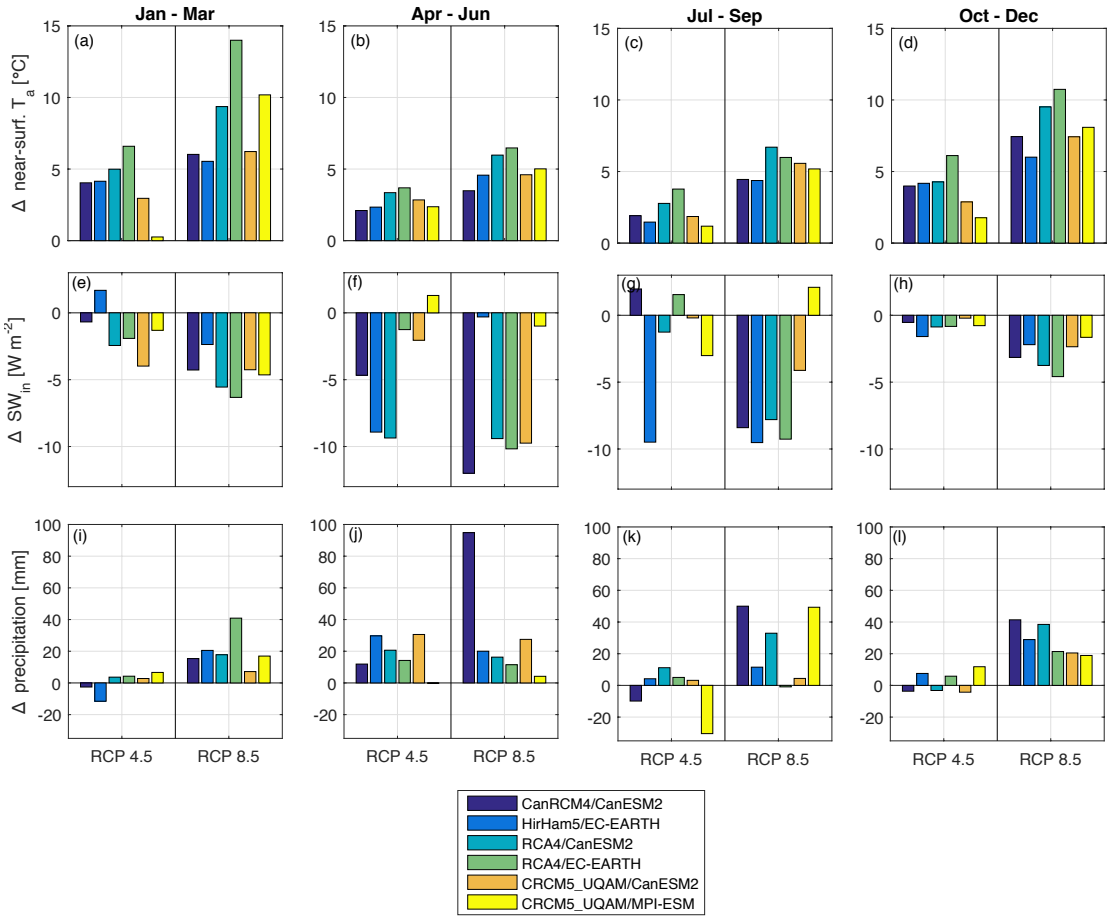

Figure 1.4 – Projected end-of-21st-century changes (2091-2100) in **(a-d)** near-surface air temperature (T_a), **(e-h)** incoming shortwave radiation (SW_{in}), and **(i-l)** precipitation compared to the current conditions (2006-2015). Changes are shown for two representative concentration pathways (RCP4.5 and RCP8.5) and for four seasons. Colors of bars indicate the regional/global climate model combination. Positive values indicate larger T_a, SW_{in}, and precipitation at the end of the 21st century.

1.3 Methodological approaches to characterize changing land-atmosphere interactions

1.3.1 Eddy covariance flux measurements

Energy and matter are transported between the land surface and the atmosphere with up- and downward moving air parcels due to turbulent atmospheric motions. The turbulent flux (densities) of energy and matter (in J m^{-2} s^{-1} and mol m^{-2} s^{-1}, respectively) can be derived with the eddy covariance technique from the covariance of high-frequency fluctuations of vertical wind speed and air temperature (T_a, °C), H_2O, CO_2, or CH_4 concentration (or density) (*Baldocchi*, 2014, 2003). High-frequency vertical wind velocity and T_a are usually derived from speed-of-sound measurements with sonic anemometers. High-frequency H_2O, CO_2, or CH_4 densities are measured with infrared CO_2/H_2O gas analyzers and laser-based CH_4 gas analyzers (e.g., *Detto et al.*, 2011; *Leuning and Moncrieff*, 1990). Two types of gas analyzer systems are currently used for eddy covariance measurements: open- and closed-path systems (Fig. 1.5). Open-path gas analyzers measure molar densities *in-situ* at the measurement height, whereas closed-path gas analyzers draw air from a tube inlet at measurement height to the spatially separated measurement cell. In contrast to open-path gas analyzers, closed-path gas analyzers reliably measure molar densities under adverse weather conditions (e.g. rain, dew) (*Novick et al.*, 2013), but require higher power supply for the operation of the pump drawing sampling air into the optical cell. Lower power consumption and less maintenance demand of open-path gas analyzers make them particularly suitable for eddy covariance measurements at remote high-latitude field sites where adequate power supply represents a major constraint on year-round flux measurements (*Goodrich et al.*, 2016). However, particularly over cold boreal forests, turbulent CO_2 flux measurements with open-path gas analyzers have been shown to be subject to large uncertainties due to their sensitivity to air temperature and humidity fluctuations (*Amiro*, 2010). Thus, closed-path gas analyzers have long been the instrument-of-choice for long-term CO_2 flux measurements at such sites (e.g., *Goulden et al.*, 2006). Recent developments in open-path CO_2/H_2O and CH_4 gas analyzers have improved their performance for high-latitude flux measure-

ments, now allowing long-term, quasi-continuous measurements of turbulent fluxes of energy, H_2O, CO_2, and CH_4 at remote field sites (Fig. 1.6a, *Goodrich et al.*, 2016; *Helbig et al.*, 2016a).

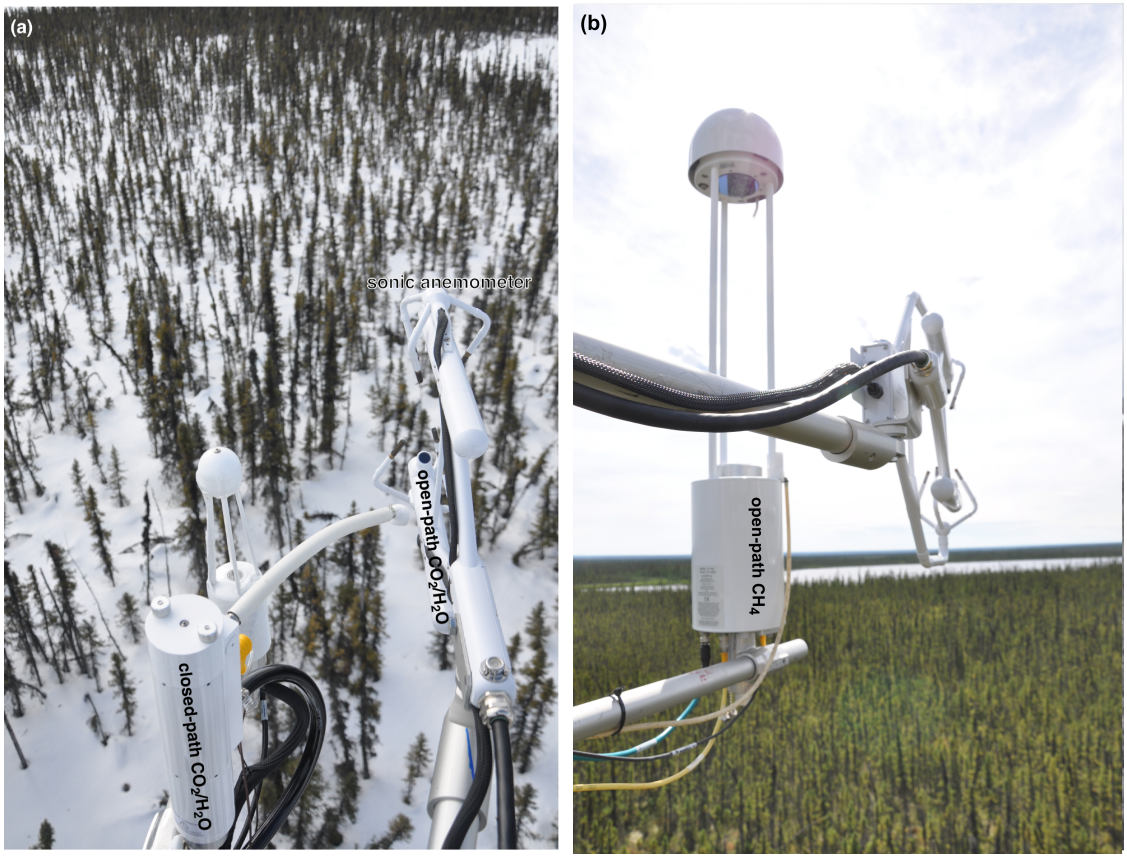

Figure 1.5 – **(a)** Eddy covariance CO_2/H_2O flux measurement setup with sonic anemometer and open- and closed-path infrared CO_2/H_2O gas analyzers. **(b)** Eddy covariance CH_4 flux measurement setup with sonic anemometer and laser-based CH_4 gas analyzer.

1.3.2 Remote sensing

Recent advances in remote sensing enable global near-realtime Earth observations of a wide variety of land surface characteristics derived from spectral signatures measured with optical sensors. *In-situ* measurements of land-atmosphere interactions (e.g., eddy covariance flux measurements) provide in-depth insights into land surface processes, but measurement footprints are restricted to a limited spatial extent (e.g., 1 km^2, *Schimel*

et al., 2015). Combining *in-situ* measurements with satellite remote sensing data thus improves the capability to assess changes in land-atmosphere interactions at broader spatial scales (e.g., from local to regional to global). Since 2000, Moderate Resolution Imaging Spectroradiometer (MODIS) products with a resolution of <1 km provide continuous time series of vegetation structure variables, such as percentage of tree cover (e.g., *Potapov et al.*, 2008), of land surface properties, such as land surface temperature (e.g., *Mildrexler et al.*, 2011, Fig. 1.6b) and albedo (e.g., *Jin et al.*, 2003), or of active wildfire perimeters (e.g., *Justice et al.*, 2002). Combined with forest service ground observation data, the latter improve wildfire activity monitoring in remote high-latitude regions (e.g., Canadian National Fire Information System, *Burton et al.*, 2008). With time series exceeding ten years, these products provide powerful tools to assess how spatio-temporal patterns in landscape structure affect land surface properties (e.g., *Jin et al.*, 2012) and how land cover and vegetation structure change over time (e.g., *Hansen et al.*, 2010).

1.3.3 Paleoecological methods

In boreal peatlands, where large organic C stocks have accumulated over centuries to millenia (e.g., *Treat et al.*, 2016), paleoecological methods can reveal important information on long-term apparent C accumulation rates (LARCA, Fig. 1.6c) and complement contemporary short-term measurements of net CO_2 and CH_4 exchange (*Roulet et al.*, 2007). The peatland LARCA is the result of long-term net CO_2 uptake, net CH_4 release, and the net lateral export of dissolved organic C (DOC) (*Roulet et al.*, 2007). Assuming that lateral export of DOC in permafrost environments is relatively small compared to net CO_2 and CH_4 fluxes (*Moore*, 2003; *Olefeldt et al.*, 2012), LARCA approximates the balance of net CO_2 uptake and CH_4 release. Both C fluxes can be measured with the eddy covariance technique (except for losses due to fire disturbance *Chapin et al.*, 2006). Their long- and short-term balance (i.e., LARCA and eddy covariance) can thus be analyzed to gain insights into historical and contemporary peatland development (*Roulet et al.*, 2007). Recent synthesis studies of peatland LARCAs across the circumpolar permafrost zone (*Treat et al.*, 2016) provide important information to

compare site-specific direct measurements of net C ($C\text{-}CO_2$ and $C\text{-}CH_4$) fluxes to long-term C dynamics of similar peat-accumulating landscapes.

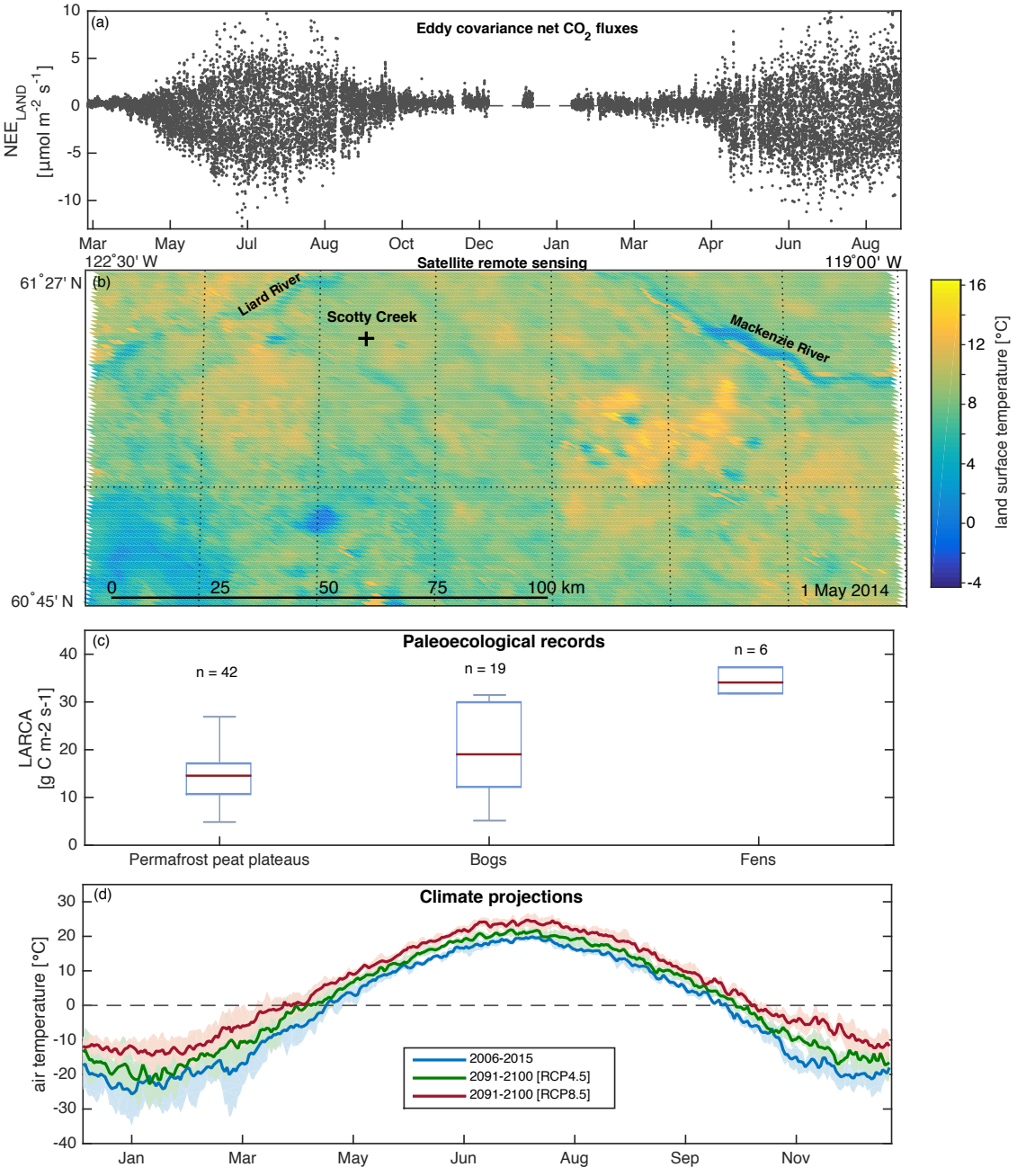

Figure 1.6 – **(a)** Net landscape CO_2 flux (NEE_{LAND}) measurements of a boreal forest-wetland landscape. **(b)** MODIS-derived land surface temperature at the end of the snow melt period in 2014 for an area surrounding the flux tower location in the southern Taiga Plains. **(c)** Boxplots of long-term apparent rates of carbon accumulation (LARCA) for three boreal peatland types in the permafrost zone of North America (data from *Treat et al.*, 2016). **(d)** Downscaled and debiased projections of air temperatures (50 km x 50 km) at the flux tower site from six regional climate/Earth system model simulations. Solid lines indicate the ensemble mean and shaded areas the mean $\pm$ one standard deviation.

1.3.4 Modeling

1.3.4.1 Combining simple models of land-atmosphere interactions with eddy covariance flux data

Eddy covariance measurements of net landscape exchange of energy, H_2O, CO_2, and CH_4 allow to quantify annual and monthly budgets and to characterize their seasonal dynamics. However, modeling approaches are required to improve the understanding of underlying processes and to assess potential future impacts on net energy, H_2O, CO_2, and CH_4 exchanges (e.g., *Fisher et al.*, 2014; *Prinn*, 2013). For example, simple atmospheric boundary layer models combined with sensible and latent heat eddy covariance flux measurements enable quantifying the impact of land cover change on near-surface climates (e.g., convective rainfall or near-surface air temperatures, *Baldocchi and Ma*, 2013; *Juang et al.*, 2007a). The underlying changes in land surface and vegetation properties can be derived by combining surface layer theory (e.g., Monin-Obukhov similarity), simple bulk models of vegetation controls on evapotranspiration, and eddy covariance measurements of sensible and latent heat fluxes (e.g., *Betts et al.*, 1999). Similarly, light- and temperature-response models are used with net CO_2 flux measurements to derive the component fluxes GPP and ER and to characterize differential ecosystem responses to meteorological forcing (e.g., *Lasslop et al.*, 2010; *Reichstein et al.*, 2005; *Runkle et al.*, 2013).

1.3.4.2 Flux footprint modeling

Thawing permafrost in boreal lowlands leads to highly fragmented landscapes with a pronounced small-scale land cover heterogeneity (*Baltzer et al.*, 2014), potentially also reflected in a pronounced small-scale hetereogeneity in net fluxes of energy, H_2O, CO_2, and CH_4 (e.g., *Bubier et al.*, 1995; *Stiegler et al.*, 2016). The spatial heterogeneity in surface fluxes is captured by eddy covariance flux measurements when changes in atmospheric conditions (e.g., wind direction, atmospheric stability) shift the source area (i.e., the flux footprint) of the measured flux (e.g., *Griebel et al.*, 2016). The variability in eddy covariance flux measurements is thus composed of both temporal (e.g., driven by

changes in soil temperature or light) and spatial flux dynamics (i.e., driven by footprint variability). Recent developments in flux footprint models (e.g., *Kljun et al.*, 2015) allow delineating the source areas of half-hourly flux measurements. Combined with high-resolution land cover classification maps, half-hourly contributions from individual land cover types can be quantified (e.g., *Helbig et al.*, 2016b). This information can be used to disentangle the temporal and spatial signals in eddy covariance fluxes and to resolve spatio-temporal dynamics in land-atmosphere interactions in spatially heterogeneous landscapes, such as thawing boreal forest-wetland landscapes.

1.3.4.3 Modeling atmospheric greenhouse gas concentrations

Long-term net greenhouse gas (CO_2 and CH_4) exchange determines if ecosystems and landscapes are sources or sinks of these gases to the atmosphere (*Chapin et al.*, 2006). Atmospheric concentration models are capable of translating the net ecosystem or landscape greenhouse gas exchange into a metric of its (warming or cooling) impact on global climate: the net radiative forcing (*Neubauer and Megonigal*, 2015). Radiative forcing is defined as the imbalance in the Earth system's energy balance (in W m^{-2}, *Myhre et al.*, 2013) imposed by a specific perturbation (e.g., change in net CO_2 or CH_4 exchange) excluding the effects of non-radiative processes (e.g., energy partitioning) on lower atmosphere temperatures (*Davin et al.*, 2007). Boreal peatland landscapes usually act as long-term CO_2 sinks and CH_4 sources to the atmosphere, but their impact on global climate may change over the course of their development as a function of CO_2 sink and CH_4 source strengths (e.g., *Frolking et al.*, 2006; *Treat et al.*, 2016). Atmospheric CO_2 and CH_4 concentration models are therefore essential for quantifying and projecting the temporal evolution of net radiative greenhouse gas forcing from land cover change-induced perturbations to the long-term net exchange of CO_2 and CH_4 (*Neubauer and Megonigal*, 2015).

1.3.4.4 Climate projections

How land-atmosphere interactions of boreal landscapes will change in the future depends on changes in physical and biological properties of the land surface and on changes in meteorological conditions in a warmer climate. Altered land surface properties affect ecosystem responses to meteorological forcing, which can be derived from direct measurements of net landscape exchanges of energy, H_2O, CO_2, and CH_4 (see above). Earth system models (ESM) simulate the temporal evolution of global climate by coupling individual sub-models for the atmosphere, the ocean, sea, ice, and the land surface (*Prinn*, 2013). The simulated climate projections provide information on important meteorological variables, such as T_a, solar radiation, and precipitation at a high temporal but low spatial resolution (*Potter et al.*, 2013). Dynamical downscaling couples regional climate models (RCM) to ESMs (e.g., *Garnaud and Sushama*, 2015) and increases the spatial resolution of ESM projections (e.g., from 1° x 1° to 50 km x 50 km, Fig. 1.6d). Combining analyses of ecosystem responses to meteorological forcing with downscaled projections of meterological forcing then allows evaluating potential direct climate change impacts (i.e., from altered meteorological conditions) on land-atmosphere interactions.

1.4 Research objectives

The overall **goal** of this thesis is to provide a better functional understanding of the impact of permafrost thaw-induced wetland expansion on land-atmosphere interactions in lowland boreal forest-wetland landscapes of northwestern Canada. The **objectives** toward this goal include the evaluation of

- the importance of permafrost thaw for regional dynamics of landscape structure in northwestern Canada (*Chapter 2*),
- the biophysical impact of thaw-induced wetland expansion on land-atmosphere interactions and on regional climate (*Chapter 3*),
- the biogeochemical climate impact of a thaw-induced increase in net CH_4 emissions in comparison to long-term net CO_2 uptake of boreal forest-wetland landscapes (*Chapter 4*), and
- thaw-induced indirect climate change effects on boreal forest-wetland landscape net CO_2 exchange and direct climate change effects of projected changes in meteorological forcing (*Chapter 5*).

To achieve these objectives, eddy covariance flux measurements, remote sensing, paleoecological records, and modeling approaches (Fig. 1.6) are combined to characterize the multi-scale impacts of thawing permafrost on land-atmosphere interactions in the southern Taiga Plains, Canada. More specifically, the research focusses on changing land-atmosphere interactions at Scotty Creek (61°18' N; 121°18' W, NT, Canada), a watershed in the sporadic permafrost zone experiencing rapid permafrost thaw and concurrent wetland expansion (*Quinton et al.*, 2011). The results of this thesis provide detailed insights into the thaw-induced changes in key ecosystem and landscape processes and their coupling to the atmosphere. To better constrain future pathways of global and regional climates, global climate models require an improved representation of such land-atmosphere interactions in the boreal zone in their land surface model components (e.g., *Ekici et al.*, 2014; *Koven et al.*, 2011; *Lee et al.*, 2012; *Piao et al.*, 2013).

CHAPTER 2

PERMAFROST THAW AND WILDFIRE: EQUALLY IMPORTANT DRIVERS OF BOREAL TREE COVER CHANGES IN THE TAIGA PLAINS, CANADA

Context within the thesis

The present chapter assesses the role of permafrost thaw and wildfire disturbance as controls on boreal forest tree cover dynamics in the Taiga Plains ecozone, stretching from the permafrost-free boreal forest in the south to the boreal-tundra ecotone on continuous permafrost in the north. In the boreal zone, fire disturbance effects on large-scale boreal forest structure have received a lot of attention. However, local-scale studies have indicated that thawing permafrost may be an important additional driver of recent forest loss (and wetland expansion) in boreal lowlands (*Baltzer et al.*, 2014; *Lara et al.*, 2016). In this study, I demonstrate that thawing permafrost is equally important to fire disturbance for recent boreal tree cover dynamics in the Taiga Plains highlighting its important role in a global environmental change context. The results of this study illustrate how thaw-induced forest loss and wetland expansion may modify the future large-scale boreal forest structure in the circumpolar permafrost zone. Thus, Chapter 2 provides the framework for the detailed analyses of land-atmosphere interactions in Chapter 3-5.

2.1 Abstract

Boreal forests cover vast areas of the permafrost zones of North America, and changes in their composition and structure can lead to pronounced impacts on the regional and global climate. We partition the variation in regional boreal tree cover changes between 2000 and 2014 across the Taiga Plains, Canada, into its main causes: permafrost thaw, wildfire disturbance, and post-fire regrowth. Moderate Resolution Imaging Spectroradiometer Percent Tree Cover (PTC) data are used in combination with maps of historic fires, and permafrost and drainage characteristics.We find that permafrost thaw is equally important as fire history to explain PTC changes. At the southern margin of the

permafrost zone, PTC loss due to permafrost thaw outweighs PTC gain from post-fire regrowth. These findings emphasize the importance of permafrost thaw in controlling regional boreal forest changes over the last decade, which may become more pronounced with rising air temperatures and accelerated permafrost thaw.

2.2 Introduction

The world's boreal forests are an integral component of the regional and global climate systems affecting biosphere-atmosphere interactions and large-scale circulation patterns (*Betts and Ball*, 1997; *Bonan*, 2008; *Bonan et al.*, 1992; *Chapin et al.*, 2000; *Eugster et al.*, 2000; *Foley et al.*, 1994; *Kurz et al.*, 2013). In addition, boreal forests provide important ecosystem services to societies (*Brandt et al.*, 2013). Global change is expected to impact forest composition, structure, and function with potentially detrimental effects on boreal forest health (*Gauthier et al.*, 2015).

About 80 % of the global boreal forests occur in the circumpolar permafrost zone (Tab. I.I). In North America, the northernmost boreal forests grow on relatively cold permafrost (e.g., < -1.5°C (*Smith et al.*, 2005)) at the transition from the continuous (i.e., > 90% in areal extent) to the discontinuous (> 50% - 90% in areal extent) permafrost zone (Fig. 2.1) (*Brandt et al.*, 2013; *Tarnocai et al.*, 2009). More southern boreal forests occur in areas with isolated ($\leq$ 10% in areal extent), sporadic (> 10% - 50% in areal extent), and discontinuous permafrost, where permafrost is in disequilibrium with the current climate, and its presence is mainly driven by ecosystem properties (e.g., vegetation structure, organic layer thickness, snow depth, and soil moisture) (*Jorgenson et al.*, 2010; *Shur and Jorgenson*, 2007). If permafrost is relatively warm and thin, climate warming can cause its rapid disappearance (e.g., *Quinton et al.*, 2009; *Smith et al.*, 2005). In poorly drained, low-lying landscapes, where ice-rich permafrost is widespread (*Shur and Jorgenson*, 2007), concurrent surface subsidence may lead to waterlogging and declining forest cover (e.g., *Baltzer et al.*, 2014; *Camill and Clark*, 1998; *Jorgenson and Osterkamp*, 2005).

Thawing permafrost (e.g., *Baltzer et al.*, 2014; *Jorgenson and Osterkamp*, 2005),

wildfires (e.g., *Goetz et al.*, 2012), insect outbreaks (e.g., *Price et al.*, 2013), and droughts (e.g., *Barber et al.*, 2000) represent major natural disturbances (*Brandt et al.*, 2013) leading to short- or long-term local decline in boreal forest, depending on post-disturbance trajectories (*Liu et al.*, 2011). Climate warming (e.g., *Chapin and Starfield*, 1997; *Kauppi et al.*, 2014) and post-fire succession (e.g., *Goulden et al.*, 2011; *Liu et al.*, 2011) have been shown to enhance vegetation growth. A decline in satellite-observed boreal forest productivity has been observed at its southern margin in North America, despite concurrent increases in T_a and atmospheric CO_2 concentrations, while increased productivity has been detected across the boreal tundra ecotone (*Beck et al.*, 2011b; *Goetz et al.*, 2005). The causes of these contrasting productivity trends are not fully understood, and it remains unclear how they translate into changes in boreal forest structure and composition (e.g., *Beck et al.*, 2011a; *Williams et al.*, 2011). While the impacts of permafrost thaw, wildfire, and post-fire regrowth on boreal forest composition and structure have been quantified on local scales (e.g., *Baltzer et al.*, 2014; *Johnstone and Chapin*, 2006; *Osterkamp et al.*, 2000) or separately on larger scales (*Goetz et al.*, 2006; *Jin et al.*, 2012; *Rogers et al.*, 2015), no attempts have been made yet to characterize regional-scale boreal forest dynamics in relation to the joint effects of these three drivers.

The goal of this study is to partition the contribution of permafrost thaw, wildfire, and post-fire regrowth to recent tree cover changes across the Taiga Plains in northwestern Canada (Fig. 2.1a), an ecozone consisting to two thirds of lowland boreal forests on thick overburden cover or ice-rich permafrost. Such landscapes account for about 20 % of the global boreal zone and are also found in northeastern Canada (Hudson and James Bay lowlands), across the Western Siberian lowlands, and in some parts of interior Alaska (Tab. I.I) (*Brown et al.*, 2002; *Gruber*, 2012; *Olson et al.*, 2001). To meet this goal, we analyzed remote sensing-derived tree cover data, maps of wildfires, and permafrost and drainage characteristics. We hypothesize that permafrost thaw, and ultimately disappearance, exerts a strong control on recent regional boreal forest tree cover changes at the southern margin of the permafrost zone being comparable to the impact of wildfires and post-fire regrowth.

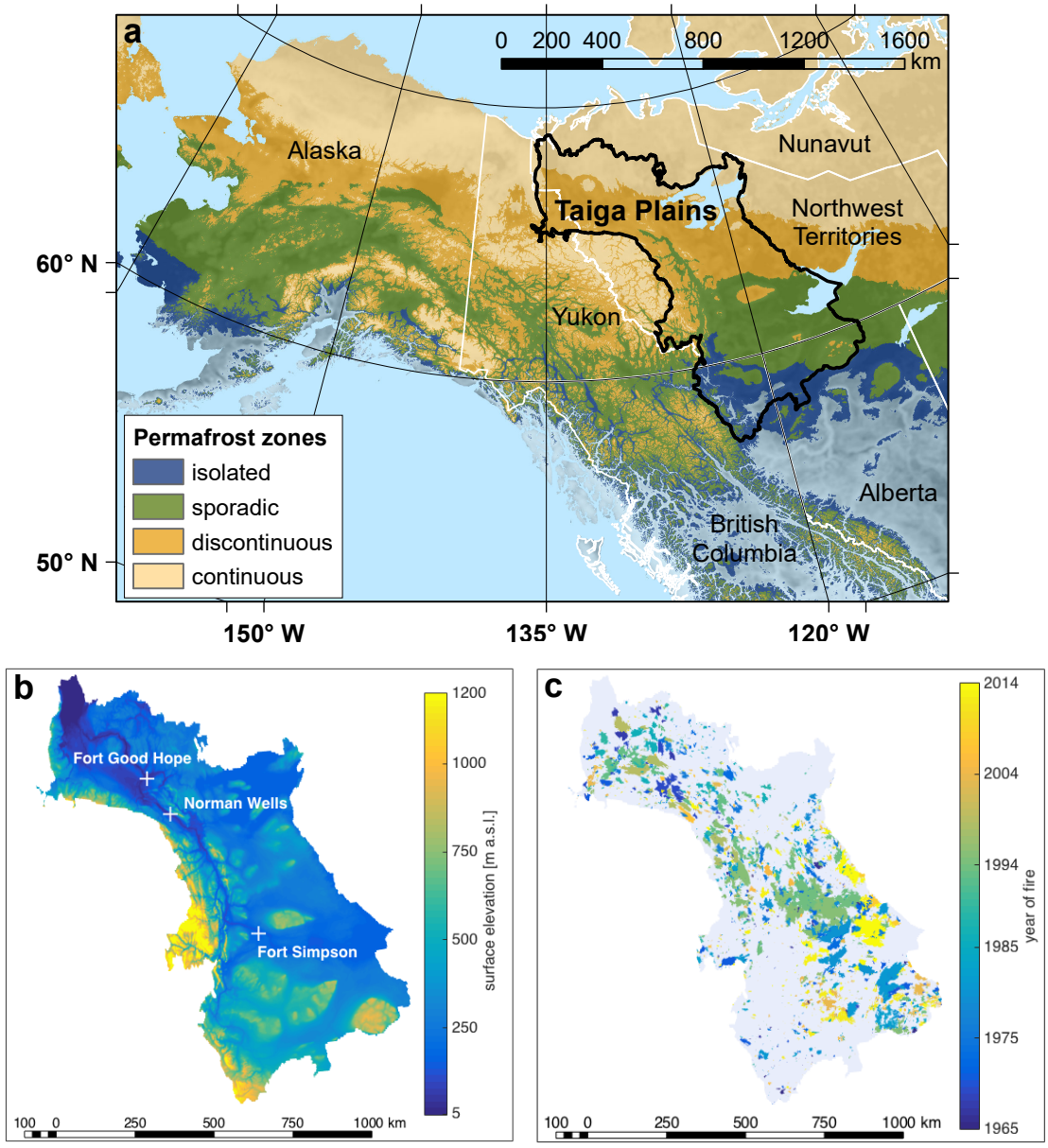

Figure 2.1 – **(a)** Permafrost zones across North America (derived from the continuous Permafrost Zonation Index, PZI, by *Gruber* (2012), i.e., isolated permafrost < 0.1 PZI, 0.1 PZI $\leq$ sporadic permafrost < 0.5 PZI, 0.5 PZI $\leq$ discontinuous permafrost < 0.9 PZI, continuous permafrost $\leq$ 0.9 PZI). The Taiga Plains ecozone is outlined with a continuous black line. **(b)** Surface elevation of the Taiga Plains and **(c)** wildfire perimeters and years of wildfire occurrence (1965 - 2014; data source: Canadian National Fire Database).

2.3 Methods

The Taiga Plains cover an area of about 550000 km^2 and are dominated by black spruce forests in the lowlands and by mixed-wood forests in the foothills of cordilleran mountain ranges and uplands. Wetlands are found throughout the boreal forest landscapes of the Taiga Plains and cover approximately 25 % to 50 % of the area (*Ecological Stratification Working Group*, 1995). The Taiga Plains are characterized by a latitudinal permafrost gradient (from north to south: continuous, discontinuous, sporadic, isolated, and no permafrost; Fig. 2.1a), following mean annual air temperatures (MAATs) and mean annual precipitation (MAP) gradients with a MAAT and MAP of 2.5°C and 390 mm at Fort Simpson, 5.0°C and 303 mm at Norman Wells, and 5.6°C and 240 mm at Fort Good Hope, respectively (2000 - 2014; Fig. 2.1b) (*Environment Canada*, 2014). Wildfires occur frequently across the Taiga Plains, resulting in a variety of regrowth stages depending on the year of fire (Fig. 2.1c).

Recent advances in satellite-derived discrete forest and continuous tree cover estimates enable consistent long-term monitoring and quantification of global and regional forest and tree cover changes (*Hansen et al.*, 2013; *Potapov et al.*, 2008). We used annual continuous Percent Tree Cover (PTC) data from the Moderate Resolution Imaging Spectroradiometer (MODIS) Vegetation Continuous Fields product (MOD44B), and we tested the impact of subgrid variability on the quantification of regional PTC. No significant differences were found between regional PTC estimates based on a 30 m and a 500 m resolution tree cover product. To assess permafrost and wildfire impacts on PTC changes, we used maps of the Permafrost Zonation Index (PZI) (*Gruber*, 2012) and yearly wildfire perimeters (1965 - 2014, Canadian National Fire Database [CNFDB]) (*Burton et al.*, 2008; *Epp and Lanoville*, 1996; *Stocks et al.*, 2003). In the Taiga Plains, declining tree cover has been mainly observed in poorly drained landscapes with thawing, ice-rich permafrost (e.g., *Baltzer et al.*, 2014). To quantify the importance of drainage conditions, we analyzed changes in regional PTC for poorly drained and well-drained areas across permafrost zones separately using drainage class information from the Soil Landscapes of Canada (SLC) database. Drainage classes were aggregated to form a

poorly drained class (including imperfectly and poorly drained SLC classes) and a well-drained (including well-drained and rapidly drained SLC classes) class (*Agriculture and Agri-Food Canada*, 2010). All data sets were resampled to a resolution of 500 m.

To quantify changes in PTC, the absolute change in PTC (ΔPTC, %) was defined as the difference between the mean 2012 - 2014 per-pixel PTC and the mean 2000 - 2002 per-pixel PTC. Three year means were used to reduce noise caused by random errors (e.g., *Montesano et al.*, 2009; *Wolfe et al.*, 2002; *Xin et al.*, 2013).

Abrupt decreases in PTC are mainly caused by wildfire disturbances (*Liu et al.*, 2011; *Song et al.*, 2014). Gradual decreases and increases of PTC across the Taiga Plains can be attributed to three main processes: (i) thawing and disappearance of permafrost along its southern edge, (ii) post-fire regrowth of vegetation, and (iii) positive impacts of warmer T_a on the growth of woody vegetation. Other processes that have been found to initiate tree cover changes, such as harvest and insect outbreaks, are considered to be negligible in the study region (*Burton et al.*, 2003; *Kurz and Apps*, 1999; *Kurz et al.*, 2013). We tested if regional drought frequencies have changed over the last few decades using gridded time series of the Palmer Drought Severity Index (*Dai*, 2011) across the Taiga Plains. No significant increases in the annual frequency of months with severe droughts between the periods 1980 to 1999 and 2000 to 2014 were found. Thus, we conclude that drought impacts play a minor role in recent PTC dynamics across the Taiga Plains.

To disentangle the main drivers of regional ΔPTC, we used regression analysis to explain regional ΔPTC with permafrost thaw (using mean PZI, mPZI, of a region as proxy), wildfires (using the fraction affected by recent fires as proxy; FR_{fire}, i.e., 2003 to 2014), and post-fire regrowth (using the fraction affected by historical fires as proxy; $FR_{regrowth}$, i.e., 1965 to 2002). Only regions within the permafrost zone (i.e., PZI $\leq$ 0.05) and with less than 10% surface water coverage or missing data were used in the regression analysis. The study region was divided into equally sized areas of increasing dimensions (from 5 km x 5 km to 80 km x 80 km) to assess the performance of the regression on varying spatial scales. We partitioned the variation in ΔPTC into parts explained uniquely by $FR_{regrowth}$, FR_{fire}, mPZI, and into a part that is explained by any

combination of these three variables (i.e., joint effect) using partial regression analysis (*Peres-Neto et al.*, 2006).

2.4 Results

Initial PTC (2000 - 2002) varied between 75% in the southwestern Taiga Plains and no tree cover in western mountainous areas and northern tundra landscapes (Fig. 2.2a). Across the Taiga Plains, 95% of ΔPTC per pixel was bounded by +12.5% and -12.5%. Increasing PTC was mainly observed in the central Taiga Plains, while decreasing PTC occurred mainly in the southern Taiga Plains (Fig. 2.2b). Between 2000 and 2014, mean PTC across the Taiga Plains increased by 0.9%, i.e., mean initial PTC of 31.8% (2000 - 2002) and 32.7% at the end (2012 - 2014) of the study period.

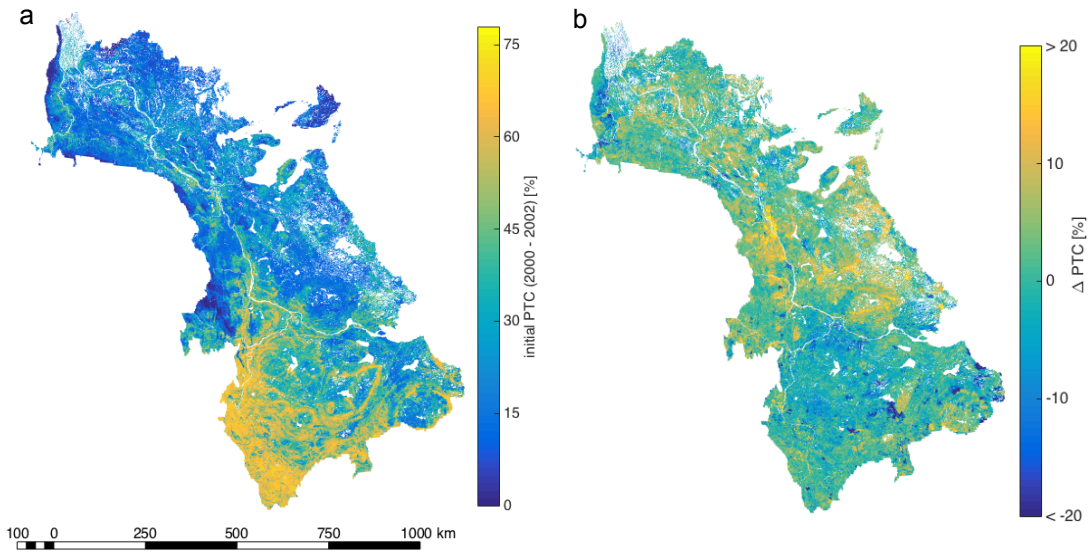

Figure 2.2 – **(a)** Percent Tree Cover (PTC) across the Taiga Plains at the beginning of the study period (i.e., mean PTC between 2000 and 2002) and **(b)** absolute change in PTC (ΔPTC) defined as difference between the mean PTC at the end of the study period (mean PTC between 2012 and 2014) and the initial PTC.

ΔPTC (for PZI bins of approximately 5000 km^2, i.e., 1% of all pixels in the permafrost zone) varied across the permafrost zones with a maximum decrease of 3.8% at the southern margin of the sporadic permafrost zone (i.e., mPZI = 0.16) and a maximum

increase of 4.7% at the transition from the sporadic to the discontinuous permafrost zone (i.e., mPZI = 0.46), where 51% of the area was affected by wildfires between 1965 and 2002. Areas outside the permafrost zone (i.e., PZI < 0 .05) showed slightly negative ΔPTC of -0.6%. In the zone of continuous permafrost, ΔPTC was small and positive ranging from 0.4% to 1.7% (Fig. 2.3).

Areas affected by wildfires between 1965 and 2002 contributed to an increase in PTC across all permafrost zones (Fig. 2.3a; green dots). A distinct positive peak in ΔPTC at the transition from the sporadic to the discontinuous permafrost zone is observed for the area with the maximum extent of wildfires between 1965 and 2002 (i.e., $FR_{regrowth}$ = 53%). Wildfires after 2002 contributed to decreases in PTC throughout the Taiga Plains (Fig. 2.3a; red dots). The maximum areal extent of wildfires after 2002 (i.e., FR_{fire} = 20%) was observed in the sporadic permafrost zone (mPZI = 0.39). Areas not affected by wildfires since 1965 contributed both to decreasing and increasing PTC depending on their location along the permafrost gradient (Fig. 2.3a; blue dots). At the southern margin of the permafrost zone, these areas show decreasing PTC, whereas areas with mPZI > 0.3 show positive ΔPTC.

Regional ΔPTC is affected by abrupt reductions in PTC by wildfires, by increasing PTC in areas that have burned since 1965 (post-fire regrowth), and by varying contributions (loss or gain in PTC) from areas that have not burned since 1965. Wildfire (FR_{fire}) and post-fire regrowth ($FR_{regrowth}$) together with mPZI explain up to 83% of the variance in ΔPTC (at a scale of 60 km x 60 km, n = 61, $p < 0.001$; Fig. 2.3b). With increasingly finer spatial resolution, the adjusted coefficient of determination drops to 0.48 (n = 14,402, $p < 0.001$) at a scale of 5 km x 5 km (Fig. 2.3b, dashed black line). While linear models describe best the relationship between FR_{fire}, $FR_{regrowth}$, and ΔPTC (Fig. I.1), a sigmoidal model describes adequately the relation between mPZI and ΔPTC (Fig. 2.3a), indicating a nonlinear dependence of permafrost thaw on mPZI. Wildfires explain the smallest part of the variance in ΔPTC with a maximum of 8% at scales between 25 km^2 and 400 km^2 and a minimum of 1% at 3600 km^2 (Fig. 2.3b, solid red line). The parts of the variance explained uniquely by mPZI are always larger than the parts explained by $FR_{regrowth}$, except for the smallest (i.e., 25 km^2) and the largest scales (i.e.,

6400 km^2). The variance explained by mPZI increases to 29% at the 4225 km^2 scale, while the maximum unique contribution of $FR_{regrowth}$ peaks at 18% at 3600 km^2. The joint part increases from 13% to 53% from the smallest to the largest scale, respectively, indicating an increasing covariation between $FR_{regrowth}$ and mPZI with increasing spatial scale (Fig. 2.3b; solid black line and Tab. I.II).

Decreasing PTC in areas not affected by wildfires since 1965 was only observed in the southern part of the sporadic and in the isolated permafrost zones and in the zone with no permafrost. Decreases in PTC mainly occurred in poorly drained landscapes with maximum declines of 2.9% in the isolated permafrost zone. In contrast, well-drained landscapes in the isolated and sporadic permafrost zones and in the zone of no permafrost were characterized by small ΔPTC between +0.1% and -0.3%. Well-drained and poorly drained landscapes in the discontinuous permafrost zone experienced both increases in PTC of 1.6% and 1.3%, respectively. Increases in PTC in the continuous permafrost zone were larger for well-drained areas compared to poorly drained areas with 1.5% and 0.1%, respectively (Fig. 2.4).

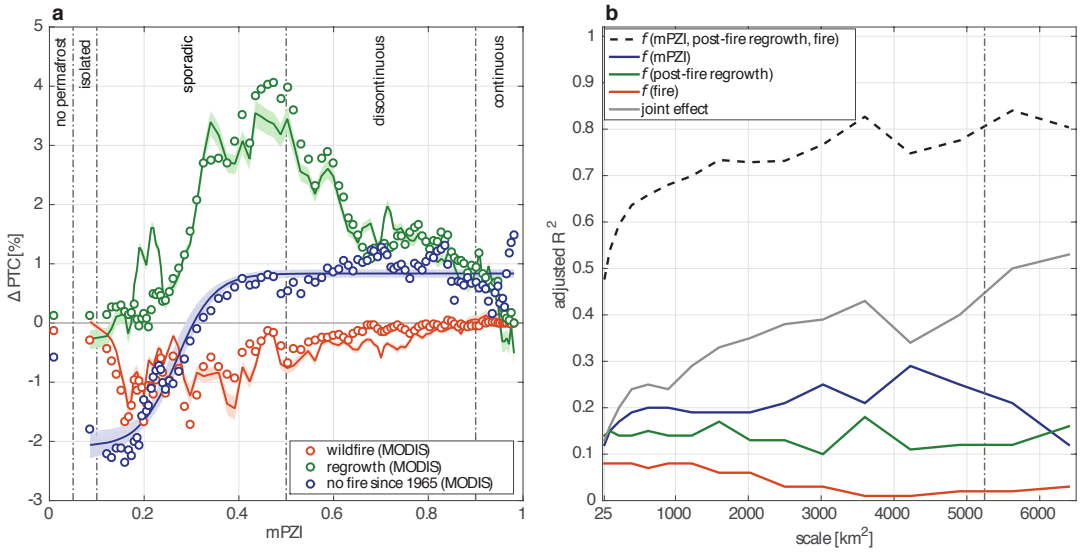

Figure 2.3 – **(a)** Contributions from areas affected by wildfire (i.e., wildfires between 2003 and 2014), post-fire regrowth (i.e., wildfires between 1965 and 2002), and from areas with no wildfires since 1965 (red, green, and blue dots, respectively) to changes in Percent Tree Cover (ΔPTC) between the periods 2000 - 2002 and 2012 - 2014. Data are binned according to mean Permafrost Zonation Index (mPZI) (1% bins, i.e., 5243 km^2 per bin). The sum of red, green, and blue dots represents net ΔPTC per bin. Red and green solid lines show modeled ΔPTC for fire and regrowth areas using a linear model of the fraction of the bins affected by wildfires between 2003 and 2014 per bin (FR_{fire}, red line, $r^2 = 0.68$, $p < 0.001$) and the fraction of the bins affected by wildfires between 1965 and 2002 ($FR_{regrowth}$, green line, $r^2 = 0.82$, $p < 0.001$), respectively. The solid blue line shows modeled ΔPTC for areas with no wildfires after 1965 using a sigmoidal model of mPZI ($R^2 = 0.93$, $p < 0.001$). The shaded area depicts the 95% confidence interval of the regressions, derived from 1,000 bootstrap realizations of the original data set. Areas outside the permafrost zone are excluded from the model fit. **(b)** Adjusted coefficient of determination (R^2) between MODIS-derived ΔPTC and the modeled ΔPTC [f(mPZI, $FR_{regrowth}$, FR_{fire})] for varying grid cell sizes across the Taiga Plains (dashed line). Solid lines indicate the part of the variance explained uniquely by the sigmoidal function of mPZI (blue line) and by linear functions of $FR_{regrowth}$ (green line) and FR_{fire} (red line). The grey line indicates the fraction explained jointly by any combination of these three drivers. The vertical dotted line shows the spatial scale of the bins in Fig. 2.3a.

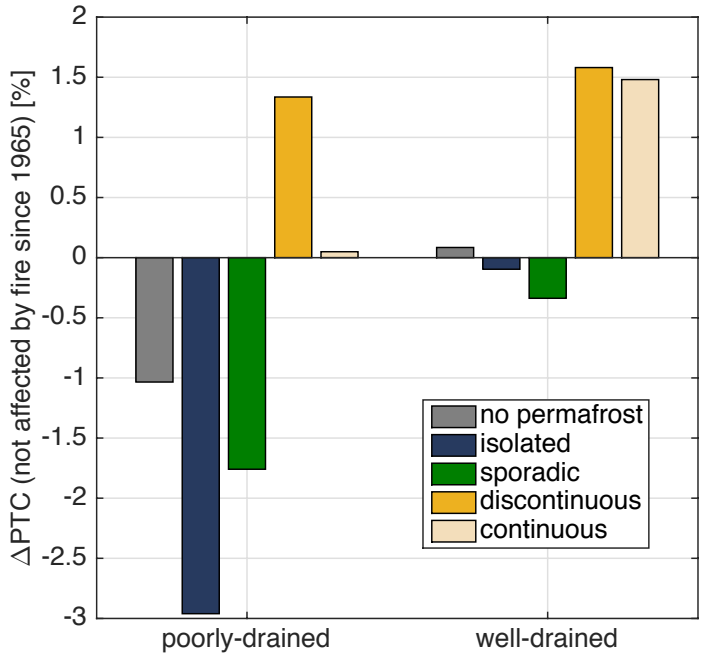

Figure 2.4 – Effect of drainage conditions on differences in Percent Tree Cover (ΔPTC) between mean PTC for the periods 2000 - 2002 and 2012 - 2014 for pixels that have not burned since 1965. Data are shown for pixels outside the permafrost zone (poorly drained: 61% of the zone; well drained: 39%), in the isolated (poorly drained: 33%; well drained: 67%), the sporadic (poorly drained: 72%; well drained: 28%), the discontinuous (poorly drained: 58%; well drained: 42%), and the continuous permafrost zone (poorly drained: 48%; well drained: 52%).

2.5 Discussion

Our analysis indicates that recent changes in boreal forest tree cover in the Taiga Plains, and possibly in similar ecozones across North America and Eurasia, are mainly controlled by permafrost conditions and wildfire history. Globally, lowland forests with thick overburden cover or ice-rich permafrost, similar to the Taiga Plains, account for 16% of the boreal forest in the isolated permafrost zone and for 32% and 29% in the sporadic and discontinuous permafrost zone, respectively. The impacts of changes in wildfire regimes on ecosystem processes in boreal forests have been discussed previously (e.g., *Bond-Lamberty et al.*, 2007; *Kasischke and Turetsky*, 2006). However, regional changes in boreal forest structure due to permafrost thaw and disappearance have not

been reported yet and have not been jointly analyzed with other main drivers of forest change (i.e., wildfires and post-fire regrowth).

Permafrost conditions explained a larger part of the spatial variation in ΔPTC than wildfires or post-fire regrowth individually. Increasing PTC is more widespread in the continuous and discontinuous permafrost zone compared to the sporadic and isolated permafrost zones. These increases in PTC are predominantly occurring in areas that have been affected by wildfires prior to the year 2002, initiating post-fire regrowth (e.g., *Goetz et al.*, 2012; *Kasischke et al.*, 1995). However, post-fire regrowth in the southern sporadic and the isolated permafrost zone is reduced compared to the discontinuous and continuous permafrost zone (Fig. I.1), likely a result of fire-induced permafrost thaw and surface subsidence (*Brown et al.*, 2015; *Camill et al.*, 2010; *Yoshikawa et al.*, 2003). Widespread post-fire regrowth between 2000 and 2010 has been documented across North America (*Li and Potter*, 2012). Post-fire regrowth represents a critical control on the composition, structure, and functioning of boreal forests (e.g., *Liu et al.*, 2011). However, we also identified increases in PTC for pixels not affected by wildfires since 1965 in the discontinuous and continuous permafrost zone. Several reasons may explain these patterns. First, some wildfires in remote northern regions prior to the mid-1970s lack documentation and are thus not included in the CNFDB (*Stocks et al.*, 2003). Second, wildfires prior to 1965 are not documented in the CNFDB. These fire-affected areas may still experience regrowth, which can continue for more than 100 years (e.g., *Yue et al.*, 2013). Across the Taiga Plains, areas affected by wildfires in 1965 still show increasing PTC (Fig. I.2). Third, tree cover may also increase due to enhanced vegetation productivity as a response to warming air temperatures (*Kauppi et al.*, 2014).

Areas affected by wildfires between 2003 and 2014 showed consistent reductions in PTC across all permafrost zones (Fig. 2.3). Boreal wildfires in North America generally result in mortality of black spruce and jack pine and immediate regeneration, initiating post-fire regrowth (*Rogers et al.*, 2015). These wildfires are characterized by strong crown fire intensities, increasing with PTC and causing drastic, temporary reductions in PTC (*Rogers et al.*, 2015; *Wooster and Zhang*, 2004). The contribution of these abrupt reductions to regional ΔPTC over the study period of 15 years was small compared to the

contributions from post-fire regrowth and from areas that have not burned since 1965.

We show that ΔPTC in areas that have not burned since 1965 are positive in the discontinuous and continuous permafrost zones. At the southern margin of the permafrost zone, where permafrost is most prone to widespread disappearance (e.g., *Osterkamp et al.*, 2000; *Quinton et al.*, 2011), these areas show declining PTC. These variations can be well explained with a sigmoidal model of mPZI, an indicator of the thermal state of permafrost (*Gruber*, 2012).

Our findings are supported by small-scale (∼500 m) studies identifying permafrost disappearance in poorly drained lowlands as drivers of decreasing forest cover in the sporadic and discontinuous permafrost zones of Canada (e.g., *Baltzer et al.*, 2014; *Camill*, 1999a; *Camill and Clark*, 1998) and Alaska (*Osterkamp et al.*, 2000). In this study, reductions in PTC were mainly observed in poorly drained areas, while well-drained areas experienced only small ΔPTC. Poorly drained landscapes are generally characterized by ice-rich permafrost leading to larger surface subsidence upon thaw compared to less ice-rich, well-drained landscapes (*Hinzman et al.*, 2005; *Jorgenson et al.*, 2001). Surface subsidence and subsequent saturation of soils have been identified as an important cause of mortality and reduced recruitment of black spruce in the northern boreal forest (*Baltzer et al.*, 2014; *Camill et al.*, 2010; *Osterkamp et al.*, 2000). Therefore, we argue that permafrost thaw and disappearance mainly cause these observed reductions in PTC. While droughts have been shown to regulate boreal forest productivity in Alaska (*Barber et al.*, 2000; *Beck et al.*, 2011a), it is unlikely that they drive the observed spatial patterns in ΔPTC in the Taiga Plains. Within the same permafrost zones, declining PTC was only observed for poorly drained landscapes, while well-drained landscapes were characterized by increasing PTC. Enhanced drought intensities and frequencies could induce PTC declines across all drainage classes (*Beck et al.*, 2011a; *Walker and Johnstone*, 2014) or improve growth conditions in poorly drained landscapes by ameliorating anoxic stress (e.g., *Baltzer et al.*, 2014; *Camill et al.*, 2010). Small ΔPTC in the zone with no permafrost further indicate that permafrost thaw is mainly causing PTC declines at its southern limit.

On a regional scale, the identification of direct causes of forest structure changes

based on satellite data alone remains challenging (e.g., *Hansen et al.*, 2010). However, across the Taiga Plains, more than 80% of the variance in regional ΔPTC (e.g., 60 km x 60 km) can be explained by wildfire history and permafrost conditions. Our study shows that besides wildfire history, permafrost thaw dynamics are crucial to understand current and future pathways of boreal forest changes. On smaller scales (e.g., 5 km x 5 km), these two drivers only explain about half of the variance indicating either that other drivers become more important (e.g., vegetation composition, soil moisture, and insect outbreaks) or that random errors in MODIS-derived PTC inflate the variance in ΔPTC. Furthermore, mPZI might not be a good indicator for fine-scale permafrost thaw dynamics, because it does not account for vegetation cover, snow drift, or soil properties (*Gruber*, 2012).

The relative importance of permafrost thaw, wildfire disturbance, and post-fire regrowth as drivers of ΔPTC varies among the permafrost zones. As a result, ΔPTC between 2000 and 2014 ranges from gains in the discontinuous (i.e., ΔPTC = +2.5%) and continuous permafrost zones (i.e., ΔPTC = +1.2%) to PTC losses in the sporadic (i.e., ΔPTC = -0.4%) and isolated (i.e., ΔPTC = -1.0%) permafrost zones. Boreal forest tree cover may be altered in the long term with changing wildfire frequencies and intensities (*Chapin and Starfield*, 1997). However, we assume that these long-term trends occur slowly over long periods and require longer time series for a robust trend assessment. In contrast, permafrost thaw can lead to forest and tree cover losses over a few decades (*Baltzer et al.*, 2014; *Jorgenson et al.*, 2001) and, in the light of climate change, aggradation of permafrost is unlikely (*Camill*, 1999b).

2.6 Conclusions

We show that PTC is decreasing at the southern limit of the permafrost zone in the Taiga Plains, with the bulk of the decline occurring in poorly drained lowland areas. Extensive areas that burned before 2003 characterize the transition from the sporadic to the discontinuous permafrost zone. Post-fire regrowth in these areas mainly causes widespread increases in PTC. Across the Taiga Plains, most of the variation in regional

ΔPTC is explained by three drivers: permafrost thaw, wildfires, and post-fire regrowth. Permafrost thaw is equally important to regional fire history in controlling ΔPTC, emphasizing the need to better understand and project future permafrost dynamics not only in the Taiga Plains but also in similar ecozones across North America and Eurasia. With increasing air temperatures in the future, permafrost thaw is expected to drastically change boreal forest structure and, therefore, to affect regional and global climate systems and boreal forest ecosystem services.

Acknowledgements

MODIS data were accessed via the LP DAAC Data Pool (`https://lpdaac.usgs.gov/data_access/data_pool`). Historical CNFDB wildfire data were downloaded from the Canadian Wildland Fire Information System Datamart (`http://cwfis.cfs.nrcan.gc.ca/datamart`). Climate data for Fort Simpson, Norman Wells, and Fort Good Hope, NT, were obtained from the Environment Canada Climate webpage (`http://climate.weather.gc.ca/`). The global Permafrost Zonation Index map was downloaded from the following webpage: `http://www.geo.uzh.ch/microsite/cryodata/pf_global/`. Drainage class information can be accessed on the Agriculture and Agri-Food Canada webpage (`http://sis.agr.gc.ca/cansis/nsdb/slc/v3.2/index.html`). Self-calibrated Palmer Drought Severity Index data was obtained from the University Corporation for Atmospheric Research webpage (`http://www.cgd.ucar.edu/cas/catalog/climind/pdsi.html`). Partial regression was conducted in the R statistical computing environment using the vegan package (*Oksanen et al.*, 2013). All other analyses were done in MATLAB (version 2015a, The Math Works).

CHAPTER 3

REGIONAL ATMOSPHERIC COOLING AND WETTING EFFECT OF PERMAFROST THAW-INDUCED BOREAL FOREST LOSS

Context within the thesis

The present chapter characterizes and quantifies the impact of thaw-induced wetland expansion in the southern Taiga Plains on land surface characteristics and regional climate. To characterize changing land surface characteristics, I combine eddy covariance flux measurements of sensible and latent heat with planetary boundary layer theory, compare boreal forest and wetland albedo dynamics, and analyze remotely sensed tree cover, land surface temperature, and albedo dynamics. To quantify impacts on near-surface air temperature and humidity, I couple the eddy covariance flux measurements with a simple dynamic atmospheric boundary layer. Chapter 3 connects to the previous chapter by analyzing the biophysical impacts of widespread thaw-induced land cover changes, as demonstrated in Chapter 2 using the example of changing tree cover in the Taiga Plains ecozone. Chapter 3, 4 and 5 address thaw impacts on energy and water fluxes, CH_4 fluxes, and CO_2 fluxes, respectively. Thus, chapter 3 focusses on biophysical climate impacts and complements chapter 4 and 5, focussing on biogeochemical climate impacts.

3.1 Abstract

In the sporadic permafrost zone of North America, thaw-induced boreal forest loss is leading to permafrost-free wetland expansion. These land cover changes alter landscape-scale surface properties with potentially large, however, still unknown impacts on regional climates. In this study, we combine nested eddy covariance flux tower measurements with satellite remote sensing to characterize the impacts of boreal forest loss on albedo, eco-physiological and aerodynamic surface properties, and turbulent energy fluxes of a lowland boreal forest region in the Northwest Territories, Canada. Planetary

boundary layer modelling is used to estimate the potential forest loss impact on regional air temperature and atmospheric moisture. We show that thaw-induced conversion of forests to wetlands increases albedo, bulk surface conductance for water vapour and decreases aerodynamic surface temperature. At the same time, heat transfer efficiency is reduced. These shifts in land surface properties increase latent at the expense of sensible heat fluxes, thus, drastically reducing Bowen ratios. Due to the lower albedo of forests and their masking effect of highly reflective snow, available energy is lower in wetlands, especially in late winter. Modelling results demonstrate that a conversion of a present-day boreal forest-wetland to a hypothetical homogeneous wetland landscape could induce a near-surface cooling effect on regional air temperatures of up to 3 - 4 °C in late winter and 1 - 2 °C in summer. An atmospheric wetting effect in summer is indicated by a maximum increase in water vapour mixing ratios of 2 mmol mol $^{-1}$. At the same time, maximum boundary layer heights are reduced by about a third of the original height. In fall, simulated air temperature and atmospheric moisture between the two scenarios do not differ. Therefore, permafrost thaw-induced boreal forest loss may modify regional precipitation patterns and slow down regional warming trends.

3.2 Introduction

A large proportion of North America's high-latitude landscapes contain permafrost, perennially cryotic ground, spanning from the tundra in the north, over subarctic woodlands, to the boreal forests further south (*Strong et al.*, 1989). About 60% of North America's boreal forests lie in the zones of discontinuous permafrost (50% to < 90% of the land surface contains permafrost) and sporadic permafrost (10% to < 50%) (e.g., *Gruber*, 2012; *Olson et al.*, 2001; *van Everdingen*, 2005, Chapter 2). Across the circumpolar permafrost zone, rapid rates of climate warming are already occurring and are projected to intensify in the near future (*Hartmann et al.*, 2013).

Climate change is expected to alter the composition and structure of boreal forest and wetland ecosystems inducing strong biophysical and biogeochemical feedbacks to global and regional climates through altered land-atmosphere interactions (e.g., *Alkama*

and Cescatti, 2016; *Bonan*, 2008; *Chapin et al.*, 2000, 2005; *Meissner et al.*, 2003). At high latitudes, biophysical feedbacks to regional climates mainly imply changes in the surface fluxes of sensible and latent heat (*Bonan*, 2008). Vegetation composition and structure strongly determine physical and biological land surface properties such as albedo, surface temperature, and bulk aerodynamic and surface conductance (*Eugster et al.*, 2000; *Kasurinen et al.*, 2014). Thus, vegetation changes alter surface properties and consequently also turbulent energy flux regimes (e.g., *Alkama and Cescatti*, 2016; *Baldocchi and Ma*, 2013; *Davin and de Noblet-Ducoudré*, 2010; *Luyssaert et al.*, 2014; *Snyder et al.*, 2004). For example, a shift from deciduous to coniferous forests decreases surface conductance and increases the Bowen ratio, the ratio of sensible to latent heat flux (*Eugster et al.*, 2000). The modified diurnal heat input to the regional planetary boundary layer (PBL) leads to altered diurnal PBL growth dynamics affecting its effective heat capacity, entrainment of dry air from the free atmosphere, and, consequently, feedbacks to regional air temperatures and convective rainfall (e.g., *Baldocchi et al.*, 2000; *Esau et al.*, 2012; *Juang et al.*, 2007a). In addition, boreal forests exert a strong biophysical influence on regional air temperatures even at latitudes far outside their zone of distribution due to its effect on the general circulation of the atmosphere (*Bonan et al.*, 1992; *Snyder et al.*, 2004).

At the southern limit of the permafrost zone in Canada and Alaska, warming air temperatures cause widespread thaw. In recent decades, thaw-induced disappearance of forested permafrost plateaus has led to a conversion of boreal forests to wetlands (e.g., *Camill*, 1999b; *Camill and Clark*, 1998; *Jorgenson et al.*, 2001; *Lara et al.*, 2016; *Quinton et al.*, 2011, Chapter 2). Permafrost plateaus dominated by coniferous tree species rooted in raised, thick organic soils, and treeless, seasonally frozen wetlands are the two predominant land cover types of the lowland boreal landscapes in the discontinuous and sporadic permafrost zones of north-western Canada (*Tarnocai*, 2006; *Zoltai and Tarnocai*, 1975). The proportional coverage of forests and wetlands is affected by the degree of permafrost thaw (*Quinton et al.*, 2011). Forested permafrost plateaus and wetlands differ in their soil moisture and temperature regimes with wetlands being substantially wetter and warmer (*Baltzer et al.*, 2014; *Chasmer et al.*, 2011; *Quinton and Baltzer*,

2013, Fig. II.2). In wetlands, root inundation and mortality inhibits tree growth, resulting in sharp forest-wetland transitions of vegetation composition and structure (e.g., *Baltzer et al.*, 2014; *Camill*, 1999a).

Despite the importance of boreal forests in the permafrost zone for the global and regional climates (*Chapin et al.*, 2000), local- to regional-scale responses of land-atmosphere interactions to thaw-induced land cover change are still poorly understood. It remains unclear as to how such vegetation shifts may affect turbulent energy fluxes and how these might modify regional trends in air temperature and atmospheric moisture. The biophysical consequences of permafrost thaw-induced boreal forest loss and ultimately disappearance have received little attention compared with deforestation in the temperate and tropical zones and wildfires in the boreal zone (e.g., *Liu et al.*, 2005; *Randerson et al.*, 2006). The impacts of disappearing permafrost on regional turbulent energy flux regimes need to be better constrained to project the trends of air temperature and atmospheric moisture in the boreal zone (*Chapin et al.*, 2000) and to evaluate the performance of current land surface schemes and terrestrial biosphere models (*Fisher et al.*, 2014). In this study, we aim to:

— quantify the impact of permafrost disappearance and concurrent tree cover loss on turbulent energy fluxes,

— identify the landscape-scale ($\sim$1 km^2) changes in land surface properties causing turbulent energy flux changes,

— quantify boreal tree cover controls on land surface properties on a regional scale ($\sim$4,000 km^2) and

— estimate potential effects of thaw-induced shifts in land cover on regional air temperature and atmospheric moisture.

3.3 Materials and Methods

3.3.1 Study site

Scotty Creek (61°180N; 121°180W, NT, Canada) is a 152-km^2 watershed located in the southern Taiga Plains and is situated in the zone of sporadic permafrost (Fig. 3.1a).

The southern part of the watershed is characterized by rapidly thawing permafrost resulting in a mosaic of forested permafrost plateaus, wetlands, forested uplands and shallow thaw lakes (*Chasmer et al.*, 2014). Permafrost-free wetlands occur as collapse-scar bogs that receive some lateral inflow of water from the surrounding forests, and as channel fens that route water towards the watershed outlet (*National Wetlands Working Group*, 1997; *Quinton et al.*, 2009). Organic soils are widespread in the region with peat thickness ranging from 0.6 to 5 m (*Aylsworth et al.*, 1993). Black spruce (*Picea mariana*) is the dominant tree species on the forested permafrost plateaus. Understorey and ground cover on the permafrost plateaus mainly consist of Labrador tea (*Rhododendron groenlandicum*), ground lichen (*Cladonia* spp.), and *Sphagnum fuscum* and *capillifolium*. *Sphagnum balticum* and *magellanicum* and ericaceous shrubs mainly populate the collapse-scar bogs (*Garon-Labrecque et al.*, 2015). The mean annual air temperature (1981-2010) in Fort Simpson, ca. 60 km north of Scotty Creek, is 2.8 °C with a mean January air temperature of -24.2 °C and a mean July air temperature of 17.4 °C. The long-term mean total annual precipitation (1981-2010) is 388 mm. Snowfall accounts for about 50% of the total annual precipitation. During the study period, from May to November 2013 and April to November 2014, mean air temperature was 2.1 and 0.2 °C warmer and total precipitation was 73 mm (26%) and 87 mm (29%) lower than the long-term average, respectively (*Environment Canada*, 2014).

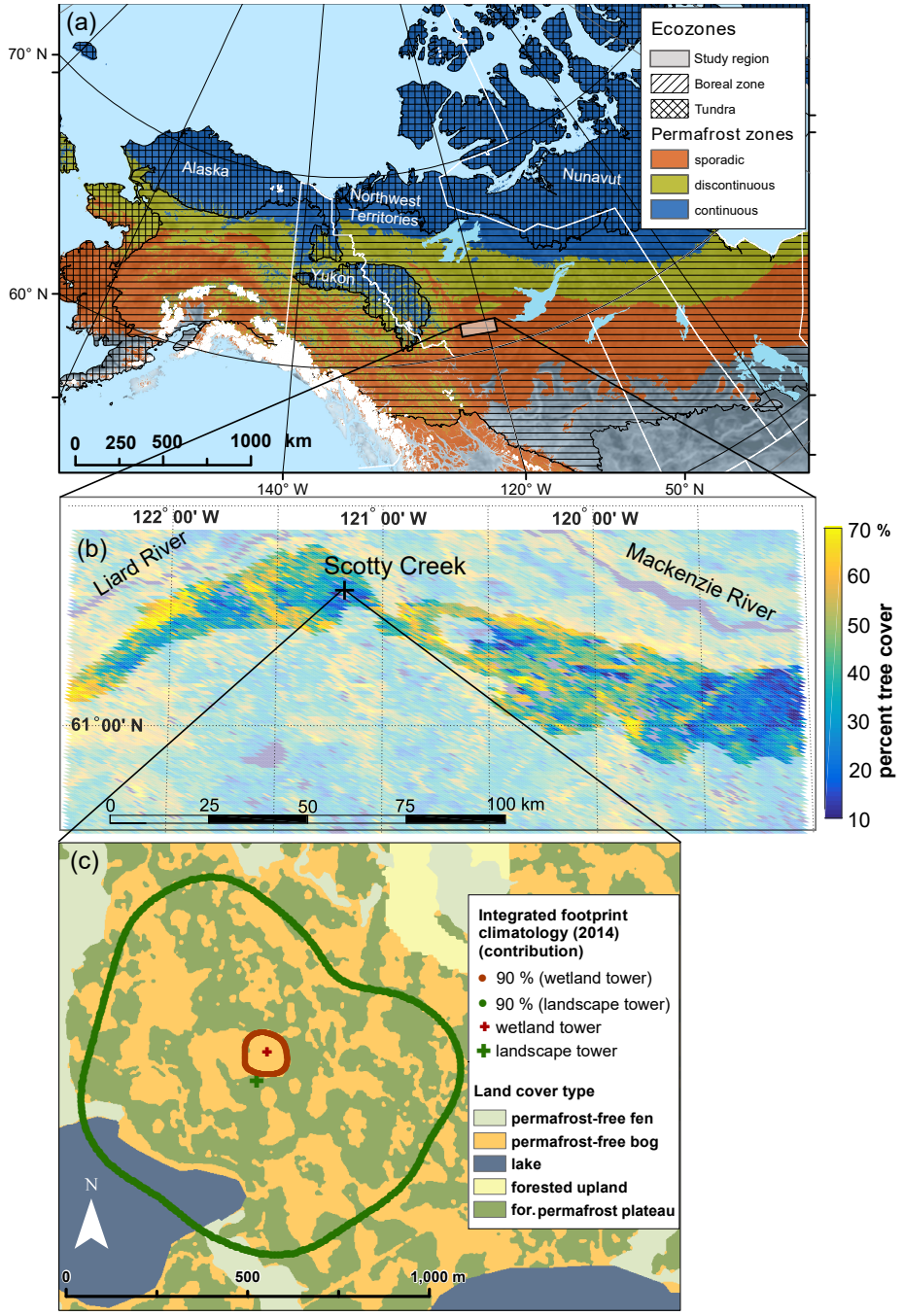

Figure 3.1 – **(a)** Location of the Scotty Creek watershed (surface elevation $\sim$ 285 m a.s.l.), zones of sporadic (10% to < 50% areal permafrost coverage), discontinuous (50% to < 90%), and continuous ($\leq$ 90%) permafrost [data from *Gruber* (2012)], and areal extent of the boreal and tundra zones [data from *Olson et al.* (2001)]. **(b)** Percent tree cover in 2010 in the southern Taiga Plains. Pixels with surface elevations < 250 m a.s.l. and > 300 m a.s.l. are shaded. **(c)** Land cover types in the vicinity of the two flux towers (*Chasmer et al.*, 2014) and their flux footprint climatologies for the period April to November 2014.

3.3.2 Eddy covariance measurements

Turbulent momentum and energy fluxes were measured at Scotty Creek using the eddy covariance technique at two nested micrometeorological towers (*Baldocchi*, 2014). One eddy covariance system was mounted on top of a 15-m tower with flux footprints originating from a boreal forest-wetland landscape (hereafter referred to as 'landscape tower', measurement period: 11 May 2013 to 07 November 2014). A second system was installed on a 2-m tower in a wetland just north of the landscape tower at 1.9 m above the ground surface (hereafter referred to as 'wetland tower', measurement period: 12 April 2014 to 07 November 2014). Its flux footprints originated mainly from the wetland and were within the landscape tower flux footprint (Fig. 3.1c).

The eddy covariance instrumentation, identical at both towers, included a sonic anemometer (CSAT3A; Campbell Scientific Inc., Logan, UT, USA) and a CO_2/H_2O open-path infrared gas analyzer (EC150; Campbell Scientific Inc.), both operating at 10-Hz frequencies. Friction velocity (u*; m s^{-1}), sensible (H, W m^{-2}) and latent heat fluxes (LE, W m^{-2}) were computed using the EddyPro software (version 5.2, LI-COR Biosciences, Lincoln, NE, USA). For the landscape tower, a planar fit method was deployed to rotate the coordinate system of the sonic anemometer into the mean streamlines of the wind field (*Wilczak et al.*, 2001). To account for small seasonal changes in the orientation of the sonic anemometer due to potential variations of the wetland surface, a double rotation method was applied for the wetland tower, so that the half-hourly mean vertical wind velocity equalled zero. Further corrections were applied to take into account spikes in the high-frequency time series (*Vickers and Mahrt*, 1997), humidity effects on sonic temperature (*Dijk et al.*, 2004), block averaging of half-hour time series, time lag detection, spectral attenuation (*Moncrieff et al.*, 2004, 1997), and air density fluctuations for water vapour fluxes (*Webb et al.*, 1980).

3.3.3 Supporting measurements

Four-component net radiometers (CNR4, Kipp & Zonen, Delft, The Netherlands) at the landscape (at a height of 13.4 m) and the wetland (2.1 m) tower measured incoming

and outgoing short- and long-wave radiation fluxes. Following *Schmid* (1997), the radiometric footprint (80% contour) at the landscape tower contained 77% forest with the remaining 23% being wetland. The radiometric footprint at the wetland tower consisted only of wetland. Therefore, the radiation fluxes at the landscape and the wetland tower were considered to represent forest and wetland surfaces, respectively. Air temperature and relative humidity probes (HC2-S3; Rotronic AG, Bassersdorf, Switzerland) were installed at 15 m and at 2.6 m at the landscape and the wetland tower, respectively. Soil heat flux at 8 cm below the moss surface at the forest and at the wetland was measured in a hummock and hollow using two ground heat flux plates (HFT3, Hukseflux, Delft, The Netherlands) at each site. To calculate soil heat storage between the heat flux plates and the moss surface, half-hourly changes in soil temperatures at 2, 4 and 8 cm below the surface (TCAV; Campbell Scientific Inc. and Type 'T'; Omega Engineering, Stamford, CT, USA) were used assuming a constant heat capacity of the peat above the heat flux plate of 2 MJ m^{-3} K^{-1} (*Hayashi et al.*, 2007). Snow depth was measured in the forest and in the wetland using an ultrasonic distance sensor (SR50; Campbell Scientific Inc.). Snow density was measured on 10 days during late winter 2014 between 25 March and 22 April using a snow tube. Half-hour changes in snow depth, mean snow density and the latent heat of fusion of water were used to calculate the forest and wetland snow melt energy flux.

3.3.4 Footprint modelling

To resolve the spatial heterogeneity within the flux tower footprints, we ran the 2D footprint parameterization of *Kljun et al.* (2015) for both towers providing not only the extent but also the width of footprints. Similar to the model of *Kljun et al.* (2004), this parameterization is based on the Lagrangian particle dispersion footprint model of *Kljun et al.* (2002) and is valid for convective to stable boundary layer conditions. The footprint model was used to calculate the half-hourly per-grid cell flux contributions for a discretized study area. Roughness lengths for momentum (z_{0m}; m) and zero-plane displacement heights (d_0; m) for each half-hour were derived from high-frequency sonic anemometer data to account for the spatial heterogeneity in canopy height and geometry

(see Appendix II). The relative half-hourly flux contributions of each land cover type to the total flux were calculated as the weighted sum of the respective per-grid cell flux contributions. The 90% flux footprints of the landscape tower mainly contained a mix of wetlands and forests, while the wetland tower predominantly contained surfaces from one ecosystem, the wetland (Fig. 3.1c).

3.3.5 Post-processing of eddy covariance measurements

A three-class quality flag system (*Mauder and Foken*, 2011) was used to remove half-hourly periods that do not meet steady-state conditions or when turbulence was not fully developed. Remaining outliers were filtered using a spike detection algorithm (*Papale et al.*, 2006). To ensure the comparability between flux measurements at the landscape and the wetland tower, we assessed their energy balance closures (EBC). The EBC was 0.79 and 0.78 for the landscape and the wetland tower, respectively, after removing wetland tower fluxes with < 95% wetland contribution and applying a u*-threshold filter (u* = 0.2 m s^{-1}) (see Appendix II). These EBC values are in good agreement with *Stoy et al.* (2013) who reported a mean EBC of 0.76 $\pm$ 0.13 and of 0.88 $\pm$ 0.23 for seven wetlands and 47 evergreen needle-leaf forest sites, respectively.

Experimental errors in eddy covariance measurements are a combination of systematic and random errors (*Moncrieff et al.*, 1996). The potential systematic error derived from the EBC analysis ($\sim$20%) does not hamper the comparability of H and LE between the two towers, assuming that the EBC residuals are similarly attributed to H and LE for the landscape and the wetland tower. Maximum instrument-specific systematic errors in LE are estimated to be 8% based on an intercomparison study of the open-path EC150 with closed-path infrared gas analysers (*Helbig et al.*, 2016a).

Random half-hourly errors in H and LE were estimated as the standard deviation of H and LE for similar meteorological conditions and flux footprints within a time window of seven days (*Lasslop et al.*, 2008). These random errors were used in regression analyses after *York et al.* (2004), accounting for errors in both the dependent and the independent variables. Mean random errors were 16.3 and 9.1 W m^{-2} in H, and 12.2 and 14.5 W m^{-2} in LE for the landscape and the wetland tower, respectively, and increased with the magnitude of both fluxes.

3.3.6 Landscape-scale surface properties

Albedo and radiometric surface temperature represent two surface properties that are sensitive to changes in ecosystem structure and composition (e.g., *Betts and Ball*, 1997; *Juang et al.*, 2007b; *Lee et al.*, 2011), thus strongly affecting land-atmosphere interactions (e.g., *Betts et al.*, 2001). Tower-based radiation measurements over the wetland (2014) and over the forest (2013 and 2014) were used to assess the effects of thaw-induced forest loss on landscape-scale albedo and radiometric surface temperature. Aerodynamic surface properties, such as bulk aerodynamic conductance for heat and water vapor (g_H; m s^{-1}; see Appendix II) and bulk surface conductance for water vapor (g_s; m s^{-1}), were derived using Monin-Obukhov similarity theory (*Betts et al.*, 1999; *Garratt*, 1994). We derived aerodynamic surface temperature (T_{as}; K) of the flux footprints from measured H and modelled g_H using the following bulk transfer relationship:

$$H = \rho C_p g_H (T_{as} - T_a) \tag{3.1}$$

where ρ is air density [kg m^{-3}], C_p is the heat capacity of air [J kg^{-1} K^{-1}], and T_a is air temperature [K].

Aerodynamic surface temperature directly controls the turbulent heat exchange between land surface and overlying atmosphere. Thus, T_{as} differs from radiometric surface temperature, which represents a weighted soil and canopy temperature as function of viewing angle of the thermal-infrared radiometer mounted on tower platforms (*Detto et al.*, 2006; *Kustas et al.*, 2006) or satellite platforms (*Wan*, 2014).

Similarly, we obtained a bulk formulation for LE by assuming the same bulk aerodynamic conductance as for sensible heat (g_H) and by adding a bulk surface conductance term, g_s (*Betts et al.*, 1999):

$$LE = \lambda \frac{g_H g_s}{g_H + g_s}[q_s(T_{as}) - q_a] \tag{3.2}$$

where λ is the latent heat of vapourization [J kg^{-1}], q_s is the saturated specific humidity of air at T_{as} [kg kg^{-1}], and q_a is the specific humidity of air at measurement height [kg kg^{-1}].

Increasing wetland coverage in the boreal forest-wetland landscape may affect the response of g_s to variations in vapour pressure deficit (VPD; kPa) and incoming shortwave radiation (SW_{in}; W m^{-2}). We applied a boundary line analysis by fitting nonlinear VPD and SW_{in} models to the upper boundary of half-hourly g_s for three flux footprint classes of increasing wetland contribution (e.g., *Grelle et al.*, 1999; *Igarashi et al.*, 2015): a 'low wetland class' with footprint contributions from wetlands < 63%, a 'medium wetland class' with contributions from wetlands between 63% and 95%, and a 'high wetland class' with contributions from wetlands > 95% (i.e., from the wetland tower). Only the maximum g_s in each VPD and SW_{in} bin (G_{s_bound}; m s^{-1}) were selected to minimize reductions in g_s due to other environmental drivers (see Appendix II).

3.3.7 Regional-scale patterns of albedo and radiometric surface temperature

To assess regional effects of permafrost thaw-induced tree cover loss on albedo and radiometric surface temperature (T_{rs}; K),we analysed several MODIS satellite products for a ~4,000-km^2 area of interest in the southern Taiga Plains (Fig. 3.1b). These products included percent tree cover from the annual MOD44B Vegetation Continuous Field product, white-sky albedo from the 16-day MCD43B3 Albedo product, and daytime and night-time T_{rs} from the 8-day MOD11A2 Land Surface Temperature/Emissivity product for the years 2000-2015. White-sky albedo does not account for the direct radiative component and is therefore not a function of solar angle and atmospheric conditions, making it suitable for the assessment of albedo variations due to changes in surface characteris-

tics (*Jin et al.*, 2012; *Schaepman-Strub et al.*, 2006).

Surface elevation from the MODIS Geolocation product (MOD03) was used to mask pixels with elevations below 250 m a.s.l. and above 300 m a.s.l. to minimize altitudinal effects on T_{rs} (e.g., *Li et al.*, 2015). Scotty Creek is located at 285 m a.s.l. Pixels classified as open water bodies by the MODIS Land Water Mask (MOD44W) were discarded from the analysis. We only analysed white-sky albedo and T_{rs} pixels with good-quality flags and with error flags indicating an average T_{rs} error $\leq$ 3 K. To remove thermal anomalies in T_{rs} due to wildfires, we masked all pixels identified as active fires by the MODIS Thermal Anomalies & Fire product (MOD14A1). All data sets were resampled to a spatial resolution of 1 km^2.

3.3.8 Planetary boundary layer modelling

The potential impact of a conversion of the present-day heterogeneous boreal forest-wetland to a hypothetical homogeneous permafrost-free, treeless wetland landscape on potential air temperature (θ_m; K) and water vapour mixing ratio (q_m; mol mol^{-1}) in the PBL was assessed with a clear-sky PBL model (*Baldocchi and Ma*, 2013; *McNaughton and Spriggs*, 1986, see Appendix II). We ran the PBL model using u*, H and LE from the landscape (representing a present-day heterogeneous landscape with permafrost) and the wetland tower (as a proxy for a hypothetical homogeneous permafrost-free landscape) and compared the diurnal θ_m and q_m dynamics. The model inputs H and LE were corrected for the observed lack of EBC maintaining the Bowen ratio (*Twine et al.*, 2000). To illustrate diurnal θ_m and q_m dynamics for the two scenarios, we analysed modelled θ_m and q_m for one clear-sky day in the summer with no gaps in the model input time series (22 June 2014: 0800 - 2100 Mountain Standard Time (MST)). The mean footprint contributions for the landscape tower fluxes on that day were 40% from wetlands, 56% from forested peat plateaus and 4% from the lake. These contributions are representative for the present-day landscape in the southern part of the Scotty Creek watershed that consisted of 57 $\pm$ 8% and 52 $\pm$ 9% forested permafrost plateaus in 2000 and 2010, respectively (*Baltzer et al.*, 2014). Additionally, we ran the PBL model for a total of 49 days between 15 May 2014 and 08 October 2014 and derived daily θ_m and

q_m differences between the two landscape scenarios at 1800 MST (see Appendix II for selection criteria for modelled days). We compared PBL dynamics as observed over the present-day boreal forest-wetland landscape to a hypothetical permafrost-free wetland landscape. However, complete disappearance of permafrost likely enhances large-scale drainage conditions (e.g., *Connon et al.*, 2014). The current conditions at the studied wetland site may therefore not be directly representative of a future, potentially drier, permafrost-free boreal landscape. Hence, the modelled absolute changes in θ_m and q_m should be seen as an upper limit.

3.4 Results

3.4.1 Changes in turbulent energy fluxes

At the end of winter in May 2014, a frost layer with a maximum depth of about 40 cm was observed in the wetland (Fig. II.2). The mean water table between April and November 2014 was 15 cm below the moss surface. In contrast, a maximum thawed layer of 40 cm overlaid cryotic soil between May and September 2014 in the forest and the decrease in water table level closely followed thaw depth during the summer. In 2014, the snow melt at the forest and the wetland occurred at the end of April and the ground was snow-covered again in October (Fig. II.2). During the snow cover period in late winter, half-hourly H at the wetland tower (H_{WET}) was negative most of the time, while H at the landscape tower (H_{LAND}) already reached maximum values of 200 W m^{-2} (Fig. 3.2a). At the same time, the largest mean midday (1200 - 1500 MST) Bowen ratio was observed for the landscape tower with 7.6 ± 0.8 (95% CI of mean), while the mean midday Bowen ratio at the wetland tower was the lowest with 0.3 ± 0.3 (Fig. 3.2c). Between May and November 2014, H_{WET} amounted to about 50% of H_{LAND} and the ratio of the two fluxes approached unity with higher contributions of wetlands in the landscape tower footprints (Fig. 3.2a, slope of H_{LAND} against H_{WET} increased significantly from 0.47 to 0.64 [$p < 0.001$ two-sample non-parametric Kolmogorov-Smirnov test] for H_{LAND} with wetland contributions $\leq$ 36% (25^{th} percentile) versus $\geq$ 63% (75^{th}). In contrast, half-hourly LE at the wetland tower (LE_{WET}) was about 54% larger than LE at

the landscape tower (LE_{LAND}, Fig. 3.2b). Slopes of LE_{LAND} against LE_{WET} were closer to unity with increasing contributions of wetlands to LE_{LAND} (slope decreased significantly from 1.63 to 1.47 [$p < 0.001$] for LE_{LAND} with wetland contributions $\leq$ 36% vs. $\geq$ 63%). Monthly mean midday Bowen ratios in the snow-free period ranged from 1.3 in July to 2.5 in October and from 0.4 in June to 0.9 in October at the landscape and the wetland tower, respectively (Fig. 3.2c). The total half-hourly turbulent energy flux (H + LE) was 13% smaller at the wetland tower compared to the landscape tower (slope = 0.87, r^2 = 0.86).

3.4.2 Changes in surface properties

Albedo. Albedo determines how much short-wave radiation is reflected at the surface and, therefore, partly controls the available energy to generate H and LE. Between April and November 2014, the wetland albedo was consistently higher than the forest albedo, except for a 3-day period (28-30 April 2014) shortly after snow melt when the wetland was flooded. Maximum albedo differences of 0.5 were observed during the snow cover period (April and October - November 2014). During the snow-free period, the wetland albedo exceeded the forest albedo by about 0.1. The regional median albedo (2000 - 2015; $\sim$4,000 km^2) in the southern Taiga Plains (Fig. 3.1b) showed similar seasonal dynamics as the albedo measured at the two towers. Median percent tree cover of the region was 35% (2.5 percentile: 9%, 97.5 percentile: 69%). The forest albedo at Scotty Creek corresponded to the values at the lower end of the distribution of regional albedo, whereas the wetland albedo was consistently higher than the 95% confidence interval (except for the flooded period, Fig. 3.3).

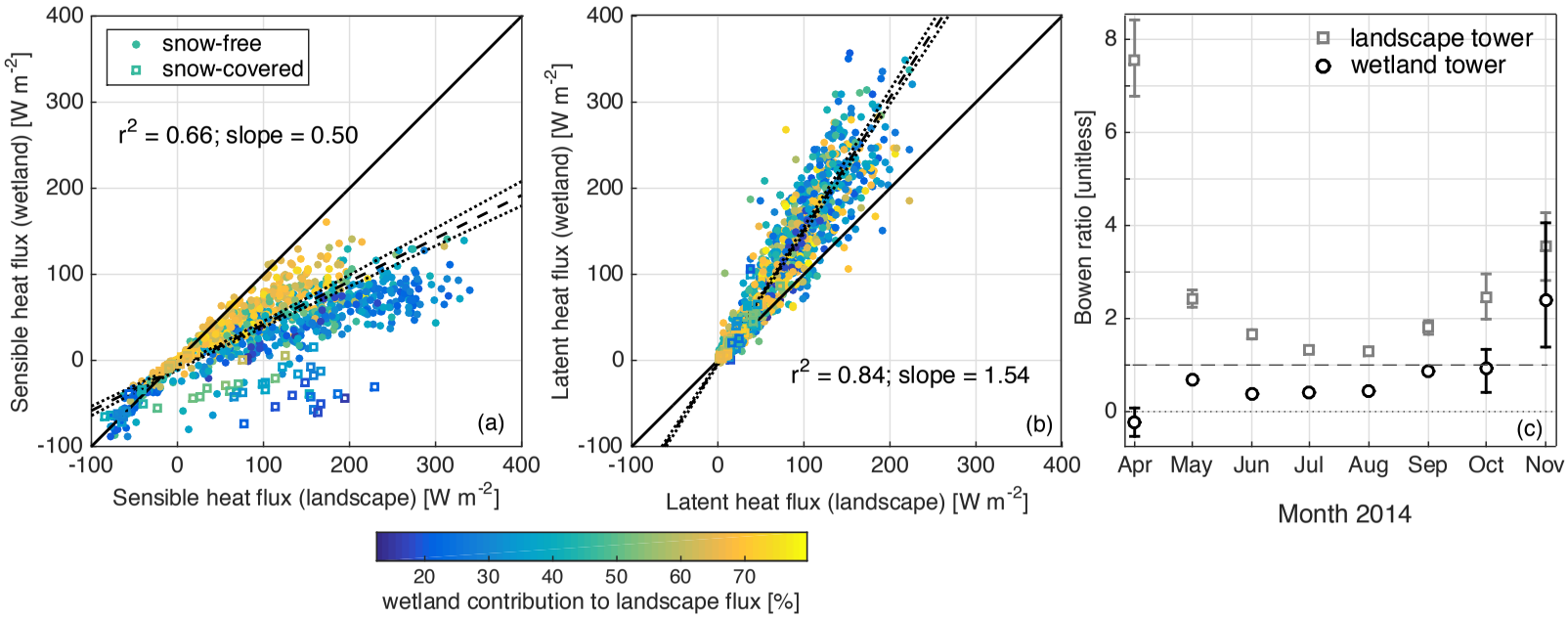

Figure 3.2 – **(a)** Turbulent sensible and **(b)** latent heat fluxes at the landscape (over a boreal forest-wetland landscape) and at the wetland tower (over a permafrost-free wetland) between 12 April and 07 November 2014. Colors of dots indicate relative contributions of wetlands to landscape tower fluxes. Best-fit lines with errors in both variables (*York et al.*, 2004) for the snow-free period are indicated as black dashed lines and slopes were significant at $\alpha = 0.001$. Dotted black lines indicate 95% confidence intervals (CI) of the regression as derived from 1,000 bootstrap simulations of the data. **(c)** Monthly mean midday (1200-1500 MST) Bowen ratio (sensible heat flux/latent heat flux) for the landscape and the wetland tower. Error bars indicate the 95% CI of the means.

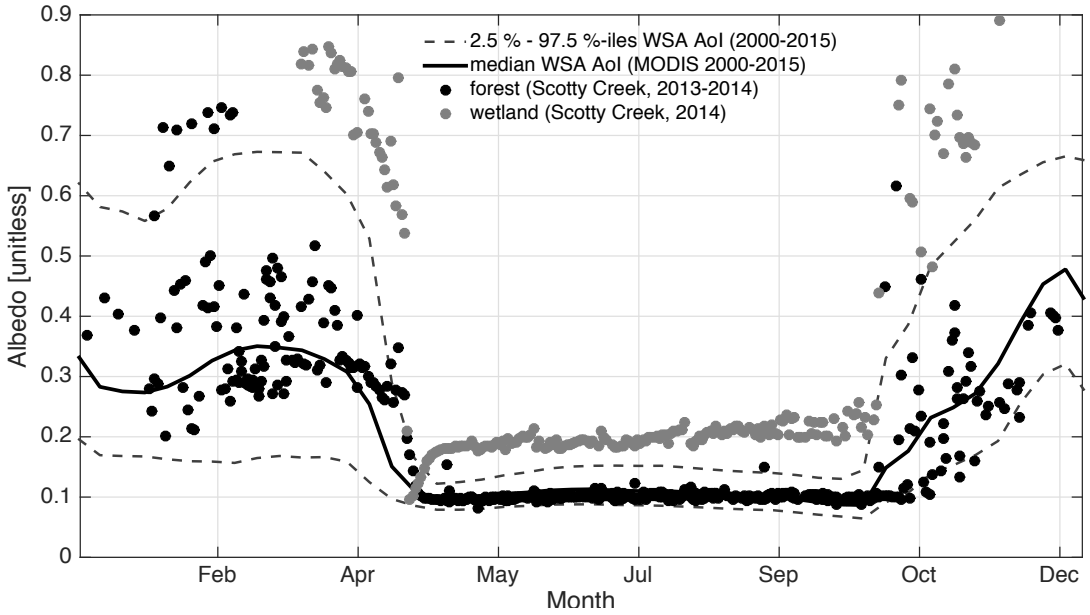

Figure 3.3 – Daily albedo of a boreal forest on a permafrost plateau (black dots, 2013-2014) and an adjacent permafrost-free wetland (grey dots, 2014), derived from four-component net radiometers at 1200 MST, and median (solid line, 2000-2015) and 2.5 percentile and 97.5 percentile (dotted lines) of 8-day 1-km white-sky albedo (WSA) across a ~4,000 km^2 area of interest (AoI) in the southern Taiga Plains (derived from MCD43B3). Percentiles show spatial variability across the AoI.

Aerodynamic conductance. The median bulk aerodynamic conductance for heat (g_H) was 37.8 mm s^{-1} (2.5 percentile: 15.8 mm s^{-1}, 97.5 percentile: 69.8 mm s^{-1}) for the landscape and 23.7 mm s^{-1} (2.5 percentile: 16.6 mm s^{-1}, 97.5 percentile: 40.8 mm s^{-1}) for the wetland tower. Differences between g_H at the landscape and the wetland tower decreased with increasing wetland contributions to the landscape fluxes (Fig. 3.4). Median-weighted LiDAR-derived canopy height (see Appendix II) within the flux footprints was 2.0 m (2.5 percentile: 1.1 m, 97.5 percentile: 3.7 m) and 0.3 m (2.5 percentile: 0.1 m, 97.5 percentile: 0.4 m) for the landscape and the wetland tower, respectively. Surface roughness length (z_0) increased linearly with the mean weighted LiDAR-derived canopy height ($r^2 = 0.75$, $p < 0.001$) and wetland contributions to flux footprints ($r^2 = 0.57$, $p < 0.001$; data not shown).

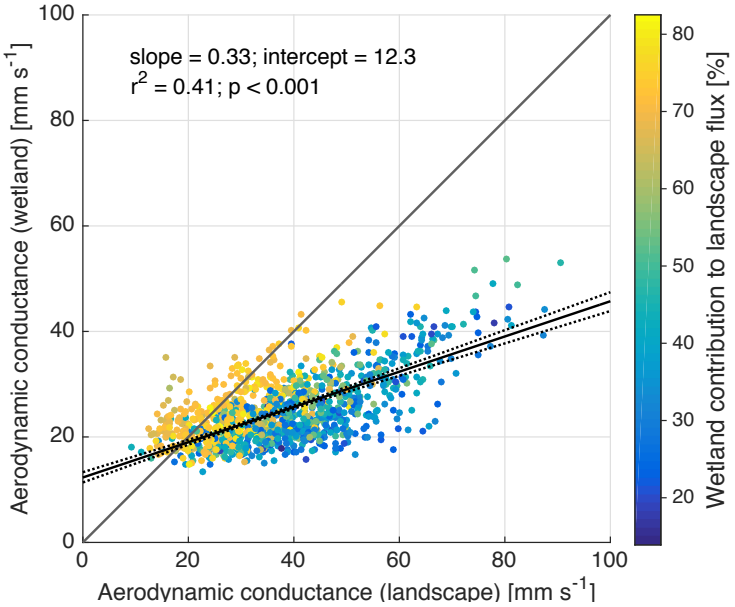

Figure 3.4 – Bulk aerodynamic conductance for heat in the footprints of the landscape and wetland tower. Colours of dots indicate contributions of wetlands to landscape tower fluxes. The total least-squares regression fit is shown as a solid black line. Dotted black lines indicate the 95% confidence interval of the regression as derived from 1,000 bootstrap simulations of the data.

Aerodynamic surface temperature. A surface cooling effect of wetlands is indicated by increasingly warmer T_{as} of the landscape tower footprints (T_{as_LAND}) with decreasing wetland contributions compared to T_{as} of the wetland (T_{as_WET}). The strongest cooling effect of 0.08 K per percent wetland contribution (K $\%^{-1}$) was observed for the snow cover period (Fig. 3.5a). During the snow-free period, wetland cooling ranged from 0.02 to 0.06 K $\%^{-1}$ and coefficients of determination between differences in T_{as_LAND} and T_{as_WET} and wetland contributions to landscape fluxes increased from 0.10 in May to 0.24 in September (Figs. 3.5b-g). Both, daytime and night-time T_{as_LAND}, were warmer than T_{as_WET} during the snow cover period. During the snow-free period, night-time T_{as_LAND} was consistently warmer than T_{as_WET}, whereas daytime T_{as_LAND} was at times colder than T_{as_WET} (Fig. 3.5).

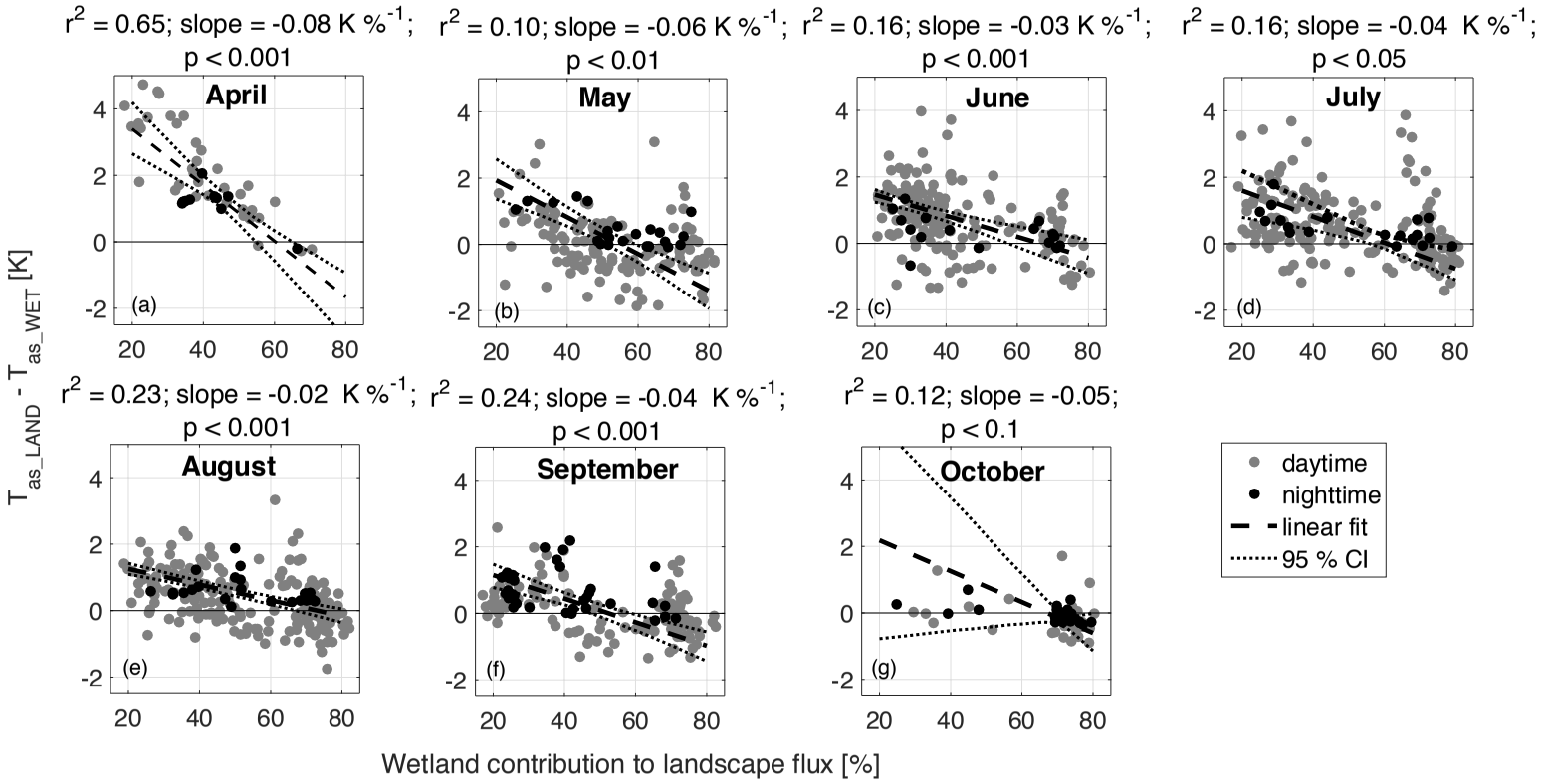

Figure 3.5 – Differences between aerodynamic surface temperatures of the landscape (T_{as_LAND}) and the wetland tower flux footprints (T_{as_WET}) as a function of wetland contributions to the landscape tower fluxes between April and October 2014. Daytime (grey dots) and night-time (black dots) differences are shown separately. Night-time is defined as periods with < 50 W m^{-2} incoming short-wave radiation. Best-fit lines with errors in both variables (*York et al.*, 2004) are shown as dashed lines. Dotted lines indicate the 95% confidence intervals of best-fit lines as derived from 1,000 bootstrap simulations of the data.

Surface conductance. In May and June 2013 and 2014, maximum bulk surface conductance (g_{s_0}; G_{s_bound} at a VPD of 0 kPa, see Appendix II) increased from 7.2 mm s^{-1} (Fig. 3.6a and Tab. 3.I) for the 'low wetland class' to 34.5 mm s^{-1} for the 'high wetland class'. In late summer, a similar increase was observed, but g_{s_0} for the high wetland class was reduced to 18.0 mm s^{-1}. The sensitivity of G_{s_bound} to VPD ($G_{s\_bound} = g_{s\_0}\ e^{-b_d\ VPD}$; see Appendix II) was most pronounced for the 'high wetland class' for May and June with the slope parameter b_d being 0.57 kPa^{-1}, whereas the 'medium wetland class' had the strongest sensitivity of G_{s_bound} to VPD between July and August with a b_d of 0.48 kPa^{-1}. The 'low wetland class' was the least sensitive during both periods (Tab. 3.I and Fig. 3.6). The limit of G_{s_bound} at infinite SW_{in} (g_{s_max} in $G_{s\_bound} = g_{s\_max}\ \frac{SW_{in}}{b_{infl}+SW_{in}}$; see Appendix II) increased with increasing flux footprint contributions from wetlands peaking in July and August at 33.8 mm s^{-1}. The inflection point of the G_{s_bound} vs. SW_{in} relationship (b_{infl} [W m^{-2}], see Appendix II) ranged between 45.8 W m^{-2} and 1337.2 W m^{-2} and was always highest for the 'high wetland class'. However, b_{infl} between classes were not significantly different, except for b_{infl} for the 'high wetland class' for July-August, which was significantly higher (Tab. 3.I). In July and August, g_{s_max} and b_{infl} were poorly constrained for the 'high wetland class' with 95% CI of 138.1 mm s^{-1} and 7531.4 W m^{-2}, respectively (Fig. 3.6).

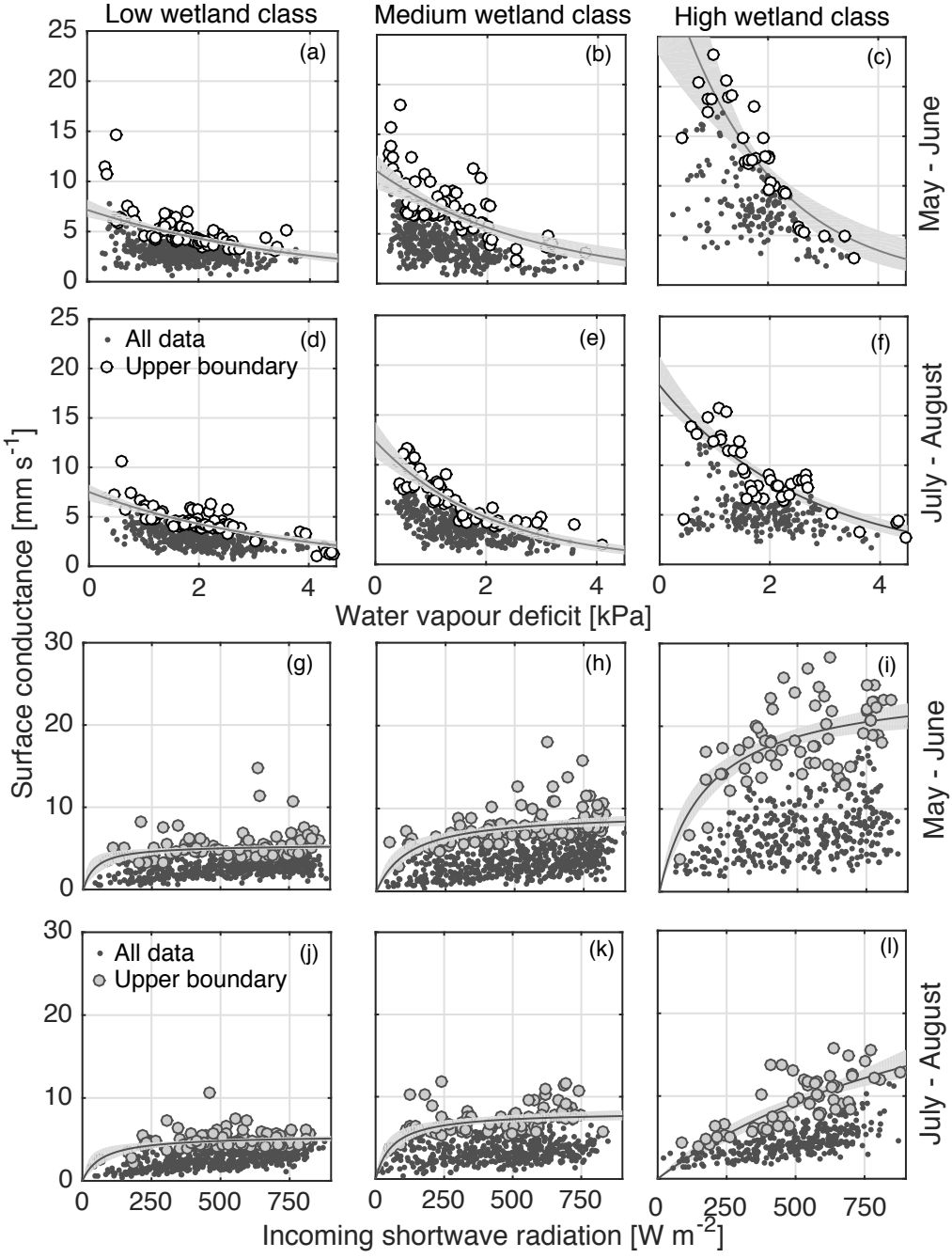

Figure 3.6 – Response of bulk surface conductance to **(a-f)** vapour pressure deficit and **(g-l)** incoming short wave radiation for the periods **(a-c & g-i)** May and June and **(d-f & j-l)** July and August for three classes of increasing permafrost-free wetland contributions ('low', 'medium', 'high'). Nonlinear model fits to the upper 15% of bulk surface conductance per 0.5 kPa (white circles) and 100 W m^{-2} bins (grey circles) are shown as solid lines. 95% confidence intervals are shown as shaded areas.

Table 3.I – Best parameter estimates and their 95% confidence intervals (CI) for vapour pressure deficit ($G_{s\_bound} = g_{s\_0}\, e^{-b_d\, VPD}$) and incoming shortwave radiation models ($G_{s\_bound} = g_{s\_max}\, \frac{SW_{in}}{b_{infl}+SW_{in}}$) of the upper boundary of bulk surface conductance (G_{s_bound}) for the periods May-June and July-August and for three classes of increasing permafrost-free wetland contribution to flux footprints. G_{s_bound} at a vapour pressure deficit of 0 kPa is given by g_{s_0}, while b_d is a slope parameter. G_{s_bound} at infinite shortwave incoming radiation is given by g_{s_max}, while b_{infl} is the inflection point (i.e., indicates the radiation value at which half of g_{s_max} is reached).

	Vapour pressure deficit (VPD) model				Incoming shortwave radiation (SW_{in}) model			
Wetland class	g_{s_0} [mm s^{-1}]	95% CI	b_d [kPa^{-1}]	95% CI	g_{s_max} [mm s^{-1}]	95% CI	b_{infl} [W m^{-2}]	95% CI
	May-June							
Low	7.2	6.4-8.2	0.25	0.19-0.32	5.5	5.1-6.1	45.8	12.2-107.1
Medium	11.3	9.5-12.9	0.35	0.23-0.45	9.6	8.4-10.9	120.6	51.8-197.1
High	34.5	23.2-53.1	0.57	0.36-0.80	25.3	22.0-29.4	175.4	96.7-279.3
	July-August							
Low	7.5	6.6-8.3	0.28	0.22-0.33	5.5	4.9-6.2	71.4	20.6-144.7
Medium	12.4	10.7-14.3	0.48	0.39-0.59	8.2	7.4-9.3	63.1	28.8-113.5
High	18.0	16.4-21.0	0.38	0.32-0.46	33.8	20.2-158.3	1337.2	567.8-8099.2

3.4.3 Regional-scale controls on surface properties in the lowlands of the southern Taiga Plains

To assess the regional-scale relationships between tree cover and daytime and night-time T_{rs} and albedo, we analysed 1-km MODIS percent tree cover, T_{rs}, and white-sky albedo between 2000 and 2015 for the southern Taiga Plains (Fig. 3.1b). The strongest relationships between daytime and night-time T_{rs} and tree cover were observed for March and April with r^2 of 0.34 and 0.27, respectively (Fig. 3.7a). During the night, areas with high tree cover were characterized by warmer T_{rs} throughout the year with maximum T_{rs} sensitivities to tree cover of 0.08 K $\%^{-1}$ in late winter. During the snow-free period (May to November), sensitivities were smaller with about 0.01 K $\%^{-1}$ (expressed as increase in K per one percent tree cover). Similarly, during the day, T_{rs} increased with tree cover during the winter (November to April) peaking at 0.06 K $\%^{-1}$ in mid-April. In contrast, high tree cover areas were characterized by colder T_{rs} compared to areas with low tree cover during the snow-free period (negative slopes of up to 0.04 K $\%^{-1}$, Fig. 3.7b).

The strongest relationships between T_{rs} and tree cover in late winter coincided with the strongest relationship between tree cover and albedo (maximum slope of 0.55% $\%^{-1}$ in March; r^2 = 0.62; Fig. 3.7c). In April, slopes and r^2 between tree cover and albedo rapidly decreased and remained small until September before they gradually increased again to a slope of 0.38% $\%^{-1}$ and an r^2 of 0.36 in early November (Fig. 3.7c).

In comparison, tower-based T_{rs} for the forest and wetland during the snow-free period indicate that median T_{rs} of the forest was 0.5 K colder during the day (1030 MST) and 1.7 K warmer during the night (2230 MST). During late winter, just before snow melt (13-30 April 2014), median daytime and nighttime T_{rs} of the forest was consistently warmer than T_{rs} of the wetland with differences of 1.2 and 1.8 K, respectively (data not shown).

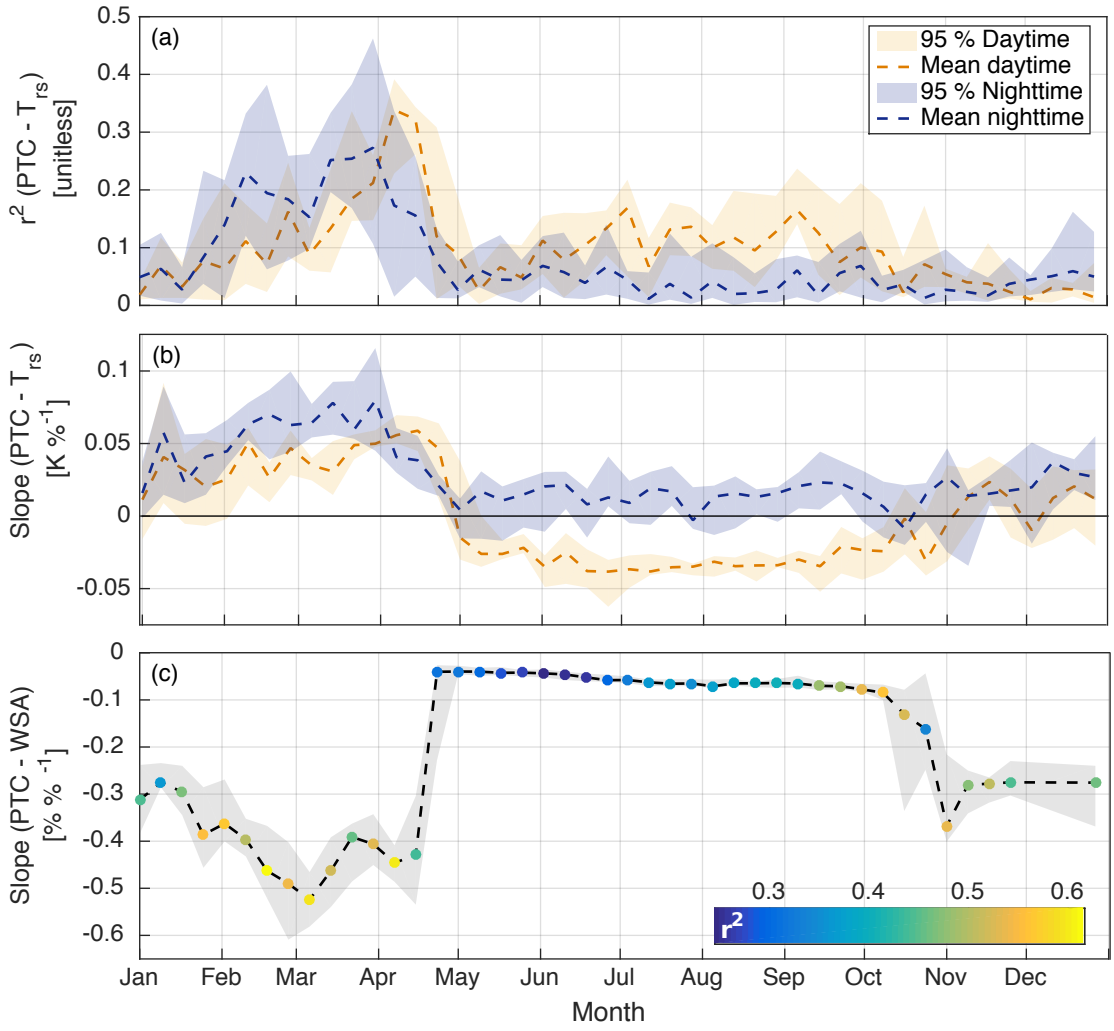

Figure 3.7 – **(a)** Seasonal dynamics of mean coefficients of determination (r^2) between 1-km per cent tree cover (PTC; MODIS VCF MOD44B) and 1-km daytime and nighttime radiometric surface temperature (T_{rs} at about 1230 and 0030 MST, respectively; MODIS Land Surface Temperature/Emissivity MOD11A2) for a ~4000 km^2 area in the southern Taiga Plains. **(b)** Seasonal dynamics of mean slopes of the regression between PTC and T_{rs}. **(c)** Seasonal dynamics of mean slopes between PTC and white-sky albedo (WSA, MODIS Albedo MOD43A3). Colors of dots represent mean r^2. Shaded areas indicate the 95% confidence intervals of the means for the period 2000-2015. All slopes are significant at $\alpha = 0.001$.

3.4.4 Permafrost thaw-induced boreal forest loss effects on regional air temperature and atmospheric moisture

To estimate the potential effects of permafrost thaw-induced boreal forest loss on air temperature and atmospheric moisture, we modelled diurnal dynamics of PBL height, θ_m, and q_m for 49 clear-sky days in 2014 for two scenarios: a present-day heterogeneous boreal forest-wetland landscape ('present-day landscape') and a hypothetical homogeneous, permafrost-free, treeless wetland landscape ('permafrost-free landscape'). Results for one clear-sky day (22 June 2014) are discussed in detail.

Clear-sky conditions are usually characterized by a smooth diurnal curve of SW_{in} as observed on 22 June 2014 (Fig. 3.8a). Heat flux for the present-day scenario peaked at 1300 MST. In comparison, the sensible heat flux for the permafrost-free scenario was consistently smaller and peaked at 1200 MST. For the permafrost-free scenario, LE was larger than the present-day scenario LE between 1000 MST and 2030 MST and was slightly smaller during the morning hours (Fig. 3.8a). Modelled θ_m fitted measured θ_m with a RMSE of 0.7 °C, while modelled q_m had a RMSE of 0.7 mmol mol^{-1}. The present-day scenario was warmer and drier than the permafrost-free scenario with differences of 2.0 °C in θ_m and 1.9 mmol mol^{-1} in q_m just before the PBL collapsed (Fig. 3.8b & c).

The PBL height was consistently larger for the present-day scenario compared to the permafrost-free scenario with differences of up to around 600 m. The mean effective heat capacity of the PBL for the present-day scenario was 52% higher. For the present-day and the permafrost-free scenario, 35% and 54% of the total sensible heat input was entrained with warm air from above the mixed layer. The total sensible heat input from the entrainment layer was 27% larger for the permafrost-free scenario just before the collapse of the PBL, mainly due to an enhanced gradient for this scenario between θ_m and potential temperature of the entrainment layer. The entrainment of dry air exceeded the surface input of water vapor for the present-day scenario causing a gradual q_m decrease during the day. For the permafrost-free scenario, the entrainment of dry air exceeded the water vapor input from the surface until 1430 MST. Afterwards, q_m gradually increased as the surface water vapor input (LE) exceeded the entrainment of dry air.

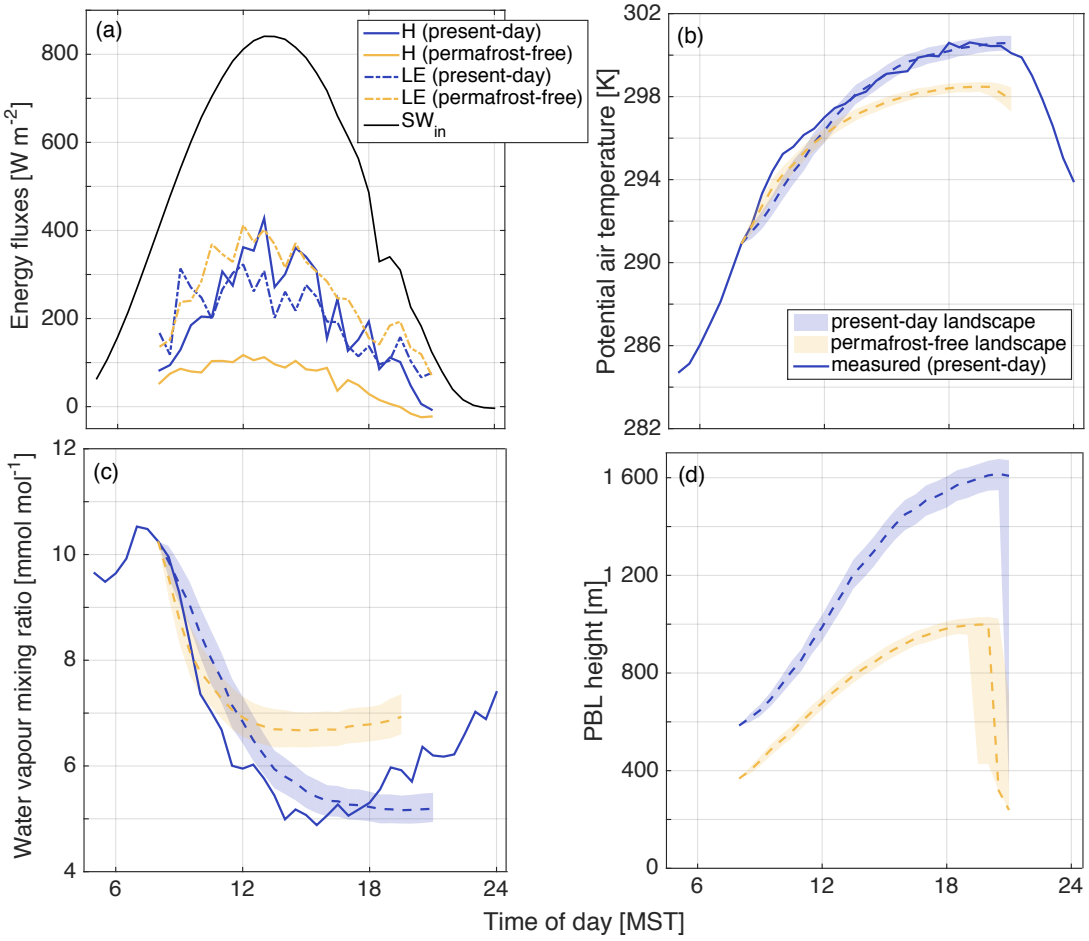

Figure 3.8 – **(a)** Sensible (H) and latent (LE) heat fluxes for a present-day heterogeneous boreal forest-wetland landscape with sporadic permafrost ('present-day landscape') and for a permafrost-free wetland landscape scenario ('permafrost-free landscape') and incoming shortwave radiation (SW_{in}) for 22 June 2014. **(b)** Measured and modelled potential air temperatures in the mixed layer (θ_m). **(c)** Measured and modelled water vapour mixing ratios (q_m) and **(d)** modelled planetary boundary layer (PBL) heights. Shaded areas represent uncertainty due to random errors in flux measurements. q_m is modelled only for the time period before the PBL collapsed.

The largest mean differences in θ_m between the present-day and the permafrost-free scenario were observed during April 2014 when θ_m in the permafrost-free scenario were 3.6 ± 2.4 °C (one standard deviation; $n = 3$) colder. During the summer, the permafrost-free scenario was 1.25 ± 0.8 (May and June; $n = 22$) and 1.58 ± 0.9 °C (July and August;

n = 16) colder. In September, θ_m for the permafrost-free and the present-day scenario were similar with differences of 0.02 $\pm$ 1.4 °C (n = 8). Water vapor mixing ratios were higher for the permafrost-free scenario throughout the observation period with maximum differences in July and August of 2.06 $\pm$ 1.3 mmol mol^{-1}. The permafrost-free scenario was 1.42 $\pm$ 1.2 mmol mol^{-1} wetter in May and June and only marginally wetter in April and September with 0.30 $\pm$ 0.2 and 0.17 $\pm$ 0.9 mmol mol^{-1}, respectively.

3.5 Discussion

3.5.1 Permafrost thaw impacts on turbulent energy fluxes

Permafrost thaw-induced boreal forest loss in the sporadic permafrost zone accelerates and actively changes vegetation composition and structure (e.g., *Baltzer et al.*, 2014; *Lara et al.*, 2016, Chapter 2). However, little is known about the biophysical impacts of these changes on local- to regional-scale land-atmosphere interactions. Insights from global climate models are limited by their spatial resolution (*Oleson et al.*, 2004). Remote sensing allows biophysical impact assessment of deforestation on climate (e.g. surface and air temperature) across the globe (*Alkama and Cescatti*, 2016; *Li et al.*, 2015) whereas in situ eddy covariance measurements in combination with local-scale modelling are useful to gain in-depth understanding of the underlying ecosystem processes (*Juang et al.*, 2007a, b; *Stiegler et al.*, 2016; *Vanden Broucke et al.*, 2015). Here, we combine landscape-scale eddy covariance measurements with regional-scale remote sensing data to quantify an atmospheric cooling and wetting effect of thaw-induced boreal forest loss. Similar to this study, a decrease of about 50% in annual H was observed for a fire-induced transition from a black spruce forest to bunch grasses in Alaska (*Liu et al.*, 2005) with the largest reduction at the end of the winter. In late winter, large albedo increases over treeless wetlands compared to forests drastically reduce available energy following thaw-induced forest-to-wetland conversion. Liquid water is unavailable for LE until snow melt, and all available energy is transferred to H (*Betts et al.*, 2001). During the summer, differences between boreal forest and wetland albedo are much smaller (e.g., *Betts and Ball*, 1997). Thus, larger H over the forested landscape

in the summer is mainly explained by different partitioning of energy between coniferous forests and wetlands (*Eugster et al.*, 2000). Increased post-thaw LE and decreased Bowen ratios are consistent with the thaw-induced increase in soil moisture availability (*Baltzer et al.*, 2014; *Quinton et al.*, 2011). A similar thaw-induced change in the partitioning of available energy to LE was reported for a tundra ecosystem in northern Sweden (*Stiegler et al.*, 2016). In temperate and tropical regions, deforestation is generally reducing LE (*Bala et al.*, 2007). Similarly, LE of a black spruce forest in Alaska decreased during the early treeless post-fire regeneration stages (*Liu et al.*, 2005). Thus, impacts of thaw-induced boreal forest loss on land-atmosphere interactions contrast deforestation impacts caused by fire disturbance or clear-cutting due to the associated shift toward higher post-thaw soil moisture.

In contrast to the strong control of wetland coverage on H_{LAND}, the control of wetland coverage on LE_{LAND} is less pronounced, indicating a more complex spatial pattern of water vapor fluxes across the landscape. Transpiration fluxes across the transition from wetlands to forests show a strong spatial heterogeneity (*Baltzer et al.*, 2014; *Patankar et al.*, 2015) and, additionally, LE may vary within wetlands due to spatial variations in water table position. In the center of collapse-scar bogs, the water table is deeper due to long-term peat accumulation (*Turetsky et al.*, 2007; *Zoltai*, 1993). At the recently thawed forest edges, the water table is closest to the moss surface enhancing the LE contribution of open water evaporation. In contrast to the landscape tower, these transition zones contributed only little to the wetland tower footprints. The complex spatial patterns in LE may reflect these small-scale heterogeneity of surface evaporation sources across boreal forest-wetland landscapes (*Angstmann et al.*, 2013; *Brown et al.*, 2010).

3.5.2 Permafrost thaw and landscape-scale changes in land surface properties

In a well-mixed PBL, atmospheric conditions (e.g., SW_{in}, VPD, T_a) over individual wetlands are similar to conditions over the larger boreal forest-wetland landscape, if the surface structure of the landscape is disorganized at length scales < 10 km (*Garratt*, 1994; *Shuttleworth*, 1988). Thus, contrasts in albedo, and eco-physiological and

aerodynamic attributes between permafrost-free ecosystems (wetlands) and ecosystems with permafrost (forests) mainly produce the observed differences in turbulent energy fluxes. In boreal forests, black spruce stands with low reflectance mask the highly reflective snow or ground cover (e.g., lichen, shrubs) resulting in a lower albedo compared to wetlands. The most pronounced albedo differences occur during the snow cover period when the non-forested ecosystems (e.g., wetlands) are entirely covered by snow. The higher available energy over forest stands (*Betts and Ball*, 1997; *Liu et al.*, 2005; *Lohila et al.*, 2010; *Zhao and Jackson*, 2014) indicates that albedo differences mainly induce the thaw-related decrease in H during the late winter. In the summer, with smaller albedo contrasts, differences in eco-physiological and aerodynamic properties enhance post-thaw LE and attenuate H.

Several studies have assessed the land use and land cover change impacts on remotely sensed T_{rs} (e.g., *Houspanossian et al.*, 2013; *Li et al.*, 2015; *Zhao and Jackson*, 2014). However, T_{as} represents the surface temperature driving H and can substantially differ from T_{rs}, particularly in boreal forests with relatively sparse tree density, strong atmospheric coupling of the tree tops, and a ground surface that is more decoupled from the atmosphere (*Friedl*, 2002; *Kustas et al.*, 2006; *Sun and Mahrt*, 1995). We suggest that studies of forest loss impacts on remotely sensed T_{rs} should be complemented with analyses of T_{as} (e.g., derived from eddy covariance measurements) to better characterize the effects on local climate (e.g., *Baldocchi and Ma*, 2013). In this study, we show that thaw-induced forest loss leads to strong late winter cooling of T_{as} and T_{rs}. Summer, cooling of T_{as} instead is moderate, while remotely sensed T_{rs} for the same period indicates a daytime warming effect of forest loss. In contrast to tropical and temperate forests that are affected by large transpirational cooling (*Bonan*, 2008; *Lee et al.*, 2011), LE of black spruce forests is small (*Baldocchi et al.*, 2000). Thus, boreal forests have a minimal transpirational cooling effect (*Lee et al.*, 2011). At the same time, large LE over permafrost-free wetlands substantially cools the surface, which explains their lower T_{as} despite lower g_H. Reduced g_H and thus heat transfer efficiency with decreasing forest cover are consistent with lower aerodynamic roughness of low stature ecosystems, such as wetlands, compared to forests (*Juang et al.*, 2007b; *Kelliher et al.*, 1993; *Rotenberg*

and Yakir, 2010).

The thaw-induced decrease in Bowen ratios is mainly caused by increased post-thaw soil moisture (*Baltzer et al.*, 2014; *Wright et al.*, 2009). In addition, the limited stomatal control of LE in wetlands, dominated by *Sphagnum* and *Carex* species (*Camill*, 1999a), favours larger maximum g_s and consequently enhances LE. Consistently low g_s is typical for black spruce dominated boreal forests making them more drought resistant compared to other boreal tree species (*Baldocchi et al.*, 2000; *Ewers et al.*, 2005). Additionally, black spruce has a low light-saturation limit of photosynthesis, preventing stomata to open further at higher light levels (e.g., $SW_{in} > 400$ W m^{-2}; *Baldocchi et al.*, 2000; *Dang et al.*, 1998; *Goulden et al.*, 1997; *Kelliher et al.*, 1993). The steady increase of wetland g_s even at high light levels in wetlands may be explained by the forest-wetland differences in soil moisture, their high *Sphagnum* coverage, and their lack of stomata control (*Betts et al.*, 1999; *McFadden et al.*, 2003; *Nichols and Brown*, 1980). Similarly, soil moisture limitation on evapotranspiration is reduced and g_s is increased upon thaw in tundra environments in Sweden (*Stiegler et al.*, 2016).

3.5.3 Regional tree cover controls on surface characteristics

Decreasing tree cover in the southern Taiga Plains favours warmer daytime T_{rs} in summer, contrasting the consistent cooling effect of thaw-induced forest loss on T_{as}. Such a summertime warming effect of forest loss on daytime T_{rs} was previously reported for the boreal zone (*Li et al.*, 2015). Similar to our study, *Li et al.* (2015) found a daytime T_{rs} cooling effect in winter and a year-round cooling effect on night-time T_{rs}. Albedo is most sensitive to tree cover in late winter, when SW_{in} and Bowen ratios are high (*Betts et al.*, 2001; *Liu et al.*, 2005), indicating that albedo differences are the main cause for the observed cooling effect of forest and tree cover loss on T_{rs} (e.g., *Betts*, 2000; *Li et al.*, 2015; *Zhao and Jackson*, 2014). In contrast, the warming effect on daytime T_{rs} in the summer is likely caused by eco-physiological and aerodynamic effects exceeding the impacts of smaller summer albedo differences (e.g., *Juang et al.*, 2007b). Transpirational cooling of forests is small and unlikely causing these patterns due to lower LE over forests compared to wetlands. To explain the warming effect of tree cover

loss on daytime T_{rs} in the summer, we argue that, with increasing tree cover, sensible heat is more efficiently exchanged between the land surface and the atmosphere and ground surface shading is enhanced (e.g., *Mahrt and Vickers*, 2004; *Sun and Mahrt*, 1995). The ground surface, which receives less SW_{in} beneath denser canopies due to below-canopy shading (*Chasmer et al.*, 2011), is strongly affecting remotely sensed T_{rs}. The observed warming effect of tree cover loss on daytime T_{rs} suggests enhanced summertime soil heat input in areas with declining tree cover. This warming effect is consistent with the absence of permafrost in mostly treeless wetlands and the occurrence of permafrost in forested plateaus (*Quinton et al.*, 2009; *Zoltai*, 1993).

Warmer night-time T_{rs} in densely forested areas may be related to the night-time biomass release of heat storage accumulated during the day (*Lindroth et al.*, 2010). Larger radiative cooling of open- compared to closed-canopy sites was reported for Scotty Creek (*Chasmer et al.*, 2011). Additionally, forests can be warmer at night because trees reduce the formation of stable stratification allowing a more efficient transport of warm air from above to the surface (*Lee et al.*, 2011). Our results highlight the importance to distinguish between T_{rs} and T_{as} when analysing land cover change impacts and to account for potentially contrasting effects between the snow and snow-free periods as well as between daytime and night-time observations.

3.5.4 Effects of permafrost thaw-induced boreal forest loss on air temperatures and atmospheric moisture

Due to the complex interactions of various biophysical impacts on near-surface climates (*Betts et al.*, 2001), previous studies demonstrated that forest loss appears to have either a cooling or a warming effect on surface air temperature (*Alkama and Cescatti*, 2016; *Juang et al.*, 2007b, b; *Lee et al.*, 2011; *Mildrexler et al.*, 2011). *Lee et al.* (2011) observed warmer daytime and night-time air temperatures over mid- to high-latitude forests compared to nearby open land due to the combined effects of decreased albedo and increased surface roughness and Bowen ratios. *Juang et al.* (2007b) showed that increased g_H of forests compared to agricultural fields can lead to a cooling effect of afforestation on surface temperature despite concurrent decreases in albedo. On a global

scale, a warming effect of forest loss on air temperatures was explained by the decrease in surface roughness and reduced transpirational cooling (e.g., *Alkama and Cescatti*, 2016; *Mildrexler et al.*, 2011). In this study, we show that thaw-induced boreal forest loss reduces H and increases LE (i.e., reducing Bowen ratios), exerting a cooling effect on regional air temperature along with an increase in atmospheric moisture. Reduced diurnal H inputs to the PBL over permafrost-free wetlands result in more shallow PBL depths compared to the typically deeper PBL depths characteristic for intact boreal forests (*Betts et al.*, 2001). More shallow PBL depths reduce the effective heat capacity of the PBL (*Snyder et al.*, 2004), generally amplify surface temperature variability (*Davy and Esau*, 2014; *Esau et al.*, 2012), and, thus, can have profound impacts on regional climates (*Esau and Zilitinkevich*, 2010). The large diurnal entrainment of warm and dry air into the PBL over boreal forests decreases q_m causing a surface-PBL feedback by further increasing VPD, inducing further decreases in g_s, resulting in enhanced partitioning of available energy to H, and eventually further PBL growth (*Baldocchi et al.*, 2000; *Hill et al.*, 2008). However, boreal forest loss and conversion to wetlands with high *Sphagnum* coverage decrease stomata control of LE, which could slow down this positive feedback mechanism.

Changes in PBL depth, air temperature and water vapour dynamics may also affect cloud formation and regional precipitation patterns (e.g., *Juang et al.*, 2007a). A decrease in air temperature and a concurrent increase in atmospheric moisture would result in a lower lifting condensation level (height at which condensation of a lifting air parcel occurs) and could potentially increase cloud cover and the frequency of convective rainfall events (e.g., *Betts*, 2009). However, as thaw-induced boreal forest loss also leads to decreases in PBL depth, the probability of more frequent convective rainfall events may not increase if the PBL height stays below the lifting condensation level (*Juang et al.*, 2007a). Further research using more complex PBL models is required to better characterize the impacts of thaw-induced boreal forest loss on regional precipitation dynamics (e.g., *de Arellano et al.*, 2012; *Juang et al.*, 2007a).

Permafrost thaw and ultimately its disappearance are likely to continue causing boreal forest loss and wetland expansion in the lowlands of the sporadic permafrost zone

in North America. Similar to the southern Taiga Plains, thaw-induced forest loss accelerates in the Tanana Flats in central Alaska. However, there, loss is mainly attributed to decreasing birch forest coverage with a concurrent wetland area increase (*Lara et al.*, 2016). The biophysical impacts of deciduous forest loss are likely to differ from the loss of coniferous forests (*Juang et al.*, 2007b), even when resulting in similar post-thaw wetland ecosystems. Deciduous forests are generally characterized by a higher albedo, a larger g_s and larger LE compared to boreal coniferous forests (*Amiro et al.*, 2006; *Baldocchi et al.*, 2000; *Betts and Ball*, 1997; *Liu et al.*, 2005). Thus, to better understand how permafrost thaw-induced land cover change affects land-atmosphere interactions and consequently regional and global climates, the biophysical impacts of varying pathways of permafrost thaw need to be assessed in addition to its biogeochemical impacts.

Acknowledgements

I am thankful to Dr. C. Hopkinson for providing LiDAR data and to E. Houghton for supplying snow density measurements.

CHAPTER 4

THE POSITIVE NET RADIATIVE GREENHOUSE GAS FORCING OF INCREASING METHANE EMISSIONS FROM A THAWING BOREAL FOREST-WETLAND LANDSCAPE

Context within the thesis

The present chapter quantifies the impact of recent thaw-induced wetland expansion on landscape-scale net CH_4 emissions and the associated net greenhouse gas radiative forcing (accounting additionally for potential long-term net CO_2 uptake). To achieve this goal, I combine nested eddy covariance net CH_4 flux measurements, recent wetland expansion rates at Scotty Creek, and long-term apparent rates of C accumulation from 63 North American boreal peatlands. These data are used as input to an atmospheric CO_2 and CH_4 concentration model. Using the model output, I demonstrate the time evolution of the net radiative greenhouse gas forcing induced by thaw-induced wetland expansion during the 21st century. Chapter 4 addresses biogeochemical climate impacts of land cover changes in the southern Taiga Plains and, thus, complements the results on tree cover dynamics in the Taiga Plains in chapter 2, and on biophysical climate impacts in chapter 3. Chapter 4 provides the context for chapter 5, which addresses both land cover change and direct climate change effects on CO_2 fluxes in more detail. Long-term net CO_2 fluxes in chapter 4 are derived from paleoecological studies and one year of eddy covariance flux measurements.

4.1 Abstract

At the southern margin of permafrost in North America, climate change causes widespread permafrost thaw. In boreal lowlands, thawing forested permafrost peat plateaus ('forest') lead to expansion of permafrost-free wetlands ('wetland'). Expanding wetland area with saturated and warmer organic soils is expected to increase landscape methane (CH_4) emissions. Here, we quantify the thaw-induced increase in CH_4 emissions for

a boreal forest-wetland landscape in the southern Taiga Plains, Canada, and evaluate its impact on net radiative forcing relative to potential long-term net carbon dioxide (CO_2) exchange. Using nested wetland and landscape eddy covariance net CH_4 flux measurements in combination with flux footprint modeling, we find that landscape CH_4 emissions increase with increasing wetland-to-forest ratio. Landscape CH_4 emissions are most sensitive to this ratio during peak emission periods, when wetland soils are up to 10 °C warmer than forest soils. The cumulative growing season (May to October) wetland CH_4 emission of $\sim$13 g CH_4 m^{-2} is the dominating contribution to the landscape CH_4 emission of $\sim$7 g CH_4 m^{-2}. In contrast, forest contributions to landscape CH_4 emissions appear to be negligible. The rapid wetland expansion of 0.26$\pm$0.05 % yr^{-1} in this region causes an estimated growing season increase of 0.034$\pm$0.007 g CH_4 m^{-2} yr^{-1} in landscape CH_4 emissions. A long-term net CO_2 uptake of more than 200 g CO_2 m^{-2} yr^{-1} is required to offset the positive radiative forcing of increasing CH_4 emissions until the end of the 21st century as indicated by an atmospheric CH_4 and CO_2 concentration model. However, long-term apparent carbon accumulation rates in similar boreal forest-wetland landscapes and eddy covariance landscape net CO_2 flux measurements suggest a long-term net CO_2 uptake between 49 and 157 g CO_2 m^{-2} yr^{-1}. Thus, thaw-induced CH_4 emission increases likely exert a net radiative greenhouse gas forcing through the 21st century.

4.2 Introduction

Current global climate change is mainly attributed to rapidly rising atmospheric concentrations of two greenhouse gases, carbon dioxide CO_2 and methane CH_4 (*Myhre et al.*, 2013). The climate system impacts of changing greenhouse gas concentrations and other forcings is commonly expressed by their influence on the top-of-atmosphere net energy flux, referred to as radiative forcing (W m^{-2}; *Myhre et al.*, 2013). From 1750 to 2011, the radiative forcing resulting from increasing atmospheric CH_4 concentrations was equivalent to about 25% of the radiative forcing from rising CO_2 concentrations. The recent increase in radiative forcing from CH_4 emissions has been mainly attributed

to increasing anthropogenic CH_4 emissions (*Myhre et al.*, 2013; *Nisbet et al.*, 2014). Wetlands represent the largest natural CH_4 source to the atmosphere contributing about a third (177-284 Tg CH_4 yr^{-1}) of the total global CH_4 emissions (500 to 600 Tg CH_4 yr^{-1}; *Bridgham et al.*, 2013; *Dlugokencky et al.*, 2011; *Kirschke et al.*, 2013; *Melton et al.*, 2013). Inter-annual variations in wetland CH_4 emissions contribute 70% of the variability in total global CH_4 emissions (*Bousquet et al.*, 2006). Despite the importance of wetlands for the global atmospheric CH_4 budget, estimates of wetland CH_4 emissions are still poorly constrained (*Kirschke et al.*, 2013).

Many boreal wetlands have slowly accumulated thick peat layers since the last ice age (*Treat et al.*, 2016), storing now about 436 Pg of soil organic C as peat (i.e., north of 45°N; *Loisel et al.*, 2014). Despite their large C stocks and prevailing anoxic conditions, these boreal peatlands contribute relatively little ($\sim$20%) to global wetland CH_4 emissions (*Bridgham et al.*, 2013) due to the temperature-limitation in microbial CH_4 production (*Dunfield et al.*, 1993; *Frolking et al.*, 2011; *Treat et al.*, 2014). Thus, boreal peatlands sequester CO_2 from the atmosphere and, ultimately, re-emit a small proportion of the fixed C as CH_4 (*Frolking et al.*, 2011). About 278 Pg C is contained in peatlands of the northern circumpolar permafrost region (*Tarnocai et al.*, 2009). Increasingly warmer air temperatures, altered hydrology, and thawing of perennially frozen organic soils within this region, however, could result in enhanced microbial CH_4 production through warmer soils and higher water levels (e.g., *Schuur et al.*, 2015). Additionally, permafrost thaw in boreal peatlands often leads to shifts in vegetation communities toward more aquatic species (e.g., sedges; *Camill*, 1999a). Increasing sedge density with deeper roots may enhance CH_4 production through the addition of easily decomposable root litter and exudates (*Chanton et al.*, 2008; *Prater et al.*, 2007). Additionally, the presence of sedges may enhance plant-mediated CH_4 transport through their aerenchymous tissue. Methane oxidation above the water table is then minimized as CH_4 bypasses the otherwise diffusional CH_4 transport through the aerobic soil layers (*Olefeldt et al.*, 2013; *Treat et al.*, 2007). Ebullition, the transport of CH_4 with gas bubbles, also minimizes CH_4 oxidation and has been observed to increase with thawing permafrost and associated flooding of surface soils (*Klapstein et al.*, 2014). Better-constrained CH_4 emission

estimates for boreal peatlands in the permafrost region and a better understanding of their environmental drivers are, thus, crucial for well-constrained projections of boreal peatland contributions to global net radiative forcing (*Bousquet et al.*, 2006; *Dlugokencky et al.*, 2009; *Schuur et al.*, 2015).

Permafrost at the southern margin of its distribution persists in disequilibrium with the current climate (e.g., *Camill and Clark*, 1998). Here, increased energy input has resulted in extensive permafrost loss in boreal lowlands of North America where relatively dry forested permafrost peat plateaus ('forest') are replaced with wetter, treeless, permafrost-free collapse-scar bogs and fens ('wetland') resulting in highly fragmented landscapes (see Chapter 2; *Baltzer et al.*, 2014; *Lara et al.*, 2016; *Quinton et al.*, 2011). Chamber-based studies in such heterogeneous boreal forest-wetland landscapes have identified wetlands as major CH_4 emission sources, while forests remain comparatively small net CH_4 sources or sinks (*Bubier et al.*, 2005; *Johnston et al.*, 2014; *Liblik et al.*, 1997; *Moore et al.*, 1994; *Turetsky et al.*, 2002). Current thaw-induced wetland expansion and associated forest loss in northwestern Canada (e.g., *Baltzer et al.*, 2014) in combination with increasing air and soil temperatures are therefore expected to further enhance regional CH_4 emissions over the next few decades (*Johnston et al.*, 2014; *Liblik et al.*, 1997; *Moore et al.*, 1998).

Here, we first integrate nested eddy covariance ecosystem and landscape net CH_4 flux (F_{CH4}; nmol m^{-2} s^{-1}) measurements (*Desai et al.*, 2015) with flux footprint modeling and remotely sensed land cover data (e.g., *Chasmer et al.*, 2008; *Kljun et al.*, 2015) to better understand the spatial and temporal variability of F_{CH4} across a heterogeneous and rapidly thawing boreal forest-wetland landscape in the southern Taiga Plains ecozone of northwestern Canada. Next, we quantify the net radiative greenhouse gas (CH_4 and CO_2) forcing of thaw-induced F_{CH4} changes of the boreal forest-wetland landscape using a dynamic atmospheric CH_4 and CO_2 concentration model (*Frolking et al.*, 2006). The objectives of our study are to

— describe how F_{CH4} of a boreal forest-wetland landscape vary spatially with wetland extent and temporally with soil temperature and water table depth,

— quantify the impact of thaw-induced wetland expansion on landscape F_{CH4}, and

— assess the net radiative forcing of thaw-induced landscape F_{CH4} changes and concurrent net CO_2 uptake rates.

4.3 Materials and Methods

4.3.1 Study site

The study site, the Scotty Creek watershed, NT (61°18' N; 121°18' W), is located in the sporadic permafrost zone (> 10% - 50% in areal extent) of the southern Taiga Plains ecozone of northwestern Canada (*Quinton et al.*, 2011). The southern part of Scotty Creek is dominated by forested permafrost peat plateaus (*Picea mariana*, ericaceous shrubs [mainly *Rhododendron groenlandicum*], lichens [*Cladonia* spp.] and bryophythes [*Sphagnum fuscum* and *S. capillifolium*]) and treeless, permafrost-free collapse-scar bogs (ericaceous shrubs [*Chamaedaphne calyculata, Andromeda polifolia, Vaccinium oxycoccos*], bryophytes [*Sphagnum balticum* and *S. magellanicum*], pod grass [*Scheuchzeria palustris*]) (*Garon-Labrecque et al.*, 2015) with an organic layer thickness of >3 m and a mean total organic carbon content of 167±11 kg C m^{-2} (n = 3; N. Pelletier, unpublished results). More detailed descriptions of the study site can be found in *Quinton et al.* (2011), *Baltzer et al.* (2014), and *Garon-Labrecque et al.* (2015).

4.3.2 Eddy covariance measurements, flux data processing, and ancillary measurements

Between May 2013 and May 2016, F_{CH4} of the boreal forest-wetland landscape (F_{CH4_LAND}; nmol m^{-2} s^{-1}) was measured at a 15-m eddy covariance ('landscape') tower. Molar densities of CH_4 were measured with an open-path CH_4 analyzer (LI-7700, LI-COR Biosciences, Lincoln, NE) and the 3-D wind velocities with a sonic anemometer (CSAT3A, Campbell Scientific Inc., Logan, UT). Net water vapor (H_2O) and CO_2 fluxes were measured using an open-path CO_2/H_2O infrared gas analyzer (EC150, Campbell Scientific Inc., Logan, UT), except for the period March to June 2015 when an enclosed-path CO_2/H_2O infrared gas analyzer (LI-7200, LI-COR Biosciences) was used (see *Helbig et al.*, 2016a). The horizontal distance between the LI-7700 and the CSAT3A was

0.3 m and the vertical separation was 0.23 m.

At a nearby nested 2-m eddy covariance wetland (collapse-scar bog) tower, ecosystem F_{CH4} (F_{CH4_WET}; nmol m^{-2} s^{-1}) was measured between April 2014 and May 2016 using an instrumental setup identical to the landscape tower. The LI-7700 was installed at the same height as the CSAT3A, but was horizontally separated by 0.48 m. For both towers high-frequency 10-Hz turbulence data and CH_4, CO_2, and H_2O densities were recorded with CR3000 dataloggers (Campbell Scientific Inc.). At the end of the growing seasons, the LI-7700's were taken down (early November [2014 and 2015] and early September [2013]) and re-installed in late winter (between mid-March [2015 and 2016] and mid-April [2014]). The calibration of the LI-7700s was checked at the beginning and at the end of each growing season and twice during the growing season using the same zero (Ultra Zero Ambient Air, Praxair Canada Inc, Mississauga, ON, Canada) and 2.02-ppm CH_4 span gas ($\pm$0.1 ppm; Praxair Canada Inc.). No appreciable span or zero drift was observed. Forest (T_{s_FOR}, °C) and wetland soil temperatures (T_{s_WET}, °C) were measured near the eddy covariance towers at 32 cm below the moss surface using type T thermocouples (Omega Engineering, Stamford, CT, USA). Wetland water table depth (WTD, cm relative to the moss surface [center of wetland]) was measured in a perforated PVC tube using a vented pressure transducer (OTT PLS, Mellingen, Switzerland). A negative WTD indicates a water table below the moss surface. A more detailed description of the instrumental setup is given in Chapter 3.

Turbulent gas fluxes were calculated using the EddyPro software (version 6.1.0, LI-COR Biosciences). Briefly, we used a double rotation for sonic anemometer tilt correction, removed spikes in the high-frequency time series (*Vickers and Mahrt*, 1997), corrected sonic temperature for humidity effects (*Dijk et al.*, 2004), and used block averaging for half-hour time series and a covariance maximization procedure to detect time lags. Analytical spectral corrections according to *Moncrieff et al.* (1997) and *Moncrieff et al.* (2004) were applied to account for low- and high-pass filtering effects, respectively. Temperature- and humidity-induced density fluctuations were compensated according to *Webb et al.* (1980) ['WPL term']. To calculate F_{CH4_WET}, corrections for spectroscopic effects were incorporated in the WPL term (*McDermitt et al.*, 2010). Half-hourly F_{CH4}

were discarded when turbulence was not fully developed or non-stationary (*Mauder and Foken*, 2011), or when F_{CH4} were identified as outliers (*Papale et al.*, 2006). F_{CH4} was not used in the analyses when the CH_4 signal quality was low (indicated by a LI-7700 Relative Signal Strength Indicator [RSSI] < 20%) or when turbulence was weak (i.e., a friction velocity threshold of 0.17 m s^{-1} [95% confidence interval: 0.12 - 0.25 m s^{-1}] as determined according to *Papale et al.* (2006)).

Flux footprints for both towers were modeled according to *Kljun et al.* (2015) and coupled to a land cover classification map (*Chasmer et al.*, 2014) to derive the relative contributions from each land cover type to half-hourly flux measurements. The landscape flux footprints consisted mainly of forests and wetlands. In contrast, the wetland flux footprints mainly originated from the wetland just north of the landscape tower and were entirely located within its long-term flux footprint (see Chapter 3). Landscape F_{CH4} were excluded from the analyses when contributions from a nearby lake exceeded 5% and F_{CH4_WET} were excluded when wetland contributions were less than 95%.

To obtain cumulative F_{CH4} (ΣF_{CH4}, g CH_4 m^{-2}), we gap-filled F_{CH4_LAND} and F_{CH4_WET} using the 'marginal distribution sampling' method (*Reichstein et al.*, 2005), an extended look-up table method taking into account temporal autocorrelation. For the look-up tables, we used T_{s_WET}, WTD, and wind speed. We chose T_{s_WET} at 32 cm because maximum CH_4 production in peatlands was found to peak at about 20 cm below the water table (e.g., *Kettunen et al.*, 1999), corresponding to a depth of about 30 cm in the studied wetland (median WTD $\approx$ -10 cm). Look-up table gap-filling methods yield reliable annual ΣF_{CH4} estimates with an uncertainty of about $\pm$10% (*Hommeltenberg et al.*, 2014). Growing season landscape ΣF_{CH4} (ΣF_{CH4_LAND}; g CH_4 m^{-2}) and wetland ΣF_{CH4} (ΣF_{CH4_WET}; g CH_4 m^{-2}; defined for the snow-free period from May to October) were obtained by combining F_{CH4_LAND} and F_{CH4_WET} between May to August 2014 and September to October 2015 due to large gaps in F_{CH4_WET} in both years (Fig. 4.1). After quality control, gaps in F_{CH4_LAND} and F_{CH4_WET} totaled 64% and 58%, respectively. The uncertainty in ΣF_{CH4_LAND} and ΣF_{CH4_WET} was estimated as a combination of uncertainties introduced by the friction velocity threshold selection, by random errors in F_{CH4} measurements, and by uncertainties in gap-filled

F_{CH4}. Briefly, ΣF_{CH4_LAND} and ΣF_{CH4_WET} was calculated for 100 friction velocity thresholds derived according to *Papale et al.* (2006). For each of the 100 F_{CH4_LAND} and F_{CH4_WET} time series, we randomly sampled 100 times from the error distributions of directly measured (random observation error) and gap-filled half hours (gap-filling error), resulting in 10,000 ΣF_{CH4_LAND} and ΣF_{CH4_WET} estimates. We used the standard deviation of F_{CH4} for similar meteorological conditions within $\pm$7-day windows, as derived from the gap-filling algorithm, to obtain half-hourly random observation and gap-filling error estimates (*Lasslop et al.*, 2008; *Moffat et al.*, 2007). Random observation errors were then scaled with the magnitude of gap-filled F_{CH4} and RSSI to obtain continuous time series of half-hourly random observation errors. We derived continuous time series of half-hourly gap-filling errors by scaling gap-filling errors with the magnitude of gap-filled F_{CH4} (*Lasslop et al.*, 2008). Then, 95% confidence intervals were derived from the 10,000 ΣF_{CH4_LAND} and ΣF_{CH4_WET} estimates. By combining F_{CH4_LAND} and F_{CH4_WET} from 2014 (colder and drier than normal [1981 - 2010]) and 2015 (warmer and wetter), two years with differing meteorological conditions (*Environment Canada*, `http://climate.weather.gc.ca/climate_data/daily_data_e.html?StationID=52780`), we assume that growing season ΣF_{CH4_LAND} and ΣF_{CH4_WET} were approximately representative of their respective long-term growing season cumulative F_{CH4} sums.

4.3.3 Spatial and temporal controls and spectral decomposition of F_{CH4}

Methane production in anoxic soils increases with microbial activity and may be limited by, amongst others, temperature or substrate availability (*Dunfield et al.*, 1993). With the water table position close to the surface or with a minimized CH_4 oxidation potential due to plant-mediated CH_4 transport or ebullition, most of the produced CH_4 is emitted to the atmosphere (*Bellisario et al.*, 1999; *Kettunen et al.*, 1999; *Moore et al.*, 2011; *Sundh et al.*, 1994). In this case, temporal F_{CH4} variations are closely linked to CH_4 production rates, which are often controlled by soil temperature or vegetation productivity (e.g., *Christensen et al.*, 2003; *Shannon and White*, 1994). The strong seasonality in soil temperature and vegetation productivity results in a strong low-frequency

component of F_{CH4} (e.g., weeks to months; *Rinne et al.*, 2007). In contrast, the spectral signature of the spatial F_{CH4} footprint heterogeneity is expected to correspond to higher frequency components (e.g., hours), related to rapid changes in footprint composition with instantaneous effects on F_{CH4} measurements. This spatial footprint variability has often been classified as part of the random error in eddy covariance flux measurements (*Moncrieff et al.*, 1996). Recent developments in flux footprint models and remote sensing open new opportunities to analyze the direct control of such footprint heterogeneity on eddy covariance fluxes (e.g., *Chasmer et al.*, 2008; *Kljun et al.*, 2015).

To decompose F_{CH4_LAND} and F_{CH4_WET} into low- (F_{CH4_sf}, nmol m^{-2} s^{-1}) and high-frequency components (F_{CH4_hf}, nmol m^{-2} s^{-1}), we used a modification of Singular Spectrum Analysis (SSA; *Schoellhamer*, 2001). This time series analysis technique accounts for missing data in time series (*Schoellhamer*, 2001) and enhances the signal-to-noise ratio (*Mahecha et al.*, 2007). The time series is decomposed into linearly superimposed frequency-specific sub-signals that can then be partially reconstructed by specifying individual frequencies. We calculated F_{CH4_sf} by selecting frequencies longer than one week (seasonal) and F_{CH4_hf} by selecting frequencies between two hours to seven days (sub-weekly). Frequencies smaller than two hours were not analyzed to reduce noise introduced by F_{CH4_LAND} and F_{CH4_WET} measurements during periods with low RSSI signal strength. A detailed discussion of SSA for eddy covariance flux studies can be found in *Mahecha et al.* (2007).

The control of flux footprint composition (i.e., contributions from wetlands [FP_{WET}, %]) on F_{CH4_LAND} and F_{CH4_WET} and WTD on F_{CH4_LAND} and F_{CH4_WET} were analyzed independently. Linear regressions between FP_{WET} and F_{CH4_LAND} were applied to three-day moving windows. By constraining linear regressions to a short time period, the seasonal evolution of spatial F_{CH4} heterogeneities in landscape flux footprints can be tracked. To assess the most important seasonal F_{CH4_LAND} and F_{CH4_WET} (i.e., F_{CH4_sf}) controls, we conducted a multiple linear regression applying a stepwise forward selection procedure (*Legendre and Legendre*, 2012) for the variables T_{s_WET}, WTD, and the interaction term between T_{s_WET} and WTD. For the regression, we used 10,000 randomly selected subsets of 30 F_{CH4_sf} data points to minimize the effects of temporal autocorrelation.

Wetland flux footprints almost exclusively comprised wetland surfaces. In contrast, landscape flux footprints comprised varying contributions from wetland and forest surfaces, but forests never contributed more than 90% to the flux footprints. Thus, we fitted Q_{10}-models to F_{CH4_LAND} and F_{CH4_WET} for classes of increasing forest contribution to flux footprints to scale F_{CH4} to a hypothetical forest-only landscape (F_{CH4_FOR}; nmol m^{-2} s^{-1}) and to assess its response to T_{s_WET}:

$$F_{CH4\_i} = F_{CH4\_base\_i} Q_{10\_i}^{\frac{T_{s\_WET}-10}{10}} \tag{4.1}$$

where *i* stands for the *i*-th forest contribution class, F_{CH4_base} is the reference F_{CH4} at T_{s_WET} = 10 °C, and Q_{10} is an indicator of the temperature sensitivity of F_{CH4_i}. The Q_{10} models were fitted to F_{CH4} with < 10% forest footprint contributions (i.e., F_{CH4_WET}) and to four classes of increasing forest contribution to landscape flux footprints (i.e., F_{CH4_LAND}).

4.3.4 Net radiative greenhouse gas forcing

The net radiative greenhouse gas forcing (W m^{-2}) of persistent thaw-induced increases in CH_4 emissions and concurrent net CO_2 exchange was calculated using a dynamic model of atmospheric CH_4 and CO_2 pools (*Frolking et al.*, 2006; *Neubauer and*

Megonigal, 2015). The time-dependent evolution of the atmospheric CH_4 concentration perturbation (r_{CH4}; g CH_4 m^{-2}) of an annual CH_4 emission (r_{0_CH4}; g CH_4 m^{-2} yr^{-1}) was computed as a simple exponential decay:

$$r_{CH4}(t) = r_{0\_CH4} exp^{\frac{-t}{\tau_{CH4}}} \tag{4.2}$$

where the atmospheric lifetime of CH_4 (τ_{CH4}) is 12.4 years (*Myhre et al.*, 2013). The evolution of the atmospheric CO_2 concentration perturbation (r_{CO2}, g CO_2 m^{-2}) of annual CO_2 uptake (r_{0_CO2}; g CO_2 m^{-2} yr^{-1}) was modeled as the sum of exponentials for five atmospheric pools with lifetimes (τ_i) ranging from the 'slowest' pool with 10^8 years to the 'fastest' pool with 3.4 years accounting for the varying redistribution timescales of CO_2 within the ocean, the land biosphere, and the atmosphere. A fraction of r_{0_CO2} (α_i) is attributed to each atmospheric CO_2 pool (*Joos et al.*, 2013). Values for τ_i and α_i in:

$$r_{CO2}(t) = \sum_{i=0}^{4} \alpha_i r_{0\_CO2} exp^{\frac{-t}{\tau_i}} \tag{4.3}$$

are as in *Frolking et al.* (2006). Both models were run for 100-year time series of r_{0_CH4} and r_{0_CO2}. The radiative forcing (RF, W m^{-2}) of greenhouse gas i (CH_4 and CO_2) is then calculated as follows:

$$RF_i = f_i A_i r_i \tag{4.4}$$

where f_i for CH_4 (1.65, *Myhre et al.*, 2013) accounts for indirect CH_4 effects on ozone concentrations and stratospheric H_2O and is 1 for CO_2, A_i is the radiative efficiency ($1.27*10^{-13}$ W m^{-2} kg^{-1} for CH_4 and $1.7517*10^{-15}$ W m^{-2} kg^{-1} for CO_2), and r_i is the current time atmospheric concentration perturbation of the respective greenhouse gas due to all previous emissions/uptake since a reference year (see *Frolking et al.*, 2006).

To estimate the future landscape CH_4 emissions (r_{0_CH4} in Eq. 4.2), we derived and applied a mean annual wetland expansion rate of $0.26 \pm 0.05\%$ yr^{-1} ($\pm 95\%$ confidence interval; $n = 7$) from historical wetland extent changes between 1977 and 2010 for seven

areas of interest at Scotty Creek (*Baltzer et al.*, 2014), resulting in an increase in wetland extent from 39% in 1977 to 65% in 2077. We estimated the trajectory of annual growing season $\Sigma F_{CH4\_LAND\_i}$ (Eq. 4.2; where *i* stands for the year between 1977 and 2077) by combining the temporal trajectory of wetland fraction of the landscape (*wet_i*) with ΣF_{CH4_WET} and ΣF_{CH4_FOR}:

$$\Sigma F_{CH4\_LAND\_i} = wet_i \Sigma F_{CH4\_WET} + (1 - wet_i) \Sigma F_{CH4\_FOR} \tag{4.5}$$

The prescribed $\Sigma F_{CH4\_LAND\_i}$ time series was then used as r_{0_CH4} in the atmospheric concentration model (Eq. 4.2). Uncertainties in the prescribed $\Sigma F_{CH4\_LAND\_i}$ were estimated based on the 95% confidence interval of annual wetland expansion rates. Simulations were run for 100 years (1977-2077), where 1977 is the reference year, the first year with an estimate of the spatial wetland extent at Scotty Creek (*Baltzer et al.*, 2014).

Long-term annual net CO_2 uptake in high-latitude peatland landscapes could potentially offset the positive radiative forcing of increasing landscape CH_4 emissions (*Frolking et al.*, 2006). To quantify radiative forcing related to net CO_2 exchange, we used long-term apparent rates of carbon accumulation (LARCA, g C m^{-2} yr^{-1}) from 63 boreal peatlands in the circumpolar permafrost zone in North America with a basal peat age of more than 1,000 years, including (collapse-scar) bogs, (forested) peat plateaus, and fens (*Treat et al.*, 2016). Peatland LARCA itself is the result of long-term net CO_2 uptake, CH_4 emissions, and net aquatic C exports. We assume the latter to be negligible across the thawing boreal forest-wetland landscape (e.g., *Moore*, 2003; *Neubauer*, 2014; *Olefeldt et al.*, 2012). Carbon losses related to CH_4 emissions, approximated as the measured growing season ΣF_{CH4_LAND}, were added to LARCA to calculate the mean long-term net CO_2 uptake (r_{0_CO2} in the atmospheric concentration model; Eq. 4.3). Using the mean long-term annual net CO_2 uptake rate accounts for interannual variability in net CO_2 uptake and disturbance losses of CO_2 (e.g., wildfires) and is therefore a more appropriate measure than, for example, annual net primary production, which does not account for decomposition after litterfall (*Chapin et al.*, 2006). Annual net ecosystem CO_2 exchange (NEE; g CO_2 m^{-2} yr^{-1}) accounts for such decomposition, but year-round

NEE measurements are only available for a few boreal peatlands in the permafrost zone (e.g., *Dunn et al.*, 2007; *Euskirchen et al.*, 2014), do not account for CO_2 losses from fire disturbances (*Chapin et al.*, 2006), and uncertainties due to interannual NEE variability are usually large (*Roulet et al.*, 2007). To compare annual eddy covariance NEE to mean long-term net CO_2 uptake derived from LARCA, we also used annual landscape NEE at Scotty Creek for r_{0_CO2} (Eq. 4.3). Our NEE estimate for Scotty Creek was based on one year of eddy covariance net CO_2 flux measurements at the landscape tower.

4.4 Results

4.4.1 Spatial and temporal controls of F_{CH4}

To identify the most important drivers of F_{CH4_LAND} and F_{CH4_WET}, we analyzed the decomposed F_{CH4} signals at seasonal low-frequency (F_{CH4_sf}) and at sub-weekly high-frequency time scales (F_{CH4_hf}). At the wetland tower, F_{CH4_sf} contributed more to the total F_{CH4} variance (75%) than at the landscape tower (40%). In turn, F_{CH4_hf} contributed less to the total F_{CH4} variance at the wetland tower (12%) compared to the landscape tower (39%) (Fig. 4.1), highlighting the more pronounced heterogeneity of F_{CH4} in the landscape flux footprints.

Seasonal landscape and wetland F_{CH4_sf} were mainly controlled by ${T_{s\_WET}}^2$ (landscape r^2 = 0.82, $p < 0.001$ and wetland r^2 = 0.84, $p < 0.001$; Fig. III.1). In July and August, T_{s_WET} peaked at $\sim$16 °C and remained between 0 °C and 1 °C from December to April (Fig. II.2). With a mean annual T_{s_WET} of 5.2$\pm$5.6 °C ($\pm$one standard deviation, for 2015) the wetland soil was substantially warmer than T_{s_FOR} (1.1$\pm$2.8 °C). The average WTD during the study period was -11$\pm$6 cm. The WTD peaked at +10 cm (i.e., above the moss surface) shortly after snowmelt (late April/early May in 2014 and 2015) and reached its lowest position below the surface with -20 cm in October 2014 (Fig. II.2). The negative relationship between WTD and F_{CH4_sf} (i.e., larger F_{CH4_sf} with lower water table) explained 47% of the variance in F_{CH4_sf} at the wetland tower (p = 0.002), but was not significant at the landscape tower (p = 0.12; Fig. III.1). For a multiple linear regression with ${T_{s\_WET}}^2$, WTD, and their interaction term as explanatory variables of

F_{CH4_sf}, only $T_{s\_WET}{}^2$ was significant at $\alpha = 0.05$ for both the landscape and the wetland tower.

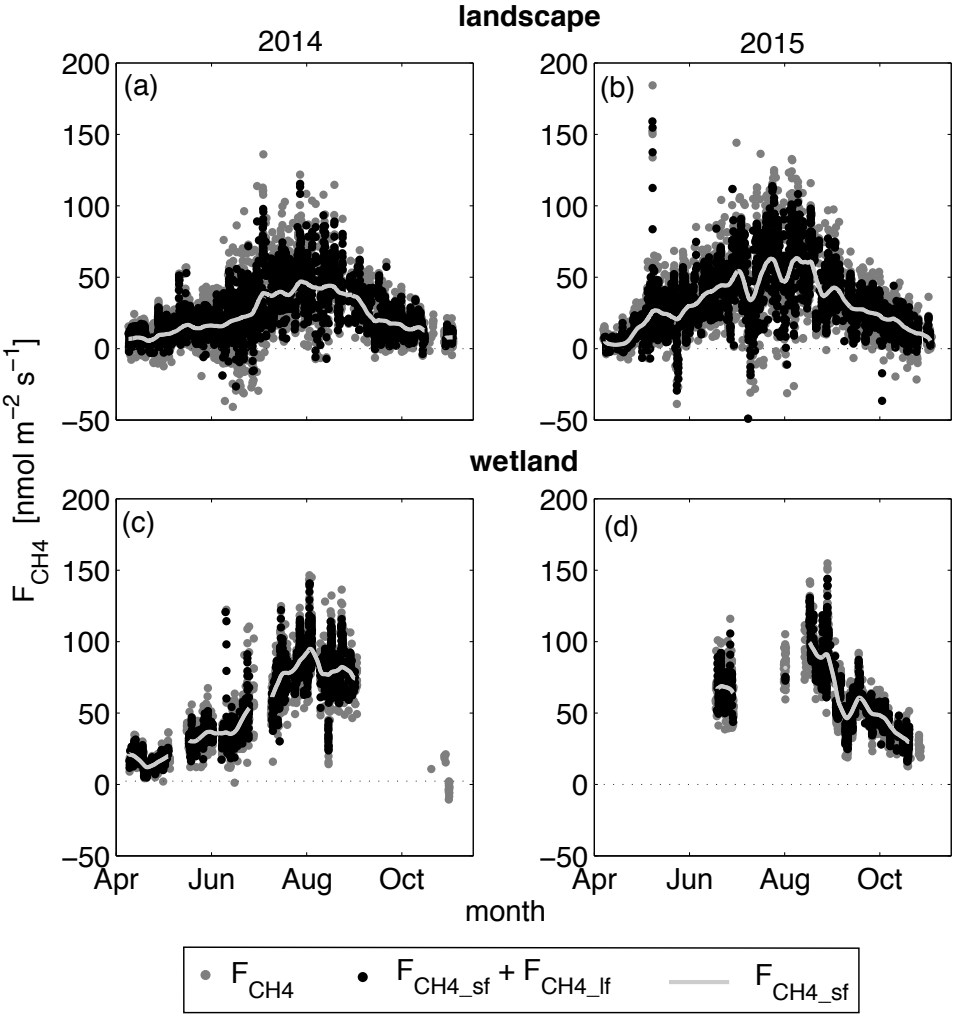

Figure 4.1 – Decomposition of net CH_4 flux measurements (F_{CH4}; nmol m^{-2} s^{-1}) into seasonal (F_{CH4_sf}; > seven days) and sub-weekly signals (F_{CH4_hf}; two hours - seven days) for the **(a & b)** landscape and the **(c & d)** wetland tower for the 2014 and 2015 growing seasons.

In contrast to the wetland tower where F_{CH4_sf} dominated F_{CH4_WET}, F_{CH4_sf} and F_{CH4_hf} contributed equally to F_{CH4_LAND}. Sub-weekly F_{CH4_LAND} was mainly controlled by footprint composition when differences between T_{s_WET} and T_{s_FOR} were largest (Fig. 4.2). With decreasing T_{s_WET}-T_{s_FOR} differences, the sensitivity of F_{CH4_LAND}

to FP_{WET} diminished. Thus, F_{CH4} contrasts between wetlands and forests were small in the winter with cold T_{s_WET} and T_{s_FOR} ($\sim$0 °C), and large in the summer when T_{s_WET} were up to 10 °C warmer than T_{s_FOR}.

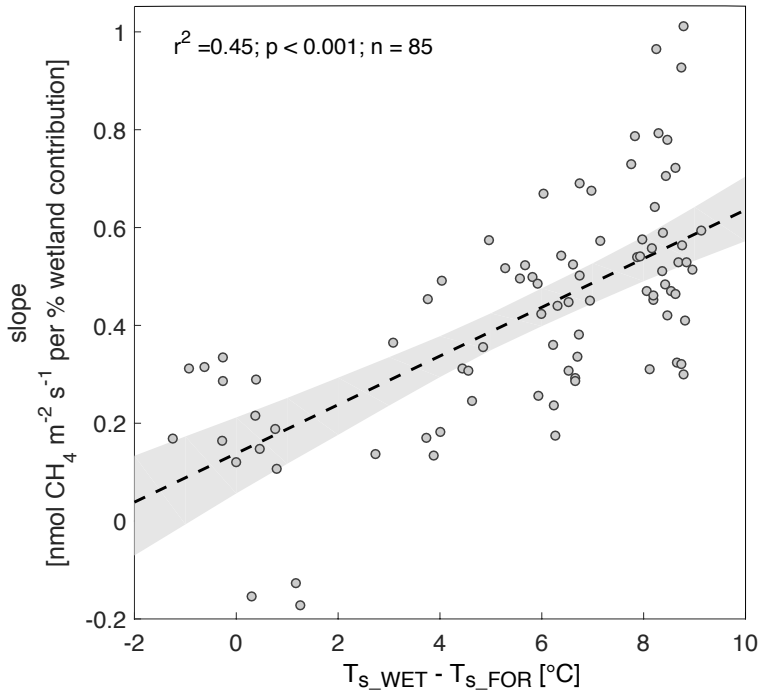

Figure 4.2 – Linear regression slopes between wetland contributions to landscape flux footprints and landscape methane fluxes (F_{CH4_LAND}), and mean differences in soil temperatures at a depth of 32 cm in the wetland (T_{s_WET}) and the forest (T_{s_FOR}) for three-day windows. The dashed line shows the best linear fit and the shaded area the 95% confidence interval of the regression.

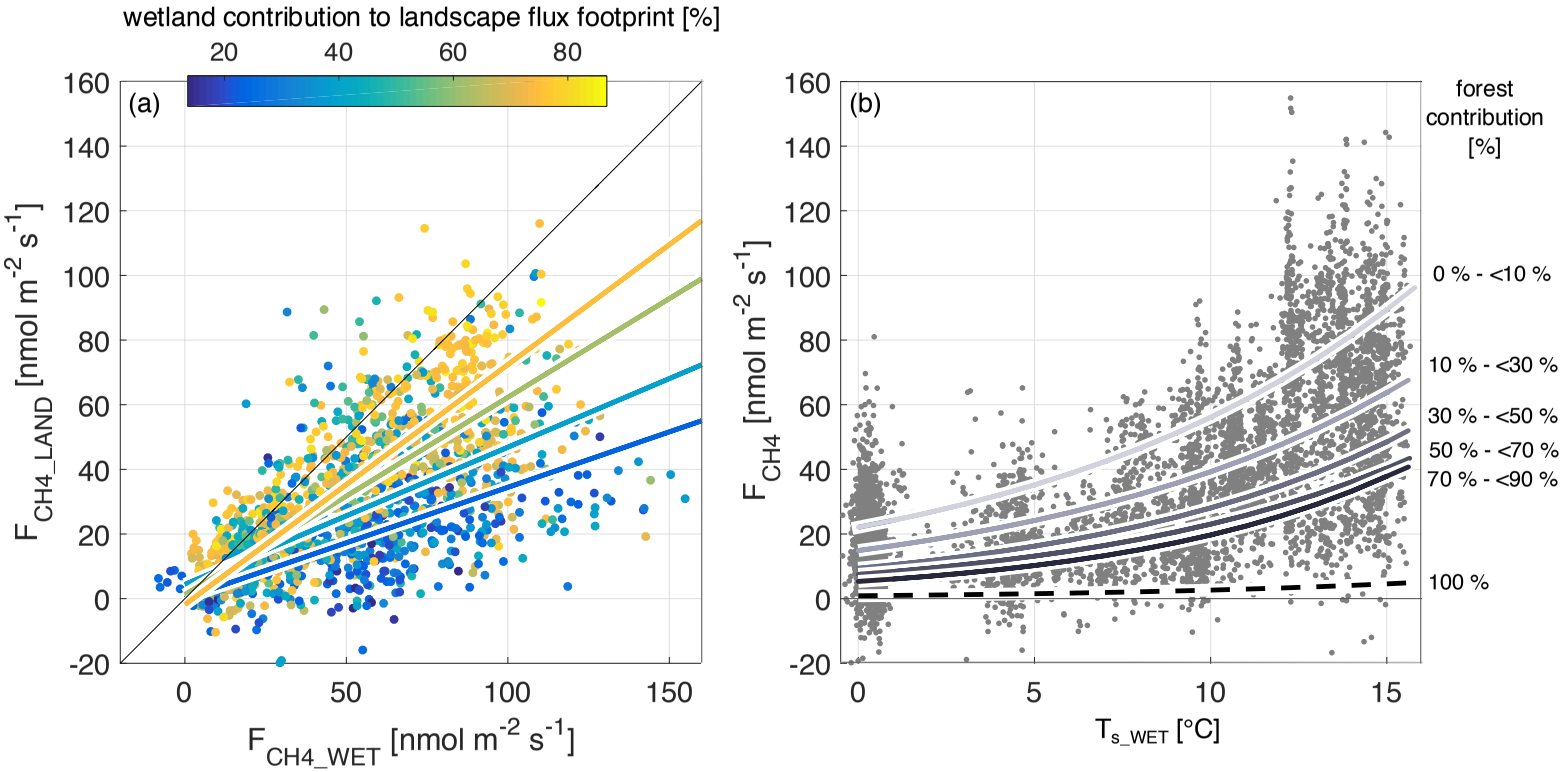

Figure 4.3 – **(a)** Wetland (F_{CH4_WET}) and landscape methane fluxes (F_{CH4_LAND}) and linear regressions (see Tab. 4.I) for increasing classes of wetland contribution to landscape flux footprints. Dots are colored according to wetland contribution to landscape flux footprints and best-fit regression lines are colored according to the median of the respective wetland contribution class. **(b)** Best-fit Q_{10}-models (see Tab. 4.II) for classes of varying forest contributions to (wetland and landscape) flux footprints (solid lines) and measured methane fluxes (F_{CH4}, grey dots) against soil temperature at the wetland (T_{s_WET}). The dashed line indicates the estimated Q_{10}-model for forest-only contributions (i.e., F_{CH4_FOR}).

4.4.2 The impact of changing wetland extents on landscape F_{CH4}

Eddy covariance measurements at the landscape tower and flux footprint modeling suggest that wetlands are the main CH_4 sources within the landscape (Fig. 4.2). Direct comparisons of F_{CH4_WET} to F_{CH4_LAND} support this result, as F_{CH4_LAND} were consistently smaller than F_{CH4_WET} (Fig. 4.3a). The two fluxes became more similar with increasing wetland contribution to landscape flux footprints (Tab. 4.I). When wetland contributions to F_{CH4_LAND} were large (70% - < 90%), the F_{CH4_WET}-F_{CH4_LAND} regression slope was closest to unity with 0.74, and decreased to 0.34 with decreasing wetland contributions (10% - < 30%), thus confirming the dominant contribution of wetlands to F_{CH4_LAND}.

Table 4.I – Linear regression statistics and 95% confidence intervals (CI) of wetland against landscape methane fluxes for different classes of wetland footprint (FP) contributions to landscape flux footprints.

wetland FP contribution	slope	CI	intercept	CI	r^2	n
10% - < 30%	0.34	0.27-0.43	0.1	-4.5-4.3	0.23	257
30% - < 50%	0.43	0.36-0.50	4.4	1.1-7.4	0.28	505
50% - < 70%	0.61	0.54-0.68	1.2	-1.4-3.6	0.53	330
70% - < 90%	0.74	0.69-0.79	-1.8	-4.3-0.5	0.62	580

The smallest F_{CH4_LAND} and the weakest response to T_{s_WET} were observed for the largest forest contributions (Fig. 4.3b). From the smallest to the largest forest contributions, F_{CH4_base} (see Eq. 4.2) decreased consistently from 56 nmol m^{-2} s^{-1} to 20 nmol m^{-2} s^{-1}, while Q_{10} values changed only slightly (Tab. 4.II). To estimate the forest-only F_{CH4}, F_{CH4_FOR}, we derived a Q_{10}-model using a mean Q_{10} value (Tab. 4.II) and a scaled F_{CH4_base} estimate for forest-only contributions. To scale F_{CH4_base}, we conducted a regression of the median forest contributions of the five forest contribution classes (see Tab. 4.II) against F_{CH4_base} (r^2 = 0.91; p = 0.01; n = 5). The estimated F_{CH4_base} was not significantly different from zero with 2.6 nmol m^{-2} s^{-1} (95% CI: -23 - 14 nmol m^{-2} s^{-1}) and modelled F_{CH4_FOR} remained <10 nmol m^{-2} s^{-1}, even at warm T_{s_WET} (Fig. 4.3b). Thus, F_{CH4_FOR} was insensitive to T_{s_WET} and negligible compared to F_{CH4_WET}.

Table 4.II – Best-fit Q_{10}-model parameters and corresponding 95% confidence intervals (CI) and regression statistics of measured against modeled methane fluxes. Model fits were conducted for classes of varying forest contribution to flux footprints (FP).

Forest FP contribution	F_{CH4_base}	CI	Q_{10}	CI	r^2	n
0% - < 10%	56.1	55.4-56.9	2.5	2.5-2.6	0.69	2152
10% - < 30%	39.3	38.6-40.0	2.6	2.5-2.8	0.59	1746
30% - < 50%	28.1	27.9-29.1	3.0	2.8-3.3	0.48	1048
50% - < 70%	23.0	22.3-23.8	3.1	2.8-3.4	0.36	1788
70% - < 90%	19.7	17.9-21.2	3.7	2.8-5.1	0.35	324

Between April and October, monthly ΣF_{CH4_LAND} and ΣF_{CH4_WET} showed a distinct seasonal cycle (Fig. 4.3a & b). Monthly ΣF_{CH4_LAND} increased from a minimum monthly ΣF_{CH4_LAND} of 0.2 g CH_4 m^{-2} in April 2015 & 2016 to a peak monthly ΣF_{CH4_LAND} of 2.2 g CH_4 m^{-2} in July & August 2015 before decreasing again to a minimum monthly ΣF_{CH4_LAND} of 0.5 g CH_4 m^{-2} in October 2014. Similarly, monthly ΣF_{CH4_WET} increased from a minimum of 0.5 g CH_4 m^{-2} in April 2016 to a peak monthly ΣF_{CH4_WET} of 3.9 g CH_4 m^{-2} in August 2015 before decreasing again to a minimum monthly ΣF_{CH4_WET} of 1.4 g CH_4 m^{-2} in October 2015. The largest relative interannual differences in monthly ΣF_{CH4_LAND} occurred in May & June 2014 with ΣF_{CH4_LAND} being about 50% smaller than ΣF_{CH4_LAND} during the same months in 2015. During these months, T_{s_WET} was about 5 °C colder in 2014, while WTD was similar with differences of $\pm$2 cm (Fig. 4.4c).

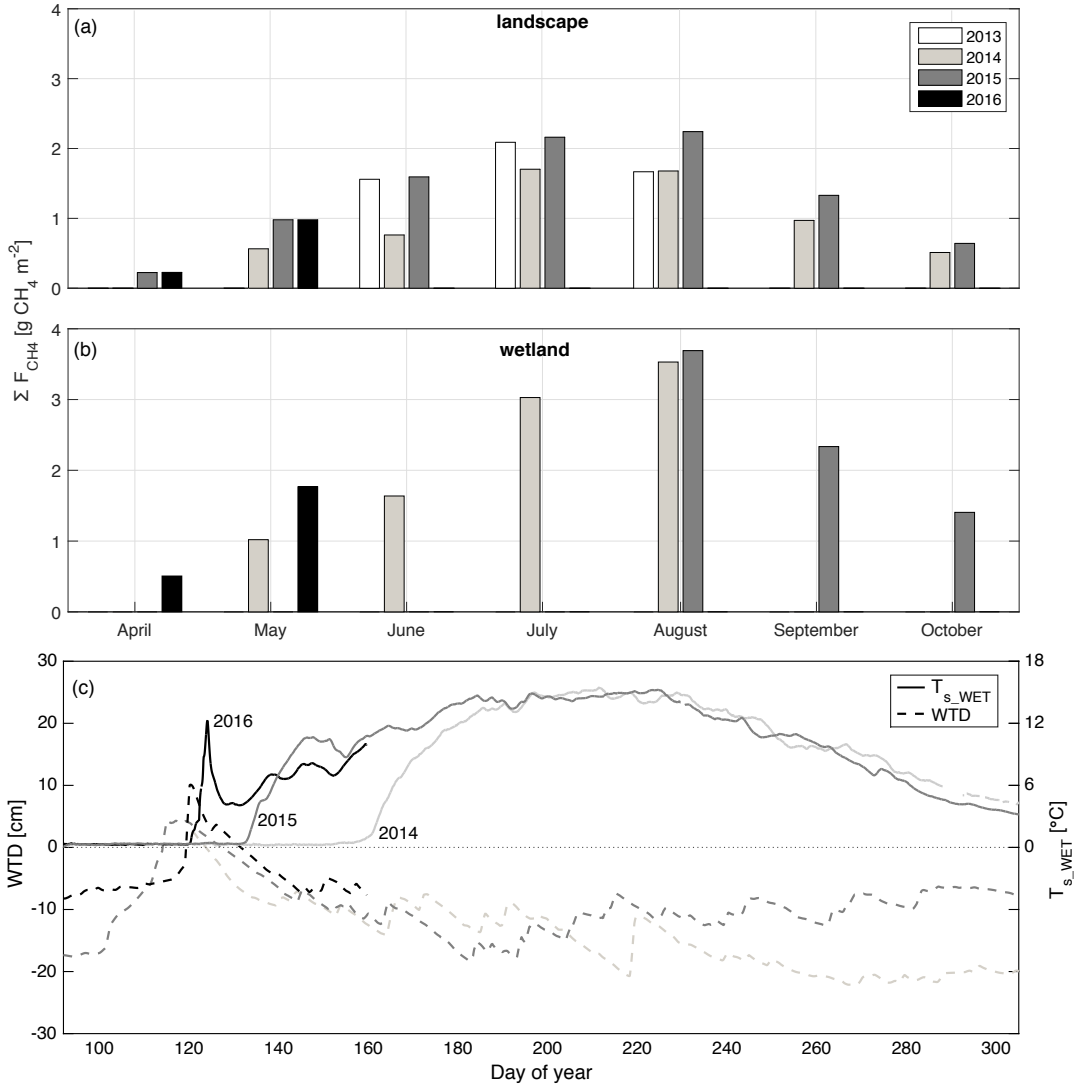

Figure 4.4 – Monthly cumulative growing season methane fluxes (ΣF_{CH4_WET}) at **(a)** the landscape tower (2013-2016) and **(b)** the wetland tower (2014-2016) and **(c)** growing season dynamics of wetland water table depth (WTD) and soil temperature at 32 cm (T_{s_WET}) for three years. WTD and T_{s_WET} measurements started in 2014.

Total growing season ΣF_{CH4_WET} was about twice (13.0 g CH_4 m^{-2}; 95% CI: 12.8 - 13.1 g CH_4 m^{-2}) the ΣF_{CH4_LAND} (6.7 g CH_4 m^{-2}; 95% CI: 6.6 - 6.8 g CH_4 m^{-2}; Fig. 4.5). The mean growing season forest contribution to landscape flux footprints was 46% with wetlands contributing 52% and the lake only 2%. Wetland flux footprints always consisted of > 95% wetlands. To scale future growing season ΣF_{CH4_LAND} with

changes in wetland-to-forest ratio (Eq. 4.5), we assumed that growing season ΣF_{CH4_FOR} was negligible and independent of T_{s_WET} (Fig. 4.3b). Consequently, ΣF_{CH4_WET} was the dominant contribution to ΣF_{CH4_LAND} and a thaw-induced wetland expansion rate of 0.26 ± 0.05 yr^{-1} increases growing season ΣF_{CH4_LAND} by 0.034 ± 0.007 g CH_4 m^{-2} yr^{-1} ($\sim$0.5% of current ΣF_{CH4_LAND}).

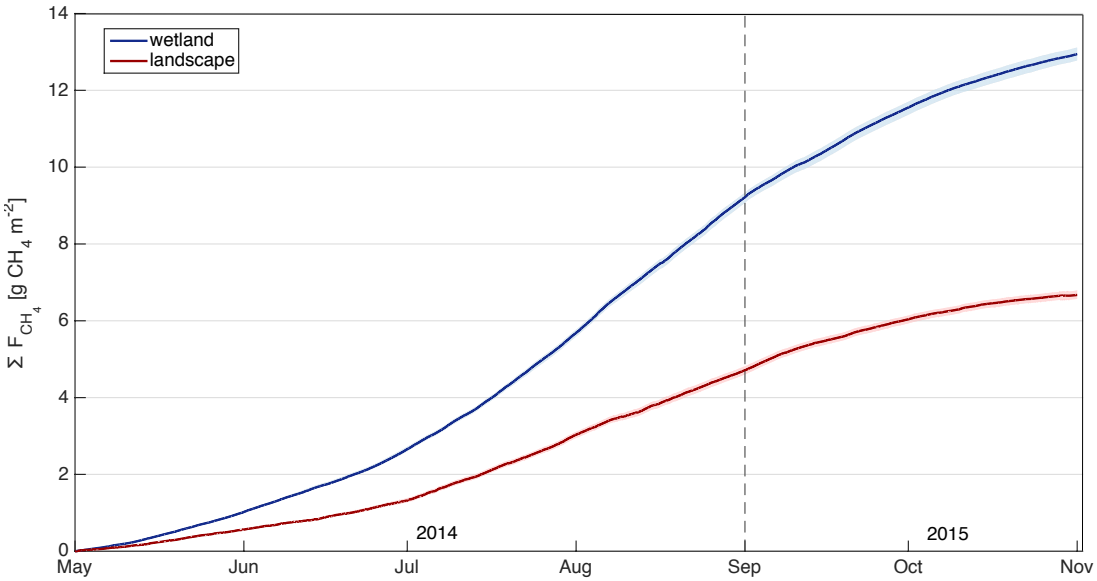

Figure 4.5 – Cumulative growing season CH_4 fluxes (ΣF_{CH4}) at the landscape and the wetland tower. Growing season fluxes in 2014 and 2015 were combined to derive a full growing season budget. Shaded areas indicate ΣF_{CH4} uncertainties due to the selection of the friction velocity threshold and due to random observation and gap-filling errors.

4.4.3 Net radiative greenhouse gas forcing of a thawing boreal landscape

In the absence of long-term net CO_2 uptake, the increasing ΣF_{CH4_LAND} causes a steady rise in radiative forcing totaling 12.3 ± 2.4 fW m^{-2} (fW = 10^{-15} W) after 100 years. An annual net CO_2 uptake of $\sim$200 g CO_2 m^{-2} yr^{-1} would fully compensate for this positive radiative forcing (Fig. 4.6). However, long-term net CO_2 uptake rates between 49 g CO_2 m^{-2} yr^{-1} and 157 g CO_2 m^{-2} yr^{-1} are characteristic for boreal peatlands similar to Scotty Creek (i.e., 90% confidence interval of long-term net CO_2 uptake), with bogs and forested peat plateaus taking up less CO_2 than fens. The long-term annual net CO_2

uptake, required to compensate for the positive radiative CH_4 forcing is thus outside the range of both the observed annual NEE at Scotty Creek (-71 g CO_2 m^{-2} yr^{-1}, indicating a net CO_2 uptake) and the long-term net CO_2 uptake from similar boreal peatlands.

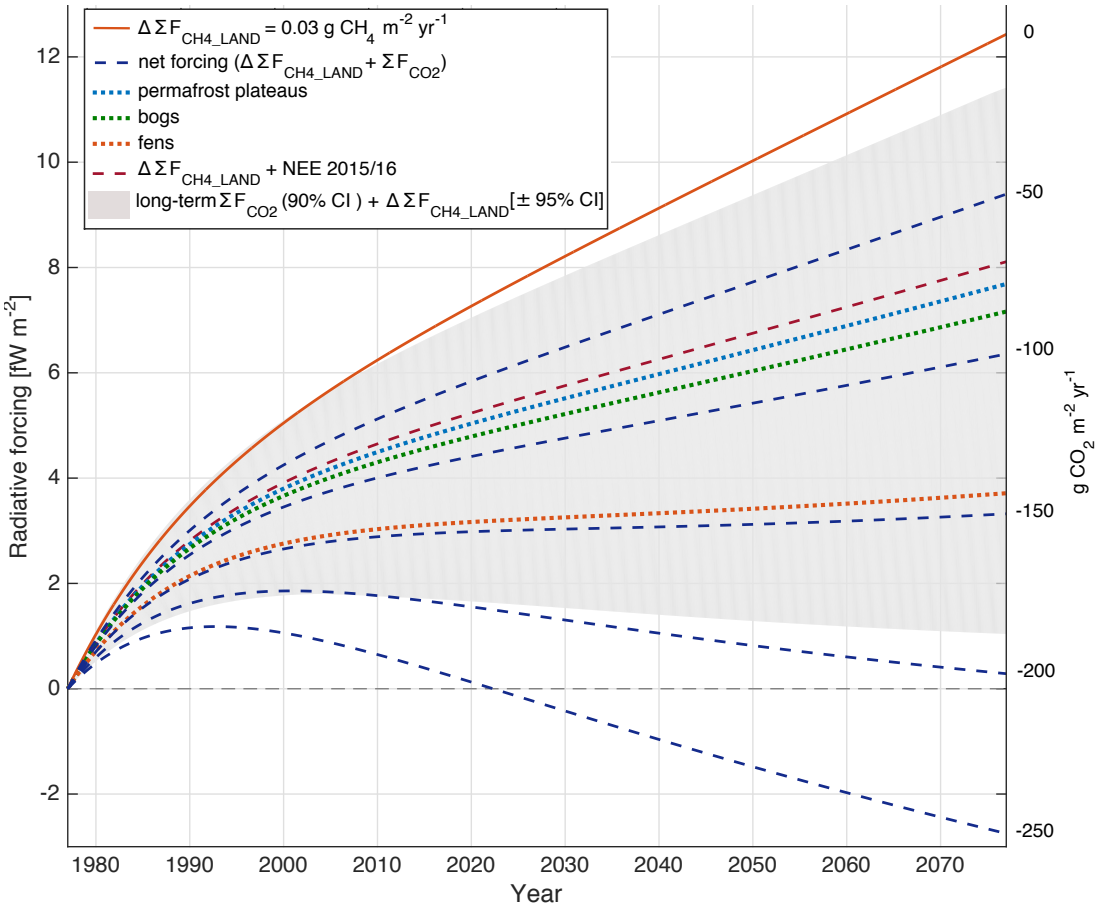

Figure 4.6 – Net radiative greenhouse gas forcing of the thaw-induced (i.e., wetland expansion) increase in growing season landscape CH_4 fluxes (ΣF_{CH4_LAND}) referenced to the year 1977. The solid red line represents the scenario with no net CO_2 uptake. Dashed lines show net radiative forcing for varying levels of annual net CO_2 uptake (ΣF_{CO2}) and for annual net ecosystem CO_2 exchange (NEE) measured at the landscape tower (unpublished data): negative signs indicate a net CO_2 uptake. The shaded area defines the range of net radiative forcing for long-term ΣF_{CO2} of similar peatlands including the uncertainty in the wetland expansion rate estimate. Long-term ΣF_{CO2} is based on the 90% confidence interval (CI) of long-term apparent carbon accumulation rates (for 'forested peat plateaus', 'bogs', 'fens'; *Treat et al.* (2016)). Dotted lines indicate the net radiative forcing for median net CO_2 uptake rates for different peatland types. 1 fW = 10^{-15} Watts.

4.5 Discussion

4.5.1 Soil temperature and water table depth controls of temporal F_{CH4} variation

At the seasonal time scale, T_{s_WET} mainly controls F_{CH4_WET} and thus F_{CH4_LAND} (Fig. 4.1 & Fig. 4.2). In contrast, WTD exerts only a minor control over the seasonality of F_{CH4_WET} and F_{CH4_LAND}. At Scotty Creek, the wetland and forest water table positions are closest to the moss surface shortly after snowmelt, but decline as the growing season progresses with increasing evapotranspiration and lateral drainage (see Chapter 3 & *Connon et al.*, 2015, Fig. 4.4c). This water table drawdown occurs concurrently with T_{s_WET} getting warmer, inducing increasing F_{CH4_WET}, and consequently increasing F_{CH4_LAND}. Similarly, *Bellisario et al.* (1999) observed increasing CH_4 emissions with decreasing WTD for a boreal peatland with WTD > -15 cm. In a boreal minerotrophic fen with a similar WTD range as reported here, water table position only weakly affected F_{CH4} after accounting for soil temperature effects (*Rinne et al.*, 2007). At Scotty Creek, wetland WTD was > -15 cm during 75% of the growing season (May - October). The negative relationship between WTD and F_{CH4} may be reversed in drier years when the water table position falls below a certain threshold (e.g., below the zone of labile root exudate inputs; *Treat et al.* (2007)). *Christensen et al.* (2003) referred to the WTD control on F_{CH4} as an 'on-off switch'; if the water table is within $\sim$10 cm of the surface its effect on F_{CH4} is small compared to other environmental variables. Additionally, in some parts of the wetland, absolute water table fluctuations may be partly compensated by the vertical displacement of the peat surface itself (e.g., *Bubier et al.*, 1995; *Sonnentag et al.*, 2010). Methane emissions from wetlands with ground surface fluctuations are often less dependent on fluctuations in the absolute water table position (*Hartley et al.*, 2015).

Similar to the seasonal control of T_{s_WET} on F_{CH4}, T_{s_WET} may also control interannual ΣF_{CH4} variability. At Scotty Creek, smaller monthly ΣF_{CH4_LAND} in the early summer of 2014 appeared to be caused by $\sim$5 °C colder wetland soils compared to 2015 (Fig. 4.4). This reduction in ΣF_{CH4_LAND} highlights the importance of T_{s_WET} for both seasonal and interannual F_{CH4} variability (*Christensen et al.*, 2003; *Rask et al.*, 2002).

Interannual ΣF_{CH4} variability may additionally be controlled by the average seasonal water table (*Bubier et al.*, 2005; *Moore et al.*, 2011). At Scotty Creek, WTD and T_s differences between forested peat plateaus and wetlands partly control the spatial variability of F_{CH4}. In the future, water table dynamics at Scotty Creek could be altered by increasing growing season evapotranspiration (see Chapter 3), and/or changing snowmelt inputs (*Houghton et al.*, in preparation) and drainage patterns (*Connon et al.*, 2014). Interannual and long-term water table changes may then alter F_{CH4_LAND}; better projections of hydrological conditions in the future would therefore strengthen our ability to predict future F_{CH4_LAND} in the lowland boreal zone of North America (e.g., *Lawrence et al.*, 2015).

4.5.2 Wetland extent as control on spatial F_{CH4} variation

At Scotty Creek, F_{CH4_LAND} of the thawing boreal forest-wetland landscape increases with wetland extent (Fig. 4.3). Forests with permafrost are characterized by relatively dry, cold soils with a thick unsaturated zone. In contrast, the wetlands are permafrost-free, warmer, and have water tables that remain close to the moss surface due to differences in local topography between the forest and wetland surfaces (Fig. II.2). Methane production is enhanced and oxidation is reduced in the warmer, saturated wetland soils (e.g., *Sundh et al.*, 1994). In the permafrost-affected forest soils, aerobic soil conditions and the cooler T_{s_FOR} may result in smaller methanogen populations, unresponsive to soil temperature variations, thus suppressing CH_4 production (*Yavitt et al.*, 2006). Consequently, F_{CH4_LAND} increases with increasing wetland-to-forest ratio due to the characteristic differences in soil thermal and moisture conditions related to the absence of permafrost in wetlands and the presence of permafrost in the forests (*Baltzer et al.*, 2014).

Previous chamber flux measurements at similar boreal peatlands corroborate the larger CH_4 emissions of permafrost-free wetlands compared to forested permafrost peat plateaus (*Bubier et al.*, 1995; *Liblik et al.*, 1997; *Turetsky et al.*, 2002). Forested permafrost peat plateaus have been identified as small net CH_4 sinks (> -0.1 g CH_4 m^{-2} yr^{-1}; *Bubier et al.*, 2005; *Flessa et al.*, 2008; *Liblik et al.*, 1997; *Turetsky et al.*, 2002) or

small net CH_4 sources (< +20 mg CH_4 m^{-2} day^{-1} *Bubier et al.*, 1995) with net CH_4 sink-source strengths only weakly depending on soil temperature (e.g., *Bubier et al.*, 2005). In accordance with our findings, *Savage et al.* (1997) report a chamber-based growing season ΣF_{CH4} estimate of 0.03±0.05 g CH_4 m^{-2} (May to September) for a forested permafrost peat plateau in northern Manitoba, Canada.

4.5.3 Integrated growing season landscape and wetland ΣF_{CH4}

The growing season ΣF_{CH4_WET} of 13.0 g CH_4 m^{-2} (Fig. 4.5) compares well to the annual ΣF_{CH4} of 12.6 g CH_4 m^{-2} from a boreal minerotrophic fen in Finland (*Rinne et al.*, 2007), to the annual ΣF_{CH4} of 15.3 g CH_4 m^{-2} from a boreal poor fen in Sweden (*Nilsson et al.*, 2008), and to the growing season ΣF_{CH4} of 11 g CH_4 m^{-2} of a thawing sub-Arctic Swedish peatland complex (*Johansson et al.*, 2006), but is smaller than the growing season ΣF_{CH4} of 24.4 g CH_4 m^{-2} for a patterned boreal fen in Saskatchewan, Canada (*Suyker et al.*, 1996). In contrast, growing season ΣF_{CH4_WET} at Scotty Creek exceed the growing season ΣF_{CH4} of collapse-scar bogs in Alaska (see studies by *Euskirchen et al.*, 2014; *Myers-Smith et al.*, 2007; *Wickland et al.*, 2006, Tab. 4.III). The July and August ΣF_{CH4} of 6.2 g CH_4 m^{-2} reported by *Liblik et al.* (1997) for a collapse-scar bog in the southern Taiga Plains compares well to the 6.6 g CH_4 m^{-2} for July and August 2014 at the wetland at Scotty Creek. Similarly, the growing season ΣF_{CH4} of 11.4 g CH_4 m^{-2} (15 May - 15 September) reported by *Bubier et al.* (1995) for a collapse-scar bog in northern Manitoba, Canada, is of similar magnitude as the May to September ΣF_{CH4_WET} of 11.6 g CH_4 m^{-2} found in this study. Growing season ΣF_{CH4} for forested peatlands range between -0.1 g CH_4 m^{-2} and 1.1 g CH_4 m^{-2} (Tab. 4.III), suggesting that, generally, net CH_4 fluxes from these peatlands are negligible compared to treeless wetlands.

Table 4.III – Cumulative methane fluxes (ΣF_{CH4}) derived from growing season F_{CH4} studies for different types of boreal peatlands with or without permafrost (PF). Studies refer to varying lengths of measurement periods and, for comparison, ΣF_{CH4} are normalized for periods of 120 days (i.e., mean daily F_{CH4} x 120 days). Studies are either based on eddy covariance (EC) or chamber (CH) flux measurements.

Ecosystem type	PF	ΣF_{CH4} [study period] g CH_4 m^{-2}	Study period	ΣF_{CH4} [120 days] g CH_4 m^{-2}	Method	Reference
collapse-scar bog	no	5.0	21 Apr - 21 Sep	3.9	EC	*Euskirchen et al.* (2014)
collapse-scar bog	no	6.2	01 Jul - 31 Aug	12.5	CH	*Liblik et al.* (1997)
collapse-scar bog	no	2.0	15 Jun - 19 Sep	2.4	CH	*Myers-Smith et al.* (2007)
collapse-scar bog	no	2.0	16 May - 20 Sep	1.6	CH	*Wickland et al.* (2006)
collapse-scar bog	no	11.8	15 May - 15 Sep	10.4	CH	*Bubier et al.* (1995)
collapse-scar bog	no	13.0	01 Apr - 31 Oct	7.3	EC	this study
forested peat plateau	yes	0.0	01 Jul - 31 Aug	-0.1	CH	*Liblik et al.* (1997)
forested peat plateau	yes	1.1	16 May - 20 Sep	0.8	CH	*Wickland et al.* (2006)
forested peat plateau	yes	0.0	15 May - 15 Sep	0.0	CH	*Savage et al.* (1997)
black spruce forest	yes	0.4	14 May - 07 Oct	0.3	EC	*Iwata et al.* (2015)
treed bog	yes	0.4	10 Jun - 15 Oct	0.4	CH	*Moore et al.* (1994)
treeless bog plateau	yes	-0.1	01 Aug - 31 Nov	-0.1	CH	*Flessa et al.* (2008)
palsa fen	yes	6.9	30 May - 16 Nov	4.9	EC	*Hanis et al.* (2013)
minerotrophic fen	no	24.4	19 May - 04 Oct	21.0	EC	*Suyker et al.* (1996)
minerotrophic fen	no	11.4	29 Apr - 30 Nov	6.3	EC	*Rinne et al.* (2007)
collapse-scar fen	no	8.7	15 May - 15 Sep	8.4	CH	*Bubier et al.* (1995)
palsa mire	yes/no	23.0	18 Apr - 22 Oct	4.8	EC	*Jackowicz-Korczyński et al.* (2010)
boreal forest-wetland	yes/no	6.7	01 Apr - 31 Oct	3.8	EC	this study

In this study, ΣF_{CH4_WET} and ΣF_{CH4_LAND} do not include winter ΣF_{CH4}. During winter, surface peat in the wetlands overlays unfrozen peat deposits while forest peat soils are frozen through the entire profile (Fig. II.2). However, small but continuously positive F_{CH4} during long boreal winters have been shown to substantially (> 10%) contribute to annual ΣF_{CH4} of boreal wetlands and other high-latitude ecosystems (e.g., *Christensen et al.*, 2012; *Jackowicz-Korczyński et al.*, 2010; *Rinne et al.*, 2007; *Zona et al.*, 2016). For our study site, we expect forests with negligible growing season F_{CH4_FOR} also to be negligible winter CH_4 sinks-sources. Using average F_{CH4_WET} and F_{CH4_LAND} in November, March, and April (wetland [n = 233] and landscape tower [n = 1,375]), winter ΣF_{CH4_WET} and ΣF_{CH4_LAND} (snow-cover period: November - April) are estimated to account for 3.3 g CH_4 m^{-2} (25% of snow-free ΣF_{CH4_WET}) and 1.5 g CH_4 m^{-2} (23% of snow-free ΣF_{CH4_LAND}), respectively. These winter estimates are derived with open-path CH_4 gas analyzers and need to be cautiously interpreted because large density effects (WPL term) and small 'true' F_{CH4} may lead to large relative F_{CH4} uncertainties (*Goulden et al.*, 2006). A small bias accumulated over several months could lead to an under- or overestimation of winter ΣF_{CH4}. Additionally, ΣF_{CH4} derived from eddy covariance measurements may be underestimated by up to 20 %, as indicated by the widespread observation of surface energy balance non-closure at flux tower sites (*Stoy et al.*, 2013). We therefore assume that growing season ΣF_{CH4_WET} and ΣF_{CH4_LAND} for Scotty Creek represent conservative estimates of annual ΣF_{CH4_WET} and ΣF_{CH4_LAND}, mainly due to the significant but poorly constrained contribution of non-growing season fluxes.

4.5.4 Thaw-induced change in landscape F_{CH4}

Several studies have reported on seasonal CH_4 emissions from boreal peatlands (e.g., *Moore et al.*, 1994; *Rinne et al.*, 2007; *Suyker et al.*, 1996, Tab. 4.III), some provided upscaled CH_4 budgets for boreal landscapes including peatlands (e.g., Liblik et al., 1997; Bubier et al., 2005; Flessa et al., 2008), but few analyzed thaw-induced changes in landscape CH_4 emissions (e.g., *Johansson et al.* (2006) for a sub-Arctic treeless peatland complex). How changing landscape structure and composition in the North American

permafrost zone perturbs boreal forest-wetland landscape ΣF_{CH4} has not been addressed yet. Here, we have quantified thaw impacts on F_{CH4_LAND} using a nested eddy covariance tower setup.

The thaw-induced conversion of non-CH_4 emitting forests to CH_4 -emitting wetlands strengthens the growing season landscape net CH_4 emissions (ΣF_{CH4_LAND}) by 0.034 ± 0.007 g CH_4 m^{-2} yr^{-1} at Scotty Creek (Fig. 4.6). As an integrated measure of ΣF_{CH4_LAND}, eddy covariance measurements, as used in this study, avoid uncertainties characteristic for the up-scaling of small-scale, chamber-based F_{CH4} measurements related to discontinuous temporal sampling and spatial under-sampling of CH_4 emission 'hot spots' (e.g., *Bubier et al.*, 2005; *Knohl et al.*, 2008). The increasing CH_4 emissions in boreal forest-wetland landscapes can be supported by the large organic C amounts stored in forested peat plateaus (105 ± 40 kg C m^{-2} for the 42 forested peat plateaus in Fig. 4.6; *Treat et al.* (2016)). Our conservative estimate of ΣF_{CH4_LAND} changes could be exceeded in the future with increasing annual air temperatures potentially extending the growing season length and thus the period with environmental conditions favorable for CH_4 production (e.g., warm T_{s_WET}; *Moore et al.*, 1998). Additionally, change rates of ΣF_{CH4_LAND} may be larger as estimated in this study if wetland expansion accelerates along with increasingly warmer air temperatures and increased landscape fragmentation (*Baltzer et al.*, 2014; *Lara et al.*, 2016).

In contrast, some models project a decrease in ΣF_{CH4} in the permafrost zone in response to climate warming and thawing permafrost (e.g., *Lawrence et al.*, 2015). For example, the Community Land Model (CLM) projects a decrease in high-latitude ΣF_{CH4} due to its predicted improved drainage conditions following permafrost thaw, and drier soils limiting CH_4 production (e.g., *Koven et al.*, 2011; *Lawrence et al.*, 2015). However, the current CLM, similar to other land surface schemes, does not account for thaw-induced land surface subsidence and thus may not adequately capture future wetland extents in lowland boreal forest-wetland landscapes (*Gao et al.*, 2013; *Lee et al.*, 2014).

4.5.5 Net radiative greenhouse gas forcing due to increasing landscape ΣF_{CH4}

Wetlands act as long-term net CO_2 sinks and CH_4 sources (*Frolking et al.*, 2011). During the first decades to centuries, emerging wetlands usually exert a positive net radiative greenhouse gas forcing (warming effect) due to the CH_4 warming effect exceeding the cooling effect of net CO_2 uptake. Over longer time-scales, the net radiative greenhouse gas forcing eventually becomes negative (cooling effect) because the CO_2 cooling effect exceeds the CH_4 warming effect, even with constant CO_2 sink and CH_4 source strengths (*Frolking et al.*, 2006). Calculating the global warming potential (GWP) using a fixed timeframe neglects this temporal evolution of net radiative greenhouse gas forcing from peatlands and, by definition, does not account for temporally varying net CO_2 sink- and CH_4 source-strengths (*Neubauer and Megonigal*, 2015). Here, the warming effects of a steadily increasing landscape CH_4 source likely exceed the cooling effects of a continuous peatland net CO_2 sink through the 21st century in the dynamic net radiative greenhouse gas forcing model (Fig. 4.6). The net CO_2 uptake is derived using two approaches: eddy covariance net CO_2 flux measurements and long-term C accumulation rates of similar peatland types in the permafrost zone (*Treat et al.*, 2016). In some peatlands affected by permafrost thaw, previously frozen, relatively labile organic C in forested peat plateaus may decompose rapidly upon thaw and may weaken the contemporary peatland net CO_2 sink in the future (*O'Donnell et al.*, 2012), further increasing the positive net radiative greenhouse gas forcing. However, the landscape NEE measurements at Scotty Creek still indicate a landscape net CO_2 sink, despite rapidly thawing permafrost (Fig. 4.6).

Landscape net CO_2 uptake may vary depending on the dominant peatland types in the region. At Scotty Creek, the annual eddy covariance landscape NEE of -71 g CO_2 m^{-2} compares well to the median long-term forested peat plateau net CO_2 uptake rate of 78 g CO_2 m^{-2} and to the median bog uptake rate of 88 g CO_2 m^{-2} (*Treat et al.*, 2016). In contrast, the annual CO_2 uptake derived from eddy covariance landscape NEE measurements was only half of the long-term fen net CO_2 uptake from similar landscapes (Fig. 4.6). At the same time, fens generally emit more CH_4 (*Olefeldt et al.*, 2013,

Tab. 4.III). Channel fens at Scotty Creek, similar to collapse-scar bogs, expand with permafrost thaw (*Quinton et al.*, 2011), but are not captured by the landscape flux footprints. Channel fen F_{CH4} studies could therefore help further constraining the thaw-induced net radiative greenhouse gas forcing.

To better predict wetland expansion in the permafrost zone, improved large-scale mapping of poorly drained, organic-rich lowland boreal forests (e.g., *Thompson et al.*, 2016) is required, as these landscapes are most sensitive to thaw-induced wetland expansion (see Chapter 2 & *Lara et al.*, 2016). The future trajectories of wetland expansion may also depend on increased atmospheric water inputs to sustain high water tables. The water demand could be satisfied by projected increases in water availability at high latitudes (*Lawrence et al.*, 2015).

Here, we show that the climate warming effect of thaw-induced ΣF_{CH4} increases in a boreal forest-wetland landscape likely exceeds the cooling effect of long-term net CO_2 uptake over the current century (i.e., a positive net radiative greenhouse gas forcing; Fig. 4.6). However, the thaw-induced wetland expansion in the southern Taiga Plains also induces regional climate cooling due to increases in albedo and decreases in sensible heat fluxes (see Chapter 3). To quantify the total net radiative greenhouse gas forcing of wetland expansion in the sporadic permafrost zone and to compare it to its net radiative biophysical forcing, wetland expansion rates need to be up-scaled from local to regional scales.

In the southern Taiga Plains, current thaw-induced wetland expansion is already modifying how boreal peatlands in the sporadic permafrost zone interact with the global and regional climates. Process-based models aiming to predict such thaw impacts on climate thus need to account for various dynamic interactions between permafrost, local topography and regional hydrology, and F_{CH4}. Nested F_{CH4} measurements, such as presented in this study, offer an opportunity to evaluate the performance of such models to simulate and project changes in landscape F_{CH4} emissions against measured ecosystem and landscape F_{CH4}.

CHAPTER 5

DIRECT AND INDIRECT CLIMATE CHANGE EFFECTS ON CARBON DIOXIDE FLUXES IN A THAWING BOREAL FOREST-WETLAND LANDSCAPE

Context within the thesis

The present chapter analyzes the indirect climate change impact of thaw-induced land cover changes on NEE and the direct climate change effect of changing meteorological conditions on NEE in the southern Taiga Plains. To achieve this goal, I combine eddy covariance net CO_2 fluxes, its component fluxes GPP and ER, boundary analysis of GPP, and downscaled projections of end-of-21st-century air temperatures and incoming shortwave radiation. Chapter 5 complements results on long-term boreal peatland net CO_2 uptake (as derived from paleoecological studies) presented in chapter 4 and further explores the spatio-temporal dynamics of NEE, GPP, and ER. More specifically, the study characterizes how photosynthetic CO_2 uptake and respiratory CO_2 losses, together making up NEE, are affected by thawing permafrost. Chapter 3, 4 and 5 together provide a comprehensive analysis of thaw-induced impacts on land-atmosphere interactions by focussing on energy and water fluxes, CH_4 and CO_2 fluxes, respectively. Additionally, chapter 5 addresses, but also opens questions on direct climate change impacts on land-atmosphere interactions. While changes in landscape structure and composition may affect the land surface response to meteorological forcing, the net climate change impacts on land-atmosphere interactions are driven by the combination of changes in land surface response and in meteorological forcing.

5.1 Abstract

In the sporadic permafrost zone of northwestern Canada, boreal forest carbon dioxide (CO_2) fluxes will be altered directly by climate change through changing meteorological forcing and indirectly through changes in landscape functioning associated with

thaw-induced collapse-scar bog ('wetland') expansion. However, their combined effect on landscape-scale net ecosystem CO_2 exchange (NEE_{LAND}), resulting from changing gross primary productivity (GPP) and ecosystem respiration (ER), remains unknown. Here, we quantify indirect land cover change impacts on NEE_{LAND} and direct climate change impacts on modeled temperature- and light-limited NEE_{LAND} of a boreal forest-wetland landscape. Using nested eddy covariance flux towers, we find both GPP and ER to be larger at the landscape compared to the wetland level. However, annual NEE_{LAND} (-20 g C m^{-2}) and wetland NEE (-24 g C m^{-2}) were similar, suggesting negligible wetland expansion effects on NEE_{LAND}. In contrast, we find non-negligible direct cli- mate change impacts when modeling NEE_{LAND} using projected air temperature and incoming shortwave radiation. At the end of the 21st century, modeled GPP mainly increases in spring and fall due to reduced temperature limita- tion, but becomes more frequently light-limited in fall. In a warmer climate, ER increases year-round in the absence of moisture stress resulting in net CO2 uptake increases in the shoulder seasons and decreases during the summer. Annually, landscape net CO_2 uptake is projected to decline by 25 $\pm$ 14 g C m^{-2} for a moderate and 103 $\pm$ 38 g C m^{-2} for a high warming scenario, potentially reversing recently observed positive net CO_2 uptake trends across the boreal biome. Thus, even without moisture stress, net CO_2 uptake of boreal forest-wetland landscapes may decline, and ultimately, these landscapes may turn into net CO_2 sources under continued anthropogenic CO_2 emissions. We conclude that NEE_{LAND} changes are more likely to be driven by direct climate change rather than by indirect land cover change impacts.

5.2 Introduction

The boreal biome, with its distinct land-atmosphere exchange of sensible heat, water vapor, methane, and CO_2, plays an important role in the global and regional climate systems (*Chapin et al.*, 2000). For example, boreal forests represent an important carbon (C) sink of about 0.5 Pg C yr^{-1} (*Pan et al.*, 2011), equivalent to 17 $\pm$ 6 % of the global land CO_2 sink (*Le Quéré et al.*, 2015). Climate warming in the boreal biome

of northwestern North America has caused widespread permafrost thaw at the southern permafrost limit inducing wetland expansion leading to replacement of boreal forests in lowland regions (e.g., Chapter 2; *Chasmer and Hopkinson*, 2016; *Lara et al.*, 2016). Previous studies have shown that land cover changes in these regions affect regional land-atmosphere interactions by favoring the partitioning of available energy to latent instead of sensible heat (see Chapter 3) and by enhancing landscape methane emissions (see Chapter 4). However, it remains uncertain how climate warming and resulting land cover changes influence net ecosystem CO_2 exchange (NEE), and its component fluxes gross primary productivity (GPP) and ecosystem respiration (ER) (*Schuur et al.*, 2015).

Along the southern limit of the North American per- mafrost zone, long-term net CO_2 uptake has resulted in large organic C stocks as peat (*Robinson and Moore*, 1999; *Tarnocai et al.*, 2009; *Treat et al.*, 2016). In these organic-rich boreal landscapes, thawing permafrost makes previously frozen organic C stocks available for decomposition and ER may be enhanced by warming soils (*Koven et al.*, 2015; *Natali et al.*, 2014; *O'Donnell et al.*, 2012; *Schuur et al.*, 2009; *Treat et al.*, 2014). However, permafrost thaw in organic- and ice-rich landscapes often leads to surface subsidence and increased land surface wetness (e.g., *Baltzer et al.*, 2014; *Osterkamp et al.*, 2000). Under saturated and anoxic conditions, associated with subsidence, organic matter decomposes more slowly, causing only an attenuated post-thaw increase in ER (*Knoblauch et al.*, 2013). At the same time, GPP might increase due to increased nutrient and soil moisture availability, and warmer soil and air temperatures (T_s and T_a) (e.g., *Camill et al.*, 2001; *Finger et al.*, 2016; *Keuper et al.*, 2012; *Turetsky et al.*, 2000, 2007; *Wickland et al.*, 2006). The combination of changes in both GPP and ER in a warming climate will eventually determine whether organic-rich boreal landscapes will continue to be long-term CO_2 sinks exerting a climate cooling effect (*Frolking et al.*, 2006). Since 1985, the land net CO_2 sink in the boreal biome (50° to 60° N, excluding Europe) increased by 8-11 Tg C yr^{-1} (*Welp et al.*, 2016), but it remains unclear whether this trend will continue in an increasingly warmer climate.

Recent warming trends in northwestern Canada, in the order of 0.25-0.50 °C per decade (*DeBeer et al.*, 2016), are likely to continue and potentially accelerate during the

21st century (*Kirtman et al.*, 2013). Direct climate change effects result from instantaneous ecosystem responses to these altered meteorological conditions. For example, boreal forest GPP is suppressed at T_a below the freezing point and increases with both T_a- and light-availability (*Luyssaert et al.*, 2007; *Tanja et al.*, 2003), while ER increases with T_a and T_s (*Dunn et al.*, 2007; *Ueyama et al.*, 2014). In addition to substantially warmer regional climates at high latitudes, changes in cloud cover could alter incoming shortwave radiation (SW_{in}, W m^{-2}) in these regions (*Kirtman et al.*, 2013). In contrast, indirect climate change impacts result from changes in ecosystem composition, structure, and function thus altering how ecosystems may respond to variations in meteorological conditions. For example, a gradual increase in the temperature sensitivity of ER over several years can alter NEE of boreal forests in the absence of any warming trend (e.g., *Hadden and Grelle*, 2016). The abrupt vegetation changes following permafrost thaw in lowland boreal forests may trigger shifts in ecosystem functioning (*Camill et al.*, 2001). Thus, both direct and indirect climate change effects on GPP and ER need to be assessed to better constrain the future NEE of peatland landscapes in the permafrost zone.

Recent warming trends in northwestern Canada, in the order of 0.25-0.50 °C per decade (*DeBeer et al.*, 2016), are likely to continue and potentially accelerate during the 21st century (*Kirtman et al.*, 2013). Direct climate change effects result from instantaneous ecosystem responses to these altered meteorological conditions. For example, boreal forest GPP is suppressed at T_a below the freezing point and increases with both T_a and light availability (*Luyssaert et al.*, 2007; *Tanja et al.*, 2003), while ER increases with T_a and T_s (*Dunn et al.*, 2007; *Ueyama et al.*, 2014). In addition to substantially warmer regional climates at high latitudes, future changes in cloud cover could alter incoming shortwave radiation (SW_{in}, W m^{-2}) in these regions (*Kirtman et al.*, 2013). In contrast, indirect climate change impacts result from changes in ecosystem composition, structure, and function, thus altering how ecosystems may respond to variations in meteorological conditions. For example, a gradual increase in the temperature sensitivity of ER over several years can alter NEE of boreal forests in the absence of any warming trend (e.g., *Hadden and Grelle*, 2016). The abrupt vegetation changes following per-

mafrost thaw in lowland boreal forests may trigger shifts in ecosystem function (*Camill et al.*, 2001). Thus, both direct and indirect climate change effects on GPP and ER need to be assessed to better constrain the future NEE of organic-rich boreal landscapes in the permafrost zone.

Here, we examine the direct climate change effects of altered meteorological conditions and the indirect effects of thaw-induced wetland expansion on NEE and its component fluxes GPP and ER for a boreal forest-wetland landscape in a rapidly thawing lowland region at the southern limit of permafrost in northwestern Canada (*Baltzer et al.*, 2014; *Quinton et al.*, 2011). We use nested eddy covariance net CO_2 flux measurements to compare NEE of the thawing landscape to NEE of a nearby permafrost-free wetland within the heterogeneous landscape, both exposed to the same meteorological conditions. Downscaled regional climate projections are used to assess the GPP, ER, and NEE response to a changing climate. We analyze:

— how thaw-induced wetland expansion and associated forest loss indirectly affect NEE, GPP, and ER of the boreal forest-wetland landscape, and

— how how these indirect climate change effects compare to direct effects of projected changes in T_a and SW_{in} over the 21st century.

5.3 Materials and Methods

5.3.1 Study site

Scotty Creek (61°18' N; 121°18' W) is a 152-km^2 watershed in the sporadic permafrost zone (10–50 % of land area underlain by permafrost) near Fort Simpson, NT in the southern Taiga Plains of northwestern Canada. With 70 Pg of soil organic C in the top 3 m, the Taiga Plains store about 15 % of the total organic C stocks (< 3 m) in the North American permafrost zone (data from *Hugelius et al.*, 2013). The dry continental climate of the Fort Simpson region is characterized by a mean T_a of -2.8 °C and a mean total precipitation of 388 mm with 149 mm falling as snow (1981-2010; *Environment Canada*, 2014). The southern part of Scotty Creek is characterized by a mosaic of forested permafrost (peat) plateaus, wetlands, forested uplands, and shallow lakes

(*Chasmer et al.*, 2014). Permafrost-free wetlands ('wetlands') occur mainly as collapse-scar bogs dominated by bryophytes (*Sphagnum balticum* and *S. magellanicum*), ericaceous shrubs (*Chamaedaphne calyculata, Andromeda polifolia, Vaccinium oxycoccos*), pod grass (*Scheuchzeria palustris*), and a few isolated black spruce (*Picea mariana*) and tamarack (*Larix laricina*). In contrast, forested permafrost plateaus ('forests') are characterized by a denser overstory of black spruce with a shrub understory and a ground cover comprising ericaceous shrubs (mainly *Rhododendron groenlandicum*), and lichens (*Cladonia* spp.) and bryophythes (*Sphagnum fuscum* and *S. capillifolium*), respectively (*Garon-Labrecque et al.*, 2015). Abiotic and biotic characteristics change abruptly between these two ecosystem types as indicated by contrasting overstory leaf area index ($\geq$ 1 vs. $\leq$ 0.5 for forest and wetland, respectively) and soil moisture conditions ($\leq$ 30 % for the forests compared to $\geq$ 70 % for the wetlands). An active layer (i.e., seasonally thawed surface soil) of approximately 50 cm overlays near-surface permafrost in the forests. No near-surface permafrost is present in the wetlands (*Baltzer et al.*, 2014). These changes occur over several meters across transition zones with inundated, warmer peat soils (*Baltzer et al.*, 2014; *Bubier et al.*, 1995, Fig. 5.1). Warm soils in the wetlands cause lateral thawing of near-surface permafrost underlying the forests and, thus, a rapid expansion of permafrost-free wetlands *Kurylyk et al.* (2016).

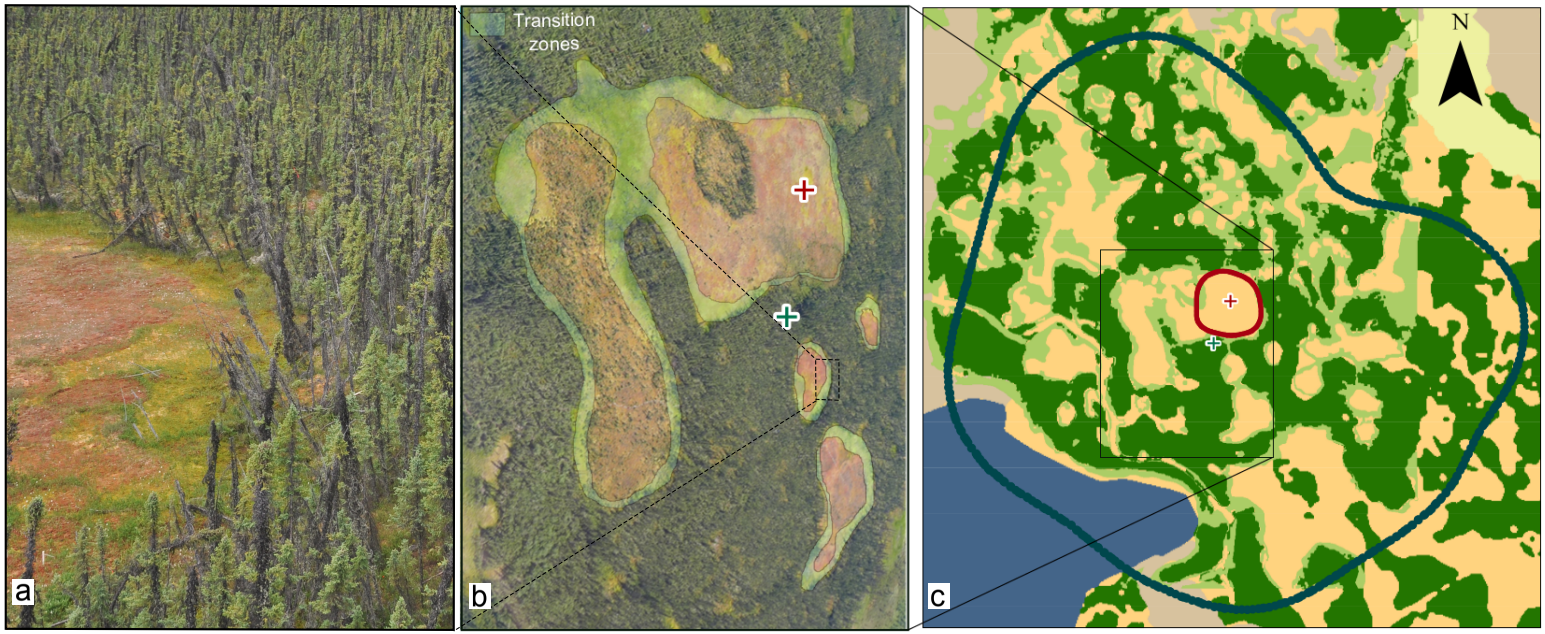

Figure 5.1 – **(a)** Oblique photograph of an actively thawing transition zone between wetland and forest. **(b)** Oblique photograph of the studied boreal forest-wetland landscape taken from a helicopter. Bright green areas represent visually delineated transition zones (several metres in lateral extent). **(c)** Land cover types in the flux footprints of the wetland (red cross) and the landscape tower (green cross): forested permafrost peat plateaus (dark green) and wetlands [collapse-scar bogs (yellow), fens (light brown), and an upland on post-glacial till (greenish yellow in the top right corner, outside the footprint)]. Wetland areas that have been converted from forested permafrost peat plateaus since 1977 (transition zones as identified using historical aerial photographs) are indicated in light green. Note that the extent of the transition zone map in (c) is limited to the east and south. Solid lines show landscape (dark green) and wetland tower (red) 90 % flux footprint climatology.

At Scotty Creek, forests and wetlands comprise thick organic peat soils of $\geq$ 3 m with a mean total organic C content of 167 $\pm$ 11 kg C m^{-2} (n = 3; *Pelletier et al.*, 2017). About 20 % of North America's boreal forests grow in the circumpolar permafrost zone on ice-rich permafrost and thick overburden cover and are thus prone to thaw-induced surface subsidence and to forest loss in a warming climate (see Chapter 2 & *Olefeldt et al.*, 2016).

5.3.2 Eddy covariance flux measurements

Eddy covariance net CO_2 flux measurements were conducted at a landscape tower at 15.2 m above the mean lichen-moss surface of the permafrost plateau (March 23, 2015 to August 30, 2016) and at a nested wetland tower at 1.9 m above the mean moss surface (June 10, 2015 to August 30, 2016). At the wetland and the landscape tower, high-frequency (10 Hz) fluctuations of vertical wind velocity and sonic temperature were measured with a sonic anemometer (CSAT3A; Campbell Scientific, Logan, UT, USA) and CO_2 and water vapor densities with a colocated open-path infrared gas analyzer (EC150; Campbell Scientific). At the beginning of the study period (March 23, 2015 to August 16, 2015), an enclosed infrared gas analyzer (LI-7200; LI-COR Biosciences, Lincoln, NE, USA) was used for CO_2 and water vapor density measurements at the landscape tower. Differences in net CO_2 fluxes derived from the LI-7200 and the EC150 were less than 5 % and cumulative net CO_2 fluxes over 57 days differed by 8 % (*Helbig et al.*, 2016a). Net ecosystem CO_2 exchange for the landscape (NEE_{LAND}; μmol m^{-2} s^{-1}) and the wetland tower (NEE_{WET}; μmol m^{-2} s^{-1}) was calculated as the sum of the turbulent net CO_2 flux and a storage term. The storage term was derived from half-hourly CO_2 concentration changes at the measurement heights. We follow the micrometeorological NEE convention where net landscape/ecosystem CO_2 uptake is indicated by a negative sign and net CO_2 release to the atmosphere by a positive sign. Net ecosystem CO_2 exchange was filtered for periods with insufficient turbulence using a landscape tower friction velocity threshold of 0.13 m s^{-1} (95 % confidence interval (CI): 0.10–0.21 m s^{-1}), derived according to *Papale et al.* (2006). The 95 % CI was derived by using 100 bootstrapped nighttime NEE time series as input. The same threshold was used

for the wetland and the landscape tower as the wetland is nested in the landscape tower footprints. All flux calculations were performed using the EddyPro software (version 6.1.0; LI-COR Biosciences). A more detailed description of the instrumental setup and the flux processing procedure is given in Chapter 3 and *Helbig et al.* (2016a). For the entire study period, 55 % (daytime: 68 %; nighttime: 39 %) and 43 % (daytime: 56 %; nighttime: 28 %) of NEE passed the quality control at the landscape and wetland tower, respectively.

5.3.3 Assessing indirect climate change impacts on CO_2 fluxes using nested eddy covariance fluxes

Footprint modeling. Half-hourly 2-D flux footprints for the wetland and the landscape tower [defined as half-hourly probability maps of flux contribution per unit area (% per m^{-2})] were obtained according to *Kljun et al.* (2015).. The flux footprints were combined with a land cover classification map (*Chasmer et al.*, 2014), as described in Chapter 3 and 4, to derive sums of half-hourly probabilities of flux contributions for individual land cover types (i.e., flux footprint contributions from forests and wetlands; Fig. 5.1). Additionally, transition zones were delineated based on aerial photographs as areas of wetland expansion (and thus of forest loss) since 1977 (see *Chasmer et al.*, 2010). Within a radius of 350 m around the landscaper tower, 21 % of the land surface was classified as transition zone. Their flux footprint contributions were then separately derived for each half-hourly flux measurement. Transition zones are part of the wetland land cover type and their definition is to some extent arbitrary, as a reference year (here 1977, the first year of available aerial photography) is used to differentiate between gradual transition zones and interior wetlands. As the half-hourly variability in transition zone contribution was relatively small (standard deviation: 2 % for wetland tower and 5 % for landscape tower), only their average flux footprint contribution to the two flux towers over the entire study period was analyzed. Wetland NEE was discarded when forest contributions were greater than 5 %, and NEE_{LAND} was discarded when contributions from a nearby lake were larger than 5 % (Fig. 5.1). On average, forest contributions to landscape tower footprints were 48 %, whereas wetlands contributed

50 % (48 % from bogs and 2 % from fens). The remaining contributions originated from the nearby lake. The wetland tower was located in a collapse-scar bog, and $\geq$ 95 % of the wetlands within the landscape tower footprint were collapse-scar bogs. In the following, 'wetlands' therefore refer to collapse-scar bogs. Fens represent a second permafrost-free wetland ecosystem type covering about 12 % of the entire Scotty Creek watershed (*Chasmer et al.*, 2014). Similar to collapse-scar bogs, fens are expanding due to permafrost thaw (*Chasmer and Hopkinson*, 2016). Due to their differing hydrology, vegetation composition, and nutrient availability, CO_2 flux dynamics of fens most likely differ from CO_2 flux dynamics of collapse-scar bogs (e.g., *Bubier et al.*, 1995; *Treat et al.*, 2016; *Yu*, 2006).

Flux partitioning. Gaps in NEE were filled using the mar- ginal distribution sampling method (*Reichstein et al.*, 2005) with SW_{in}, T_a, and water vapor pressure deficit (VPD, kPa) as look-up table variables. We calculated annual NEE for 100 friction velocity thresholds (as derived from bootstrapped night-time NEE) to derive the 95 % CI of annual NEE.

To partition NEE into its component fluxes, GPP (μmol m^{-2} s^{-1}) and ER (μmol m^{-2} s^{-1}), we used a bulk partitioning approach (e.g., *Runkle et al.*, 2013). The non-gap-filled, half-hourly daytime NEE (SW_{in} > 5 W m^{-2}) was fit to a bulk model combining a rectangular hyperbola function (for GPP) and an empirical Q10 model (for ER):

$$NEE = -GPP + ER = \underbrace{-\frac{GPP_{max}\alpha_i SW_{in}}{GPP_{max} + \alpha SW_{in}}}_{\text{Term A}} + \underbrace{ER_{base} Q_{10}^{\frac{T_a - T_{ref}}{\gamma}}}_{\text{Term B}} \tag{5.1}$$

GPP_{max} (μmol m^{-2} s^{-1}) is the maximum canopy photosynthetic capacity, α_i (μmol m^{-2} s^{-1} per W m^{-2}) is the initial canopy quantum efficiency, ER_{base} (μmol m^{-2} s^{-1}) is the basal respiration at a reference temperature (T_{ref} = 15 °C), Q_{10} indicates the sensitivity of ER to T_a, and γ = 10 °C is a constant (e.g., *Mahecha et al.*, 2010). For the Q_{10} model, we selected T_a measurements within the forest canopy at 2 m above the lichen-moss surface because T_a represents an integrated tem- perature measure for the landscape, whereas soil temperature varies spatially (laterally and vertically) across the

heterogeneous landscape (see Chapter 4). We fixed the Q_{10} parameter in a first iteration (Q_{10} = 2.5 [landscape] and Q_{10} = 1.1 [wetland]) before deriving the final GPP_{max}, α, and ER_{base}, as described in *Reichstein et al.* (2005). To derive a complete ER time series, we combined gap-filled nighttime NEE (i.e., ER) with the modeled daytime ER (see Term B in Eq. 5.1). Ecosystem respiration was then subtracted from measured NEE to derive GPP. Using only daytime NEE to obtain daytime ER, we account for potential light inhibition of leaf respiration during the day (Wehr et al., 2016) and avoid prob- lems of extrapolating relationships between nighttime Ta and ER to daytime conditions (e.g., Lasslop et al., 2010). We assessed indirect land cover change impacts on CO_2 fluxes by analyzing differences between NEE and derived component fluxes from the two eddy covariance flux towers with contrasting flux footprint composition.

Modeling NEE and GPP. In this study, we assess how daily light and temperature conditions affect mean daily NEE_{LAND}. Net ecosystem CO_2 exchange is the small difference between its two large component fluxes GPP and ER. Ecosystem respiration is strongly controlled by temperature, whereas light and temperature are strong controls on GPP, highlighting the potentially different responses of ER and GPP to changing climatic conditions (e.g., *Fang and Moncrieff*, 2001; *Huxman et al.*, 2003; *Lafleur et al.*, 2005). We therefore modeled light regulation of GPP using the rectangular hyperbola function in Eq. 5.1 and used a downward regulation scalar [$f(T_a)$ in Eq. 5.2] to account for temperature limitation of GPP. Mean daily GPP was fitted to the following equation with the *nlinfit* function in MATLAB (version 8.6.0; The MathWorks, Natick, MA, USA) using daily means of T_a and SW_{in}:

$$GPP = f(T_a)\frac{GPP_{max}\alpha_i SW_{in}}{GPP_{max} + \alpha SW_{in}} \tag{5.2}$$

$f(T_a)$ is implemented as a sigmoidal function ranging from 0 to 1 and accounts for instantaneous temperature constraints using mean daily T_a and for seasonal temperature constraints using a moving T_a average (i.e., average of seven preceding days, T_{a_week}; °C). The T_{a_week} constraint accounts for seasonality in biological controls other than the instantaneous GPP response to T_a, such as physiological activity (e.g., *Rayment et al.*,

2002) and thermal acclimation (e.g., *Gea-Izquierdo et al.*, 2010). According to Liebig's law, we assume that only the more limiting factor controls GPP (e.g., *Yuan et al.*, 2007):

$$f(T_{\mathrm{a}}) = min(\frac{1}{1+a^{(b-T_{\mathrm{a}})}}, \frac{1}{1+a^{(c-T_{\mathrm{a\_week}})}}) \tag{5.3}$$

where a, b, and c are model coefficients. Additionally, we constructed an ER model (ER_{MOD}) by fitting a Q_{10} model (Term B in Eq. 5.1 based on daily T_a) to mean daily ER. Modeled NEE (NEE_{MOD}) was calculated as the sum of GPP_{MOD} and ER_{MOD}. Thus, NEE_{MOD} only depends on the climatic controls T_a and SW_{in} and does not account for other environmental or biological limitations on NEE (e.g., soil moisture limitations; *Niu et al.*, 2011; *Peichl et al.*, 2013). Model uncertainties were estimated based on 1000 bootstrapped GPP and ER time series. To characterize how the potential of NEE_{LAND} (NEE_{POT}) responds to changes in thermal conditions, we defined NEE_{POT} as the most negative daily NEE_{LAND} for given daily T_a (i.e., NEE_{LAND} < 15 %ile per T_a bin with each bin containing 2.5 % of all data). Like NEE_{POT}, we defined the temperature- controlled potential of GPP_{LAND} ($GPP_{POT\_T_a}$) as the upper limit of daily GPP_{LAND} for a given daily T_a and T_{a_week}. To characterize the light control on the potential of GPP_{LAND} ($GPP_{POT\_SW_{in}}$), we defined $GPP_{POT\_SW_{in}}$ as the upper limit of daily GPP_{LAND} for a given daily SW_{in}. Sigmoidal functions were then fitted to $GPP_{POT\_T_a}$ and $GPP_{POT\_SW_{in}}$:

$$GPP_{POT\_i} = \frac{k}{1+l^{(m-x_i)}} + n \tag{5.4}$$

where GPP_{POT_i} is modeled GPP_{POT} for the variable x_i (i.e., T_a/T_{a_week} and SW_{in}), and k, m, n, and l are model coefficients. We defined GPP_{POT} as temperature-limited if $GPP_{POT\_T_a}$ for the observed daily T_a or T_{a_week} was smaller than $GPP_{POT\_SW_{in}}$ for the observed daily SW_{in}. For the opposite case, GPP_{POT} was light-limited. If differences in $GPP_{POT\_T_a}$ and $GPP_{POT\_SW_{in}}$ were less than 10 %, we assumed that GPP_{POT} was colimited by temperature and light.

Assessing direct climate change impacts on NEE. To assess direct climate change impacts on NEE_{MOD}, GPP_{MOD}, and ER_{MOD}, we used the modeling approach described above with regionally downscaled climate projections as drivers. We obtained T_a and

SW_{in} for the period 2006-2015 and 2091-2100 from the North American Coordinated Regional Climate Downscaling Experiment (CORDEX; http://www.cordex.org) and extracted daily time series for Scotty Creek. The CORDEX provides downscaled climate projections at 50-km resolution for various combinations of Earth system models (ESM) and regional climate models (RCM). We used the ensemble means of six CORDEX projections for two Representative Concentration Pathway (RCP) scenarios: the medium warming RCP4.5 and the high warming RCP8.5 scenario (for selected RCM/ESM simulations, see Fig. 1.4; https://na-cordex.org/simulations-modeling-group). We used both RCPs to compare the scenario leading to the strongest warming (RCP8.5) with a more moderate scenario (RCP4.5). Currently, global net CO_2 emissions follow the most pessimistic CO_2 emission scenario, but these may be reduced depending on future climate policies (*Friedlingstein et al.*, 2014a). To adjust for potential systematic differences between modeled (CORDEX) and measured T_a, we debiased modeled T_a for each CORDEX projection before calculating ensemble means by regressing it against measurements of daily T_a (*Wilby et al.*, 2004) from the nearest weather station in Fort Simpson ($\sim$50 km; 2006-2015; Environment Canada, 2016; http://climate.weather.gc.ca/climate_data/). We constrained the regression to periods when both CORDEX and weather station $T_a > 5$ °C as the root-mean-square error between modeled and measured $T_a$for colder periods increased by about 50%.

5.4 Results

5.4.1 Half-hourly landscape and wetland NEE

Between June 10, 2015 and August 30, 2016, wetlands and forests contributed equally to landscape flux foot- prints with 50$\pm$30 % ($\pm$95 % CI) and 47$\pm$28 %, respectively (and 3 % from the lake). About a third of the wetland contributions to the landscape flux footprints originated from the forest-to-wetland transition zones (i.e., total transition zone contributions to landscape flux footprints were 18$\pm$10 %). In contrast, transition zones only contributed 3$\pm$3 % to the wetland flux footprints. NEE_{LAND} ranged from -7.9 μmol

m^{-2} s^{-1} (1^{st} percentile) to 4.8 μmol m^{-2} s^{-1} (99^{th} percentile) whereas a smaller range from -5.2 μmol m^{-2} s^{-1} (1^{st} percentile) to 3.9 μmol m^{-2} s^{-1} (99^{th} percentile) was observed for NEE_{WET} (Fig. 5.2). Positive NEE_{LAND} was more positive (i.e., more net CO_2 release) than NEE_{WET} and negative NEE_{LAND} was more negative (i.e., more net CO_2 uptake) than NEE_{WET} with a total least-squares (TLS) slope between NEE_{WET} and NEE_{LAND} of 1.49$\pm$0.03 and an intercept of 0.24$\pm$0.03 μmol m^{-2} s^{-1}. Slopes for this relationship were independent of wetland contributions (FP_{WET}; %) to landscape flux footprints. The slope for periods with FP_{WET} smaller than or equal to 50 % (1.50$\pm$0.05) was not significantly different (α = 0.05) from the slope for periods with FP_{WET} larger than 50 % (1.43$\pm$0.03). Slopes were consistently positive for night- and day-time NEE_{LAND}-NEE_{WET} relationships. However, the nighttime slope for low FP_{WET} (1.32$\pm$0.18) was significantly smaller than the slope for high FP_{WET} (1.81$\pm$0.15), indicating that nighttime NEE_{LAND} differed more from NEE_{WET} when wetland contributions to landscape flux footprints were large. For the daytime NEE_{WET} and NEE_{LAND} relationships, the slope for high FP_{WET} of 1.52$\pm$0.05 was significantly smaller than the slope for low FP_{WET} of 1.71$\pm$0.07. NEE_{LAND} and NEE_{WET} relationships were independent of wind direction as slopes for periods with northerly winds with overlapping wetland and landscape flux footprints were similar to slopes for periods with non-overlapping footprints (data not shown).

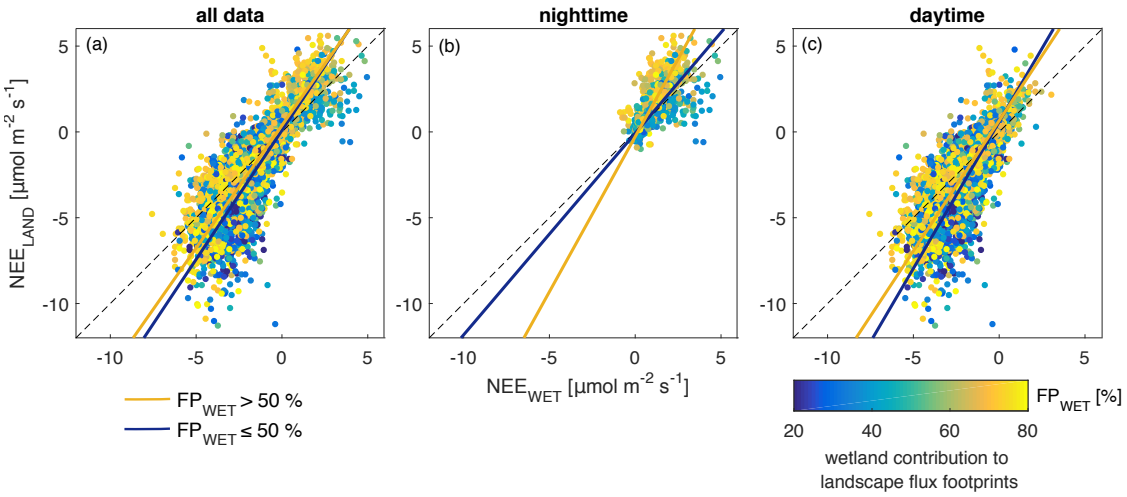

Figure 5.2 – Comparison of half-hourly net ecosystem carbon dioxide exchange at the landscape (NEE_{LAND}) and wetland scale (NEE_{WET}) for (a) all, (b) only nighttime, and (c) only daytime measurements. Data points are color-coded according to the wetland contribution to landscape flux footprints (FP_{WET}). The solid blue and yellow lines show the total least-squares regressions for low (FP_{WET} < 50 %) and high FP_{WET} ($FP_{WET} \geq$ 50 %), respectively.

5.4.2 Daily landscape and wetland NEE and their component fluxes

Monthly medians of daily NEE_{LAND} and NEE_{WET} were negative from May to August (i.e., net CO_2 uptake period) when minimum daily T_a was generally warmer than 0 °C and positive for the remaining 8 months with minimum daily T_a at or below 0 °C for most of the days (Fig. 5.3a, Fig. IV.2 & IV.1). Maximum positive daily NEELAND and NEEWET were observed in November 2015 with medians of 0.48 μmol m^{-2} s^{-1} and 0.46 μmol m^{-2} s^{-1}, respectively, when T_a was below 0 °C, maximum SW_{in} smaller than 200 W m^{-2}, but soil temperatures in the wetlands (at 32 cm) still between 1 °C and 2.5 °C (Fig. IV.1). Minimum negative NEE_{WET} and NEE_{LAND} in 2016 occurred in July with -0.86 μmol m^{-2} s^{-1} and -1.01 μmol m^{-2} s^{-1}, respectively. From May to July 2015, monthly medians of daily NEE_{LAND} were more negative than NEE_{WET} (Wilcoxon signed-rank test; $p < 0.05$). In contrast, the median of daily NEE_{LAND} was less negative than NEE_{WET} in August 2015 ($p < 0.001$) and not significantly different during the same month in 2016. Monthly medians of daily NEE_{LAND} in September, October, and

December were more positive than NEE_{WET} while no significant differences were observed for the remaining winter months. Differences in the derived daily component fluxes GPP and ER were more pronounced with monthly medians of daily GPP_{WET} and ER_{WET} being significantly smaller than GPP_{LAND} and ER_{LAND} from March to November (Fig. 5.2b & c). During the winter months between December and April, differences in landscape and wetland GPP and ER were smaller than 0.1 μmol m^{-2} s^{-1}.The largest GPP and ER differences were observed in June 2015 with monthly medians of GPP_{WET} being 1.8 μmol m^{-2} s^{-1} smaller than medians of GPP_{LAND} and monthly medians of ER_{WET} being 1.6 μmol m^{-2} s^{-1} smaller than medians of ER_{LAND}. In 2016, the largest dif- ferences in monthly medians of GPP and ER were observed in July with 1.5 μmol m^{-2} s^{-1} and 1.3 μmol m^{-2} s^{-1}, respectively. Between 2015 and 2016, the patterns and magnitude of NEE, GPP, and ER from both towers were similar for the overlapping months April to August.

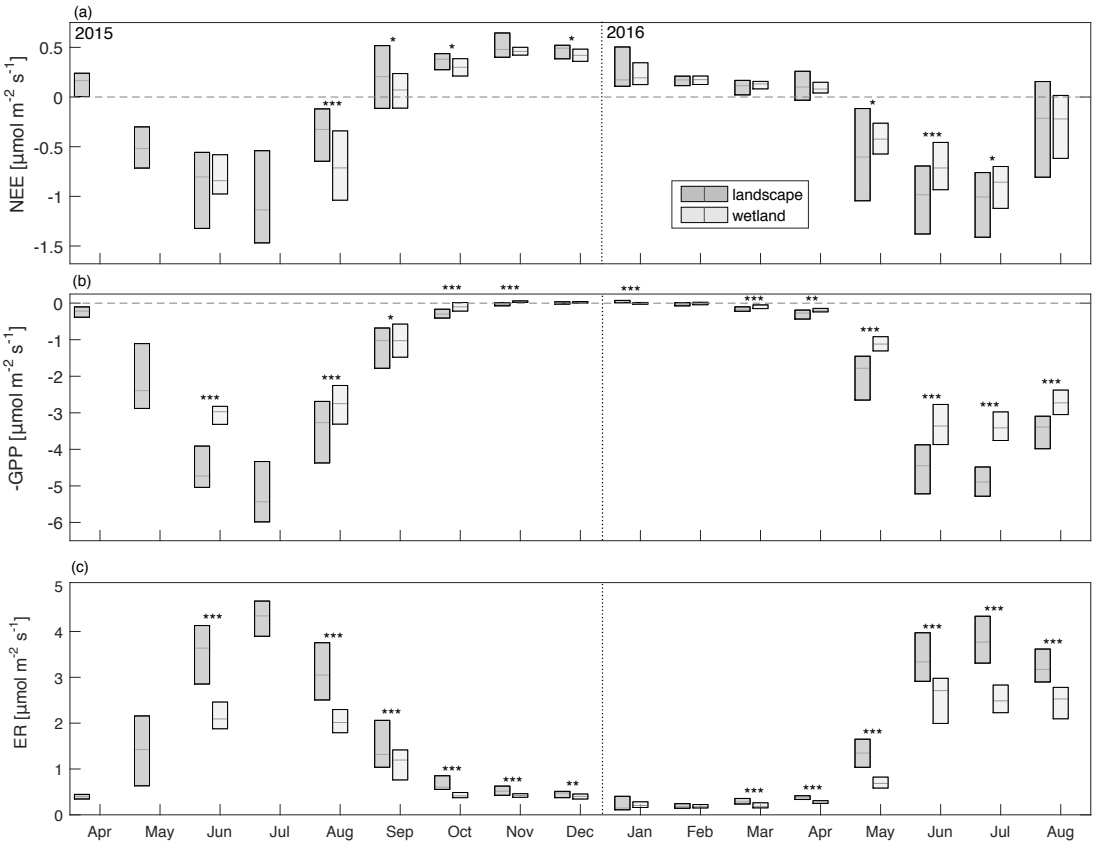

Figure 5.3 – **(a)** Daily net ecosystem carbon dioxide exchange (NEE), **(b)** gross primary productivity (GPP), and **(c)** ecosystem respiration (ER) from the wetland and landscape (including wetlands and forests) tower for individual months. Boxes show 25th and 75th percentiles; gray lines inside the boxes show medians. Asterisks indicate if monthly medians are significantly different (Wilcoxon signed-rank test; * $\alpha = 0.05$ / ** $\alpha = 0.01$ / *** $\alpha = 0.001$). Note that data from the wetland tower is missing for April, May, and July 2015 due to sensor malfunctioning.

5.4.3 Annual landscape and wetland NEE

Annual NEE_{LAND} and NEE_{WET} (ΣNEE, g C-CO_2 m^{-2}; ; August 1, 2015 to July 31, 2016) were not significantly different with -20.1 g C-CO_2 m^{-2} (-14.6 to -26.9 g C-CO_2 m^{-2} [95 % CI]) and -23.5 g C-CO_2 m^{-2} (-19.6 to -35.1 g C-CO_2 m^{-2}), respectively (Fig. 5.4). Both the landscape and the wetland were thus small net CO_2 sinks. Shortly after snow melt, the landscape and wetland wintertime net CO_2 source switched to a net CO_2 sink. From August 2015 until the end of snow melt in 2016, ΣNEE_{LAND} was more

positive (65.1 g C-CO_2 m^{-2}) than ΣNEE_{WET} (39.3 g C-CO_2 m^{-2}).. The following larger landscape net CO_2 uptake between May and July 2016 reduced the annual ΣNEE differences to 3.4 g C-CO_2 m^{-2}. Only in the beginning of January, wetland soil temperature (at 32 cm) dropped to near freezing temperature of water (Fig. IV.1), and the mean early winter (October to December) respiratory net CO_2 losses at the wetland and landscape tower dropped by more than 50 %, remaining low until snow melt (January to April). In contrast to ΣNEE_{LAND} and ΣNEE_{WET}, the ΣGPP_{LAND} of 532 g C-CO_2 m^{-2} was larger than the ΣGPP_{WET} of 378 g C-CO_2 m^{-2}. Similarly, the ΣER_{LAND} (512 g C-CO_2 m^{-2}) exceeded the ΣER_{WET} (355 g C-CO_2 m^{-2}, data not shown).

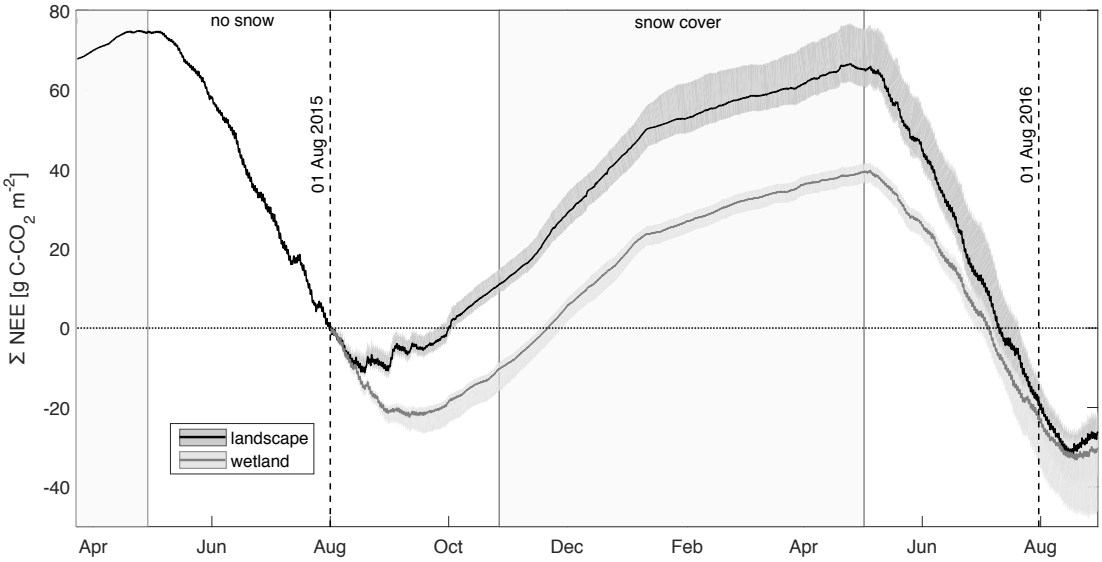

Figure 5.4 – Cumulative gap-filled net ecosystem carbon dioxide exchange at the landscape and wetland scale (ΣNEE_{LAND} & ΣNEE_{WET}, solid lines). Gray shaded areas indicate 95 % confidence intervals of ΣNEE between August 2015 and 2016 due to the friction velocity threshold and random errors in NEE measurements.

5.4.4 Meteorological controls of potential NEE, GPP, and ER

While both GPP_{LAND} and ER_{LAND} increased consistently with T_a, the largest mean daily net CO_2 uptake (NEE_{LAND}) was observed at mean daily T_a of approximately 15 °C (Tab. 5.I). Daily mean NEE_{POT} was ∼0 μmol m^{-2} s^{-1} for mean daily T_a < 2 °C and

became increasingly more negative at warmer T_a reaching a minimum of ~-2 μmol m^{-2} s^{-1} at about 15 °C, before it became again slightly less negative for warmer T_a (Fig. 5.5a). Currently, mean daily T_a at Fort Simpson is below 2 °C on more than 50 % of the days of the year (median of 0.2 °C; 2006–2015). In contrast, only about 43 % of days are projected to be below this threshold at the end of the 21st century for the RCP 8.5 scenario (median of 4.8 °C; 2091–2100). Under the current climate, 15 % of daily T_a exceeds the optimum NEE_{POT} temperature of 15 °C. The fraction of days with daily T_a above this threshold is projected to rise to 30 % (RCP8.5) by the end of the 21st century. Both T_a and SW_{in} limit GPP_{POT} (Fig. 5.5b - d). Maximum mean daily GPP_{LAND} of ~6 μmol m^{-2} s^{-1} was observed when mean daily T_a and T_{a_week} were warmer than 15 °C and mean daily SW_{in} was larger than ~200 W m^{-2}. Mean daily ER_{LAND} rapidly increased with T_a above the freezing point reaching a maximum ER_{LAND} of ~5 μmol m^{-2} s^{-1} at ~20 °C. The T_a-based Q_{10} model explained 75 % of the variance in daily ER_{LAND} [root-mean-square error (RMSE): 0.8 μmol m^{-2} s^{-1}; for model parameters, see Fig. 5.6]. The combined T_a-SW_{in} model of GPP_{LAND} explained 88 % of the variance in daily $GPPGPP_{LAND}$ (RMSE: 0.7 μmol m^{-2} s^{-1}). Modeled $NEEGPP_{MOD}$ - the difference between $GPPGPP_{MOD}$ and $ERGPP_{MOD}$ – explained 45 % of the variance in mean daily $NEEGPP_{LAND}$ (RMSE: 0.7 μmol m^{-2} s^{-1}).

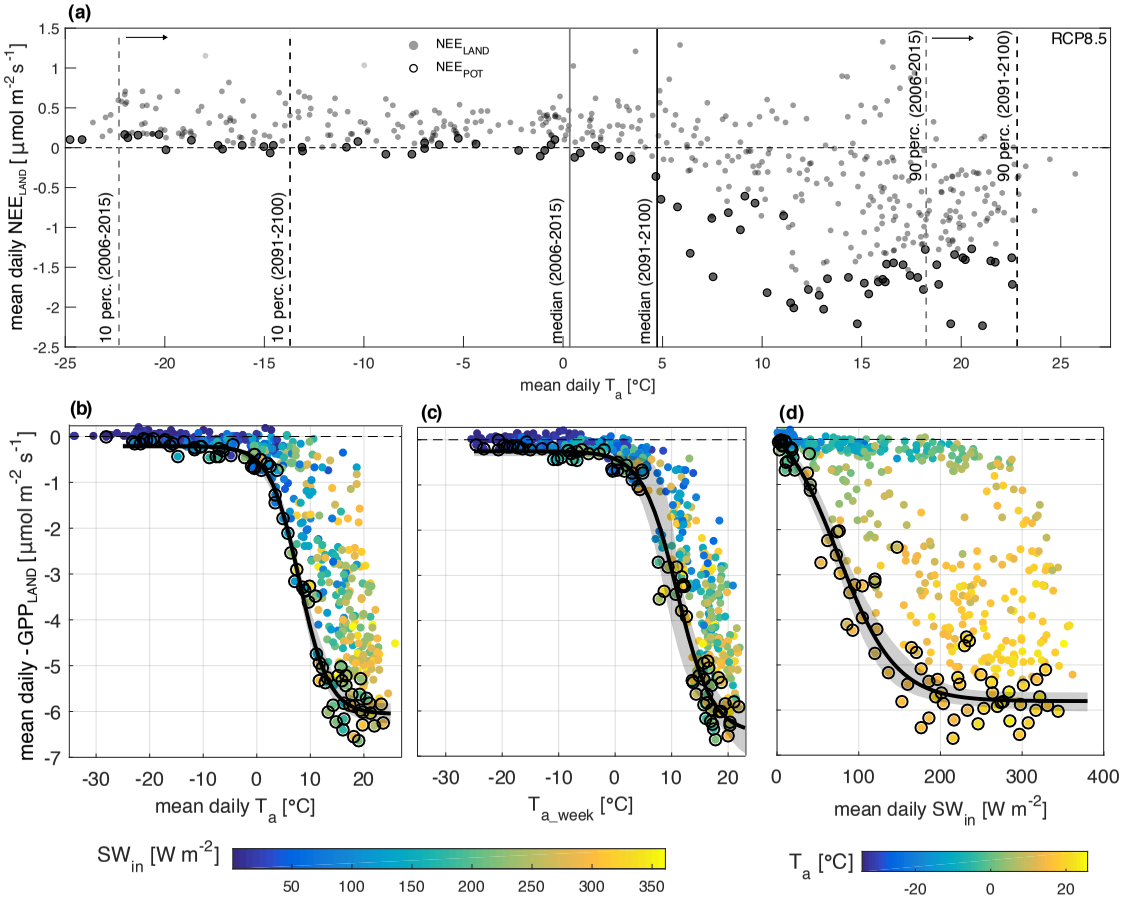

Figure 5.5 – **(a)** Mean daily air temperature (T_a) and net ecosystem carbon dioxide exchange at the landscape tower (NEE_{LAND}). Closed circles show measured NEE_{LAND}, and open circles show potential NEE. Solid lines indicate the current and projected median of daily T_a between 2006 and 2015, and 2091 and 2100. Dashed lines show the respective 10^{th} and 90^{th} percentiles. Mean daily gross primary productivity derived from NEE_{LAND} (GPP_{LAND}) against **(b)** mean daily T_a and **(c)** the seven-day moving average of T_a. Solid lines are best model fits to potential GPP (circles), and shaded areas indicate the 95 % confidence interval. Color-coding of data points represents mean daily incoming shortwave radiation (SW_{in}). **(d)** GPP_{LAND} against SW_{in}. Color-coding shows T_a.

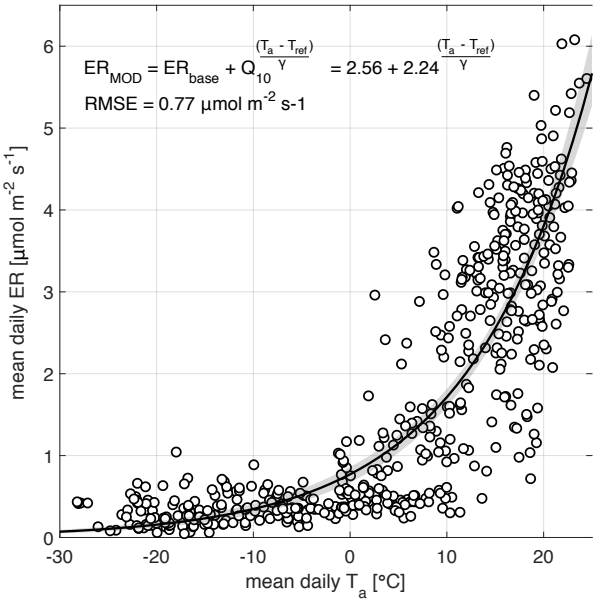

Figure 5.6 – Mean daily ecosystem respiration at the landscape tower (ER_{LAND}) against mean daily T_a. Solid line shows the best-fit Q_{10}-model.

Table 5.I – Mean daily net ecosystem CO_2 exchange (NEE_{LAND}), gross primary productivity (GPP_{LAND}), and ecosystem respiration (ER_{LAND}) at landscape-level ($\pm$ one standard deviation) for 5 °C-daily air temperature (T_a) bins between March 23, 2015 and August 30, 2016. Number of days (*n*) for bins for the observation period at Scotty Creek and the percentage of days with T_a within the bins at Fort Simpson between 2006 and 2015 (data from: Environment Canada, 2014; `http://climate.weather.gc.ca/climate_data/`).

T_a bin	$NEE_{LAND} \pm$ std	$GPP_{LAND} \pm$ std	$ER_{LAND} \pm$ std	*n*	Days
					%
°C	μmol m^{-2} s^{-1}	μmol m^{-2} s^{-1}	μmol m^{-2} s^{-1}		
$T_a \leq$ -2.5 °C	+0.28±0.22	0.04±0.11	0.33±0.17	169	45.6
-2.5 < $T_a \leq$ 2.5	+0.28±0.27	0.21±0.19	0.49±0.22	53	8.5
2.5 < $T_a \leq$ 7.5	+0.16±0.56	0.72±0.68	0.88±0.62	52	9.1
7.5 < $T_a \leq$ 12.5	-0.45±0.65	2.26±1.32	1.81±1.03	63	10.5
12.5 < $T_a \leq$ 17.5	-0.67±0.85	3.74±1.40	3.08±1.06	90	15.2
17.5 < $T_a \leq$ 22.5	-0.80±0.58	4.35±1.32	3.55±1.07	86	9.8
T_a > 22.5	-0.59±0.52	5.15±0.59	4.56±0.74	12	1.3

5.4.5 Temperature- and light limitation of GPP_{POT}

During the measurement period, GPP_{POT} was mainly temperature-limited in late winter (until early May) with cold T_a suppressing GPP despite high SW_{in} (Fig. 5.5d & Fig. 5.7a). With warming T_a in June 2016, the fraction of days when GPP_{POT} was T_a-limited dropped to 33% compared to 94% in May 2016 (Fig. 5.7a). In July 2016, GPP_{POT} was co-limited by T_a and SW_{in} on 74% of days (Fig. 5.7b). Light limitation of GPP was rare until July ($\leq$ 10% of days) and became more frequent in August and October with 19% and 23% of days, respectively (Fig. 5.7c). From July to September, the fraction of days with T_a-limited GPP_{POT} increased again from 13% to 87%.

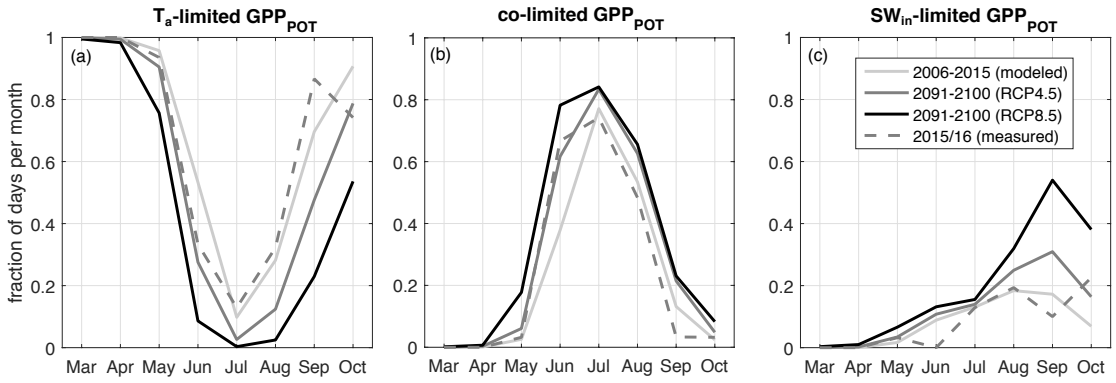

Figure 5.7 – Monthly fraction of days when potential gross primary productivity (GPP_{POT}) is limited by **(a)** air temperature (T_a), **(c)** incoming shortwave radiation (SW_{in}), or **(b)** co-limited by both variables. The dashed line shows GPP_{POT}-limitation for T_a and SW_{in} measured at Scotty Creek between August 2015 and July 2016. Solid lines indicate ensemble mean GPP_{POT}-limitation for the recent and projected modelled T_a and SW_{in} from six combinations of four regional climate and three Earth system models.

Until the end of the 21st century (2091-2100), mean daily T_a between April and September at Scotty Creek is projected to increase by 2.5 °C for the RCP4.5 or by 5.2 °C for the RCP8.5 scenario compared to the period 2006 to 2015 (Fig. 1.4a-d). In contrast, mean daily SW_{in} for the same period is projected to decrease by 3 W m^{-2} (RCP4.5) and by 6.6 W m^{-2} (RCP8.5), most likely due to increased cloudiness as indicated by concurrent increases in precipitation (Fig. 1.4e-l). These projected changes consistently reduce T_a-limitation of GPP_{POT} between April and October. The largest reduction in the frac-

tion of days with T_a-limited GPP_{POT} is expected in June and September with -26% and -22% for the RCP4.5 scenario and with -45% and -47% for the RCP8.5 scenario, respectively. The largest increase in days with colimited GPP_{POT} is projected for June (+24% [RCP4.5] and +40% [RCP8.5]). Increases in the fraction of days with SW_{in}-limited GPP_{POT} are most pronounced in September with 14% (RCP4.5) and 37% (RCP8.5). Between March and July, projected increases in days with SW_{in}-limited GPP_{POT} are smaller than 10% (RCP4.5 and RCP8.5).

5.4.6 Projected changes in GPP_{MOD}, ER_{MOD}, and NEE_{MOD}

By the end of the 21st century, the projected changes in T_a and SW_{in} enhance GPP_{MOD} with maximum increases in May (Fig. 5.8). For the RCP 8.5 scenario, the projected increase in annual GPP_{MOD} is about twice as large as for the RCP 4.5 scenario. However, the increase in annual ER_{MOD} for the RCP 8.5 scenario is 2.5 times larger than for the RCP 4.5 scenario due to warmer T_a.In contrast to GPP_{MOD}, monthly ER_{MOD} is expected to increase most strongly in August and July. The differences in the timing of increases in GPP_{MOD} and ER_{MOD} result in a more negative NEE_{MOD} early in the summer and less negative NEE_{MOD} in July – the warmest summer month. Annual NEE_{MOD} switches its sign from -9±39 g C-CO_2 m^{-2} (±95% CI; 2006-2015) to +16±42 g C-CO_2 m^{-2} (2091-2100) for the RCP 4.5 scenario and becomes a significant net CO_2 m source with +94±54 g C-CO_2 m^{-2} (2091–2100) for the RCP 8.5 scenario. Similar annual NEE_{MOD} for the wetland (i.e., NEE_{MOD} derived from GPP_{WET} and ER_{WET}) was modeled with projected annual NEE_{MOD} (2091-2100) of -9±27 and +60±31 g C-CO_2 m^{-2} for the RCP 4.5 and the RCP 8.5 scenario, respectively (Fig. IV.3). While climatic changes both in winter and summer contribute

While climatic changes both in winter and summer contribute to this change in annual NEE_{POT_m}, the bulk of the reduction occurs during the summer months (May to September) for the RCP8.5 scenario (69 %) and in the winter months (October to April) for the RCP4.5 scenario (68 %).

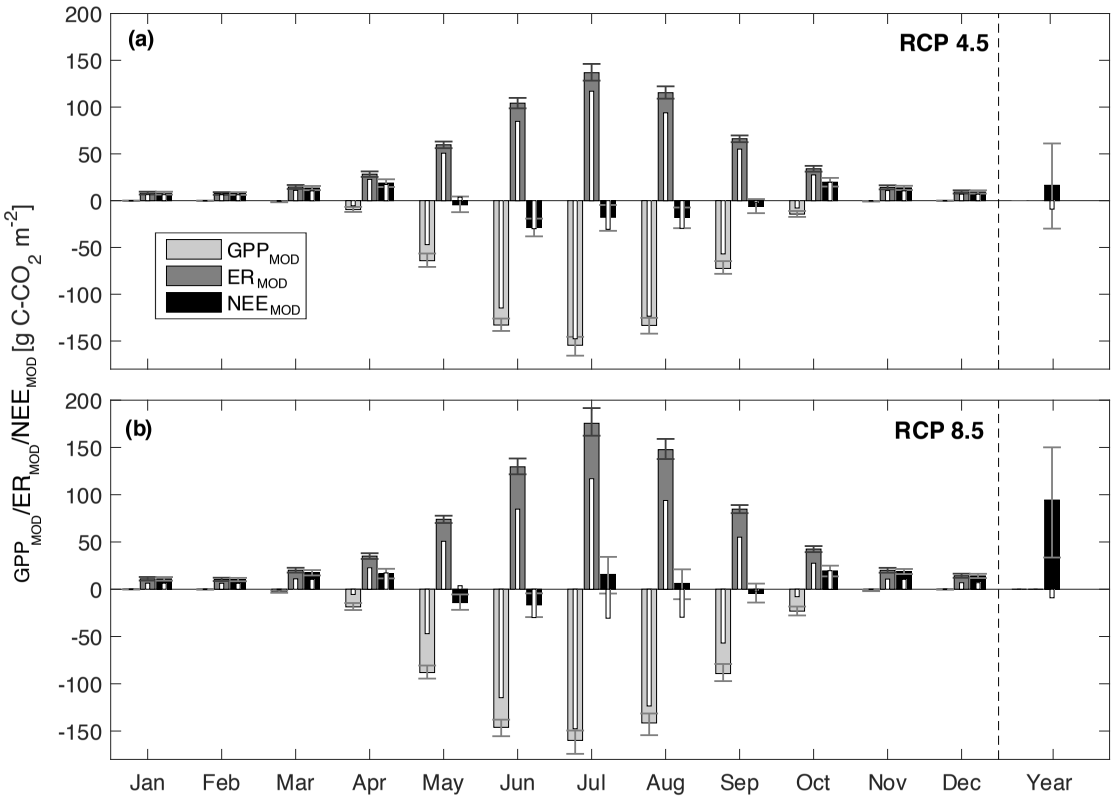

Figure 5.8 – Projections (2091–2100) of monthly modeled gross primary productivity (GPP_{MOD}), ecosystem respiration (ER_{MOD}), and net ecosystem carbon dioxide exchange (NEE_{MOD}) for the landscape at Scotty Creek **(a)** for the RCP 4.5 and **(b)** for the RCP 8.5 scenarios. For comparison, narrow white bars show recent (2006–2015) GPP_{MOD}, ER_{MOD}, and NEE_{MOD}. Error bars indicate uncertainties (95 % confidence intervals) in the GPP and ER model.

5.5 Discussion

5.5.1 Indirect thaw-induced climate change impact on carbon dioxide fluxes

At Scotty Creek, both half-hourly net CO_2 uptake during the day and net CO_2 release during the night were larger for the boreal forest-wetland landscape compared to the wetland (Fig. 5.2). However, half-hourly NEE_{LAND} differed more from NEE_{WET} with increasing wetland contributions to landscape flux footprints. In contrast, sensible and latent heat (see Chapter 3) and methane fluxes (see Chapter 4) were found to scale with wetland contributions in previous studies at Scotty Creek. An analysis of mean flux footprint contributions from forest-wetland transition zones revealed that these contributions were about six times larger for landscape than for wetland tower flux footprints (Fig. 5.1c). The transition zones with higher soil moisture and warmer soil temperatures (*Baltzer et al.*, 2014; *Bubier et al.*, 1995) may be characterized by larger GPP and ER compared to the interior of the wetlands and to the forests, both characterized by drier surface soils. Such spatial patterns of GPP and ER have previously been observed in similar permafrost peatlands using chamber methods (*Myers-Smith et al.*, 2007; *Turetsky et al.*, 2002; *Wickland et al.*, 2006). Methane fluxes may be more uni- form across the wetland as these are more sensitive to variations in water table position compared to variations in surface soil moisture (e.g., *Bubier et al.*, 1995; *Kettunen*, 2003). In contrast, the productivity of the dominant plant genus in the wetland, *Sphagnum* spp., is strongly controlled by surface moisture (e.g., *Schipperges and Rydin*, 1998), potentially explaining the differing spatial patterns of NEE and methane fluxes.

Similar findings were reported for a thawing tundra landscape, where both GPP and ER of actively thawing patches within the landscape were larger than the integrated landscape GPP and ER (*Belshe et al.*, 2012). Permafrost thaw increases the availability of nitrogen (*Finger et al.*, 2016), increases surface soil moisture, and induces vegetation shifts toward more aquatic species (*Camill*, 1999a; *Camill et al.*, 2001), potentially enhancing both productivity and respiration in the transition zones. Compared to the permafrost-free wetland, the larger extent of actively thawing transition zones in the boreal forest-wetland landscape may therefore cause larger GPP_{LAND} and ER_{LAND} (Fig. 5.2).

In contrast to ΣGPP and ΣER, annual ΣNEE_{LAND} and ΣNEE_{WET} did not differ significantly significantly at Scotty Creek (Fig. 5.3), suggesting that thaw-induced wetland expansion and forest loss might have a negligible short-term impact on ΣNEE. The long-term negative ΣNEE (i.e., net CO_2 uptake) is a major component of peatland C budgets in addition to the typical C losses due to methane emissions and due to net lateral export of dissolved organic C (e.g., *Roulet et al.*, 2007). At Scotty Creek, wetlands emit 12 g C-CH_4 m^{-2} per year as opposed to 6 g C-CH_4 m^{-2} at the landscape level (see Chapter 4), suggesting a similar wetland and landscape net C uptake of -12 g C m^{-2} yr^{-1} (-24 g C-CO_2 m^{-2} + 12 g C-CH_4 m^{-2}) and -14 g C m^{-2} yr^{-1} (-20 g C-CO_2 m^{-2} + 6 g C-CH_4 m^{-2}), respectively [excluding lateral export of dissolved organic C (DOC)]. For a boreal peatland landscape in the discontinuous permafrost zone of Manitoba, *Moore* (2003) reports small annual DOC exports between 1.7 and 3.2 g C m^{-2} yr^{-1}. If DOC exports at Scotty Creek are of a similar magnitude, a current net C uptake of approximately 10 g C m^{-2} yr^{-1} can be expected. A multisite synthesis study reports similar long-term C accumulation rates for boreal permafrost peatlands [14 g C m^{-2} yr^{-1}] and for permafrost-free bogs [18 g C m^{-2} yr^{-1}] (*Treat et al.*, 2016). Similarly, growing-season NEE was not significantly different across a thaw chronosequence from a forested permafrost peat plateau to a collapse-scar bog in Alaska (*Johnston et al.*, 2014). For a permafrost peatland landscape in northern Manitoba, aboveground net primary production of permafrost peat plateaus and of collapse-scar bogs was similar, but a twofold increase in the accumulation of peat was observed following thaw (*Camill et al.*, 2001). Post-thaw increases in C accumulation have been reported for several thawing permafrost peatlands in Manitoba, Saskatchewan, Alberta, and Alaska (*Camill*, 1999b; *Jones et al.*, 2013; *Turetsky et al.*, 2000, 2007).

However, enhanced decomposition of thawed forest peat has also been shown to exceed increased C accumulation rates in near-surface collapse-scar bog peat, inducing a rapid post-thaw net C loss (*O'Donnell et al.*, 2012). Particularly transition zones may be subject to rapid net C losses, before they slowly return to a net C sink after about a decade (*Jones et al.*, 2016). Our findings suggest that thawing boreal forest-wetland landscapes can still act as net CO_2 sinks - and most likely as net C sinks - under the

current climate. The continuing net CO_2 sink may be the result of integrating large areas with small net CO_2 uptake (e.g., forested permafrost plateaus and interior of permafrost-free wetlands) and small areas with potentially large net CO_2 loss (e.g., recently thawed transition zones). While the thaw-induced wetland expansion may affect long-term C cycle dynamics through its effect on regional hydrology (*Connon et al.*, 2014), species-specific productivity (*Camill et al.*, 2001), and fire regimes (*Camill et al.*, 2009), the immediate indirect climate-warming impact of such land cover change on landscape NEE appears to be small.

5.5.2 Direct climate change impacts on carbon dioxide fluxes

In contrast to the small indirect thaw-induced climate change impact on NEE, direct climate change effects appear to be larger and may depend strongly on the future CO_2 emission trajectories as represented by RCPs (Fig. 5.8). At Scotty Creek, early summer NEE_{MOD} increases with warming T_a, but decreases later in the summer. Such a seasonal pattern is supported by multi-year observations of NEE at other northern and alpine ecosystems (*Huxman et al.*, 2003; *Piao et al.*, 2008). Mid-summer GPP is often light-saturated and warmer summer T_a only marginally enhances plant productivity. ER is mainly temperature-limited (in the absence of moisture stress) and warmer mid-summer T_a reduces NEE by enhancing ER (*Huxman et al.*, 2003). In a warmer climate with more hot summer days (Fig. 5.5a), this increase in ER may eventually exceed GPP (*Runkle et al.*, 2013). At the tree level, increased white spruce tree-ring growth in Alaska has been related to warmer spring temperatures for some individuals but also to decreased growth in response to warmer summer temperatures for other individuals (*Wilmking et al.*, 2004). Similar to this study, recent tree-ring and modeling analyses highlight the negative impacts of warmer summer T_a - and an associated increase in autotrophic respiration - on net primary productivity of black spruce forests (*Girardin et al.*, 2016). Additionally, warmer summer T_a may accelerate evapotranspiration rates, decrease moisture availability, and enhance atmospheric water demand, potentially slowing down GPP and/or ER during peak growing season (e.g., *Barber et al.*, 2000; *Kljun et al.*, 2007; *Novick et al.*, 2016).

In fall, light-limitation of GPP is more frequent than in spring (*Niu et al.*, 2011, Fig. 5.7), potentially explaining the larger spring response in GPP_{MOD} to warmer T_a. For a subalpine forest, *Huxman et al.* (2003) found two NEE minima in early and late summer with a reduction in net CO_2 uptake in mid-summer. Here, we observed only one NEE minimum in July for the current seasonal NEE pattern at Scotty Creek. However, similar to *Huxman et al.* (2003), projected NEE_{MOD} is characterised by two minima in June and August for the RCP4.5 scenario. In the RCP8.5 scenario, the NEE_{MOD} minima in early and late summer are even more pronounced (Fig. 5.8).

In a recent modeling synthesis study, *McGuire et al.* (2016) found that moderate warming in the northern circumpolar permafrost region increased GPP, and vegetation C stocks, but decreased soil C stocks over a 50-year time period in most ESMs. Atmospheric inversion models indicate an increasing net CO_2 sink in the boreal zone for the period 1985 to 2012 (*Welp et al.*, 2016, ; 50° - 60° N). These results are supported by site-level NEE measurements for temperate and boreal forests indicating that earlier spring onset (i.e., warmer T_a) consistently increases GPP, and to a lesser extent ER (*Kljun et al.*, 2007; *Richardson et al.*, 2009, 2010). However, the positive productivity response of evergreen coniferous forests appears to be smaller compared to deciduous forests (*Richardson et al.*, 2010; *Welp et al.*, 2007). In a boreal forest ecosystem in the sporadic permafrost zone, longer growing seasons did not increase net CO_2 uptake as the positive productivity response was offset by enhanced respiration (*Dunn et al.*, 2007). In a boreal forest warming experiment, bud burst of black spruce trees occurred earlier and greater shoot lengths were observed (*Bronson et al.*, 2009). The increase in photosynthetic tissue may therefore enhance aboveground net primary productivity, even in the absence of changes in light-saturated photosynthesis and foliage respiration per m^2 of foliage (*Bronson and Gower*, 2010). Concurrent observations of decreases in fine root net primary productivity may, however, result in unchanged total net primary productivity (*Bronson et al.*, 2008).

Availability of organic C in permafrost peatland landscapes, such as Scotty Creek, is not limited (*Treat et al.*, 2016). Warmer T_a may therefore gradually increase ER while the dominant temperature limitation of GPP may switch to a more dominant light lim-

itation, limiting the productivity benefits of warming T_a (Fig. 5.5 and Fig. 5.6). Air temperature effects on ER have been shown to exert a strong control on interannual variation of boreal forest NEE, exceeding the impacts of variations in GPP (*Ueyama et al.*, 2009, 2014). In boreal forests, the NEE response to T_a often follows a parabolic curve with a temperature optimum of NEE followed by decreasing net CO_2 uptake with T_a above this threshold (*Grant et al.*, 2009; *Niu et al.*, 2011, Fig. 5.5a). At Scotty Creek, this T_a threshold appears to be around 15 °C, slightly warmer than the 11-year mean T_a optimum of NEE of 11±2 °C (± one standard deviation) for a boreal forest in the sporadic permafrost zone of northern Manitoba (*Niu et al.*, 2012). It should be noted that, in the long-term, the NEE temperature optimum might change with thermal adaptation of the vegetation or species composition shifts (*Yuan et al.*, 2011). In a warmer climate, the T_a threshold is likely to be exceeded more often during the summer (Fig. 5.5a), potentially decreasing summertime net CO_2 uptake. Our results suggest that, with continuously rising T_a, increases in net CO_2 uptake of boreal forest-wetland landscapes may therefore eventually slow down, and their long-term net CO_2 uptake may potentially decrease depending on the climate-warming scenario.

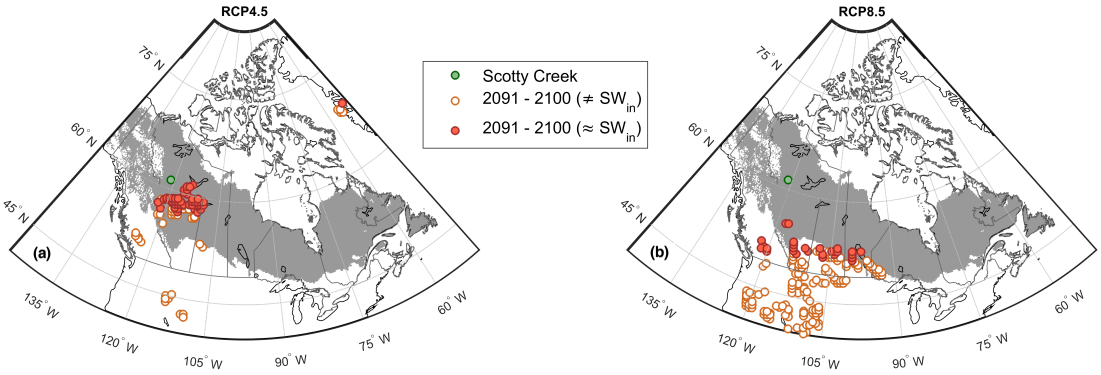

Figure 5.9 – Current climate analogues (2006-2015) of the projected end-of-21st-century (2091-2100) climate at Scotty Creek **(a)** for the RCP4.5 scenario and **(b)** for the RCP8.5 scenario. Circles show all climate analogues from six different regional/global climate model combinations. The green circle indicates the location of Scotty Creek. Orange circles show locations of current climates similar to the projected climate for Scotty Creek ($\pm$10 % difference in mean annual precipitation and $\pm$0.5 °C of mean annual air temperature). Red circles indicate locations where, additionally, differences in annual incoming shortwave radiation (SW_{in}) are $\pm$30 %. Gray shaded area is the current extent of the boreal biome (data from *Brandt*, 2009).

A decreasing potential of boreal forest-wetland landscapes to sequester CO_2 in a warmer climate is supported by a projected C loss at the southern edge of the boreal zone where ecosystems with low potential for long-term C accumulation are expected to replace current boreal organic C-rich ecosystems in a warmer climate (*Koven et al.*, 2013). A diminishing potential net CO_2 uptake may 'push' the current C-accumulating landscapes to an unstable state increasing the potential for an abrupt transition to landscapes with lower C stocks and a loss of their CO_2 sink function (*Scheffer et al.*, 2012). For the RCP4.5 scenario, current climates (i.e., mean annual T_a and total precipitation) similar to the projected end-of-the-century climate of Scotty Creek are found within the boreal biome in northern Alberta. For the RCP8.5 scenario, similar climates are currently found at the limit or south of the boreal biome in Canada and the northwestern United States (Fig. 5.2). In contrast to changes in T_a and precipitation, SW_{in} is more strongly bound to latitude. The limited duration of the period providing sufficient light for photosynthetic CO_2 uptake combined with warmer T_a and more precipitation is therefore likely to increase ER more than GPP, particularly for the RCP8.5 scenario (Fig. 5.8). A shift from permafrost peatland landscapes with large organic C stocks [mean of 106±45 kg m^{-2} [± one standard deviation] for forested peat plateaus [n = 158]; 117±65 kg m^{-2} for collapse-scar bogs [n = 52]; data from *Treat et al.* (2016)] to landscapes with low C stocks would result in large net CO_2 emissions. Our results suggest that the magnitude of these emissions will strongly depend on future anthropogenic CO_2 emission pathways (Fig. 5.8).

5.5.3 Comparison with Earth system models and CO_2 flux inversion modeling

A comparison with five end-of-21st-century ESM projections of NEE (from the Coupled Model Intercomparison Project [from the Coupled Model Intercomparison Project (CMIP5; `http://cmip-pcmdi.llnl.gov/cmip5/`); *Friedlingstein et al.* (2014b); Fig. IV.4] shows that three of five ESMs project NEE changes similar to our findings. More specifically, for the southern Taiga Plains region, no ESM shows significant changes in mean annual NEE for the moderate RCP4.5 scenario (two-sample t-test; α = 0.05; n = 10). For the warmer RCP8.5 scenario, three of the five ESMs indicate de-

creases in net CO_2 uptake (7-36 g C-CO_2 m^{-2} less negative NEE with one ESM showing a significant decrease; $p = 0.04$; $n = 10$; see Fig. IV.4). Two ESMs even indicate a switch from a net CO_2 sink to a net CO_2 source. Similar to our study, all ESMs project the largest monthly increase in net CO_2 uptake between April and June (except for July in the RCP8.5 scenario of one ESM) and smaller increases or even decreases in net CO2 uptake later in summer.

For the period 2006 to 2015, all five ESMs indicate a mean net CO_2 sink for the southern Taiga Plains region with differences of less than 20 g C-CO_2 m^{-2} yr^{-1} to measured annual NEE at Scotty Creek (except for a larger difference for one ESM; Fig. IV.5). Compared to the annual landscape NEE of -20 g C-CO_2 m^{-2} yr^{-1} at Scotty Creek, global CO_2 flux inversions (1° x 1° resolution, CarbonTracker, version CT2015; *Peters et al.* (2007), with updates documented at `http://carbontracker.noaa.gov`) suggest a mean annual NEE (2006 - 2015) of -39±52 g C-CO_2 m^{-2} yr^{-1} [± one standard deviation] with a similar monthly NEE seasonality and magnitude (Fig. IV.4a). However, four out of five ESMs overestimate the maximum monthly net CO_2 uptake in the summer and the maximum monthly net CO_2 loss in the winter. The ESMs simulate both direct and indirect climate change effects on NEE, but their NEE response may vary due to differing representations of land surface processes (e.g., dynamic vegetation models, phenology, CO_2 fertilization, nutrient dynamics) (e.g., *Friedlingstein et al.*, 2014b; *Wieder et al.*, 2015). Disentangling the individual contributions from these processes to diverging NEE projections is difficult due to the complex interactions between the individual model components (e.g., *Friedlingstein et al.*, 2014b). However, an improved understanding of temperature- and light-limitation of NEE may help reducing the wide spread in modeled boreal landscape NEE response to climate change and minimize the deviation between measured and modeled seasonality of NEE.

5.5.4 Potential responses of ecosystem functioning to a changing climate

How vegetation productivity and respiration respond to changes in temperature and light may be affected by factors other than shifts in landscape and ecosystem composition and structure. Rising atmospheric CO_2 concentrations and the related fertilization

effect on plant productivity may stimulate and enhance GPP (*McGuire et al.*, 2016). This CO_2 fertilization effect could directly increase GPP through its positive impact on maximum GPP (*Ueyama et al.*, 2016), favoring a larger potential for net CO_2 uptake than projected in this study. However, the magnitude of the CO_2 fertilization effect in boreal forests remains poorly constrained: both no productivity response (*Kroner and Way*, 2016) and a positive response was observed (*Tjoelker et al.*, 1998) in CO_2 fertilization experiments of Norway spruce (*Picea abies*) and black spruce seedlings. A small, positive GPP response of 0.16 % ppm^{-1} (2002-2014) was estimated for an Alaskan black spruce forest (*Ueyama et al.*, 2016). Net primary productivity, the balance between GPP and autotrophic respiration, of about half of the black spruce forests in North America (south of 60° N) was projected to decline at the end of the 21st century in a modeling study, despite a positive CO_2 fertilization effect on GPP (*Girardin et al.*, 2016). For *Sphagnum* spp. and vascular bog species, only small or negative CO_2 effects on productivity were reported (*Berendse et al.*, 2001; *Heijmans et al.*, 2002). To some extent, plants can acclimate to warmer T_a by modifying their photosynthetic and respiratory apparatus. In warming and CO_2 enrichment experiments, the thermal optimum of light-saturated net CO_2 uptake of both Norway spruce and black spruce seedlings increased in the warming treatments while leaf respiration was suppressed. At the same time, light-saturated net CO_2 uptake was found to decrease for the warmest treatments (+8 °C) (*Kroner and Way*, 2016; *Way and Sage*, 2008). A better constraint of the impacts of CO_2 fertilization and thermal acclimation on the productivity of boreal plant species is therefore needed to fully understand the response of boreal forest-wetland landscape CO_2 fluxes to climate change.

Our focus on meteorological controls (temperature and light) of GPP only constrains the GPP_{MOD} response given no other limiting factors. Actual GPP, however, may be reduced by additional environmental limitations. For example, earlier spring onset in boreal and temperate forests has been observed to decrease peak summer productivity due to soil moisture deficits later in the summer (*Buermann et al.*, 2013; *Wolf et al.*, 2016). Particularly in late summer and fall, soil moisture deficits can add another environmental constraint on GPP (*Niu et al.*, 2011). In peatlands, fluctuating water levels

may also modify the temperature-sensitivity of heterotrophic soil respiration (e.g., *Silvola et al.*, 1996) and affect GPP (e.g., *Chivers et al.*, 2009). Changes in net primary productivity may alter C substrate availability to soil microbes through changes in litter fall (*Beier et al.*, 2008; *Bond-Lamberty et al.*, 2004), and changes in GPP may affect autotrophic respiration through the allocation of photosynthates (*Janssens et al.*, 2001). Such indirect effects of ecosystem acclimation may modify the overall temperature sensitivity of ER and, therefore, additionally affect NEE responses to a changing climate. The temperature-response of ER in a warmer climate could also be attenuated if increasing net C losses diminish the fraction of labile organic C, exposing more recalcitrant organic matter from deeper peat layers, or induce temperature- related changes in soil microbial communities (*Bradford et al.*, 2008; *Hogg et al.*, 1992). Understanding how these environmental controls interact with the warming-related shifts in the seasonality of GPP and ER will help constraining the NEE response to a warmer climate.

Here, we show that thaw-induced wetland expansion and associated boreal forest loss appears to have negligible indirect climate change effects on landscape net CO_2 uptake of $\sim$20 g C-CO_2 m^{-2} yr^{-1}. However, even without moisture stress, potential net CO_2 uptake of boreal forest-wetland landscapes is likely to decline by the end of the 21^{st} century due to direct climate change impacts of changing meteorological forcing. This projected reduction is about five times larger for a high climate-warming scenario (103 g C-CO_2 m^{-2} yr^{-1}) compared to a moderate scenario (25 g C-CO_2 m^{-2} yr^{-1}). In an exceedingly warmer climate, the recently observed increasing net CO_2 uptake of the boreal biome may therefore turn into a decreasing net CO_2 sink during the 21st century, reducing the ability of boreal landscapes to sequester atmospheric CO_2.

CHAPTER 6

CONCLUSIONS

In this thesis, I have characterized how widespread permafrost thaw-induced wetland expansion (and associated boreal forest loss) modifies land-atmosphere interactions in the southern Taiga Plains. Changing landscape structure and composition in boreal landscapes alters the land surface response to meteorological forcing and affects regional and global climates. Thaw-induced land cover change induces two opposite climate impacts: a biophysical regional atmospheric cooling and wetting and a biogeochemical global warming effect. This thesis quantifies these first-order effects of thaw-induced land cover change and may serve as a baseline for further investigations of interactions and feedbacks of and between biophysical and biogeochemical climate impacts (i.e., second-order effects). In the future, a more detailed understanding of these second-order effects could be gained from modeling experiments.

In the Taiga Plains, permafrost thaw was found to be equally important to wildfire as driver of boreal tree cover dynamics (chapter 1). Particularly in the southern Taiga Plains, where permafrost is sporadic, permafrost thaw and concurrent surface subsidence leads to declining tree cover. The boreal forest loss causes a widespread replacement of forest by wetlands in the region and the rate of permafrost thaw is expected to further increase in an increasingly warmer climate. Despite the importance of these changes for boreal landscape structure and composition, thaw-induced land cover change impacts on land-atmosphere interactions are still poorly constrained. In contrast, wildfire impacts on land-atmosphere interactions have been widely studied in the past. To fill this knowledge gap, I have presented a detailed analysis of thaw-induced land cover change impacts on land-atmosphere interactions.

Thaw-induced wetland expansion was found to only slightly decrease the sum of sensible and latent heat flux during the growing season (chapter 2). However, I demonstrate that particularly the increasing partitioning of available energy to latent - instead of to sensible heat - causes an atmospheric cooling effect in the summer (Fig. 6.1).

This change in energy partitioning is estimated to induce a decrease in maximum daily summer air temperatures between 1-2 °C for a hypothetical permafrost-free, all-wetland landscape. At the same time, maximum daily summer water vapor mixing ratios were found to increase by 2 mmol mol^{-1}. In the summer, altered eco-physiological and aerodynamic surface properties are the main drivers of these air temperature and humidity changes. In contrast, particularly in late winter, strong differences in the albedo of snow-covered boreal forest and wetland cause 3-4 °C cooler wintertime air temperatures for the all-wetland landscape. These biophysical climate impacts may attenuate regional warming trends at the southern limit of permafrost in North America and modify regional precipitation dynamics.

In contrast to the biophysical cooling effect of thaw-induced land cover change, wetland expansion is likely to have a biogeochemical climate warming effect (chapter 3, Fig. 6.1). I demonstrate how increasing wetland extent at Scotty Creek enhances growing season landscape CH_4 emissions and quantify the thaw-induced increase in landscape CH_4 emissions by combining landscape and wetland net CH_4 flux measurements with current wetland expansion rates. While boreal forest-wetland landscapes usually act as long-term net CO_2 sinks to the atmosphere, their climate cooling effect is unlikely to balance the climate warming effect of increasing CH_4 emissions through the 21st century. The typical long-term net CO_2 uptake of boreal North American peatlands between 49 and 157 g CO_2 m^{-2} yr^{-1} is too small to balance the estimated growing season CH_4 emission increase of 0.034 ± 0.007 g CH_4 m^{-2} yr^{-1} as indicated by a positive net radiative greenhouse gas forcing throughout the 21st century.

Net CO_2 flux measurements at the wetland- and the landscape-level at Scotty Creek indicate that a rapidly thawing boreal forest-wetland landscape can still act as a net CO_2 sink (chapter 5). While the component fluxes of NEE (i.e., GPP and ER) seem to be enhanced by thawing permafrost during the forest-to-wetland transition, changes in NEE itself are small (Fig. 6.1). Thus, indirect climate change effects related to thaw-induced land cover change seem to be negligible. In contrast, warmer air temperatures and reduced incoming shortwave radiation, as projected for the end of the 21st century by various Earth system models, are expected to impact NEE more as modeled ER in-

creases exceed GPP increases. These direct climate change impacts on NEE were found to be about five times larger for a high warming scenario compared to a moderate warming scenario (Fig. 6.1). The combination of direct and indirect climate change impacts is therefore unlikely to lead to an increased long-term net CO_2 uptake, supporting the findings of an overall net positive greenhouse gas forcing from thaw-induced wetland expansion (Fig. 6.1).

6.1 Future directions

In this thesis, I highlight the importance of widespread thaw-induced wetland expansion for land-atmosphere interactions and characterize its climate impacts. To fully quantify the related net regional and global climate impacts, improved circumpolar projections of the extent of these land cover changes are needed. In this regard, recent remote sensing efforts to map treed boreal peatlands (*Thompson et al.*, 2016) and areas of increased vulnerability to thermokarst development (*Olefeldt et al.*, 2016) could provide important information for global Earth system models. Modeling post-thaw surface subsidence in these ice-rich permafrost regions (e.g., *Lee et al.*, 2014) is a first step to better representing thaw-induced land cover change in such models.

Second-order effects of thaw-induced land cover changes (e.g., long-term hydrological change) could be assessed with fully-coupled land-atmosphere models. Potential climate feedback mechanisms could also be quantified with such models as they account for the multitude of interactions between ecological, hydrological, and atmospheric processes. For example, it remains unknown if the increase in high-latitude precipitation and water availability (e.g., *Lawrence et al.*, 2015) is sufficient to provide enough moisture to supply further expansion of wetlands and how thaw-induced changes in catchment morphology affect regional water balances in the boreal permafrost zone (e.g., changing runoff dynamics, *Connon et al.*, 2014).

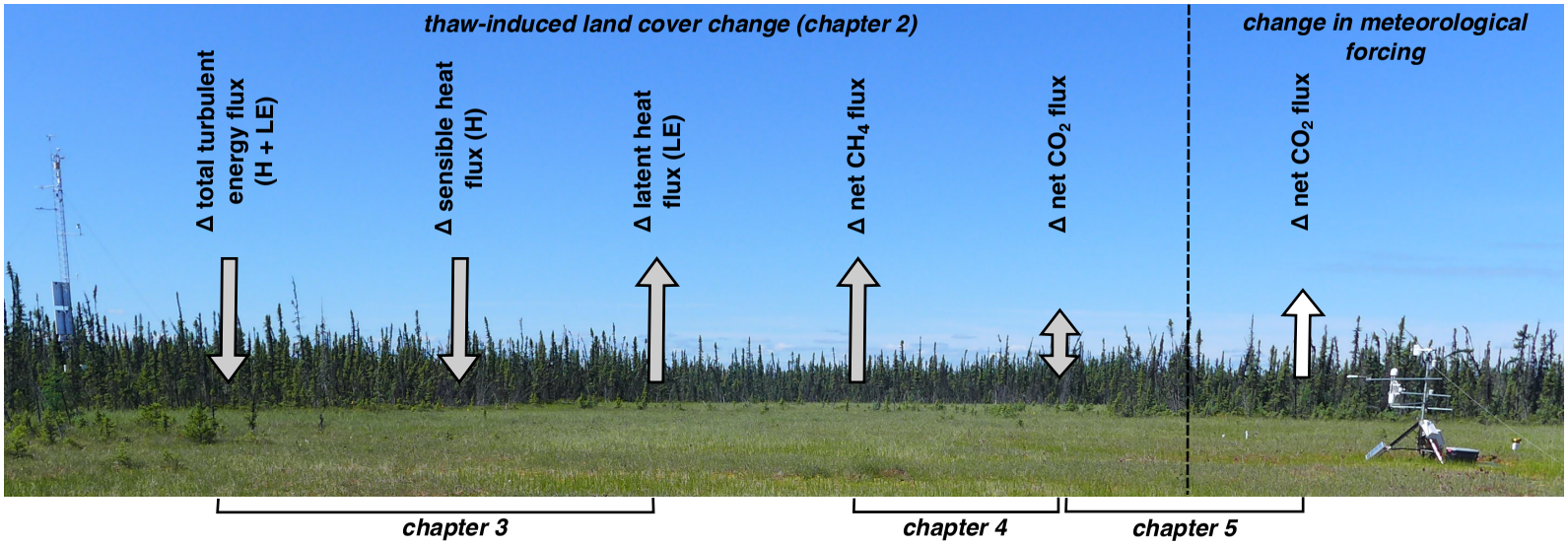

Figure 6.1 – Permafrast-thaw induced land cover change impacts on land-atmosphere interactions in the southern Taiga Plains (grey arrows). Upward pointing arrows indicate an increase in the respective flux with permafrost-free wetland expansion (downward pointing arrows indicate a decrease). The white arrow indicates the direct climate change effect of changing meteorological conditions on net CO_2 fluxes in a warming climate.

The results of this thesis provide an important opportunity to improve and evaluate land-atmosphere model performance for rapidly thawing boreal forest-wetland landscape. Fully-coupled Earth system models with an improved representation of land-atmosphere interactions for boreal permafrost landscapes could then be used to assess the net impacts of thaw-induced land cover change on regional and global climates. It remains, however, challenging to define a metric accounting for the differing scales of biophysical and biogeochemical climate impacts of climate-induced land cover change (*Chapin et al.*, 2000). Net radiative forcing is a metric quantifying only global climate impacts related to radiative processes (e.g., effects of well-mixed greenhouse gases on longwave radiation), but non-radiative processes of land cover changes (e.g., changes in energy partitioning) can have pronounced impacts on regional climates (e.g., *Davin et al.*, 2007). Many ecological and atmospheric processes, such as plant growth, ecosystem respiration, and evapotranspiration respond to local-scale meteorological conditions (e.g., *Potter et al.*, 2013; *Scheffer et al.*, 2005). As land cover change may induce biophysical and biogeochemical climate impacts of opposite sign at contrasting scales, as shown in this thesis, the assessment of its net climate impact needs to account for such scale-discrepancy.

BIBLIOGRAPHY

Agriculture and Agri-Food Canada, Soil Landscapes of Canada. version 3.2, 2010.

Alkama, R., and A. Cescatti, Biophysical climate impacts of recent changes in global forest cover, *Science*, *351*(6273), 600–604, 2016.

Amiro, B., Estimating annual carbon dioxide eddy fluxes using open-path analysers for cold forest sites, *Agricultural and Forest Meteorology*, *150*, 1366–1372, 2010.

Amiro, B., et al., Carbon, energy and water fluxes at mature and disturbed forest sites, Saskatchewan, Canada, *Agricultural and Forest Meteorology*, *136*, 237–251, 2006.

Angstmann, J. L., B. E. Ewers, J. Barber, and H. Kwon, Testing transpiration controls by quantifying spatial variability along a boreal black spruce forest drainage gradient, *Ecohydrology*, *6*, 783–793, 2013.

Aylsworth, J. M., I. M. Kettles, and B. J. Todd, Peatland distribution in the Fort Simpson area, Northwest Territories with a geophysical study of peatland-permafrost relationship at Antoine Lake, in *Current Research, Part E*, chap. Paper 93-1, pp. 141–148. Geological Survey of Canada, 1993.

Bala, G., K. Caldeira, M. Wickett, T. J. Phillips, D. B. Lobell, C. Delire, and A. Mirin, Combined climate and carbon-cycle effects of large-scale deforestation, *Proceedings of the National Academy of Sciences*, *104*, 6550–6555, 2007.

Baldocchi, D., Measuring fluxes of trace gases and energy between ecosystems and the atmosphere - the state and future of the eddy covariance method, *Global Change Biology*, *20*, 3600–3609, 2014.

Baldocchi, D. D., Assessing the eddy covariance technique for evaluating carbon dioxide exchange rates of ecosystems: past, present and future, *Global Change Biology*, *9*, 479–492, 2003.

Baldocchi, D. D., and S. Ma, How will land use affect air temperature in the surface boundary layer? Lessons learned from a comparative study on the energy balance of an oak savanna and annual grassland in California, USA, *Tellus B*, *65*, 19994, 2013.

Baldocchi, D. D., J. Finnigan, K. Wilson, K. T. Paw U, and E. Falge, On measuring net ecosystem carbon exchange over tall vegetation on complex terrain, *Boundary-Layer Meteorology*, *96*, 257–291, 2000.

Baltzer, J. L., T. Veness, L. E. Chasmer, A. E. Sniderhan, and W. L. Quinton, Forests on thawing permafrost: fragmentation, edge effects, and net forest loss, *Global Change Biology*, *20*, 824–834, 2014.

Barber, V. A., G. P. Juday, and B. P. Finney, Reduced growth of Alaskan white spruce in the twentieth century from temperature-induced drought stress., *Nature*, *405*(6787), 668–673, 2000.

Barr, A., K. Morgenstern, T. Black, J. McCaughey, and Z. Nesic, Surface energy balance closure by the eddy-covariance method above three boreal forest stands and implications for the measurement of the CO_2 flux, *Agricultural and Forest Meteorology*, *140*, 322–337, 2006.

Beck, P. S. A., G. P. Juday, C. Alix, V. A. Barber, S. E. Winslow, E. E. Sousa, P. Heiser, J. D. Herriges, and S. J. Goetz, Changes in forest productivity across Alaska consistent with biome shift, *Ecology Letters*, *14*(4), 373–379, 2011a.

Beck, P. S. A., S. J. Goetz, M. C. Mack, H. D. Alexander, Y. Jin, J. T. Randerson, and M. M. Loranty, The impacts and implications of an intensifying fire regime on Alaskan boreal forest composition and albedo, *Global Change Biology*, *17*, 2853–2866, 2011b.

Beier, C., et al., Carbon and nitrogen cycles in European ecosystems respond differently to global warming, *Science of the Total Environment*, *407*, 692–697, 2008.

Beljaars, A. C. M., and A. A. M. Holtslag, Flux parameterization over land surfaces for atmospheric models, *Journal of Applied Meteorology*, *30*, 327–341, 1991.

Bellisario, L. M., J. L. Bubier, and T. R. Moore, Controls on CH_4 emissions from a northern peatland, *Global Biogeochemical Cycles*, *13*, 81–91, 1999.

Belshe, E. F., E. A. G. Schuur, B. M. Bolker, and R. Bracho, Incorporating spatial heterogeneity created by permafrost thaw into a landscape carbon estimate, *Journal of Geophysical Research: Biogeosciences*, *117*, G01026, 2012.

Berendse, F., et al., Raised atmospheric CO_2 levels and increased N deposition cause shifts in plant species composition and production in Sphagnum bogs, *Global Change Biology*, *7*, 591–598, 2001.

Betts, A. K., Land-surface-atmosphere coupling in observations and models, *Journal of Advances in Modeling Earth Systems*, *1*(4), 1–18, 2009.

Betts, A. K., and J. H. Ball, Albedo over the boreal forest, *Journal of Geophysical Research*, *102*(D24), 28901–28909, 1997.

Betts, A. K., M. L. Goulden, and S. C. Wofsy, Controls on Evaporation in a Boreal Spruce Forest, *Journal of Climate*, *12*, 1601–1618, 1999.

Betts, A. K., J. H. Ball, and J. McCaughey, Near-surface climate in the boreal forest, *Journal of Geophysical Research*, *106*(D24), 33529–33541, 2001.

Betts, R. A., Offset of the potential carbon sink from boreal forestation by decreases in surface albedo, *Nature*, *408*, 187–190, 2000.

Blanken, P. D., T. Black, P. Yang, H. H. Neumann, Z. Nesic, R. Staebler, G. den Hartog, M. D. Novak, and X. Lee, Energy balance and canopy conductance of a boreal aspen forest: Partitioning overstory and understory components, *Journal of Geophysical Research*, *102*(D24), 28915–289267, 1997.

Bonan, G. B., Forests and climate change: forcings, feedbacks, and the climate benefits of forests., *Science*, *320*(5882), 1444–1449, 2008.

Bonan, G. B., D. Pollard, and S. L. Thompson, Effects of boreal forest vegetation on global climate, *Nature*, *359*, 716–718, 1992.

Bond-Lamberty, B., C. Wang, and S. T. Gower, A global relationship between the heterotrophic and autotrophic components of soil respiration?, *Global Change Biology*, *10*, 1756–1766, 2004.

Bond-Lamberty, B., S. D. Peckham, D. E. Ahl, and S. T. Gower, Fire as the dominant driver of central Canadian boreal forest carbon balance, *Nature*, *450*(7166), 89–92, 2007.

Bousquet, P., et al., Contribution of anthropogenic and natural sources to atmospheric methane variability, *Nature*, *443*(7110), 439–43, 2006.

Bradford, M. A., C. A. Davies, S. D. Frey, T. R. Maddox, J. M. Melillo, J. E. Mohan, J. F. Reynolds, K. K. Treseder, and M. D. Wallenstein, Thermal adaptation of soil microbial respiration to elevated temperature, *Ecology Letters*, *11*(12), 1316–1327, 2008.

Brandt, J., The extent of the North American boreal zone, *Environmental Reviews*, *17*, 101–161, 2009.

Brandt, J. P., M. Flannigan, D. G. Maynard, I. Thompson, and W. J. A. Volney, An introduction to Canada's boreal zone: Ecosystem processes, health, sustainability, and environmental issues, *Environmental Reviews*, *21*, 207–226, 2013.

Bridgham, S. D., H. Cadillo-Quiroz, J. K. Keller, and Q. Zhuang, Methane emissions from wetlands: biogeochemical, microbial, and modeling perspectives from local to global scales, *Global Change Biology*, *19*, 1325–1346, 2013.

Bronson, D., S. T. Gower, M. Tanner, S. Linder, and I. Van Herk, Response of soil surface CO2 flux in a boreal forest to ecosystem warming, *Global Change Biology*, *14*, 856–867, 2008.

Bronson, D. R., and S. T. Gower, Ecosystem warming does not affect photosynthesis or aboveground autotrophic respiration for boreal black spruce, *Tree Physiology*, *30*(4), 441–449, 2010.

Bronson, D. R., S. T. Gower, M. Tanner, and I. Van Herk, Effect of ecosystem warming on boreal black spruce bud burst and shoot growth, *Global Change Biology*, *15*(6), 1534–1543, 2009.

Brown, D. R. N., M. T. Jorgenson, T. A. Douglas, V. E. Romanovsky, K. Kielland, C. Hiemstra, E. S. Euskirchen, and R. W. Ruess, Interactive effects of wildfire and climate on permafrost degradation in Alaskan lowland forests, *Journal of Geophysical Research: Biogeosciences*, *120*, 1619–1637, 2015.

Brown, J., O. Ferrians Jr., J. Heginbottom, and E. Melnikov, Circum-arctic map of permafrost and ground ice conditions, 2002.

Brown, S. M., R. M. Petrone, C. Mendoza, and K. J. Devito, Surface vegetation controls on evapotranspiration from a sub-humid Western Boreal Plain wetland, *Hydrological Processes*, *24*, 1072–1085, 2010.

Brutsaert, W., *Evaporation to the atmosphere*. Springer, Dordrecht, 1982.

Bubier, J., T. Moore, L. Bellisario, N. Comer, and P. Crill, Ecological controls on methane emissions from a northern peatland complex in the zone of discontinuous permafrost, Manitoba, Canada, *Global Biogeochemical Cycles*, *9*, 455–470, 1995.

Bubier, J., T. Moore, K. Savage, and P. Crill, A comparison of methane flux in a boreal landscape between a dry and a wet year, *Global Biogeochemical Cycles*, *19*, GB1023, 2005.

Buermann, W., P. R. Bikash, M. Jung, D. H. Burn, and M. Reichstein, Earlier springs decrease peak summer productivity in North American boreal forests, *Environmental Research Letters*, *8*, 024027, 2013.

Burton, P. J., C. Messier, G. F. Weetman, E. E. Prepas, W. L. Adamowicz, and R. Tittler, The current state of boreal forestry and the drive for change, in *Towards Sustainable Management of the Boreal Forest*, edited by P. J. Burton, C. Messier, D. W. Smith, and W. L. Adamowicz, p. 1046. NRC Research Press, Ottawa, Canada, 2003.

Burton, P. J., M. A. Parisien, J. a. Hicke, R. J. Hall, and J. T. Freeburn, Large fires as agents of ecological diversity in the North American boreal forest, *International Journal of Wildland Fire*, *17*, 754–767, 2008.

Camill, P., Patterns of boreal permafrost peatland vegetation across environmental gradients sensitive to climate warming, *Canadian Journal of Botany*, *77*, 721–733, 1999a.

Camill, P., Peat accumulation and succession following permafrost thaw in the boreal peatlands of Manitoba, Canada, *Écoscience*, *6*(4), 592–602, 1999b.

Camill, P., and J. S. Clark, Climate change disequilibrium of boreal permafrost peatlands caused by local processes., *The American Naturalist*, *151*(3), 207–22, 1998.

Camill, P., J. A. Lynch, J. S. Clark, J. B. Adams, and B. Jordan, Changes in biomass, aboveground net primary production, and peat accumulation following permafrost thaw in the boreal peatlands of Manitoba, Canada, *Ecosystems*, *4*, 461–478, 2001.

Camill, P., A. Barry, E. Williams, C. Andreassi, J. Limmer, and D. Solick, Climate-vegetation-fire interactions and their impact on long-term carbon dynamics in a boreal peatland landscape in northern Manitoba, Canada, *Journal of Geophysical Research*, *114*, G04017, 2009.

Camill, P., L. Chihara, B. Adams, C. Andreassi, A. Barry, S. Kalim, J. Limmer, M. Mandell, and G. Rafert, Early life history transitions and recruitment of Picea mariana in thawed boreal permafrost peatlands., *Ecology*, *91*(2), 448–59, 2010.

Chanton, J. P., P. H. Glaser, L. S. Chasar, D. J. Burdige, M. E. Hines, D. I. Siegel, L. B. Tremblay, and W. T. Cooper, Radiocarbon evidence for the importance of surface vegetation on fermentation and methanogenesis in contrasting types of boreal peatlands, *Global Biogeochemical Cycles*, *22*, GB4022, 2008.

Chapin, F. S., and A. M. Starfield, Time lags and novel ecosystems in response to transient climate change in arctic Alaska, *Climatic Change*, *35*, 449–461, 1997.

Chapin, F. S., et al., Arctic and boreal ecosystems of western North America as components of the climate system, *Global Change Biology*, *6*(S1), 211–223, 2000.

Chapin, F. S., et al., Role of land-surface changes in arctic summer warming, *Science*, *310*, 657–660, 2005.

Chapin, F. S., et al., Reconciling Carbon-cycle Concepts, Terminology, and Methods, *Ecosystems*, *9*, 1041–1050, 2006.

Chasmer, L., and C. Hopkinson, Threshold Loss of Discontinuous Permafrost and Landscape Evolution, *Global Change Biology*, 2016.

Chasmer, L., N. Kljun, A. Barr, A. Black, C. Hopkinson, H. McCaughey, and P. Treitz, Influences of vegetation structure and elevation on CO_2 uptake in a mature jack pine forest in Saskatchewan, Canada, *Canadian Journal of Forest Research*, *38*, 2746–2761, 2008.

Chasmer, L., C. Hopkinson, and W. Quinton, Quantifying errors in discontinuous permafrost plateau change from optical data, Northwest Territories, Canada: 1947-2008, *Canadian Journal of Remote Sensing*, *36*(S2), 211–223, 2010.

Chasmer, L., W. Quinton, C. Hopkinson, R. Petrone, and P. Whittington, Vegetation Canopy and Radiation Controls on Permafrost Plateau Evolution within the Discontinuous Permafrost Zone, Northwest Territories, Canada, *Permafrost and Periglacial Processes*, *22*, 199–213, 2011.

Chasmer, L., C. Hopkinson, T. Veness, W. Quinton, and J. Baltzer, A decision-tree classification for low-lying complex land cover types within the zone of discontinuous permafrost, *Remote Sensing of Environment*, *143*, 73–84, 2014.

Chivers, M. R., M. R. Turetsky, J. M. Waddington, J. W. Harden, and A. D. McGuire, Effects of experimental water table and temperature manipulations on ecosystem CO_2 fluxes in an Alaskan rich fen, *Ecosystems*, *12*, 1329–1342, 2009.

Christensen, T. R., N. S. Panikov, M. Oequist, B. H. Svensson, H. Nykänen, P. J. Martikainen, and H. Oskarsson, Factors controlling large scale variations in methane emissions from wetlands, *Geophysical Research Letters*, *30*, 10–13, 2003.

Christensen, T. R., M. Jackowicz-Korczyński, M. Aurela, P. Crill, M. Heliasz, M. Mastepanov, and T. Friborg, Monitoring the Multi-Year Carbon Balance of a Subarctic Palsa Mire with Micrometeorological Techniques, *AMBIO: A Journal of the Human Environment*, *41*, 207–217, 2012.

Cleveland, C. C., S. C. Reed, A. B. Keller, D. R. Nemergut, S. P. O'Neill, R. Ostertag, and P. M. Vitousek, Litter quality versus soil microbial community controls over decomposition: a quantitative analysis., *Oecologia*, pp. 283–294, 2013.

Connon, R. F., W. L. Quinton, J. R. Craig, and M. Hayashi, Changing hydrologic connectivity due to permafrost thaw in the lower Liard River valley, NWT, Canada, *Hydrological Processes*, *28*, 4163–4178, 2014.

Connon, R. F., W. L. Quinton, J. R. Craig, J. Hanisch, and O. Sonnentag, The hydrology of interconnected bog complexes in discontinuous permafrost terrains, *Hydrological Processes*, *29*, 3831–3847, 2015.

Dai, A., Characteristics and trends in various forms of the Palmer Drought Severity Index during 1900-2008, *Journal of Geophysical Research*, *116*, D12115, 2011.

Dang, Q.-L., H. A. Margolis, and G. J. Collatz, Parameterization and testing of a coupled photosynthesis-stomatal conductance model for boreal trees, *Tree Physiology*, *18*, 141–153, 1998.

Davidson, E. A., and I. A. Janssens, Temperature sensitivity of soil carbon decomposition and feedbacks to climate change., *Nature*, *440*, 165–173, 2006.

Davies-Barnard, T., P. J. Valdes, J. S. Singarayer, A. J. Wiltshire, and C. D. Jones, Quantifying the relative importance of land cover change from climate and land use in the representative concentration pathways, *Global Biogeochemical Cycles*, *29*, 842–853, 2015.

Davin, E. L., and N. de Noblet-Ducoudré, Climatic impact of global-scale Deforestation: radiative versus nonradiative processes, *Journal of Climate*, *23*, 97–112, 2010.

Davin, E. L., N. de Noblet-Ducoudré, and P. Friedlingstein, Impact of land cover change on surface climate: Relevance of the radiative forcing concept, *Geophysical Research Letters*, *34*, L13702, 2007.

Davy, R., and I. Esau, Global climate models' bias in surface temperature trends and variability, *Environmental Research Letters*, *9*, 114024, 2014.

de Arellano, J. V.-G., C. C. van Heerwaarden, and J. Lelieveld, Modelled suppression of boundary-layer clouds by plants in a CO_2-rich atmosphere, *Nature Geoscience*, *5*(10), 701–704, 2012.

DeBeer, C. M., H. S. Wheater, S. K. Carey, and K. P. Chun, Recent climatic, cryospheric, and hydrological changes over the interior of western Canada: a synthesis and review, *Hydrology and Earth System Sciences*, *20*, 1573–1598, 2016.

Desai, A. R., et al., Landscape-level terrestrial methane flux observed from a very tall tower, *Agricultural and Forest Meteorology*, *201*, 61–75, 2015.

Detto, M., N. Montaldo, J. D. Albertson, M. Mancini, and G. Katul, Soil moisture and vegetation controls on evapotranspiration in a heterogeneous Mediterranean ecosystem on Sardinia, Italy, *Water Resources Research*, *42*, W08419, 2006.

Detto, M., J. Verfaillie, F. Anderson, L. Xu, and D. Baldocchi, Comparing laser-based open- and closed-path gas analyzers to measure methane fluxes using the eddy covariance method, *Agricultural and Forest Meteorology*, *151*, 1312–1324, 2011.

Dijk, A. V., A. F. Moene, and H. A. R. de Bruin, The principles of surface flux physics: theory, practice and description of the ECPACK library, Internal Report 2004/1, Tech. rep., Meteorology and Air Quality Group, Wageningen University, Wageningen, Netherlands, 2004.

Dioumaeva, I., S. Trumbore, E. A. G. Schuur, M. L. Goulden, M. Litvak, and A. I. Hirsch, Decomposition of peat from upland boreal forest: Temperature dependence and sources of respired carbon, *Journal of Geophysical Research*, *108*, 8222, 2002.

Dlugokencky, E. J., et al., Observational constraints on recent increases in the atmospheric CH_4 burden, *Geophysical Research Letters*, *36*, L18803, 2009.

Dlugokencky, E. J., E. G. Nisbet, R. Fisher, and D. Lowry, Global atmospheric methane: budget, changes and dangers, *Philosophical Transactions of the Royal Society A*, *369*, 2058–2072, 2011.

Dunfield, P., R. Knowles, R. Dumont, and T. Moore, Methane production and consumption in temperate and subarctic peat soils: Response to temperature and pH, *Soil Biology and Biochemistry*, *25*, 321–326, 1993.

Dunn, A. L., C. C. Barford, S. C. Wofsy, M. L. Goulden, and B. C. Daube, A long-term record of carbon exchange in a boreal black spruce forest: means, responses to interannual variability, and decadal trends, *Global Change Biology*, *13*, 577–590, 2007.

Dyer, A. J., A review of flux-profile relationships, *Boundary-Layer Meteorology*, *7*, 363–372, 1974.

Ecological Stratification Working Group, A National Ecological Framework for Canada, Tech. rep., Agriculture & Agri-Food Canada and Environment Canada, Ottawa/Hull, 1995.

Ekici, A., C. Beer, S. Hagemann, J. Boike, M. Langer, and C. Hauck, Simulating high-latitude permafrost regions by the JSBACH terrestrial ecosystem model, *Geoscientific Model Development*, *7*, 631–647, 2014.

Environment Canada, Canadian Climate Normals: 1981 - 2010, 2014.

Epp, H., and R. Lanoville, Satellite data and geographic information systems for fire and resource management in the Canadian Arctic, *Geocarto International*, *11*(2), 97–103, 1996.

Esau, I., and S. Zilitinkevich, On the role of the planetary boundary layer depth in the climate system, *Advances in Science and Research*, *4*, 63–69, 2010.

Esau, I., R. Davy, and S. Outten, Complementary explanation of temperature response in the lower atmosphere, *Environmental Research Letters*, *7*, 044026, 2012.

Eugster, W., et al., Land-atmosphere energy exchange in Arctic tundra and boreal forest: available data and feedbacks to climate, *Global Change Biology*, *6*, 84–115, 2000.

Euskirchen, E. S., C. Edgar, M. R. Turetsky, M. P. Waldrop, and J. W. Harden, Differential response of carbon fluxes to climate in three peatland ecosystems that vary in the presence and stability of permafrost, *Journal of Geophysical Research: Biogeosciences*, *119*, 1576–1595, 2014.

Euskirchen, E. S., A. P. Bennett, A. L. Breen, H. Genet, M. A. Lindgren, T. A. Kurkowski, A. D. McGuire, and T. S. Rupp, Consequences of changes in vegetation and snow cover for climate feedbacks in Alaska and northwest Canada, *Environmental Research Letters*, *11*, 105003, 2016.

Ewers, B. E., S. T. Gower, B. Bond-Lamberty, and C. K. Wang, Effects of stand age and tree species on canopy transpiration and average stomatal conductance of boreal forests, *Plant, Cell and Environment*, *28*, 660–678, 2005.

Fang, C., and J. B. Moncrieff, The dependence of soil CO_2 efflux on temperature, *Soil Biology and Biochemistry*, *33*, 155–165, 2001.

Finger, R. A., M. R. Turetsky, K. Kielland, R. W. Ruess, M. C. Mack, and E. S. Euskirchen, Effects of permafrost thaw on nitrogen availability and plant-soil interactions in a boreal Alaskan lowland, *Journal of Ecology*, *104*, 1542—-1554, 2016.

Fisher, J. B., D. N. Huntzinger, C. R. Schwalm, and S. Sitch, Modeling the Terrestrial Biosphere, *Annual Review of Environment and Resources*, *39*, 91–123, 2014.

Flessa, H., et al., Landscape controls of CH_4 fluxes in a catchment of the forest tundra ecotone in northern Siberia, *Global Change Biology*, *14*, 2040–2056, 2008.

Foken, T., *Micrometeorology*. Springer, Heidelberg, 1st edn., 2008.

Foley, J. A., J. E. Kutzbach, M. T. Coe, and S. Levis, Feedbacks between climate and boreal forests during the Holocene epoch, *Nature*, *371*, 52–54, 1994.

Friedl, M., Forward and inverse modeling of land surface energy balance using surface temperature measurements, *Remote Sensing of Environment*, *79*, 344–354, 2002.

Friedlingstein, P., et al., Persistent growth of CO_2 emissions and implications for reaching climate targets, *Nature Geoscience*, *7*, 709–715, 2014a.

Friedlingstein, P., M. Meinshausen, V. K. Arora, C. D. Jones, A. Anav, S. K. Liddicoat, and R. Knutti, Uncertainties in CMIP5 climate projections due to carbon cycle feedbacks, *Journal of Climate*, *27*, 511–526, 2014b.

Frolking, S., N. Roulet, and J. Fuglestvedt, How northern peatlands influence the Earth's radiative budget: Sustained methane emission versus sustained carbon sequestration, *Journal of Geophysical Research*, *111*, G01008, 2006.

Frolking, S., J. Talbot, M. C. Jones, C. C. Treat, J. B. Kauffman, E.-S. Tuittila, and N. T. Roulet, Peatlands in the Earth's 21st century climate system, *Environmental Reviews*, *19*, 371–396, 2011.

Gao, X., C. Adam Schlosser, A. Sokolov, K. W. Anthony, Q. Zhuang, and D. Kicklighter, Permafrost degradation and methane: low risk of biogeochemical climate-warming feedback, *Environmental Research Letters*, *8*, 035014, 2013.

Garnaud, C., and L. Sushama, Biosphere-climate interactions in a changing climate over North America, *Journal of Geophysical Research: Atmospheres*, *120*, 1091–1108, 2015.

Garon-Labrecque, M.-E., É. Léveillé-Bourret, K. Higgins, and O. Sonnentag, Additions to the Boreal Flora of the Northwest Territories with a Preliminary Vascular Flora of Scotty Creek, *Canadian Field-Naturalist*, *129*, 349–367, 2015.

Garratt, J., Review: the atmospheric boundary layer, *Earth-Science Reviews*, *37*, 89–134, 1994.

Gauthier, S., P. Bernier, T. Kuuluvainen, A. Z. Shvidenko, and D. G. Schepaschenko, Boreal forest health and global change, *Science*, *349*(6250), 819–822, 2015.

Gea-Izquierdo, G., et al., Modeling acclimation of photosynthesis to temperature in evergreen conifer forests, *New Phytologist*, *188*, 175–186, 2010.

Girardin, M. P., E. H. Hogg, P. Y. Bernier, W. A. Kurz, X. J. Guo, and G. Cyr, Negative impacts of high temperatures on growth of black spruce forests intensify with the anticipated climate warming, *Global Change Biology*, *22*, 627–643, 2016.

Goetz, S. J., A. G. Bunn, G. J. Fiske, and R. A. Houghton, Satellite-observed photosynthetic trends across boreal North America associated with climate and fire disturbance, *Proceedings of the National Academy of Sciences*, *102*, 13521–13525, 2005.

Goetz, S. J., G. J. Fiske, and A. G. Bunn, Using satellite time-series data sets to analyze fire disturbance and forest recovery across Canada, *Remote Sensing of Environment*, *101*, 352–365, 2006.

Goetz, S. J., et al., Observations and assessment of forest carbon dynamics following disturbance in North America, *Journal of Geophysical Research: Biogeosciences*, *117*, G02022, 2012.

Goodrich, J., W. Oechel, B. Gioli, V. Moreaux, P. Murphy, G. Burba, and D. Zona, Impact of different eddy covariance sensors, site set-up, and maintenance on the annual balance of CO_2 and CH_4 in the harsh Arctic environment, *Agricultural and Forest Meteorology*, *228-229*, 239–251, 2016.

Goulden, M. L., B. C. Daube, S.-M. Fan, D. J. Sutton, A. Bazzaz, J. W. Munger, and S. C. Wofsy, Physiological responses of a black spruce forest to weather, *Journal of Geophysical Research*, *102*(D24), 28987–28996, 1997.

Goulden, M. L., G. C. Winston, A. M. S. McMillan, M. E. Litvak, E. L. Read, A. V. Rocha, and J. Rob Elliot, An eddy covariance mesonet to measure the effect of forest age on land-atmosphere exchange, *Global Change Biology*, *12*, 2146–2162, 2006.

Goulden, M. L., A. M. S. Mcmillan, G. C. Winston, a. V. Rocha, K. L. Manies, J. W. Harden, and B. P. Bond-Lamberty, Patterns of NPP, GPP, respiration, and NEP during boreal forest succession, *Global Change Biology*, *17*, 855–871, 2011.

Grant, R. F., H. A. Margolis, A. G. Barr, T. A. Black, A. L. Dunn, P. Y. Bernier, and O. Bergeron, Changes in net ecosystem productivity of boreal black spruce stands in response to changes in temperature at diurnal and seasonal time scales, *Tree Physiology*, *29*, 1–17, 2009.

Grelle, A., A. Lindroth, and M. Mölder, Seasonal variation of boreal forest surface conductance and evaporation, *Agricultural and Forest Meteorology*, *98-99*, 563–578, 1999.

Griebel, A., L. T. Bennett, D. Metzen, J. Cleverly, G. G. Burba, and S. K. Arndt, Effects of inhomogeneities within the flux footprint on the interpretation of seasonal, annual, and interannual ecosystem carbon exchange, *Agricultural and Forest Meteorology*, *221*, 50–60, 2016.

Grimmond, C. S. B., and T. R. Oke, Aerodynamic Properties of Urban Areas Derived from Analysis of Surface Form, *Journal of Applied Meteorology*, *38*, 1262–1292, 1999.

Gruber, S., Derivation and analysis of a high-resolution estimate of global permafrost zonation, *The Cryosphere*, *6*, 221–233, 2012.

Hadden, D., and A. Grelle, Changing temperature response of respiration turns boreal forest from carbon sink into carbon source, *Agricultural and Forest Meteorology*, *223*, 30–38, 2016.

Hanis, K. L., M. Tenuta, B. D. Amiro, and T. N. Papakyriakou, Seasonal dynamics of methane emissions from a subarctic fen in the Hudson Bay Lowlands, *Biogeosciences*, *10*, 4465–4479, 2013.

Hansen, M. C., S. V. Stehman, and P. V. Potapov, Quantification of global gross forest cover loss, *Proceedings of the National Academy of Sciences*, *107*, 8650–8655, 2010.

Hansen, M. C., et al., High-resolution global maps of 21st-century forest cover change, *Science*, *342*, 850–854, 2013.

Hartley, I. P., et al., Quantifying landscape-level methane fluxes in subarctic Finland using a multiscale approach, *Global Change Biology*, *21*, 3712–3725, 2015.

Hartmann, D., et al., Observations: Atmosphere and Surface, in *Climate Change 2013: The Physical Science Basis. Contribution of Working Group I to the Fifth Assessment Report of the Intergovernmental Panel on Climate Change*, edited by T. Stocker, D. Qin, G.-K. Plattner, M. Tignor, S. Allen, J. Boschung, A. Nauels, Y. Xia, V. Bex, and P. Midgley, chap. 2, pp. 159–254. Cambridge University Press, Cambridge, United Kingdom and New York, NY, USA, 2013.

Hayashi, M., N. Goeller, W. L. Quinton, and N. Wright, A simple heat-conduction method for simulating the frost-table depth in hydrological models, *Hydrological Processes*, *21*, 2610–2622, 2007.

Heijmans, M. M. P. D., H. Klees, W. De Visser, and F. Berendse, Response of a Sphagnum bog plant community to elevated $C0_2$ and N supply, *Plant Ecology*, *162*, 123–134, 2002.

Helbig, M., et al., Addressing a systematic bias in carbon dioxide flux measurements with the EC150 and the IRGASON open-path gas analyzers, *Agricultural and Forest Meteorology*, *228-229*, 349–359, 2016a.

Helbig, M., K. Wischnewski, N. Kljun, L. Chasmer, W. L. Quinton, M. Detto, and O. Sonnentag, Regional atmospheric cooling and wetting effect of permafrost thaw-induced boreal forest loss, *Global Change Biology*, 2016b.

Hill, T. C., M. Williams, and J. B. Moncrieff, Modeling feedbacks between a boreal forest and the planetary boundary layer, *Journal of Geophysical Research*, *113*, D15122, 2008.

Hill, T. C., T. Quaife, and M. Williams, A data assimilation method for using low-resolution Earth observation data in heterogeneous ecosystems, *Journal of Geophysical Research*, *116*(D8), 08117, 2011.

Hinzman, L. D., et al., Evidence and implications of recent climate change in northern Alaska and other arctic regions, *Climatic Change*, *72*, 251–298, 2005.

Hogg, E. T., V. J. Lieffers, and R. W. Wein, Potential carbon losses from peat profiles: effects of temperature, drought cycles, and fire, *Ecological Applications*, *2*(3), 298–306, 1992.

Hommeltenberg, J., M. Mauder, M. Drösler, K. Heidbach, P. Werle, and H. Peter, Ecosystem scale methane fluxes in a natural temperate bog-pine forest in southern Germany, *Agricultural and Forest Meteorology*, *198-199*, 273–284, 2014.

Houspanossian, J., M. Nosetto, and E. G. Jobbágy, Radiation budget changes with dry forest clearing in temperate Argentina, *Global Change Biology*, *19*, 1211–1222, 2013.

Hugelius, G., et al., A new data set for estimating organic carbon storage to 3 m depth in soils of the northern circumpolar permafrost region, *Earth System Science Data*, *5*, 393–402, 2013.

Humphreys, E. R., P. M. Lafleur, L. B. Flanagan, N. Hedstrom, K. H. Syed, A. J. Glenn, and R. Granger, Summer carbon dioxide and water vapor fluxes across a range of northern peatlands, *Journal of Geophysical Research*, *111*(G4), G04011, 2006.

Huxman, T. E., a. a. Turnipseed, J. P. Sparks, P. C. Harley, and R. K. Monson, Temperature as a control over ecosystem CO_2 fluxes in a high-elevation, subalpine forest., *Oecologia*, *134*, 537–546, 2003.

Igarashi, Y., T. Kumagai, N. Yoshifuji, T. Sato, N. Tanaka, K. Tanaka, M. Suzuki, and C. Tantasirin, Environmental control of canopy stomatal conductance in a tropical deciduous forest in northern Thailand, *Agricultural and Forest Meteorology*, *202*, 1–10, 2015.

Iwata, H., Y. Harazono, M. Ueyama, A. Sakabe, H. Nagano, Y. Kosugi, K. Takahashi, and Y. Kim, Methane exchange in a poorly-drained black spruce forest over permafrost observed using the eddy covariance technique, *Agricultural and Forest Meteorology*, *214-215*, 157–168, 2015.

Jackowicz-Korczyński, M., T. R. Christensen, K. Bäckstrand, P. Crill, T. Friborg, M. Mastepanov, and L. Ström, Annual cycle of methane emission from a subarctic peatland, *Journal of Geophysical Research*, *115*, G02009, 2010.

Janssens, I. A., et al., Productivity overshadows temperature in determining soil and ecosystem respiration across European forests, *Global Change Biology*, *7*(3), 269–278, 2001.

Jin, Y., C. B. Schaaf, C. E. Woodcock, F. Gao, X. Li, A. H. Strahler, W. Lucht, and S. Liang, Consistency of MODIS surface bidirectional reflectance distribution function and albedo retrievals: 2. Validation, *Journal of Geophysical Research*, *108*(D5), 4159, 2003.

Jin, Y., J. T. Randerson, S. J. Goetz, P. S. A. Beck, M. M. Loranty, and M. L. Goulden, The influence of burn severity on postfire vegetation recovery and albedo change during early succession in North American boreal forests, *Journal of Geophysical Research: Biogeosciences*, *117*, G01036, 2012.

Joabsson, A., T. R. Christensen, and B. Wallén, Vascular plant controls on methane emis-

sions from northern peatforming wetlands, *Trends in Ecology & Evolution*, *14*(10), 385–388, 1999.

Johansson, T., N. Malmer, P. M. Crill, T. Friborg, J. H. Akerman, M. Mastepanov, and T. R. Christensen, Decadal vegetation changes in a northern peatland, greenhouse gas fluxes and net radiative forcing, *Global Change Biology*, *12*, 2352–2369, 2006.

Johnston, C. E., S. a. Ewing, J. W. Harden, R. K. Varner, K. P. Wickland, J. C. Koch, C. C. Fuller, K. Manies, and M. T. Jorgenson, Effect of permafrost thaw on CO_2 and CH_4 exchange in a western Alaska peatland chronosequence, *Environmental Research Letters*, *9*, 085004, 2014.

Johnstone, J. F., and F. S. Chapin, Effects of soil burn severity on post-fire tree recruitment in boreal forest, *Ecosystems*, *9*, 14–31, 2006.

Jones, M. C., R. K. Booth, Z. Yu, and P. Ferry, A 2200-year record of permafrost dynamics and carbon cycling in a collapse-scar bog, Interior Alaska, *Ecosystems*, *16*, 1–19, 2013.

Jones, M. C., J. Harden, J. O'Donnell, K. Manies, T. Jorgenson, C. Treat, and S. Ewing, Rapid carbon loss and slow recovery following permafrost thaw in boreal peatlands, *Global Change Biology*, 2016.

Joos, F., et al., Carbon dioxide and climate impulse response functions for the computation of greenhouse gas metrics: A multi-model analysis, *Atmospheric Chemistry and Physics*, *13*, 2793–2825, 2013.

Jorgenson, M. T., and T. E. Osterkamp, Response of boreal ecosystems to varying modes of permafrost degradation, *Canadian Journal of Forest Research*, *35*, 2100–2111, 2005.

Jorgenson, M. T., C. H. Racine, J. C. Walters, and T. E. Osterkamp, Permafrost degradation and ecological changes associated with a warming climate in central alaska, *Climatic Change*, *48*, 551–579, 2001.

Jorgenson, M. T., V. Romanovsky, J. Harden, Y. Shur, J. O'Donnell, E. A. G. Schuur, M. Kanevskiy, and S. Marchenko, Resilience and vulnerability of permafrost to climate change, *Canadian Journal of Forest Research*, *40*, 1219–1236, 2010.

Juang, J.-Y., G. G. Katul, A. Porporato, P. C. Stoy, M. S. Siqueira, M. Detto, H.-S. Kim, and R. Oren, Eco-hydrological controls on summertime convective rainfall triggers, *Global Change Biology*, *13*, 887–896, 2007a.

Juang, J. Y., G. Katul, M. Siqueira, P. Stoy, and K. Novick, Separating the effects of albedo from eco-physiological changes on surface temperature along a successional chronosequence in the southeastern United States, *Geophysical Research Letters*, *34*, L21408, 2007b.

Justice, C. O., et al., The MODIS fire products, *Remote Sensing of Environment*, *83*, 244–262, 2002.

Kasischke, E. S., and M. R. Turetsky, Recent changes in the fire regime across the North American boreal region—Spatial and temporal patterns of burning across Canada and Alaska, *Geophysical Research Letters*, *33*, L09703, 2006.

Kasischke, E. S., N. L. Christensen, and B. J. Stocks, Fire, Global Warming, and the Carbon Balance of Boreal Forests, *Ecological Applications*, *5*(2), 437–451, 1995.

Kasurinen, V., et al., Latent heat exchange in the boreal and arctic biomes, *Global Change Biology*, *20*, 3439–3456, 2014.

Kauppi, P. E., M. Posch, and P. Pirinen, Large Impacts of Climatic Warming on Growth of Boreal Forests since 1960, *PLoS ONE*, *9*(11), e111340, 2014.

Kelliher, F. M., R. Leuning, and E. D. Schulze, Evaporation and canopy characteristics of coniferous forests and grasslands, *Oecologia*, *95*(2), 153–163, 1993.

Kettunen, A., Connecting methane fluxes to vegetation cover and water table fluctuations at microsite level: A modeling study, *Global Biogeochemical Cycles*, *17*, 1051, 2003.

Kettunen, A., V. Kaitala, A. Lehtinen, A. Lohila, J. Alm, J. Silvola, and P. J. Martikainen, Methane production and oxidation potentials in relation to water table fluctuations in two boreal mires, *Soil Biology and Biochemistry*, *31*(12), 1741–1749, 1999.

Keuper, F., P. M. van Bodegom, E. Dorrepaal, J. T. Weedon, J. van Hal, R. S. P. van Logtestijn, and R. Aerts, A frozen feast: thawing permafrost increases plant-available nitrogen in subarctic peatlands, *Global Change Biology*, *18*, 1998–2007, 2012.

Kimball, J. S., P. E. Thornton, M. A. White, and S. W. Running, Simulating forest productivity and surface-atmosphere carbon exchange in the BOREAS study region., *Tree Physiology*, *17*, 589–599, 1997.

Kirschke, S., et al., Three decades of global methane sources and sinks, *Nature Geoscience*, *6*, 813–823, 2013.

Kirtman, B., et al., Near-term Climate Change: Projections and Predictability, in *Climate Change 2013: The Physical Science Basis. Contribution of Working Group I to the Fifth Assessment Report of the Intergovernmental Panel on Climate Change*, edited by T. Stocker, D. Qin, G.-K. Plattner, M. Tignor, S. Allen, J. Boschung, A. Nauels, Y. Xia, V. Bex, and P. Midgley, pp. 953–1028. Cambridge University Press, Cambridge, United Kingdom and New York, NY, USA, 2013.

Klapstein, S. J., M. R. Turetsky, A. D. McGuire, J. W. Harden, C. I. Czimczik, X. Xu, J. P. Chanton, and J. M. Waddington, Controls on methane released through ebullition in peatlands affected by permafrost degradation, *Journal of Geophysical Research: Biogeosciences*, *119*, 418–431, 2014.

Kljun, N., M. W. Rotach, and H. P. Schmid, A three-dimensional backward Lagrangian footprint model for a wide range of boundary-layer stratifications, *Boundary-Layer Meteorology*, *103*, 205–226, 2002.

Kljun, N., P. Calanca, M. W. Rotach, and H. P. Schmid, A simple parametrisation for flux footprint predictions, *Boundary-Layer Meteorology*, *112*, 503–523, 2004.

Kljun, N., T. A. Black, T. J. Griffis, A. G. Barr, D. Gaumont-Guay, K. Morgenstern, J. H. McCaughey, and Z. Nesic, Response of net ecosystem productivity of three boreal forest stands to drought, *Ecosystems*, *10*, 1039–1055, 2007.

Kljun, N., P. Calanca, M. W. Rotach, and H. P. Schmid, A simple two-dimensional parameterisation for Flux Footprint Predictions (FFP), *Geoscientific Model Development*, *8*, 3695–3713, 2015.

Knoblauch, C., C. Beer, A. Sosnin, D. Wagner, and E.-M. Pfeiffer, Predicting long-term carbon mineralization and trace gas production from thawing permafrost of Northeast Siberia, *Global Change Biology*, *19*, 1160–1172, 2013.

Knohl, A., A. R. B. Søe, W. L. Kutsch, M. Göckede, and N. Buchmann, Representative estimates of soil and ecosystem respiration in an old beech forest, *Plant and Soil*, *302*, 189–202, 2008.

Koven, C. D., Boreal carbon loss due to poleward shift in low-carbon ecosystems, *Nature Geoscience*, *6*(6), 452–456, 2013.

Koven, C. D., B. Ringeval, P. Friedlingstein, P. Ciais, P. Cadule, D. Khvorostyanov, G. Krinner, and C. Tarnocai, Permafrost carbon-climate feedbacks accelerate global warming, *Proceedings of the National Academy of Sciences*, *108*, 14769–14774, 2011.

Koven, C. D., W. J. Riley, and A. Stern, Analysis of Permafrost Thermal Dynamics and Response to Climate Change in the CMIP5 Earth System Models, *Journal of Climate*, *26*, 1877–1900, 2013.

Koven, C. D., et al., A simplified, data-constrained approach to estimate the permafrost carbon – climate feedback, *Philosophical Transactions of the Royal Society A*, *373*, 20140423, 2015.

Krishnan, P., T. A. Black, N. J. Grant, A. G. Barr, E. T. H. Hogg, R. S. Jassal, and K. Morgenstern, Impact of changing soil moisture distribution on net ecosystem productivity of a boreal aspen forest during and following drought, *Agricultural and Forest Meteorology*, *139*, 208–223, 2006.

Kroner, Y., and D. A. Way, Carbon fluxes acclimate more strongly to elevated growth temperatures than to elevated CO_2 concentrations in a northern conifer, *Global Change Biology*, *22*, 2913–2928, 2016.

Kurylyk, B. L., M. Hayashi, W. L. Quinton, J. C. Mckenzie, and C. I. Voss, Influence of vertical and lateral heat transfer on permafrost thaw, peatland landscape transition, and groundwater flow, *Water Resources Research*, *52*, 1286–1305, 2016.

Kurz, W. A., and M. J. Apps, A 70-year retrospective analysis of carbon fluxes in the Canadian Forest Sector, *Ecological Applications*, *9*(2), 526–547, 1999.

Kurz, W. A., C. H. Shaw, C. Boisvenue, G. Stinson, J. Metsaranta, D. Leckie, A. Dyk, C. Smyth, and E. T. Neilson, Carbon in Canada's boreal forest - A synthesis, *Environmental Reviews*, *292*, 260–292, 2013.

Kustas, W. P., M. C. Anderson, J. M. Norman, and F. Li, Utility of radiometric-aerodynamic temperature relations for heat flux estimation, *Boundary-Layer Meteorology*, *122*, 167–187, 2006.

Lafleur, P. M., T. R. Moore, N. T. Roulet, and S. Frolking, Ecosystem respiration in a cool temperate bog depends on peat temperature but not water table, *Ecosystems*, *8*, 619–629, 2005.

Lara, M. J., et al., Thermokarst rates intensify due to climate change and forest fragmentation in an Alaskan boreal forest lowland, *Global Change Biology*, *22*, 816–829, 2016.

Larmola, T., J. L. Bubier, C. Kobyljanec, N. Basiliko, S. Juutinen, E. R. Humphreys, M. Preston, and T. R. Moore, Vegetation feedbacks of nutrient addition lead to a weaker carbon sink in an ombrotrophic bog, *Global Change Biology*, *19*, 3729–3739, 2013.

Lasslop, G., M. Reichstein, J. Kattge, and D. Papale, Influences of observation errors in eddy flux data on inverse model parameter estimation, *Biogeosciences*, *5*, 1311–1324, 2008.

Lasslop, G., M. Reichstein, D. Papale, A. D. Richardson, A. Arneth, A. Barr, P. Stoy, and G. Wohlfahrt, Separation of net ecosystem exchange into assimilation and respiration using a light response curve approach: critical issues and global evaluation, *Global Change Biology*, *16*, 187–208, 2010.

Lawrence, D. M., C. D. Koven, S. C. Swenson, W. J. Riley, and A. G. Slater, Permafrost thaw and resulting soil moisture changes regulate projected high-latitude CO_2 and CH_4 emissions, *Environmental Research Letters*, *10*, 094011, 2015.

Le Quéré, C., et al., Global Carbon Budget 2015, *Earth System Science Data*, *7*, 349–396, 2015.

Lee, H., E. a. G. Schuur, J. G. Vogel, M. Lavoie, D. Bhadra, and C. L. Staudhammer, A spatially explicit analysis to extrapolate carbon fluxes in upland tundra where permafrost is thawing, *Global Change Biology*, *17*, 1379–1393, 2011.

Lee, H., E. A. G. Schuur, K. S. Inglett, M. Lavoie, and J. P. Chanton, The rate of permafrost carbon release under aerobic and anaerobic conditions and its potential effects on climate, *Global Change Biology*, *18*, 515–527, 2012.

Lee, H., S. C. Swenson, A. G. Slater, and D. M. Lawrence, Effects of excess ground ice on projections of permafrost in a warming climate, *Environmental Research Letters*, *9*, 124006, 2014.

Legendre, P., and L. Legendre, *Numerical Ecology*. Elsevier B.V., Amsterdam, The Netherlands, 3rd edn., 2012.

Leuning, R., and J. Moncrieff, Eddy-covariance CO_2 flux measurements using open- and closed-path CO_2 analysers: Corrections for analyser water vapour sensitivity and damping of fluctuations in air sampling tubes, *Boundary-Layer Meteorology*, *53*, 63–76, 1990.

Li, S., and C. Potter, Vegetation regrowth trends in post forest fire ecosystems across North America from 2000 to 2010, *Natural Science*, *4*(10), 755–770, 2012.

Li, Y., N. De Noblet-Ducoudré, E. L. Davin, S. Motesharrei, N. Zeng, S. C. Li, and E. Kalnay, The role of spatial scale and background climate in the latitudinal temperature response to deforestation, *Earth System Dynamics*, *7*, 167–181, 2015.

Liblik, L., T. Moore, J. Bubier, and S. Robinson, Methane emissions from wetlands in the zone of discontinuous permafrost: Fort Simpson, Northwest Territories, Canada, *Global Biogeochemical Cycles*, *11*, 485–494, 1997.

Lindroth, A., Aerodynamic and canopy resistance of short-rotation forest in relation to leaf area index and climate, *Boundary-Layer Meteorology*, *66*, 265–279, 1993.

Lindroth, A., M. Mölder, and F. Lagergren, Heat storage in forest biomass improves energy balance closure, *Biogeosciences*, *7*, 301–313, 2010.

Liu, H., J. T. Randerson, J. Lindfors, and F. S. Chapin, Changes in the surface energy budget after fire in boreal ecosystems of interior Alaska: An annual perspective, *Journal of Geophysical Research: Atmospheres*, *110*, D13101, 2005.

Liu, S., et al., Simulating the impacts of disturbances on forest carbon cycling in North America: Processes, data, models, and challenges, *Journal of Geophysical Research: Biogeosciences*, *116*, G00K08, 2011.

Lohila, A., K. Minkkinen, J. Laine, I. Savolainen, J.-P. Tuovinen, L. Korhonen, T. Laurila, H. Tietäväinen, and A. Laaksonen, Forestation of boreal peatlands: Impacts of changing albedo and greenhouse gas fluxes on radiative forcing, *Journal of Geophysical Research*, *115*, G04011, 2010.

Loisel, J., et al., A database and synthesis of northern peatland soil properties and Holocene carbon and nitrogen accumulation, *The Holocene*, *24*(9), 1028–1042, 2014.

Luyssaert, S., et al., CO_2 balance of boreal, temperate, and tropical forests derived from a global database, *Global Change Biology*, *13*, 2509–2537, 2007.

Luyssaert, S., et al., Land management and land-cover change have impacts of similar magnitude on surface temperature, *Nature Climate Change*, *4*, 389–393, 2014.

Mahecha, M. D., M. Reichstein, H. Lange, N. Carvalhais, C. Bernhofer, T. Grünwald, D. Papale, and G. Seufert, Characterizing ecosystem-atmosphere interactions from short to interannual time scales, *Biogeosciences*, *4*, 743–758, 2007.

Mahecha, M. D., et al., Global convergence in the temperature sensitivity of respiration at ecosystem level, *Science*, *329*(5993), 838–40, 2010.

Mahrt, L., Surface Heterogeneity and Vertical Structure of the Boundary Layer, *Boundary-Layer Meteorology*, *96*, 33–62, 2000.

Mahrt, L., and D. Vickers, Bulk formulation of the surface heat flux, *Boundary-Layer Meteorology*, *110*, 357–379, 2004.

Mauder, M., and T. Foken, Documentation and Instruction Manual of the Eddy-Covariance Software Package TK3, Tech. Rep. 46, Universität Bayreuth, Abt. Mikrometeorologie, Bayreuth, Germany, 2011.

McConnell, N. A., M. R. Turetsky, A. D. McGuire, E. S. Kane, M. P. Waldrop, and J. W. Harden, Controls on ecosystem and root respiration across a permafrost and wetland gradient in interior Alaska, *Environmental Research Letters*, *8*, 045029, 2013.

McDermitt, D., et al., A new low-power, open-path instrument for measuring methane flux by eddy covariance, *Applied Physics B*, *102*, 391–405, 2010.

McFadden, J. P., W. Eugster, and F. S. Chapin, A regional study of the controls on water vapor and CO_2 exchange in arctic tundra, *Ecology*, *84*(10), 2762–2776, 2003.

McGuire, A. D., et al., Variability in the sensitivity among model simulations of permafrost and carbon dynamics in the permafrost region between 1960 and 2009, *Global Biogeochemical Cycles*, *30*, 1015–1037, 2016.

McNaughton, K. G., and T. W. Spriggs, A mixed-layer model for regional evaporation, *Boundary-Layer Meteorology*, *34*, 243–262, 1986.

Meissner, K. J., A. J. Weaver, H. D. Matthews, and P. M. Cox, The role of land surface dynamics in glacial inception: A study with the UVic Earth System Model, *Climate Dynamics*, *21*, 515–537, 2003.

Melton, J., et al., Present state of global wetland extent and wetland methane modelling: conclusions from a model inter-comparison project (WETCHIMP), *Biogeosciences*, *10*, 753–788, 2013.

Mildrexler, D. J., M. Zhao, and S. W. Running, A global comparison between station air temperatures and MODIS land surface temperatures reveals the cooling role of forests, *Journal of Geophysical Research*, *116*, G03025, 2011.

Moffat, A. M., et al., Comprehensive comparison of gap-filling techniques for eddy covariance net carbon fluxes, *Agricultural and Forest Meteorology*, *147*, 209–232, 2007.

Moncrieff, J., R. Clement, J. Finnigan, and T. Meyers, Averaging, detrending, and filtering of eddy covariance time series, in *Handbook of Micrometeorology*, edited by X. Lee, W. Massman, and B. Law, pp. 7–31. Springer Netherlands, Amsterdam, The Netherlands, 2004.

Moncrieff, J. B., Y. Malhi, and R. Leuning, The propagation of errors in long-term measurements of land-atmosphere fluxes of carbon and water, *Global Change Biology*, *2*, 231–240, 1996.

Moncrieff, J. B., et al., A system to measure surface fluxes of momentum, sensible heat, water vapour and carbon dioxide, *Journal of Hydrology*, *188-189*, 589–611, 1997.

Montesano, P. M., R. Nelson, G. Sun, H. Margolis, A. Kerber, and K. J. Ranson, MODIS tree cover validation for the circumpolar taiga-tundra transition zone, *Remote Sensing of Environment*, *113*, 2130–2141, 2009.

Moore, T. R., Dissolved organic carbon in a northern boreal landscape, *Global Biogeochemical Cycles*, *17*, 1109, 2003.

Moore, T. R., A. Heyes, and N. T. Roulet, Methane emissions from wetlands, southern Hudson Bay Lowland, *Journal of Geophysical Research-Atmospheres*, *99*(D1), 1455–1467, 1994.

Moore, T. R., N. T. Roulet, and J. M. Waddington, Uncertainty in Predicting the Effect of Climatic Change on the Carbon Cycling of Canadian Peatlands, *Climatic Change*, *40*, 229–245, 1998.

Moore, T. R., A. Young, J. L. Bubier, E. R. Humphreys, P. M. Lafleur, and N. T. Roulet, A multi-year record of methane flux at the Mer Bleue bog, southern Canada, *Ecosystems*, *14*, 646–657, 2011.

Myers-Smith, I. H., A. D. McGuire, J. W. Harden, and F. S. Chapin, Influence of disturbance on carbon exchange in a permafrost collapse and adjacent burned forest, *Journal of Geophysical Research*, *112*, G04017, 2007.

Myers-Smith, I. H., et al., Shrub expansion in tundra ecosystems: dynamics, impacts and research priorities, *Environmental Research Letters*, *6*, 045509, 2011.

Myhre, G., et al., Anthropogenic & Natural Radiative Forcing, in *Climate Change 2013: The Physical Science Basis. Contribution of Working Group I to the Fifth Assessment Report of the Intergovernmental Panel on Climate Change*, edited by T. Stocker, D. Qin, G.-K. Plattner, M. Tignor, S. Allen, J. Boschung, A. Nauels, Y. Xia, V. Bex, and P. Midgley, chap. 2, pp. 659–740. Cambridge University Press, Cambridge, United Kingdom and New York, NY, USA, 2013.

Nakai, T., Y. Kim, R. C. Busey, R. Suzuki, S. Nagai, H. Kobayashi, H. Park, K. Sugiura, and A. Ito, Characteristics of evapotranspiration from a permafrost black spruce forest in interior Alaska, *Polar Science*, *7*, 136–148, 2013.

Natali, S. M., E. A. G. Schuur, E. E. Webb, C. E. Hicks Pries, and K. G. Crummer, Permafrost degradation stimulates carbon loss from experimentally warmed tundra, *Ecology*, *95*(3), 602–608, 2014.

National Wetlands Working Group, *The Canadian Wetland Classification System*. University of Waterloo, Waterloo, Ontario, 2nd edn., 1997.

Neubauer, S. C., On the challenges of modeling the net radiative forcing of wetlands: reconsidering Mitsch et al. 2013, *Landscape Ecology*, *29*, 571–577, 2014.

Neubauer, S. C., and J. P. Megonigal, Moving beyond global warming potentials to quantify the climatic role of ecosystems, *Ecosystems*, *18*, 1000–1013, 2015.

Nichols, D. S., and J. M. Brown, Evaporation from a Sphagnum moss surface, *Journal of Hydrology*, *48*, 289–302, 1980.

Nilsson, M., J. Sagerfors, I. Buffam, H. Laudon, T. Eriksson, A. Grelle, L. Klemedtsson, P. Weslien, and A. Lindroth, Contemporary carbon accumulation in a boreal oligotrophic minerogenic mire - A significant sink after accounting for all C-fluxes, *Global Change Biology*, *14*, 2317–2332, 2008.

Nisbet, E. G., E. J. Dlugokencky, and P. Bousquet, Methane on the rise - again, *Science*, *343*, 493–495, 2014.

Niu, S., et al., Seasonal hysteresis of net ecosystem exchange in response to temperature change: patterns and causes, *Global Change Biology*, *17*, 3102–3114, 2011.

Niu, S., et al., Thermal optimality of net ecosystem exchange of carbon dioxide and underlying mechanisms., *New Phytologist*, *194*, 775–783, 2012.

Novick, K., J. Walker, W. Chan, A. Schmidt, C. Sobek, and J. Vose, Eddy covariance measurements with a new fast-response, enclosed-path analyzer: Spectral characteristics and cross-system comparisons, *Agricultural and Forest Meteorology*, *181*, 17–32, 2013.

Novick, K. A., et al., The increasing importance of atmospheric demand for ecosystem water and carbon fluxes, *Nature Climate Change*, *6*, 1023—-1027, 2016.

O'Donnell, J. A., M. T. Jorgenson, J. W. Harden, A. D. McGuire, M. Z. Kanevskiy, and K. P. Wickland, The effects of permafrost thaw on soil hydrologic, thermal, and carbon dynamics in an Alaskan peatland, *Ecosystems*, *15*, 213–229, 2012.

Ohse, B., F. Jansen, and M. Wilmking, Do limiting factors at Alaskan treelines shift with climatic regimes?, *Environmental Research Letters*, *7*, 015505, 2012.

Oksanen, J., et al., Vegan: Community Ecology Package, 2013.

Olefeldt, D., N. T. Roulet, O. Bergeron, P. Crill, K. Bäckstrand, and T. R. Christensen, Net carbon accumulation of a high-latitude permafrost palsa mire similar to permafrost-free peatlands, *Geophysical Research Letters*, *39*, L03501, 2012.

Olefeldt, D., M. R. Turetsky, P. M. Crill, and A. D. McGuire, Environmental and physical controls on northern terrestrial methane emissions across permafrost zones, *Global Change Biology*, *19*, 589–603, 2013.

Olefeldt, D., et al., Circumpolar distribution and carbon storage of thermokarst landscapes, *Nature Communications*, *7*, 13043, 2016.

Oleson, K. W., G. B. Bonan, S. Levis, and M. Vertenstein, Effects of land use change on North American climate: Impact of surface datasets and model biogeophysics, *Climate Dynamics*, *23*, 117–132, 2004.

Olson, D. M., et al., Terrestrial Ecoregions of the World: A New Map of Life on Earth, *BioScience*, *51*(11), 933–938, 2001.

Osterkamp, T. E., L. Viereck, Y. Shur, M. T. Jorgenson, C. H. Racine, A. Doyle, and R. D. Boone, Observations of thermokarst and its impact on boreal forests in Alaska, U.S.A., *Arctic, Antarctic, and Alpine Research*, *32*, 303–315, 2000.

Pan, Y., et al., A large and persisten carbon sink in the world's forests, *Science*, *333*, 988–994, 2011.

Papale, D., et al., Towards a standardized processing of Net Ecosystem Exchange measured with eddy covariance technique: algorithms and uncertainty estimation, *Biogeosciences*, *3*, 571–583, 2006.

Patankar, R., W. L. Quinton, M. Hayashi, and J. L. Baltzer, Sap flow responses to seasonal thaw and permafrost degradation in a subarctic boreal peatland, *Trees*, *29*, 129–142, 2015.

Paulson, C. A., The mathematical representation of wind speed and temperature profiles in the unstable atmospheric surface layer, *Journal of Applied Meteorology*, *9*, 857–861, 1970.

Peichl, M., et al., Convergence of potential net ecosystem production among contrasting C3 grasslands, *Ecology Letters*, *16*(4), 502–512, 2013.

Pelletier, N., J. Talbot, D. Olefeldt, M. R. Turetsky, C. Blodau, O. Sonnentag, and W. L. Quinton, Influence of Holocene permafrost aggradation and thaw on the paleoecology and carbon storage of a peatland complex in northwestern Canada, *The Holocene*, 2017.

Peres-Neto, P. R., P. Legendre, S. Dray, and D. Borcard, Variation partitioning of species data matrices: estimation and comparison of fractions, *Ecology*, *87*(10), 2614–2625, 2006.

Peters, W., et al., An atmospheric perspective on North American carbon dioxide exchange: CarbonTracker, *Proceedings of the National Academy of Sciences of the United States of America*, *104*, 18925–18930, 2007.

Piao, S., et al., Net carbon dioxide losses of northern ecosystems in response to autumn warming., *Nature*, *451*, 49–52, 2008.

Piao, S., et al., Evaluation of terrestrial carbon cycle models for their response to climate variability and to CO_2 trends, *Global Change Biology*, *19*, 2117–32, 2013.

Potapov, P., M. C. Hansen, S. V. Stehman, T. R. Loveland, and K. Pittman, Combining MODIS and Landsat imagery to estimate and map boreal forest cover loss, *Remote Sensing of Environment*, *112*, 3708–3719, 2008.

Potter, C., S. Klooster, and V. Genovese, Alaska ecosystem carbon fluxes estimated from MODIS satellite data inputs from 2000 to 2010., *Carbon balance and management*, *8*(1), 12, 2013.

Prater, J. L., J. P. Chanton, and G. J. Whiting, Variation in methane production pathways associated with permafrost decomposition in collapse scar bogs of Alberta, Canada, *Global Biogeochemical Cycles*, *21*, GB4004, 2007.

Price, D. T., et al., Anticipating the consequences of climate change for Canada's boreal forest ecosystems, *Evironmental Reviews*, *365*, 322–365, 2013.

Prinn, R. G., Development and application of earth system models, *Proceedings of the National Academy of Sciences*, *110*, 3673–3680, 2013.

Quinton, W., M. Hayashi, and L. Chasmer, Peatland Hydrology of Discontinuous Permafrost in the Northwest Territories: Overview and Synthesis, *Canadian Water Resources Journal*, *34*(4), 311–328, 2009.

Quinton, W., M. Hayashi, and L. Chasmer, Permafrost-thaw-induced land-cover change in the Canadian subarctic: implications for water resources, *Hydrological Processes*, *25*, 152–158, 2011.

Quinton, W. L., and J. L. Baltzer, The active-layer hydrology of a peat plateau with thawing permafrost (Scotty Creek, Canada), *Hydrogeology Journal*, *21*, 201–220, 2013.

Randerson, J. T., et al., The impact of boreal forest fire on climate warming, *Science*, *314*, 1130–1132, 2006.

Rask, H., J. Schoenau, and D. Anderson, Factors influencing methane flux from a boreal forest wetland in Saskatchewan, Canada, *Soil Biology and Biochemistry*, *34*(4), 435–443, 2002.

Rayment, M. B., D. Loustau, and P. J. Jarvis, Photosynthesis and respiration of black spruce at three organizational scales: shoot, branch and canopy, *Tree Physiology*, *22*, 219–29, 2002.

Reichstein, M., et al., On the separation of net ecosystem exchange into assimilation and ecosystem respiration: review and improved algorithm, *Global Change Biology*, *11*, 1424–1439, 2005.

Richardson, A. D., D. Y. Hollinger, D. B. Dail, J. T. Lee, J. W. Munger, and J. O'Keefe, Influence of spring phenology on seasonal and annual carbon balance in two contrasting New England forests, *Tree Physiology*, *29*(3), 321–331, 2009.

Richardson, A. D. A., et al., Influence of spring and autumn phenological transitions on forest ecosystem productivity, *Philosophical Transactions of the Royal Society B: Biological Sciences*, *365*, 3227–3246, 2010.

Rinne, J., T. Riutta, M. Pihlatie, M. Aurela, S. Haapanala, J. P. Tuovinen, E. S. Tuittila, and T. Vesala, Annual cycle of methane emission from a boreal fen measured by the eddy covariance technique, *Tellus, Series B: Chemical and Physical Meteorology*, *59*(3), 449–457, 2007.

Robinson, D., and T. R. Moore, Carbon and peat accumulation over the past 1200 years in a landscape with discontinuous permafrost, northwestern Canada, *Global Biogeochemical Cycles*, *13*, 591–601, 1999.

Rogers, B. M., A. J. Soja, M. L. Goulden, and J. T. Randerson, Influence of tree species on continental differences in boreal fires and climate feedbacks, *Nature Geoscience*, *8*, 228–234, 2015.

Rossby, C. G., and R. B. Montgomery, The layer of frictional influence in wind and ocean currents, *Papers in Physical Oceanography and Meteorology*, *3*(3), 1–101, 1935.

Rotenberg, E., and D. Yakir, Contribution of semi-arid forests to the climate system., *Science*, *327*, 451–454, 2010.

Roulet, N. T., P. M. Lafleur, P. J. H. Richard, T. R. Moore, E. R. Humphreys, and J. Bubier, Contemporary carbon balance and late Holocene carbon accumulation in a northern peatland, *Global Change Biology*, *13*, 397–411, 2007.

Runkle, B., C. Wille, M. Gažovič, M. Wilmking, and L. Kutzbach, The surface energy balance and its drivers in a boreal peatland fen of northwestern Russia, *Journal of Hydrology*, *511*, 359–373, 2014.

Runkle, B. R. K., T. Sachs, C. Wille, E.-M. Pfeiffer, and L. Kutzbach, Bulk partitioning the growing season net ecosystem exchange of CO_2 in Siberian tundra reveals the seasonality of its carbon sequestration strength, *Biogeosciences*, *10*(3), 1337–1349, 2013.

Ryu, Y., D. D. Baldocchi, S. Ma, and T. Hehn, Interannual variability of evapotranspiration and energy exchange over an annual grassland in California, *Journal of Geophysical Research*, *113*, D09104, 2008.

Savage, K., T. R. Moore, and P. M. Crill, Methane and carbon dioxide exchanges between the atmosphere and northern boreal forest soils, *Journal of Geophysical Research*, *102*, 29279–29288, 1997.

Schädel, C., et al., Potential carbon emissions dominated by carbon dioxide from thawed permafrost soils, *Nature Climate Change*, *6*, 950–954, 2016.

Schaepman-Strub, G., M. E. Schaepman, T. H. Painter, S. Dangel, and J. V. Martonchik, Reflectance quantities in optical remote sensing-definitions and case studies, *Remote Sensing of Environment*, *103*, 27–42, 2006.

Scheffer, M., M. Holmgren, V. Brovkin, and M. Claussen, Synergy between small- and large-scale feedbacks of vegetation on the water cycle, *Global Change Biology*, *11*, 1003–1012, 2005.

Scheffer, M., M. Hirota, M. Holmgren, E. H. Van Nes, and F. S. Chapin, Thresholds for boreal biome transitions, *Proceedings of the National Academy of Sciences*, *109*, 21384–21389, 2012.

Schimel, D., et al., Observing terrestrial ecosystems and the carbon cycle from space, *Global Change Biology*, *5*, 1762–1776, 2015.

Schipperges, B., and H. Rydin, Response of photosynthesis of Sphagnum species from contrasting microhabitats to tissue water content and repeated desiccation, *New Phytologist*, *140*, 677–684, 1998.

Schmid, H., Experimental design for flux measurements: matching scales of observations and fluxes, *Agricultural and Forest Meteorology*, *87*, 179–200, 1997.

Schoellhamer, D. H., Singular spectrum analysis for time series with missing data, *Geophysical Research Letters*, *28*, 3187–3190, 2001.

Schuur, E. A. G., J. G. Vogel, K. G. Crummer, H. Lee, J. O. Sickman, and T. E. Osterkamp, The effect of permafrost thaw on old carbon release and net carbon exchange from tundra, *Nature*, *459*, 556–559, 2009.

Schuur, E. A. G., et al., Climate change and the permafrost carbon feedback, *Nature*, *520*, 171–179, 2015.

Sellers, P. J., et al., Modeling the Exchanges of Energy, Water, and Carbon Between Continents and the Atmosphere, *Science*, *275*, 502–509, 1997.

Shannon, R. D., and J. R. White, A three-year study of controls on methane emissions from two Michigan peatlands, *Biogeochemistry*, *27*, 35–60, 1994.

Shur, Y. L., and M. T. Jorgenson, Patterns of Permafrost Formation and Degradation in Relation to Climate and Ecosystems, *Permafrost and Periglacial Processes*, *18*, 7–19, 2007.

Shuttleworth, W. J., Macrohydrology - The new challenge for process hydrology, *Journal of Hydrology*, *100*, 31–56, 1988.

Silvola, J., J. Alm, U. Ahlholm, H. Nykanen, and P. J. . Martikainen, CO_2 fluxes from peat in boreal mires under varying temperature and moisture conditions, *Journal of Ecology*, *84*, 219–228, 1996.

Smith, L. C., Y. Sheng, G. M. MacDonald, and L. D. Hinzman, Disappearing Arctic lakes, *Science*, *308*(5727), 1429, 2005.

Snyder, P. K., C. Delire, and J. A. Foley, Evaluating the influence of different vegetation biomes on the global climate, *Climate Dynamics*, *23*, 279–302, 2004.

Song, C., X. Wang, Y. Miao, J. Wang, R. Mao, and Y. Song, Effects of permafrost thaw on carbon emissions under aerobic and anaerobic environments in the Great Hing'an Mountains, China, *Science of the Total Environment*, *487*, 604–10, 2014.

Sonnentag, O., G. Van Der Kamp, A. G. Barr, and J. M. Chen, On the relationship between water table depth and water vapor and carbon dioxide fluxes in a minerotrophic fen, *Global Change Biology*, *16*, 1762–1776, 2010.

Sonnentag, O., M. Detto, R. Vargas, Y. Ryu, B. Runkle, M. Kelly, and D. Baldocchi, Tracking the structural and functional development of a perennial pepperweed (Lepidium latifolium L.) infestation using a multi-year archive of webcam imagery and eddy covariance measurements, *Agricultural and Forest Meteorology*, *151*, 916–926, 2011.

Stiegler, C., M. Johansson, T. R. Christensen, M. Mastepanov, and A. Lindroth, Tundra permafrost thaw causes significant shifts in energy partitioning, *Tellus B*, *68*, 30467, 2016.

Stocks, B. J., et al., Large forest fires in Canada, 1959–1997, *Journal of Geophysical Research*, *108*(D1), 8149, 2003.

Stoy, P. C., et al., A data-driven analysis of energy balance closure across FLUXNET research sites: The role of landscape scale heterogeneity, *Agricultural and Forest Meteorology*, *171-172*, 137–152, 2013.

Strong, W., S. Zoltai, and G. R. Ironside, Ecoclimatic regions of Canada, *Ecological Land Classification Series*, *23*, 122, 1989.

Stull, R., *An Introduction to Boundary Layer Meteorology*. Kluwer Academic Publishers, Dordrecht, 1988.

Sun, J., and L. Mahrt, Relationship of surface heat flux to microscale temperature variations: Application to BOREAS, *Boundary-Layer Meteorology*, *76*, 291–301, 1995.

Sundh, I., M. Nilsson, G. Granberg, and B. Svensson, Depth distribution of microbial production and oxidation of methane in northern boreal peatlands, *Microbial Ecology*, *27*, 253–265, 1994.

Suyker, A. E., S. B. Verma, R. J. Clement, and D. P. Billesbach, Methane flux in a boreal fen: Season-long measurement by eddy correlation, *Journal of Geophysical Research*, *101*(D22), 28637–28647, 1996.

Tanja, S., et al., Air temperature triggers the recovery of evergreen boreal forest photosynthesis in spring, *Global Change Biology*, *9*, 1410–1426, 2003.

Tarnocai, C., The effect of climate change on carbon in Canadian peatlands, *Global and Planetary Change*, *53*, 222–232, 2006.

Tarnocai, C., J. G. Canadell, E. A. G. Schuur, P. Kuhry, G. Mazhitova, and S. Zimov, Soil organic carbon pools in the northern circumpolar permafrost region, *Global Biogeochemical Cycles*, *23*, GB2023, 2009.

Thompson, D. K., B. N. Simpson, and A. Beaudoin, Using forest structure to predict the distribution of treed boreal peatlands in Canada, *Forest Ecology and Management*, *372*, 19–27, 2016.

Tjoelker, M. G., J. Oleksyn, and P. B. Reich, Seedlings of five boreal tree species differ in acclimation of net photosynthesis to elevated CO_2 and temperature, *Tree Physiology*, *18*, 715–726, 1998.

Treat, C. C., J. L. Bubier, R. K. Varner, and P. M. Crill, Timescale dependence of environmental and plant-mediated controls of CH_4 flux in a temperate fen, *Journal of Geophysical Research: Biogeosciences*, *112*, G01014, 2007.

Treat, C. C., W. M. Wollheim, R. K. Varner, a. S. Grandy, J. Talbot, and S. Frolking, Temperature and peat type control CO_2 and CH_4 production in Alaskan permafrost peats, *Global Change Biology*, *20*, 2674–2686, 2014.

Treat, C. C., et al., Effects of permafrost aggradation on peat properties as determined from a pan-Arctic synthesis of plant macrofossils, *Journal of Geophysical Research: Biogeosciences*, *121*, 78–94, 2016.

Turetsky, M., K. Wieder, L. Halsey, and D. H. Vitt, Current disturbance and the diminishing peatland carbon sink, *Geophysical Research Letters*, *29*, 1526, 2002.

Turetsky, M. R., R. K. Wieder, C. J. Williams, and D. H. Vitt, Organic matter accumulation, peat chemistry, and permafrost melting in peatlands of boreal Alberta, *Écoscience*, *7*(3), 379–392, 2000.

Turetsky, M. R., R. K. Wieder, D. H. Vitt, R. J. Evans, and K. D. Scott, The disappearance of relict permafrost in boreal north America: Effects on peatland carbon storage and fluxes, *Global Change Biology*, *13*, 1922–1934, 2007.

Twine, T., W. Kustas, J. Norman, D. Cook, P. Houser, T. Meyers, J. Prueger, P. Starks, and M. Wesely, Correcting eddy-covariance flux underestimates over a grassland, *Agricultural and Forest Meteorology*, *103*, 279–300, 2000.

Ueyama, M., Y. Harazono, Y. Kim, and N. Tanaka, Response of the carbon cycle in subarctic black spruce forests to climate change: Reduction of a carbon sink related to the sensitivity of heterotrophic respiration, *Agricultural and Forest Meteorology*, *149*, 582–602, 2009.

Ueyama, M., H. Iwata, Y. Harazona, E. S. Euskirchen, W. C. Oechel, and D. Zona, Growing season and spatial variations of carbon fluxes of Arctic and boreal ecosystems in Alaska (USA), *Ecological Applications*, *23*(8), 1798–1816, 2013.

Ueyama, M., et al., Change in surface energy balance in Alaska due to fire and spring warming, based on upscaling eddy covariance measurements, *Journal of Geophysical Research: Biogeosciences*, *119*, 1947–1969, 2014.

Ueyama, M., N. Tahara, H. Iwata, E. S. Euskirchen, H. Ikawa, H. Kobayashi, H. Nagano, T. Nakai, and Y. Harazono, Optimization of a biochemical model with eddy covariance measurements in black spruce forests of Alaska for estimating CO_2 fertilization effects, *Agricultural and Forest Meteorology*, *222*, 98–111, 2016.

van Everdingen, R., *Multi-language glossary of permafrost and related ground-ice terms*. National Snow and Ice Data Center, Boulder, CO, 2005.

Vanden Broucke, S., S. Luyssaert, E. L. Davin, I. Janssens, and N. van Lipzig, New insights in the capability of climate models to simulate the impact of LUC based on temperature decomposition of paired site observations, *Journal of Geophysical Research: Atmospheres*, *120*, 2015.

Verma, S. B., Aerodynamic resistances to transfers of heat, mass and momentum, in *Estimation of Areal Evapotranspiration*, edited by T. A. Black, D. L. Spittlehouse, M. D. Novak, and D. T. Price, no. 177, pp. 13–20. IAHS Press, Wallford, 1989.

Vickers, D., and L. Mahrt, Quality control and flux sampling problems for tower and aircraft data, *Journal of Atmospheric and Oceanic Technology*, *14*, 512–526, 1997.

Walker, X., and J. F. Johnstone, Widespread negative correlations between black spruce growth and temperature across topographic moisture gradients in the boreal forest, *Environmental Research Letters*, *9*, 064016, 2014.

Wan, Z., New refinements and validation of the MODIS Land-Surface Temperature/Emissivity products, *Remote Sensing of Environment*, *140*, 36–45, 2014.

Way, D. A., and R. F. Sage, Thermal acclimation of photosynthesis in black spruce [Picea mariana (Mill.) B.S.P.], *Plant, Cell and Environment*, *31*, 1250–1262, 2008.

Webb, E. K., G. I. Pearman, and R. Leuning, Correction of flux measurements for density effects due to heat and water vapour transfer, *Quarterly Journal of the Royal Meteorological Society*, *106*, 85–100, 1980.

Weber, M. G., and M. D. Flannigan, Canadian boreal forest ecosystem structure and function in a changing climate: impact on fire regimes, *Environmental Reviews*, pp. 145–166, 1997.

Welp, L. R., J. Randerson, and H. Liu, The sensitivity of carbon fluxes to spring warming and summer drought depends on plant functional type in boreal forest ecosystems, *Agricultural and Forest Meteorology*, *147*, 172–185, 2007.

Welp, L. R., P. K. Patra, C. Rodenbeck, R. Nemani, J. Bi, S. C. Piper, and R. F. Keeling, Increasing summer net CO_2 uptake in high northern ecosystems inferred from atmospheric inversions and comparisons to remote sensing NDVI, *Atmospheric Chemistry and Physics*, *16*, 9047–9066, 2016.

Wickland, K. P., R. G. Striegl, J. C. Neff, and T. Sachs, Effects of permafrost melting on CO_2 and CH_4 exchange of a poorly drained black spruce lowland, *Journal of Geophysical Research*, *111*, G02011, 2006.

Wieder, W. R., C. C. Cleveland, W. K. Smith, and K. Todd-Brown, Future productivity and carbon storage limited by terrestrial nutrient availability, *Nature Geoscience*, *8*, 441–U35, 2015.

Wilby, R. L., S. P. Charles, E. Zorita, B. Timbal, P. Whetton, and L. O. Mearns, Guidelines for use of climate scenarios developed from statistical downscaling methods, 2004.

Wilczak, J. M., S. P. Oncley, and S. A. Stage, Sonic anemometer tilt correction algorithms, *Boundary-Layer Meteorology*, *99*, 127–150, 2001.

Williams, A. P., C. Xu, and N. G. McDowell, Who is the new sheriff in town regulating boreal forest growth?, *Environmental Research Letters*, *6*, 041004, 2011.

Wilmking, M., G. P. Juday, V. A. Barber, and H. S. J. Zald, Recent climate warming forces contrasting growth responses of white spruce at treeline in Alaska through temperature thresholds, *Global Change Biology*, *10*, 1724–1736, 2004.

Wilson, K., et al., Energy balance closure at FLUXNET sites, *Agricultural and Forest Meteorology*, *113*, 223–243, 2002.

Wohlfahrt, G., A. Haslwanter, L. Hörtnagl, R. L. Jasoni, L. F. Fenstermaker, J. a. Arnone, and A. Hammerle, On the consequences of the energy imbalance for calculating surface conductance to water vapour, *Agricultural and Forest Meteorology*, *149*(9), 1556–1559, 2009.

Wolf, S., et al., Warm spring reduced carbon cycle impact of the 2012 US summer drought, *Proceedings of the National Academy of Science*, *113*, 5880–5885, 2016.

Wolfe, R. E., M. Nishihama, A. J. Fleig, J. A. Kuyper, D. P. Roy, J. C. Storey, and F. S. Patt, Achieving sub-pixel geolocation accuracy in support of MODIS land science, *Remote Sensing of Environment*, *83*, 31–49, 2002.

Wooster, M. J., and Y. H. Zhang, Boreal forest fires burn less intensely in Russia than in North America, *Geophysical Research Letters*, *31*, L20505, 2004.

Wright, N., M. Hayashi, and W. L. Quinton, Spatial and temporal variations in active layer thawing and their implication on runoff generation in peat-covered permafrost terrain, *Water Resources Research*, *45*, W05414, 2009.

Xin, Q., P. Olofsson, Z. Zhu, B. Tan, and C. E. Woodcock, Toward near real-time monitoring of forest disturbance by fusion of MODIS and Landsat data, *Remote Sensing of Environment*, *135*, 234–247, 2013.

Yang, R., and M. A. Friedl, Determination of roughness lengths for heat and momentum over boreal forests, *Boundary-Layer Meteorology*, *107*, 581–603, 2003.

Yavitt, J. B., N. Basiliko, M. R. Turetsky, and A. G. Hay, Methanogenesis and methanogen diversity in three peatland types of the discontinuous permafrost zone, boreal western continental Canada, *Geomicrobiology Journal*, *23*, 641–651, 2006.

York, D., N. M. Evensen, M. López, and J. D. B. Delgado, Unified equations for the slope, intercept, and standard errors of the best straight line, *American Journal of Physics*, *72*, 367–375, 2004.

Yoshikawa, K., W. R. Bolton, V. E. Romanovsky, M. Fukuda, and L. D. Hinzman, Impacts of wildfire on the permafrost in the boreal forests of Interior Alaska, *Journal of Geophysical Research*, *108*(D1), 8148, 2003.

Yu, Z., Holocene Carbon Accumulation of Fen Peatlands in Boreal Western Canada: A Complex Ecosystem Response to Climate Variation and Disturbance, *Ecosystems*, *9*(8), 1278–1288, 2006.

Yuan, F., M. A. Arain, A. G. Barr, A. A. Black, C. P. A. Bourque, C. Coursolle, H. A. Margolis, H. McCaughey, and S. C. Wofsy, Modeling analysis of primary controls on net ecosystem productivity of seven boreal and temperate coniferous forests across a continental transect, *Global Change Biology*, *14*, 1765–1784, 2008.

Yuan, W., et al., Deriving a light use efficiency model from eddy covariance flux data for predicting daily gross primary production across biomes, *Agricultural and Forest Meteorology*, *143*(3-4), 189–207, 2007.

Yuan, W., et al., Thermal adaptation of net ecosystem exchange, *Biogeosciences*, *8*, 1453–1463, 2011.

Yue, C., et al., Simulating boreal forest carbon dynamics after stand-replacing fire disturbance: insights from a global process-based vegetation model, *Biogeosciences*, *10*, 8233–8252, 2013.

Zhao, K., and R. B. Jackson, Biophysical forcings of land-use changes from potential forestry activities in North America, *Ecological Monographs*, *84*(2), 329–353, 2014.

Zoltai, S. C., Cyclic Development of Permafrost in the Peatlands of Northwestern Canada, *Arctic and Alpine Research*, *25*, 240–246, 1993.

Zoltai, S. C., and C. Tarnocai, Perennially Frozen Peatlands in the Western Arctic and Subarctic of Canada, *Canadian Journal of Earth Sciences*, *12*, 28–43, 1975.

Zona, D., et al., Cold season emissions dominate the Arctic tundra methane budget, *Proceedings of the National Academy of Science*, *113*, 40–45, 2016.

Appendix I

Chapter 2

Table I.I – Global surface area of boreal forest (data from *Olson et al.* (2001)). Boreal forest area in the isolated, sporadic, discontinuous, and continuous permafrost zone (data from *Gruber* (2012)) as percentage of the total boreal forest area. Area of lowland boreal forest on thick overburden cover or on ice-rich permafrost in the circumpolar permafrost zone (data from *Brown et al.* (2002) & *Gruber* (2012)) as percentage of the total boreal forest area and in the isolated, sporadic, discontinuous, and continuous permafrost zone as percentage of the boreal forest area in the respective permafrost zone. Global percentages are shown together with percentages for North America and Eurasia. Lowlands were defined as flat or undulating landscapes (i.e. ruggedness index less than 2.5; see *Gruber* (2012)). Landscapes with thick overburden cover and no exposed bedrock or with high ground ice content were identified using the landform and ground ice content codes by *Brown et al.* (2002), respectively.

	North America	Eurasia	Global
surface area of boreal forest			
		km^2	
	6105125	9920519	16025644
boreal forest			
		% of total boreal forest	
in isolated permafrost zone	12.7	11.0	11.6
in sporadic permafrost zone	32.9	20.5	25.2
in discontinuous permafrost zone	24.7	18.7	20.9
in continuous permafrost zone	7.5	30.2	21.6
total	77.7	80.4	79.3
lowland boreal forest on thick overburden cover or ice-rich permafrost			
		% of total boreal forest	
in circumpolar permafrost zone	22.1	20.5	21.1
		% of boreal forest in permafrost zone	
in isolated permafrost zone	27.3	7.8	15.9
in sporadic permafrost zone	30.3	33.6	32.0
in discontinuous permafrost zone	26.2	30.6	28.6
in continuous permafrost zone	21.6	23.3	23.1

Table I.II – Unique parts of the spatial variance in the change in percent tree cover (shown as adjusted coefficient of determination (R^2_{adj})) explained by the mean permafrost zonation index (mPZI, A), the fraction of the area that burned between 1965 and 2002 ($FR_{regrowth}$, B), and that burned between 2003 and 2014 (FR_{fire}, C) across different spatial scales (from 5 km x 5 km to 80 km x 80 km). The common part of the variance that is shared by any combination of A, B, and C is also shown. A nonlinear regression (using the equation: $\Delta PTC = a\ FR_{regrowth} + b\ FR_{fire} + c/[1+d^{(e-mPZI)}] + f$) was conducted at each scale, separately. Variation partitioning was conducted using partial regression as implemented in the *varpart* function of the vegan R-package. Asterisks indicate if fractions A, B, and C were significant (** $p < 0.001$; * $p < 0.05$). p-values were obtained using permutation tests of the residuals [see also *Peres-Neto et al.* (2006)]. Bold figures indicate that fire history (i.e., $FR_{regrowth}$ + FR_{fire}) explains significantly ($\alpha = 0.05$) more of the variance in the percent tree cover changes than mPZI. At scales larger than 225 km^2, there is no significant difference in the parts explained by mPZI and fire history. Differences in fractions were tested using a bootstrap test for fractions described by *Peres-Neto et al.* (2006).

		scale [km^2]															
		25	100	225	400	625	900	1225	1600	2025	2500	3025	3600	4225	4900	5625	6400
var.	index	R^2_{adj}															
mPZI	A	0.12**	0.15**	0.17**	0.19**	0.20**	0.20**	0.19**	0.19**	0.19**	0.21**	0.25**	0.21**	0.29**	0.25**	0.21**	0.12**
$FR_{regr.}$	B	**0.14****	**0.15****	**0.14****	0.14**	0.15**	0.14**	0.14**	0.17**	0.13**	0.13**	0.10**	0.18**	0.11**	0.12**	0.12**	0.16**
FR_{fire}	C	**0.08****	**0.08****	**0.08****	0.08**	0.07**	0.08**	0.08**	0.06**	0.06**	0.03*	0.03**	0.01	0.01	0.02	0.02	0.03
joint	A+B	0.05	0.06	0.08	0.1	0.12	0.12	0.15	0.19	0.21	0.25	0.25	0.31	0.26	0.27	0.36	0.41
joint	B+C	0.04	0.04	0.04	0.04	0.04	0.03	0.03	0.01	0.01	0	0	0	0	0	0	0
joint	C+A	0.02	0.03	0.04	0.05	0.04	0.03	0.05	0.07	0.06	0.07	0.07	0.06	0.03	0.08	0.12	0.09
joint	A+B+C	0.02	0.03	0.04	0.05	0.05	0.06	0.06	0.06	0.07	0.06	0.07	0.06	0.05	0.05	0.02	0.03
Res.	-	0.52	0.46	0.41	0.36	0.34	0.32	0.3	0.26	0.27	0.27	0.23	0.17	0.25	0.22	0.15	0.19

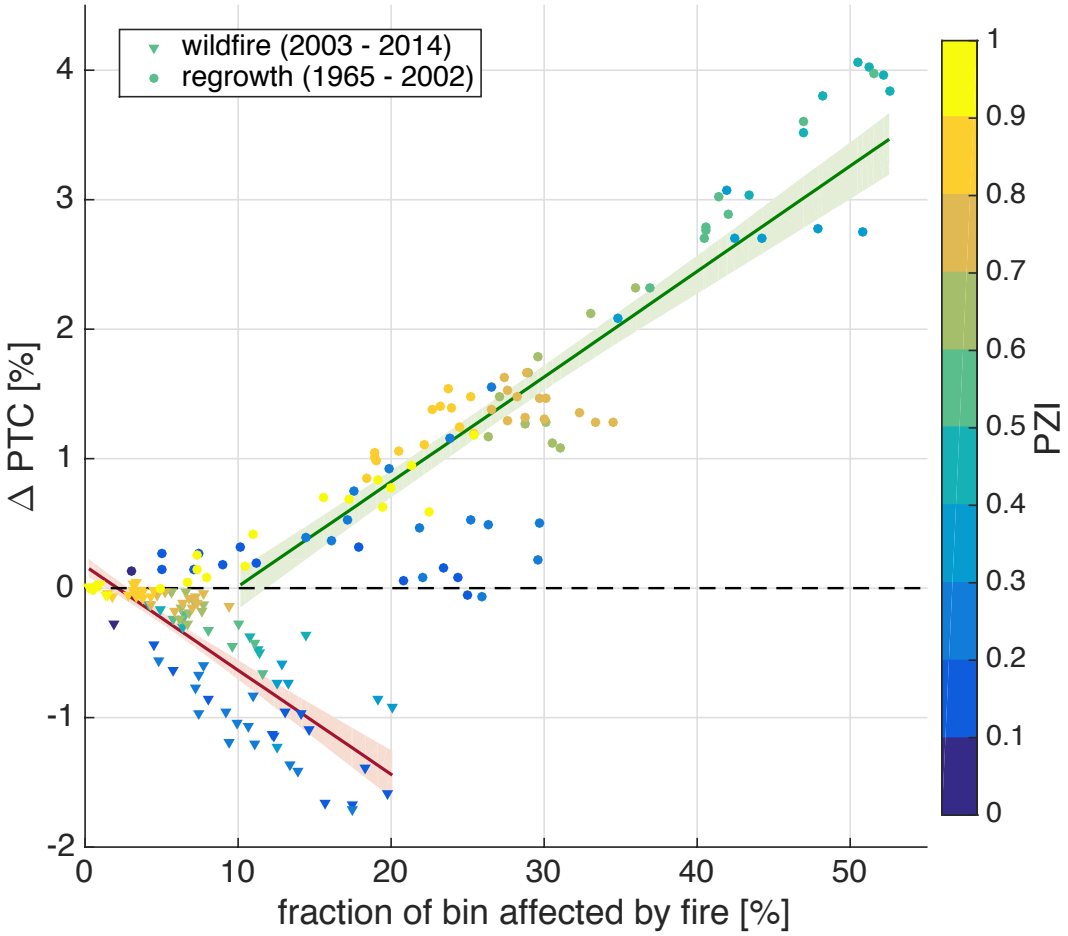

Figure I.1 – Contributions of areas affected by fire (i.e., wildfires between 2003 and 2014) and regrowth (i.e., wildfires between 1965 and 2002) per mean permafrost zonation index (PZI) bin as a function of the fraction of the area affected by wildfires between 2003 and 2014 and 1965 and 2002, respectively. Dots and triangles are color-coded according to the median PZI of the bins. Solid lines show linear model fits, while shaded areas indicate 95% confidence intervals of the linear regression, derived from 1000 bootstrap realizations of the original datasets.

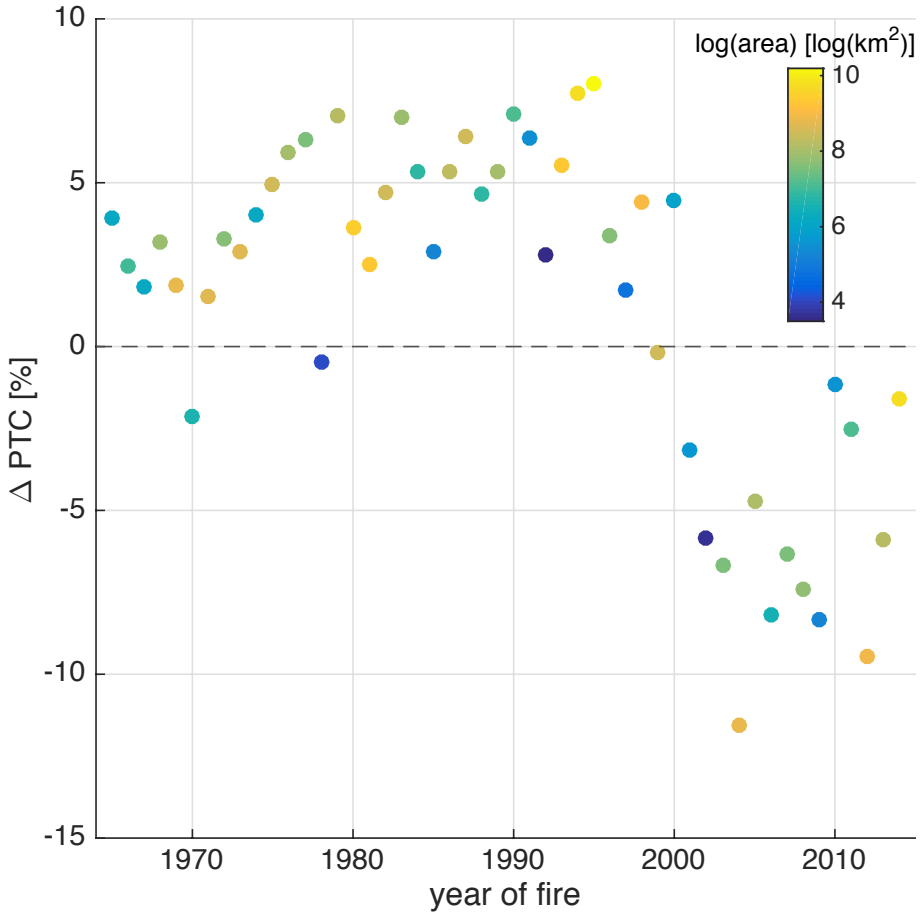

Figure I.2 – Mean change in Percent Tree Cover between 2000 to 2002 and 2012 to 2014 (ΔPTC) of pixels affected by wildfires between 1965 and 2014 across the Taiga Plains. ΔPTC is calculated for each fire year separately. Colors indicate the extent of wildfires for each year (shown as logarithm of the area affected by fire).

Appendix II

Chapter 3

Footprint modelling

The 2D flux footprint parameterization of *Kljun et al.* (2015) was applied for the landscape tower for halfhours with roughness lengths smaller than 0.95 m. With larger roughness lengths, the eddy covariance instruments were within the roughness sublayer, where measurements at one fixed point are not representative due to horizontally varying flux magnitudes (*Mahrt*, 2000). The eddy covariance system at the wetland tower was always above the roughness sublayer. The relative flux contribution matrices were projected on a LiDAR/spectral data fusion-based land cover classification with discrete classes for forests, wetlands and thaw lakes, and a LiDAR-derived canopy height map, both derived from remote sensing (*Chasmer et al.*, 2014, Fig. 3.1c).

Surface energy balance closure at the landscape and the wetland tower

Sums of H and LE measured by the eddy covariance technique were shown to be consistently smaller than available energy (i.e. lack of land surface EBC) across different ecosystems and instrumental setups (e.g., *Stoy et al.*, 2013; *Wilson et al.*, 2002). The reported discrepancies could either be caused by an overestimation of the available energy or an underestimation of turbulent energy fluxes (e.g., *Foken*, 2008). To ensure the comparability of H and LE at the landscape and the wetland tower, the EBC at the two sites was assessed as follows:

$$H + LE = R_n - G - S - Q_m - C \tag{II.1}$$

where R_n is net radiation [W m^{-2}], G is the soil heat flux [W m^{-2}], S is the rate of change of heat storage in the air column below the measurement height [W m^{-2}], as derived from one-point changes in T_a and specific humidity [q_a; kg kg^{-1}], Q_m is the snow

melt energy flux [W m^{-2}], and C [W m^{-2}] is the closure term for measurement errors or missing terms (e.g. soil thaw). Heat storage in biomass and the energy flux related to photosynthesis were assumed to be negligible due to the typically low productivity and low biomass of northern boreal forests (*Baldocchi et al.*, 2000; *Wilson et al.*, 2002). No storage term was calculated for the consumption or release of energy for thawing and freezing of the soil above the heat flux plates.

As the flux footprints of the landscape tower mainly consisted of forests and wetlands, the available energy was calculated as a weighted average of the ecosystemscale measurements of R_n, G, and Q_m at the wetland and the landscape tower. The weights were estimated for each half-hour as the relative contribution of these two land cover types to the flux measurements, quantified with the 2D footprint parameterization of *Kljun et al.* (2015) (see also *Chasmer et al.*, 2011; *Detto et al.*, 2006).

The EBC for the two towers (defined as the slope of available energy against the sum of turbulent energy fluxes) scale with the contribution of wetlands to the flux measurements, with friction velocity (u*; m s^{-1}), and soil temperature at 20 cm in the forest (T_{s_FOR}; °C) (Fig. II.1). We assume that the relationship of the EBC with T_{s_FOR} is caused by an underestimation of G early in the season due to the omission of a soil thaw energy flux (e.g., *Betts et al.*, 1999; *Nakai et al.*, 2013). In contrast, the dependence of EBC on u* is likely caused by underestimated H and LE (e.g., *Barr et al.*, 2006). For periods with T_{s_FOR} above 3 °C, u* above 0.2 m s^{-1} and wetland tower footprint contributions from the wetland larger than 95%, EBC was 0.79 and 0.78 for the landscape and the wetland tower, respectively. We therefore removed flux measurements from both towers when u* was below 0.2 m s^{-1}, and for the wetland tower when the wetland contribution to the flux footprint was < 95% (i.e. footprints extended into surrounding forest). For the landscape tower, data coverage was 50% for H and LE in 2013 (12 May 2013 - 01 November 2013). In 2014 (13 April 2014 - 07 November 2014), data coverage was 52% for H and LE at the landscape tower and 20% for H and LE at the wetland tower.

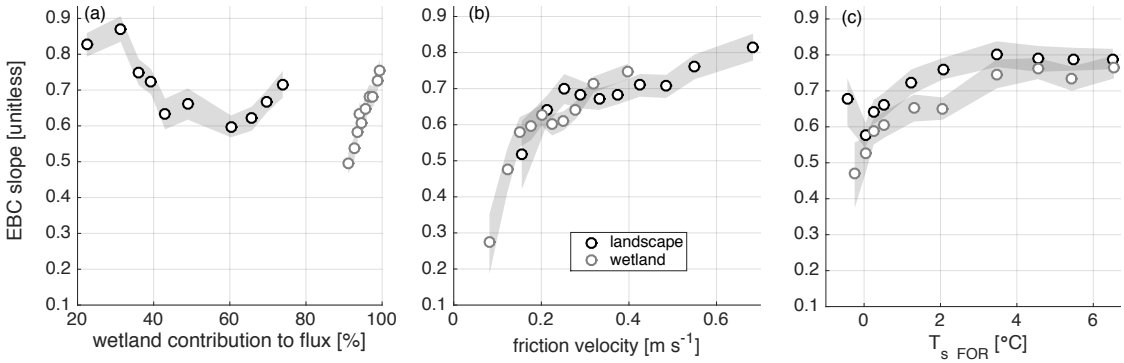

Figure II.1 – Slope of the energy balance closure (EBC) for the landscape and the wetland tower as function of **(a)** permafrost-free wetland contributions to flux footprints, **(b)** friction velocity, and **(c)** soil temperature at 20 cm on the forested permafrost plateau (T_{s_FOR}). Shaded areas show the 95% confidence interval of the slopes.

Atmospheric controls of surface conductance

Nonlinear VPD and SW_{in} models were fitted to g_s for half-hours with low wetland contributions to landscape tower footprints (FR_{WET}) (FR_{WET} < median of FR_{WET} [63%]), to g_s with high FR_{WET} ($FR_{WET} \leq$ median of FR_{WET} [63%]), and to g_s derived from fluxes at the wetland tower (contributions from wetlands $\leq$ 95%). Only daytime g_s (0900 and 2100 MST) and g_s for periods with LE > 10 W m^{-2} were used, as the expression of g_s becomes numerically unstable when LE < 10 W m^{-2}. The VPD control on G_{s_bound} was modelled as follows (e.g., *Blanken et al.*, 1997):

$$G_{s\_bound\_i} = g_{s0\_i} e^{(-b_d VPD)} \tag{II.2}$$

where i stands for the i-th data set class, g_{s_0} (m s^{-1}) is the bulk surface conductance at a VPD of 0 kPA, and b_d indicates the sensitivity of G_{s_bound} to VPD (kPa^{-1}). The model was fitted to the upper 15% of g_s per 0.5 kPa VPD window. Data for periods with SW_{in} < 300 W m^{-2} were excluded to avoid radiation-controlled g_s.

The dependence of G_{s_bound} on SW_{in} was modelled using a Michaelis-Menten function (e.g., *Grelle et al.*, 1999):

$$G_{s\_bound\_i} = g_{s\_max\_i} \frac{SW_{in}}{b_{infl} + SW_{in}} \quad \text{(II.3)}$$

where g_{s_max} is the upper limit of gs at high SW_{in} and b_{infl} is a parameter defining SW_{in} when G_{s_bound} reaches half of its upper limit. To assess the radiation dependence of G_{s_bound}, only periods with VPD > 0.3 kPa were analysed ensuring that g_s was not controlled by VPD. Uncertainties of the model fits were quantified by fitting the model to 1000 bootstrap realizations of the data sets.

The planetary boundary layer model

The time rate of change in potential air temperature of the mixed layer ($\frac{d\theta_m}{dt}$; K s^{-1} results from input of sensible heat from the surface (H) and from entrainment of warm air above the temperature inversion at the top of the mixed layer and was modelled using Eq. 1 in *McNaughton and Spriggs* (1986). The time rate of change in q_m was calculated using Eq. 2 in *McNaughton and Spriggs* (1986). Eq. 10 in *McNaughton and Spriggs* (1986) was used to model the time rate of change in PBL height:

$$\frac{dh}{dt} = \frac{H_v}{\rho C_p h \Gamma_v} \quad \text{(II.4)}$$

The vertical gradient of virtual potential air temperature [lapse rate (Γ_v); K m^{-1}] was taken as the lapse rate of moist air of 0.0065 K m^{-1}.

To model q_m at the landscape tower, we used H and LE from the landscape tower as forcing. Modelled θ_m and q_m can only be compared to measured θ_m and q_m when H and LE at the landscape tower are representative of the energy fluxes affecting instantaneous PBL dynamics, which is not always the case over a heterogeneous landscape. We included only days with clear-sky conditions and a total sum of less than five half-hours of missing or low quality (quality flag > 1) H and LE at the landscape and the wetland tower. Remaining gaps were filled using linear interpolation and days with an RMSE of the modelled θ_m > 2 K were discarded to ensure good model performance. The analysis of the EBC indicated an average underestimation of ∼20% of the sum of H and LE (see

above). Therefore, we corrected for this underestimation in our model by increasing the measured H and LE accordingly assuming that the lack of EBC was equally caused by H and LE (*Twine et al.*, 2000; *Wohlfahrt et al.*, 2009).

Air temperature and water vapour mixing ratio at Scotty Creek were only measured in the mixed layer and, thus, θ_e and q_e were not known. Potential air temperature and q_e of the entrainment layer were derived numerically by minimizing the RMSE of modelled θ_m and q_m versus measured θ_m and q_m at the landscape tower. Friction velocity was used to calculate the initial PBL height (*Rossby and Montgomery*, 1935).

Derivation of roughness parameters and aerodynamic conductance

According to Monin-Obukhov similarity theory z_{0m} and d_0 were derived as follows (see *Stull*, 1988):

$$\frac{z-d_0}{z_{0m}} = e^{[\frac{Uk}{u*}+\Psi_m(\zeta)]} \tag{II.5}$$

where z [m] is the measurement height, k = 0.4 is the von Kármán constant, and Ψ_m is the stability function for momentum, itself a function of the stability parameter $\zeta = \frac{z-d_0}{L}$ with L [m] being the Monin-Obukhov length. Both z_{0m} and d_0 were derived iteratively for each half hour constraining both variables to a mean obstacle height (h_0; m) (*Sonnentag et al.*, 2011). Thus, by replacing z_{0m} and d_0 with h_0, Eq. II.5 is solved for only one unknown variable, h_0. Based on relationships between ho and z_{0m} and d_0 reported in the literature, we assume z_{0m} = 0.1 h_0 and d_0 = 0.66 h_o (e.g., *Brutsaert*, 1982; *Grimmond and Oke*, 1999; *Lindroth*, 1993).

According to *Paulson* (1970) and *Dyer* (1974), Ψ_m under unstable conditions (i.e., $\zeta < 0$) is defined as:

$$\Psi_m = 2ln[0.5(1+x)] + ln[0.5(1+x^2)] - 2arctan[x] + \frac{\pi}{2} \tag{II.6}$$

were $x = (1-16\zeta)^{0.25}$. For stable conditions (i.e. $\zeta > 0$), Ψ_m is expressed according to *Beljaars and Holtslag* (1991):

$$\Psi_m = -b(\zeta - \frac{c}{d})exp(-d\zeta) - a\zeta - \frac{bc}{d} \tag{II.7}$$

where a = 1, b = 0.66, c = 5, and d = 0.35. Ultimately, aerodynamic conductance to heat (g_H; m s^{-1}) was calculated as:

$$g_H = \frac{u*}{\frac{1}{k}[ln(\frac{z-d_0}{z_{0H}}) - \Psi_m(\zeta)} \tag{II.8}$$

where z_{0H} is the roughness length for heat. z_{0H} is larger than z_{0m} because heat transport is less efficient than momentum transport (*Verma*, 1989). In this study, we use a ratio of $\frac{z_{0m}}{z_{0H}} = 7.4$, which is equivalent to $kB^{-1} = 2$ as used in studies of open black spruce stands (*Yang and Friedl*, 2003), savannas and grasslands (*Baldocchi and Ma*, 2013; *Ryu et al.*, 2008), and peatlands (*Humphreys et al.*, 2006; *Runkle et al.*, 2014).

The stability function for heat, Ψ_H, is expressed according to *Paulson* (1970) and *Dyer* (1974) for unstable conditions:

$$\Psi_H = 2ln[0.5(1+y)] \tag{II.9}$$

where $y = (1 - 16\zeta)^{0.5}$ and for stable conditions according to *Beljaars and Holtslag* (1991):

$$\Psi_H = -b(\zeta - \frac{c}{d})exp(-d\zeta) - (1 + \frac{2}{3}a\zeta)^{1.5} - \frac{bc}{d} + 1 \tag{II.10}$$

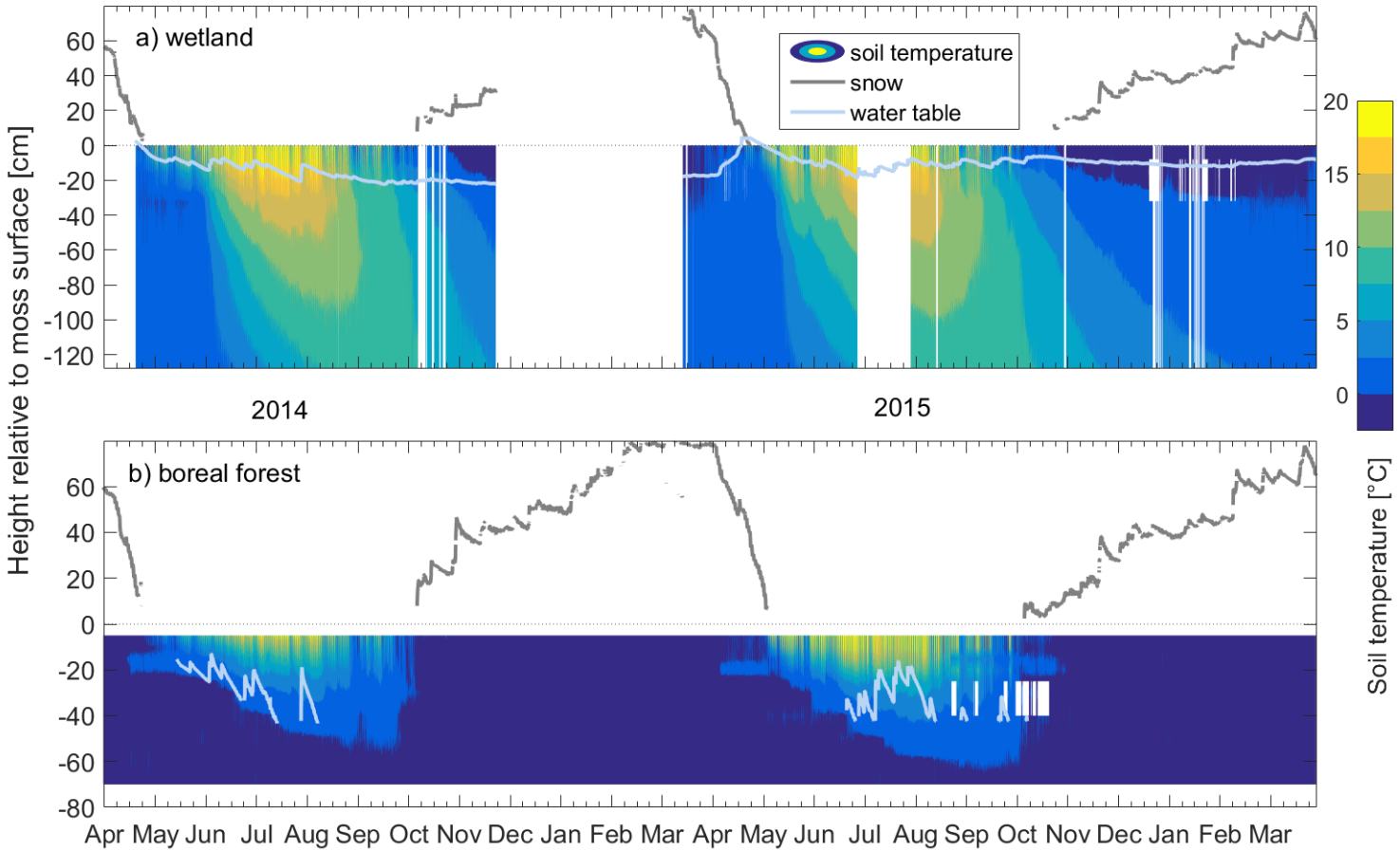

Figure II.2 – Soil temperature profiles between 2014 and 2015 as measured **(a)** in the center of the wetland and **(b)** at the landscape tower on the forested peat plateau. Dark blue colors indicate soil temperatures <0 °C. The grey line shows snow height above the moss surface and the light blue line indicates the position of the water table.

Appendix III

Chapter 4

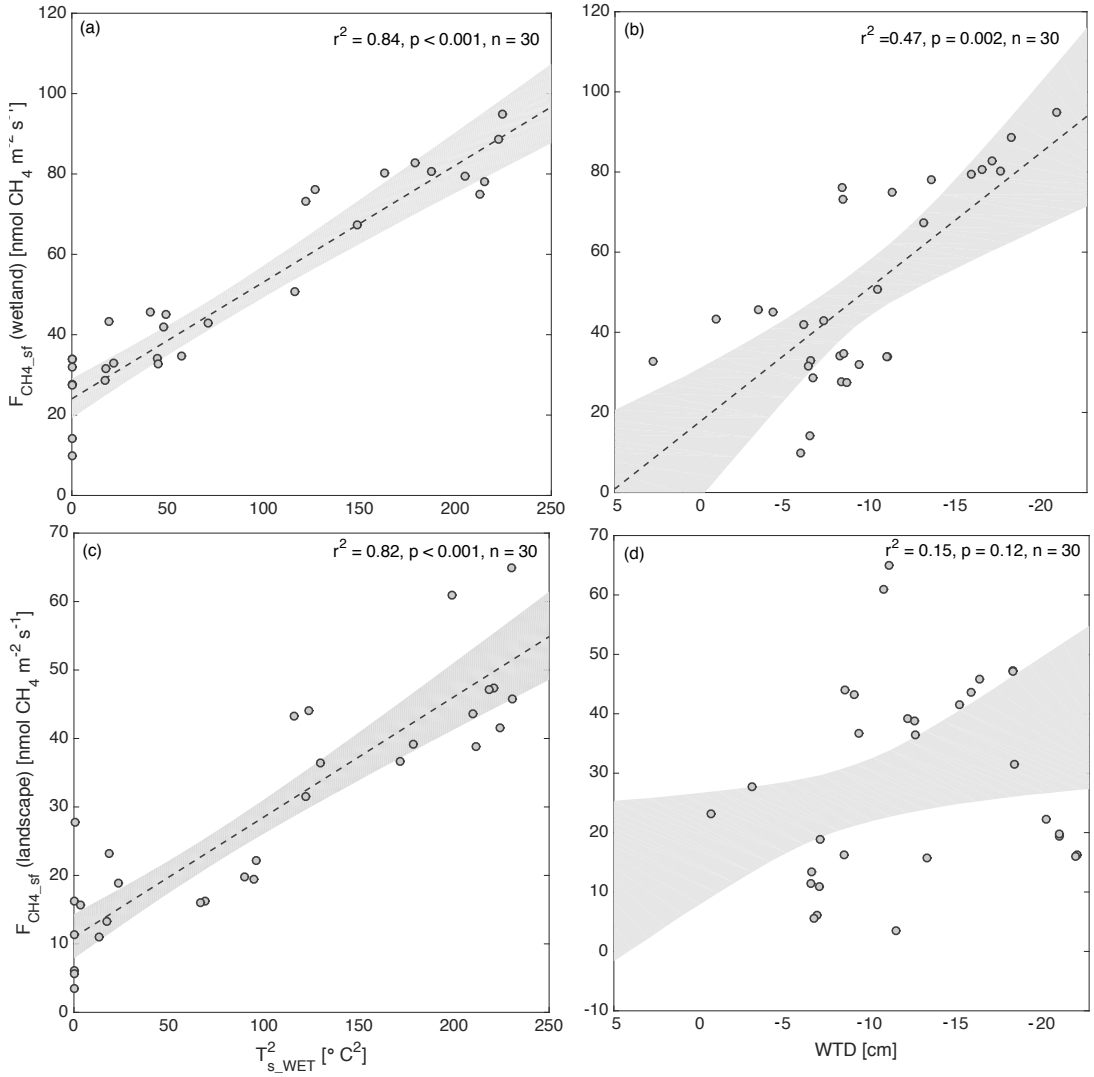

Figure III.1 – Relationship between **(a & c)** squared wetland soil temperature ($T^2_{s\_WET}$), **(b & d)** wetland water table depth (WTD) and the seasonal (> seven days) component of net methane fluxes (F_{CH4_sf}) at **(a & b)** the wetland tower and **(b & d)** the landscape tower. Mean coefficients of determination (r^2) and linear least squares regression lines (dashed) of 10,000 randomly sampled F_{CH4_sf} subsets (n = 30) are shown. The grey shaded area indicates the 95 % confidence interval of the 10,000 regression fits. Dots represent one random F_{CH4_sf} subset.

Appendix IV

Chapter 5

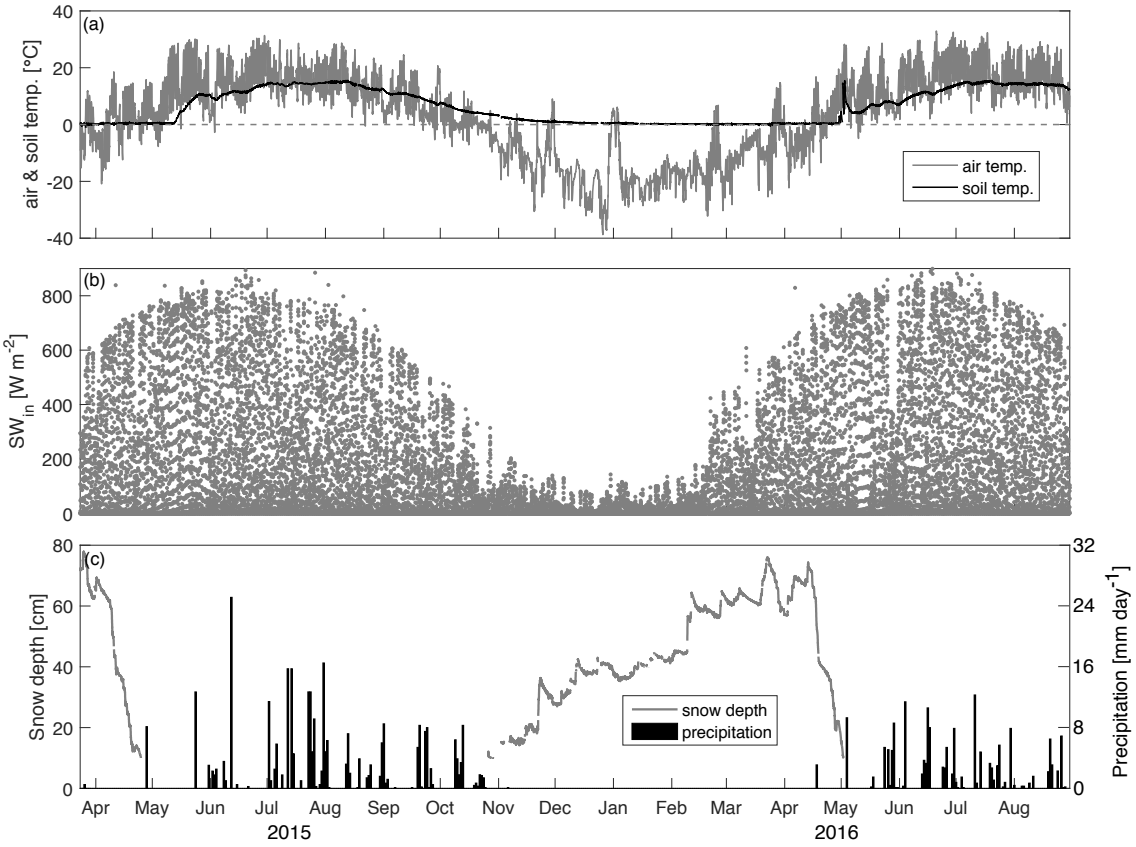

Figure IV.1 – **(a)** Air temperature at 2 m and soil temperature at 32 cm below the moss surface. **(b)** Incoming shortwave radiation (SW_{in}) measured at the landscape tower. **(c)** Snow depth and daily liquid precipitation in the wetland.

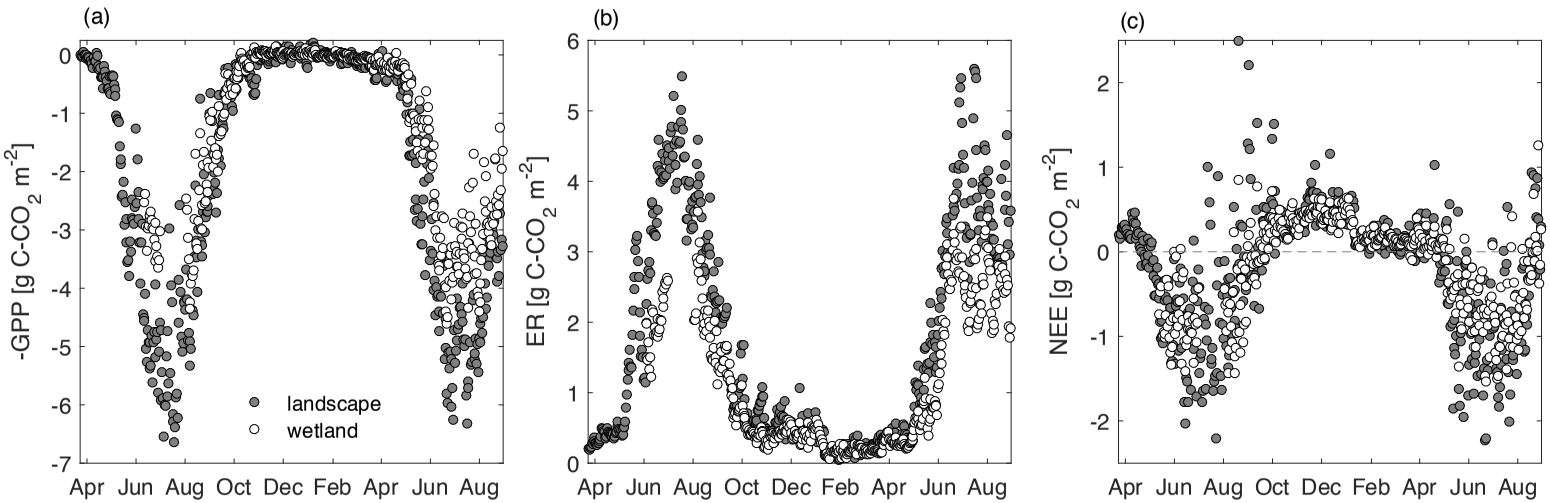

Figure IV.2 – **(a)** Daily gross primary productivity (GPP), **(b)** ecosystem respiration (ER), and **(c)** net ecosystem CO_2 exchange (NEE) for the boreal forest-wetland landscape and the wetland.

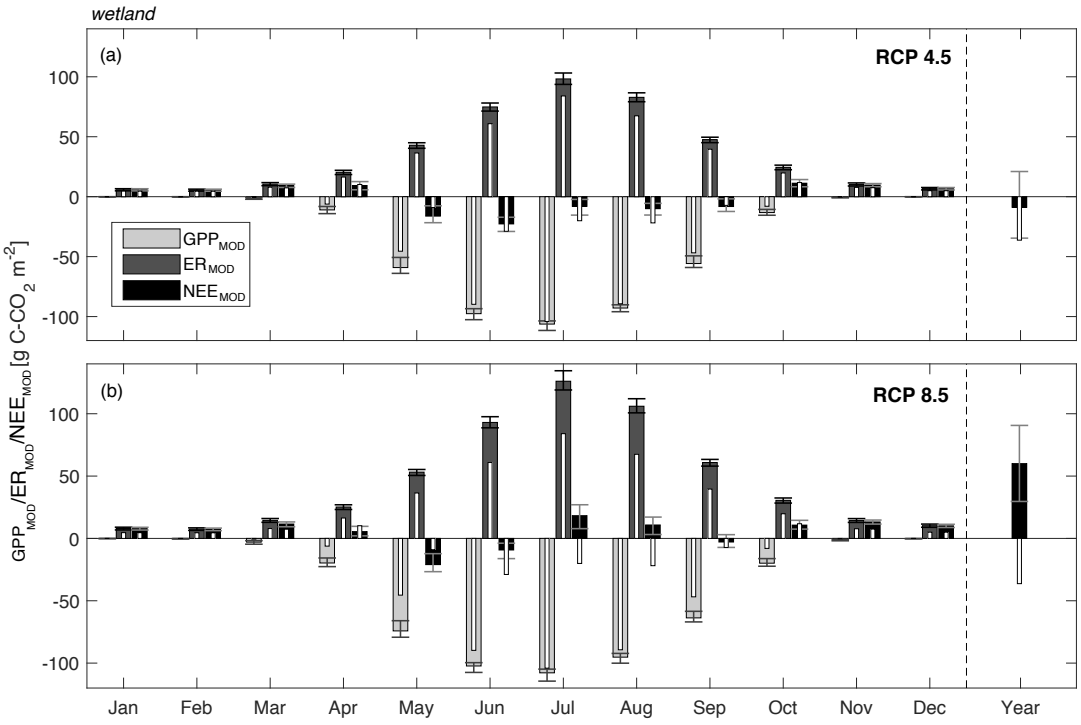

Figure IV.3 – Projections (2091-2100) of monthly modeled gross primary productivity (GPP_{MOD}), ecosystem respiration (ER_{MOD}), and net ecosystem carbon dioxide exchange (NEE_{MOD}) derived from wetland NEE measurements at Scotty Creek **(a)** with the RCP4.5 and **(b)** with the RCP8.5 scenario. For comparison, narrow white bars show recent (2006-2015) GPP_{MOD}, ER_{MOD}, and NEE_{MOD}. Error bars indicate uncertainties (95 % confidence intervals) in the GPP- and ER-model.

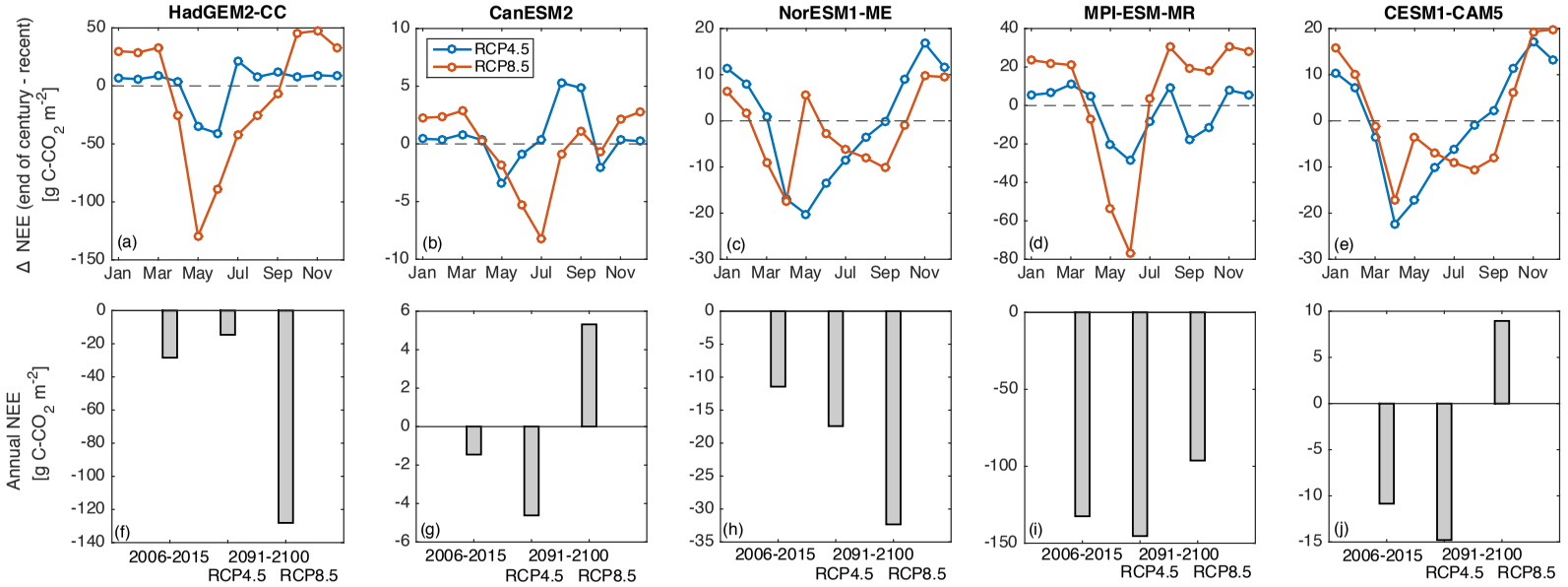

Figure IV.4 – Net ecosystem CO_2 exchange (NEE) from five Earth System Model (ESM, more details in *Friedlingstein et al.* (2014b)) simulations from phase 5 of the Coupled Model Intercomparison Project (CMIP5) for the grid cell comprising Scotty Creek (61°18' N; 121°18' W). **(a-e)** Change in mean monthly NEE between the period 2091 to 2100 and 2006 to 2015 for two Representative Concentration Pathways (RCP): RCP4.5 and RCP8.5. **(f-j)** Mean annual NEE for the same periods and RCPs. Results are shown for the ensemble member r1i1p1. Note that ESMs differ in their spatial resolution (deg): HadGEM2-CC (Met Office Hadley Centre, UK), 1.875x1.25; CanESM2 (Canadian Centre for Climate Modelling and Analysis, Canada), 2.813x2.79; NorESM1-ME (Norwegian Climate Centre, Norway), 2.5x1.895; MPIESM-MR (Max-Plank Institute for Meteorology, Germany), 1.8653x1.875; CESM1-CAM5 (National Center forAtmospheric Research, USA), 0.9424x1.25.

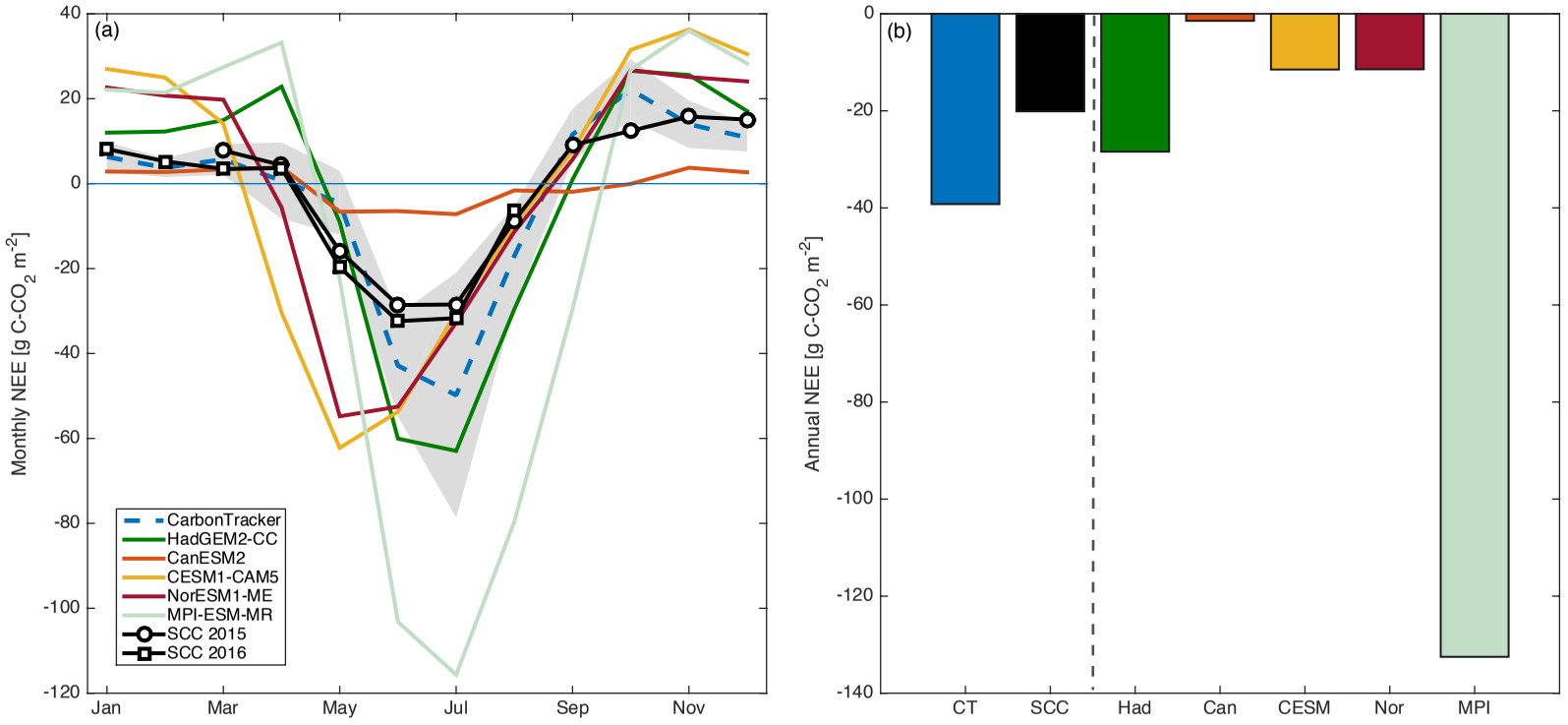

Figure IV.5 – **(a)** Mean monthly and **(b)** mean annual net ecosystem CO_2 exchange (NEE) for the period 2006 to 2015 for the grid cell comprising Scotty Creek derived using atmospheric CO_2 concentrations combined with inverse modeling (CarbonTracker) and using five Earth system models (HadGEM-CC [Had], CanESM2 [Can], CESM-CAM5 [CESM], NorESM1-ME [Nor], and MPI-ESM-MR [MPI]). Grey shaded area illustrates the standard deviation of monthly CarbonTracker NEE. Monthly and annual NEE (August 2015 to July 2016) derived from eddy covariance flux measurements at Scotty Creek is shown for comparison.